=== **TOKAMAKS** ===

Suppression of the Neoclassical Tearing Modes in Tokamaks under Anomalous Transverse Transport Conditions when the Magnetic Well Effect Predominates over the Bootstrap Drive

S. V. Konovalov[1, 2], A. B. Mikhaĭlovskiĭ[2, 3], M. S. Shirokov[2, 4], T. Ozeki[1], and V. S. Tsypin[5]

[1]*Naka Fusion Research Establishment, Japan Atomic Energy Research Institute, Ibaraki 3111-0193, Japan*
[2]*Russian Research Centre Kurchatov Institute, pl. Kurchatova 1, Moscow, 123182 Russia*
[3]*Moscow Institute of Physics and Technology, Institutskiĭ pr. 9, Dolgoprudnyĭ, Moscow oblast, 141700 Russia*
[4]*Plasma Physics Department, Moscow Engineering Physics Institute, Kashirskoe sh. 31, Moscow, 115409 Russia*
[5]*Institute of Physics, University of São Paulo, Rua do Matão, Travessa R, 187, 05508–900, São Paulo, Brazil*
Received June 7, 2004; in final form, August 19, 2004

Abstract—A study is made of the suppression of neoclassical tearing modes in tokamaks under anomalous transverse transport conditions when the magnetic well effect predominates over the bootstrap drive. It is stressed that the corresponding effect, which is called the compound suppression effect, depends strongly on the profiles of the electron and ion temperature perturbations. Account is taken of the fact that the temperature profile can be established as a result of the competition between anomalous transverse heat transport, on the one hand, and longitudinal collisional heat transport, longitudinal heat convection, longitudinal inertial transport, and transport due to the rotation of magnetic islands, on the other hand. The role of geodesic effects is discussed. The cases of competition just mentioned are described by the model sets of reduced transport equations, which are called, respectively, collisional, convective, inertial, and rotational plasmophysical models. The magnetic well is calculated with allowance for geodesic effects. It is shown that, for strong anomalous heat transport conditions, the contribution of the magnetic well to the generalized Rutherford equation for the island width W is independent of W not only in the collisional model (which has been investigated earlier) but also in the convective and inertial models and depends very weakly (logarithmically) on W in the rotational model. It is this weak dependence that gives rise to the compound effect, which is the subject of the present study. A criterion for the stabilization of neoclassical tearing modes by the compound effect at an arbitrary level of the transverse heat transport by electrons and ions is derived and is analyzed for two cases: when the electron heat transport and ion heat transport are both strong, and when the electron heat transport is strong and the ion heat transport is weak. © 2005 Pleiades Publishing, Inc.

1. INTRODUCTION AND GENERAL REVIEW OF THE PROBLEM

The problem of suppressing neoclassical tearing modes (NTMs) in tokamaks is an important issue in the development of the International Tokamak Experimental Reactor (ITER) project [1] because these modes restrict the plasma pressure in long-pulse discharges [2]. The stability of NTMs is governed by their generation by the bootstrap current (bootstrap drive) [3, 4] and also by their response to various effects, in particular, the magnetic well effect (or the effect of the magnetic field line curvature) [5–7]. In this context, it is important to recall the remark made in [8, 9], namely, that the anomalous transverse transport [10, 11] reduces the influence of the magnetic well on NTMs to a lesser extent than does the bootstrap drive. This remark leads to the idea that, when the transverse transport is sufficiently strong, the magnetic well effect can become dominant over the bootstrap drive and thereby completely stabilize NTMs. The present paper is aimed at determining whether such a situation can indeed occur in actual tokamak plasmas. In what follows, the effect in question will be called the compound suppression effect.

The history of the problem at hand is as follows: Fitzpatrick [10], who was the first to study the influence of the anomalous transverse heat transport by electrons on the bootstrap drive of NTMs, introduced the characteristic magnetic island width $W_c \sim (\chi_\perp/\chi_\parallel)^{1/4}$, which is determined by the competition between this transport and the longitudinal heat transport. Here, $\chi_\parallel$ and $\chi_\perp$ are the longitudinal and transverse thermal conductivities. In [10], the coefficient $\chi_\perp$ was assumed to be large enough to be consistent with the assumption that transverse heat transport is anomalous. It was shown that, for sufficiently strong transverse heat transport, $W_c \gg W$, the term describing the bootstrap drive in the generalized Rutherford equation decreases according to the law $(W/W_d)^2$, where $W_d = 1.8W_c$ is a certain effective critical

width. Fitzpatrick's paper [10] stimulated the study of the problem of how much strong transverse heat transport reduces the effect of the magnetic well on the NTMs. This problem was originally investigated on a largely intuitive basis [2]. Sauter *et al.* [2] suggested that the magnetic well effect in question is reduced according to the same law as the bootstrap drive and formulated the suggestion in terms of the coefficient

$$h_1^S(W) = W^2/(W^2 + W_{d,GGJ}^2), \tag{1.1}$$

which should enter the generalized Rutherford equation through the term with the magnetic well. Here, the quantity $W_{d,GGJ}$ is understood as a certain width on the order of W_d and the subscript GGJ stands for Glasser, Greene, and Johnson—the authors of paper [12] on the linear resistive modes. We also supplement coefficient $h_1(W)$ in relationship (1.1) with the superscript S in order to indicate the name of the first of the authors of [2]. A dependence of form (1.1) was then used in [13, 14], in which the width $W_{d,GGJ}$ was taken to be the effective critical width W_d in the expression for the bootstrap drive. Dependence (1.1) gave rise to the opinion that the relative roles played by the magnetic well effect and bootstrap drive are independent of the transverse heat transport. One consequence of this was that, at an arbitrary level of the transverse heat transport under the conditions prevailing in a large-aspect-ratio circular tokamak, the magnetic well effect should be weaker than the bootstrap drive. It is obvious, however, that, if this opinion were true, the compound suppression effect, which is the subject of the present study, would be impossible.

The above remark of [8, 9] is important because it implies, in contrast to the assumption made in [2], that, for strong transverse heat transport, the dependence of the magnetic well effect on W_d is given by the ratio W/W_d. Consequently, for sufficiently large values of the ratio W_d/W, the magnetic well effect can become dominant over the bootstrap drive of NTMs, thereby providing the compound suppression effect.

There is no need to perform calculations in order to reach the conclusion that, as the intensity of the transverse heat transport increases, the magnetic well effect should be weakened to a lesser extent than the bootstrap drive, because this conclusion can be derived from the following two circumstances, which stem from the preceding investigations of the NTMs: First, according to [10, 11], the perturbed plasma pressure at strong transverse heat transport is an oscillating function of the cyclic variable of the magnetic islands. Second, the bootstrap drive is described by averaging the bootstrap current over this variable [10, 11], while the magnetic well effect is associated with the oscillating component of the perturbed plasma pressure (see, e.g., [6, 7]). It is also necessary to keep in mind that averaging an oscillating function over the magnetic surface of an island leads to an additional small factor on the order of W/W_c.

It can then be predicted that, since the weakening of the bootstrap drive is characterized by the square of this ratio, $(W/W_c)^2$, the magnetic well effect should be weakened according to the law W/W_c. It is this qualitative result that was obtained in [8, 9].

The paper by Mikhaĭlovskiĭ [8] was devoted to analyzing a qualitative dependence of the magnetic well effect on the transverse heat transport. In contrast to [8], the paper by Lutjens *et al.* [9] was aimed at quantitative investigation of the effect in which we are interested here. The main result of [9] can be formulated in terms of the parameter Δ'_{eff}, which is an analogue of the standard parameter Δ' in the linear theory of tearing modes [15]. The authors of [9] obtained the following expression for Δ'_{eff}:

$$\Delta'_{eff} = (\Delta'_{eff})^{LLG} \equiv \Delta' + 2^{1/2}\pi^{3/2}D_R/W_d, \tag{1.2}$$

where D_R is the "resistive interchange parameter," which was introduced in [12], and the superscript LLG stands for Lutjens, Luciany, and Garbet—the authors of paper [9]. The above result of [9] was later reproduced in [16].

From what was said above, it might be concluded that the problem of interest has been exhaustively investigated. It is necessary, however, to bear in mind that, according to [17] and earlier studies (in particular, [18–20]), the competition between the transverse and the longitudinal heat transport, which was considered in [9, 16], is not the only mechanism whereby the perturbed temperature profile is established. In addition, according to [17], this mechanism is merely illustrative in character and is unlikely to occur in practice. In [17–20], a number of other mechanisms were considered, which were called convective, inertial, and rotational mechanisms. It would be interesting to derive expressions for Δ'_{eff} for each particular mechanism. This is one of our purposes here.

In order to investigate the stabilizing compound effect, we need to know expressions describing the bootstrap drive and the contribution of the magnetic well to the generalized Rutherford equation for the island width evolution in the case of strong transverse heat transport. The expressions describing the bootstrap drive for all of the mechanisms of interest, specifically, those by which the perturbed temperature profile is established, were obtained earlier (see [17]). This is why the main objective of our study is to calculate the magnetic well effect for each of these mechanisms.

In the context of what was said above, it is clear that our interest lies at the intersection of two lines of research in the theory of NTMs: the one that studies the effects of the anomalous transverse heat transport and the one that deals with the magnetic well effect. In our studies and calculations, we will appeal primarily to the first of these lines, whereas the magnetic well will be treated in terms of a certain free parameter U_{MI}. We will

assume that this parameter is positive, $U_{MI} > 0$, because it is only in this case that the compound suppression effect under consideration is possible.

From relationships (1.1) and (1.2) it is seen that, in [2, 9, 16], the magnetic well effect is described in terms of the parameter D_R, whereas, in the present paper, it is described in terms of the parameter U_{MI}. This naturally raises the question of why we are using the parameter U_{MI} instead of D_R. A detailed answer to this question can be found in [7]; the essence of the problem is as follows. In the theory of magnetic islands, the parameter D_R has a narrower range of applicability than the parameter U_{MI}. The reason is that, in terms of the parameter D_R, this theory is adequate only if the influence of the magnetic shear on the magnetic well effect is ignored, which corresponds to the equality $U_{MI} = -D_R$. The effects of the shear of the magnetic field and of its toroidal character should be taken into account together with the so-called geodesic effects. In this case, one has to deal with three kinds of magnetic well that are described by the parameters U_{MI}, U_0, and U_R. The first of these parameters, U_{MI}, is used in the theory of magnetic islands, and the last two, U_0 and U_R, are relevant to the problems of the ideal and resistive linear modes, respectively. This is why, in using the parameter D_R, which corresponds to the so-called "D_R-approach," the authors of [2, 9, 16] ignored geodesic effects.

It is a mistake to describe the magnetic well in the theory of magnetic islands in terms of the parameter D_R not only without allowance for geodesic effects, as was done in [2, 9, 16], but also with allowance for them (see, e.g., [21]). Meanwhile, turning to the paper by Kotschenreuther *et al.* [5], who studied for the first time the influence of the magnetic field line curvature on magnetic islands, one can see that the generalized Rutherford equation derived there does not contain the parameter D_R. Moreover, it was suggested in [5] that this parameter bears no relation to the physics of magnetic islands. The reason is that the parameter D_R arises in problems related to the modes that occur on characteristic spatial scales on the order of the dimension of the resistive layer [22, 12, 23], while the characteristic spatial scales of magnetic islands exceed this dimension. In [7], it was mentioned that, unfortunately, this physical argumentation was not always taken into account in analyzing magnetic islands.

According to [7], the relationship between D_R and U_{MI} in terms of the parameter $U_R \equiv -D_R$ can be represented in the form

$$U_R = U_{MI} - (H_R + H^2), \qquad (1.3)$$

where H is one more Glasser–Greene–Johnson parameter [12] and H_R is its so-called resistive part (see [7] for details). Both terms in parentheses on the right-hand side of representation (1.3) are positive, so this relationship predicts that, with the replacement of U_{MI} by $-D_R$,

the role of the magnetic well will be less favorable than it really is.

Following [2], the bootstrap drive in [17] was described in terms of a three-channel model in which the quantity Δ_{bs}, characterizing the contribution of the bootstrap current to the generalized Rutherford equation for the evolution of the magnetic island width, was assumed to be the sum of three terms, one being proportional to the plasma density gradient (the density gradient channel), the others being proportional to the electron and ion temperature gradients (the electron and ion temperature gradient channels). A similar representation can be introduced for the quantity Δ_{mw}, which characterizes the contribution of the magnetic well effect to the generalized Rutherford equation:

$$\Delta_{mw} = \sum_{A = n_e, T_e, T_i} \Delta_{mw, A}, \qquad (1.4)$$

where the subscript A denotes the type of the corresponding channel. In our study, we will take into account only the electron and ion temperature gradient channels; i.e., we will consider a two-channel model of the magnetic well with the representation

$$\Delta_{mw} = \sum_{A = T_e, T_i} \Delta_{mw, A}. \qquad (1.5)$$

In view of the above-said, we propose the following formulation of the problem concerning the compound effect in question. Our efforts will be mostly concentrated on calculating the magnetic well effect for sufficiently strong transverse heat transport conditions with allowance for both electron and ion heat transport, which corresponds to the two-channel model described above. After calculating the magnetic well effect in the two-channel model, we will compare the contribution of this effect to the generalized Rutherford equation with the contribution of the bootstrap drive that was calculated in [17] in terms of the same model. We will thus obtain the required information on the stabilizing compound effect. Our analysis will be based on a variety of plasmophysical models, i.e., transport equations describing the plasma behavior in the problems concerning magnetic islands. A summary of the basic transport equations used in our study is given in Appendix A.

In Section 2, we present the basic equations for calculating the magnetic well effect for strong transverse heat transport conditions. In this section, we generalize the approach developed in [7] for weak transverse heat transport conditions. The main result of Section 2 is the evaluation of the contribution of the magnetic well to the generalized Rutherford equation in terms of a spatial integral of the perturbed temperature profile, which is determined by competing effects and thereby depends on the type of transport model that has been invoked to describe the NTMs.

The history of the problem of calculating the perturbed temperature profiles is as follows: For the first time, the temperature profile was calculated numerically by Fitzpatrick [10] in a collisional model (then called the Fitzpatrick model). The first analytical calculation of the temperature profile in the Fitzpatrick model was made in [18], in which, however, merely an approximate (model) expression for the temperature profile was derived. Other results of [18] were a rigorous solution for the temperature profile in the rotational model and a model solution in the convective model. The next step—the evaluation of a model temperature profile in the inertial model—was made in [19]. Finally, in [17], rigorous analytical profiles of the perturbed temperature were obtained in the collisional, convective, and inertial models and also all of the previously calculated rigorous and model temperature profiles were systematized. In [17], it was pointed out that the model expressions for the temperature profiles are far simpler than the corresponding rigorous expressions and thus are far more attractive for qualitative analysis. Note also that, in [18], the problem of finding the temperature profiles was treated in the one-fluid approximation. The first steps to solve this problem in the two-fluid approximation were made in [19, 20]. A fuller treatment of the problem was given in [17]. By analogy with [17], the analysis of Section 2, too, is carried in the two-fluid approximation, although it might seem that some equations from this section were derived using a one-fluid approach.

In Section 3, we calculate rigorous expressions for the magnetic well from the rigorous expressions for the perturbed temperature profiles. The details of these calculations are given in Appendix B. In Appendix C, model expressions for the magnetic well are derived from the model expressions for the temperature profiles.

It is likely that, in [9, 16] too, the analytic expression for the magnetic well in the collisional model [10] was derived using an analytic temperature profile (about which, however, nothing was said in those papers).

In Section 4, we formulate a two-channel model of the magnetic well effect, or, in other words, we derive explicit expressions for the parameters $\Delta_{mw, A}$ in formula (1.5). In Section 5, we present expressions that describe the parameter Δ'_{eff}, which was introduced above through relationship (1.2), for different mechanisms whereby the electron and ion temperature profiles are established. In Section 6, we analyze the stabilizing compound effect. In Section 7, we summarize and discuss the results obtained and make final remarks. Our paper also contains Appendix D, in which we outline the essence of private communication [8].

2. BASIC EQUATIONS FOR CALCULATING THE MAGNETIC WELL EFFECT UNDER STRONG TRANSVERSE HEAT TRANSPORT CONDITIONS

2.1. Approach to Describing the Magnetic Well Contribution to the Generalized Rutherford Equation

We begin with the following generalized Rutherford equation for the evolution of the width of a magnetic island (cf. [7], Eq. (34)):

$$\frac{\partial w}{\partial t} \sim \frac{\Delta'}{4} + \Delta_{bs} + \Delta_{mw} + \Delta_p + \Delta_{ECCD}. \quad (2.1)$$

Here, w is the island half-width; the parameters Δ_{bs} and Δ_{mw} characterize, respectively, the bootstrap drive and the magnetic well effect; and the parameters Δ_p and Δ_{ECCD} account for the polarization current and electron cyclotron current drive (ECCD) [24]—effects that go beyond the scope of the present paper.

The parameter Δ_{mw} is expressed in terms of the magnetic-well-related current J_{mw} by the familiar formula (cf. [7], formula (3.5))

$$\Delta_{mw} = -\frac{2\sqrt{2}}{cs}\frac{Rq}{wB_0}\sum_{\sigma_x}\int_{-1}^{\infty}d\Omega\oint\frac{J_{mw}\cos\xi d\xi}{(\Omega + \cos\xi)^{1/2}}. \quad (2.2)$$

Here, $\sigma_x = \operatorname{sgn} x$; $x = r - r_s$ is the radial deviation from a singular equilibrium magnetic surface $r = r_s$, in whose vicinity a chain of magnetic islands is localized; ξ is the cyclic variable of the island; Ω is the dimensionless magnetic flux function of the magnetic islands; q is the safety factor; R is the major radius of the torus; s is the magnetic shear; B_0 is the equilibrium magnetic field; and c is the speed of light.

The variables ξ and Ω are introduced through the relationships

$$\xi = m\theta - n\zeta - \omega t, \quad (2.3)$$

$$\Omega = -\psi/\tilde{\psi}. \quad (2.4)$$

Here, ψ is the magnetic flux function of the islands,

$$\psi = \tilde{\psi}\cos\xi - x^2 B_0/(2L_s), \quad (2.5)$$

where $L_s \equiv qR/s$ is the shear length, $\tilde{\psi}$ is a positive constant related to the island half-width by the relationship

$$w = 2(L_s\tilde{\psi}/B_0)^{1/2}, \quad (2.6)$$

θ the ζ are the poloidal and toroidal angles, m and n are the poloidal and toroidal mode numbers, and ω is the island rotation frequency.

We restrict ourselves to analyzing a circular or a slightly noncircular tokamak. In these cases, the function J_{mw} satisfies the equation (see [7], Eq. (4.31))

$$\left(\frac{\partial J_{mw}}{\partial\xi}\right)_{\Omega} = -\frac{\sigma_x cs B_0 U_{MI}}{2^{3/2}\pi p_0' qRw(\Omega + \cos\xi)^{1/2}}\left(\frac{\partial p}{\partial\xi}\right)_x, \quad (2.7)$$

where p is the total plasma pressure (i.e., the equilibrium pressure p_0 plus the pressure perturbation) and the prime denotes the derivative with respect to the radial coordinate.

For moderately intense transverse heat transport, the function p has a flattened profile within the separatrix of a magnetic island and turns out to depend solely on the variable Ω (see [7] for details). In this case, relationship (2.2) and Eq. (2.7) yield the following well-known expression for Δ_{mw} (see [7], expression (4.37)):

$$\Delta_{mw} = -1.58 U_{MI}/w, \qquad (2.8)$$

where U_{MI} is the magnetic well of the magnetic islands (which was introduced and explained in [7]).

According to [17], if the transverse heat transport is strong enough, then the main contribution to the parameter Δ_{bs} comes from the range $\Omega \gg 1$. As will be clear later, this is also true for the parameter Δ_{mw}. For $\Omega \gg 1$, Eq. (2.7) can be substantially simplified. First of all, we can make the replacement $(\Omega + \cos\xi)^{1/2} \longrightarrow \Omega^{1/2}$ in the denominator on its right-hand side. We also take into account the fact that, in the (x, ξ) variables, the derivative $(\partial/\partial\xi)_\Omega$ has the form

$$\left(\frac{\partial}{\partial\xi}\right)_\Omega = \left(\frac{\partial}{\partial\xi}\right)_x - \frac{w^2}{4x}\sin\xi\left(\frac{\partial}{\partial x}\right)_\xi. \qquad (2.9)$$

For $\Omega \gg 1$, the second term on the right-hand side of this expression is small in comparison to the first term, so Eq. (2.7) reduces to

$$\left(\frac{\partial J_{mw}}{\partial\xi}\right)_x = -\frac{\sigma_x cs B_0 U_{MI}}{2^{3/2}\pi p_0' qRw\Omega^{1/2}}\left(\frac{\partial p}{\partial\xi}\right)_x. \qquad (2.10)$$

Let us now take into account that the range $\Omega \gg 1$ corresponds to the linear region of the magnetic islands. For this region, we can make the replacement $p \longrightarrow \tilde{p}$ (where $\tilde{p}$ is the perturbed plasma pressure) on the right-hand side of Eq. (2.10) and, moreover, we can use the representation

$$\tilde{p}(x, \xi) = p_c(x)\cos\xi + p_s(x)\sin\xi, \qquad (2.11)$$

where $p_c(x)$ and $p_s(x)$ are the cosinusoidal and sinusoidal components of the pressure perturbation amplitude. It should be noted that, in the Fitzpatrick model, the function $p_s(x)$ is identically zero (see [17] for details). Noting that, according to relationship (2.2), the only contributor to Δ_{mw} is the function $p_c(x)$, we obtain from Eq. (2.10) the expression

$$J_{mw} = -\frac{c B_0 U_{MI}}{4\pi p_0' L_s x}p_c(x)\cos\xi. \qquad (2.12)$$

Substituting expression (2.12) into relationship (2.2) and bearing in mind that $\Omega \gg 1$, we arrive at the formula

$$\Delta_{mw} = \frac{U_{MI}B_0}{\tilde{\psi}L_s p_0'}\int_0^\infty \frac{p_c(x)}{x}dx. \qquad (2.13)$$

If we calculate the function $p_c(x)$ in some particular plasmophysical model, we can obtain an expression for the parameter Δ_{mw} in this model for the case of sufficiently strong transverse heat transport. Matching the resulting expression with formula (2.8) for Δ_{mw}, we can then evaluate the parameter Δ_{mw} qualitatively for arbitrarily intense transverse heat transport.

We consider the plasmophysical models that were studied in [17] (see Appendix A). These models are based on the assumptions that the equilibrium plasma density is uniform, $n_0 = \text{const}$, and that the plasma density perturbation is negligibly small. Under these assumptions, we can make the following substitution in expression (2.13):

$$p_c(x)/p_0' \longrightarrow [T_c^e(x) + T_c^i(x)]/(T_{0e}' + T_{0i}'), \qquad (2.14)$$

where the cosinusoidal component $T_c^\alpha(x)$ of the electron or ion temperature perturbation is determined in essentially the same way as in representation (2.11) and T_{0e} and T_{0i} are the electron and ion equilibrium temperatures. Note that, in [17], use was made not of the variable x but of the dimensionless variable u, which is related to x by the relationship

$$u = 2^{3/2}x/W, \qquad (2.15)$$

where $W = 2w$ is the island width.

With relationships (2.6) and (2.15) and substitution (2.14), expression (2.13) reduces to

$$\Delta_{mw} = \sum_{\alpha = e, i} \Delta_{mw}^\alpha, \qquad (2.16)$$

where

$$\Delta_{mw}^\alpha = \frac{16 U_{MI}^\alpha}{T_{0\alpha}'}\int_0^\infty \frac{T_c^\alpha(u)}{u}du, \qquad (2.17)$$

the partial αth components U_{MI}^α of the parameter U_{MI} are given by the relationship

$$U_{MI}^\alpha = \frac{T_{0\alpha}'}{T_{0e}' + T_{0i}'}U_{MI}, \qquad (2.18)$$

and the parameters Δ_{mw}^α characterize partial contributions to the magnetic well effect.

In [17], the functions T_c^α were represented as

$$T_c^\alpha(u) = -\frac{T'_{0\alpha} W}{2^{5/2}} y^\alpha(u), \qquad (2.19)$$

where the functions $y^\alpha(u)$ are different in different plasmophysical models; i.e., they are determined by the mechanism whereby the temperature profile is established. Substituting representation (2.19) into expression (2.17) puts the latter into the form

$$\Delta_{mw}^\alpha = -2^{3/2} \frac{U_{MI}^\alpha}{W} k_{mw}^\alpha, \qquad (2.20)$$

where

$$k_{mw}^\alpha = \int_0^\infty \frac{y^\alpha(u)}{u} du. \qquad (2.21)$$

Hence, in each particular plasmophysical model, the derivation of an expression for Δ_{mw}^α reduces to a calculation of the integral k_{mw}^α with the corresponding function $y^\alpha(u)$. This calculation is the subject of Section 3 (see also Appendices B, C).

2.2. Characteristic Expressions for the Magnetic Well

2.2.1. Expressions for U_{MI} without allowance for geodesic effects. When the geodesic effects are ignored, the parameter U_{MI} reduces to

$$U_{MI} = U_0, \qquad (2.22)$$

where U_0 is the magnetic well in the theory of linear modes [25]. Accordingly, the partial components U_{MI}^α of this parameter are equal to

$$U_{MI}^\alpha = U_0^\alpha, \qquad (2.23)$$

where U_0^α are the partial components of U_0. For a slightly noncircular tokamak characterized by the ellipticity e and triangularity τ, we can then obtain (see [7] for details)

$$U_{MI}^\alpha = U_0^\alpha = \frac{\varepsilon^2 \beta_{p\alpha} r_s}{L_{T\alpha} s^2} \left(1 - \frac{1}{q^2} + 6 \frac{e\tau}{\varepsilon} \right), \qquad (2.24)$$

where $\varepsilon = r/R$ is the inverse aspect ratio, $\beta_{p\alpha}$ are the partial poloidal betas, and $L_{T\alpha} = -T_{0\alpha}/T'_{0\alpha}$.

Note that Lutjens *et al.* [9] described the parameter D_R by the expression that follows from relationships (2.22)–(2.24) with $e = \tau = 0$, i.e., by [23]

$$D_R = -U_0 = -\varepsilon^2 \beta_p r_s (1 - 1/q^2)/(L_T s^2), \qquad (2.25)$$

which, according to [23], agrees with the corresponding expression from [22].

2.2.2. Expressions for U_{MI} with allowance for geodesic effects. One of the simplest cases in which the geodesic effects cause the parameters U_{MI}, U_R, and U_0 to differ from one another corresponds to the second stability region of the ideal ballooning modes (see [7] for details). For a circular tokamak with a parabolic plasma pressure profile, the expressions for these parameters in the second stability region are presented in [7].

In the lower part of the second stability region (see [7] for details), the parameters satisfy the order-of-magnitude relationships

$$U_{MI} \simeq U_R \simeq U_0 \simeq 1. \qquad (2.26)$$

It should be noted that, in this case, the parameter U_R can be negative, while the parameter U_{MI} is positive. This implies that the linear resistive interchange modes can be unstable in the second stability region of the ideal ballooning modes, whereas the magnetic well has a stabilizing effect on the NTMs. Thereby, as was pointed out in [7], the D_R approach, which predicts destabilization, turns out to contradict the predictions of the ideal NTM theory.

2.2.3. Canonical expressions for U_{MI}. We represent the parameter U_{MI} in the form

$$U_{MI} = \frac{\varepsilon^{1/2} \beta_p r_s}{s L_T} f(r_s), \qquad (2.27)$$

where $f(r_s)$ is a form-factor. Without allowance for geodesic effects, relationship (2.24) yields

$$f(r_s) = \frac{\varepsilon^{3/2}}{s} \left(1 - \frac{1}{q^2} + \frac{6e\tau}{\varepsilon} \right). \qquad (2.28)$$

On the other hand, referring to [7], we see that the form-factor in the second stability region of the ideal ballooning modes is described not by expression (2.28) but by the expression

$$f(r_s) = \frac{\varepsilon^{3/2}}{s} \left[1 - \frac{1}{q^2} + \frac{\hat\alpha}{4\varepsilon} \left(s + \frac{3}{32} \hat\alpha^2 \right) \right], \qquad (2.29)$$

where $\hat\alpha = 4\varepsilon\beta_p$. Formulas (2.27) with the form-factor $f(r_s)$ given by expressions (2.28) or (2.29) can be called canonical expressions for U_{MI}.

2.3. Relative Role of the Magnetic Well Effect and Bootstrap Drive at Weak Transverse Heat Transport

We assume that, for weak transverse heat transport, the parameter Δ_{bs} exceeds the parameter Δ_{mw}, so we can write the condition

$$\Delta_{bs}^{(0)} > (-\Delta_{mw}^{(0)}), \qquad (2.30)$$

where the superscript (0) signifies the parameter values for weak transverse heat transport. According to [17], the parameter $\Delta_{bs}^{(0)}$ is described by the relationship

$$\Delta_{bs}^{(0)} = \frac{1}{W}(0.40\beta_{pe}C_{bs,\,e} - 0.17\beta_{pi}C_{bs,\,i}), \qquad (2.31)$$

where

$$C_{bs,\,\alpha} = 2.46 \times 2c_{bs}\varepsilon^{1/2}r_s/(sL_{T_\alpha}), \qquad (2.32)$$

with $c_{bs} = 0.79$. Using expressions (2.8) and (2.31), we reduce condition (2.30) to

$$U_{MI} < 1.23\frac{\varepsilon^{1/2}r_s}{s}\left(0.40\frac{\beta_{pe}}{L_{Te}} - 0.17\frac{\beta_{pi}}{L_{T_i}}\right). \qquad (2.33)$$

In the particular case in which $T_{0e} = T_{0i}$ and the parameter U_{MI} is given by expression (2.27), condition (2.33) becomes

$$f(r_s) < 1.23 \times 0.23 = 0.28, \qquad (2.34)$$

where the form-factor $f(r_s)$ is described by relationships (2.28) and (2.29). In the first case, namely, when the form-factor is given by relationship (2.28), assuming that the triangularity τ is sufficiently small and the shear is sufficiently large, $s \simeq 1$, we have $f(r_s) \simeq \varepsilon^{3/2}$. This ensures that condition (2.34) is satisfied under the additional assumption of a sufficiently small ε. The possibility that this condition may fail to hold with increasing triangularity and decreasing shear was discussed in [6]. In the lower part of the second stability region of the ideal ballooning modes, when $\beta_p \simeq 1/\varepsilon$ and $s \simeq \varepsilon^{2/3}$ (see [7] for details), expression (2.29) yields the estimate $f(r_s) \simeq \varepsilon^{-1/6}$. In this case, condition (2.34) is violated. This is why the lower part of the second stability region will be excluded from further analysis, for simplicity.

3. CALCULATIONS OF THE MAGNETIC WELL EFFECT AT STRONG TRANSVERSE HEAT TRANSPORT

3.1. Collisional Model

In the collisional model (see Appendix A), two expressions for the function $y^\alpha(u)$ were obtained—model [18] and rigorous. The rigorous expression was derived in [17] from the rigorous solution to the corresponding heat conduction equation for the perturbed temperature. Of course, the rigorous expression for $y^\alpha(u)$ is better suited for our purposes here. At the same time, calculating the integrals k_{mw}^α by using the model expression for $y^\alpha(u)$ produces results fairly close to those reached with the rigorous expression. This is an additional argument showing that it is expedient to use simple analytic expressions for the perturbed temperature profile in studying the physics of NTMs.

According to [17], the rigorous expression for the function $y^\alpha(u)$ in the collisional model has the form

$$y^\alpha(u) = \lambda_{col}(t)/(2\Omega_{col})^{1/2}. \qquad (3.1)$$

Here, $\Omega_{col} = (W_{col}/W)^2$, where

$$W_{col} = 2^{3/2}\left(\frac{L_s^2\chi_\perp}{k_y^2\chi_\|}\right)^{1/4}, \qquad (3.2)$$

with $k_y = m/r_s$ being the poloidal component of the wave vector. The function $\lambda_{col}(t)$ is defined by the relationship

$$\lambda_{col}(t) = t^{1/4}\left[I_{1/4}(t)\int_t^\infty K_{1/4}(t_1)t_1^{1/4}dt_1 \right.$$
$$\left. + K_{1/4}(t)\int_0^t I_{1/4}(t_1)t_1^{1/4}dt_1\right], \qquad (3.3)$$

where the variable t is defined as $t = u^2/(2\Omega_{col})$ and $I_{1/4}(t)$ and $K_{1/4}(t)$ are Bessel functions of the imaginary arguments of the first and second kinds, respectively.

With relationships (3.1) and (3.2), expression (2.21) becomes (see Appendix B for details)

$$k_{mw}^\alpha = k_{mw}^{col} \equiv \pi^{3/2}/(4\Omega_{col}^{1/2}) = 1.39/\Omega_{col}^{1/2}. \qquad (3.4)$$

This expression, together with expression (2.20), justifies and quantitatively refines the qualitative analysis carried out in Appendix D (see formula (D.13)).

3.2. Convective Model

In the convective model (see Appendix A), as in the collisional model (which was considered in Section 3.1), we deal with the rigorous expression for the function $y^\alpha(u)$ that was derived in [17] and with the model expression derived in [18, 20]. Correspondingly, in the convective model, we can obtain both rigorous and model expressions for k_{mw}^α.

According to [17], the rigorous expression for the function $y^\alpha(u)$ has the form

$$y^\alpha(u) = \operatorname{Re} Y(u). \qquad (3.5)$$

Here,

$$Y(u) = \frac{(\sqrt{3} + i) \times 2^{1/3}t^{1/3}}{3^{2/3}\Omega_{conv}^{1/2}}$$
$$\times \left[I_{1/3}(t)\int_t^\infty K_{1/3}(t_1)dt_1 + K_{1/3}(t)\int_0^t I_{1/3}(t_1)dt_1\right], \qquad (3.6)$$

where $t = 2^{1/2}(1 + i)\alpha_{conv}^{3/4}u^{3/2}/3$, $\alpha_{conv} = 2^{4/3}/\Omega_{conv}$, $\Omega_{conv} = (W_{conv}/W)^2$;

$$W_{conv} = \left(\frac{2^{11/2}\chi_\perp L_s}{c_s k_y}\right)^{1/3}, \quad (3.7)$$

and the generalized speed of sound c_s is introduced by the relationship $c_s = [5T_0/(3M)]^{1/2}$, with M being the mass of a particle.

Using expressions (2.21) and (3.5), we find (see Appendix B for details)

$$k_{mw}^\alpha = k_{mw}^{conv} \equiv 2.14/\Omega_{conv}^{1/2}, \quad (3.8)$$

which is qualitatively equivalent to expression (3.4) with the replacement $W_{col} \longrightarrow W_{conv}$.

3.3. Inertial Model

In the inertial model (see Appendix A), as in Sections 3.1 and 3.2, we again have two expressions for the function $y^\alpha(u)$, specifically, the model expression derived in [19] and the rigorous one, derived in [17].

According to [17], the function $y^\alpha(u)$ is given by rigorous expression (3.5) with $Y(u)$ of the form

$$Y(u) = -\frac{i\pi}{2^{3/2}a^{3/2}\Omega_i^2}t^{1/4}$$
$$\times \left[I_{1/4}(t)\int_t^\infty t_1^{1/4}K_{1/4}(t_1)dt_1 + K_{1/4}(t)\int_0^t t_1^{1/4}I_{1/4}(t_1)dt_1\right]. \quad (3.9)$$

Here, $t = au^2$, $a = 2^{-3/2}(1 - i)\alpha_i$, $\alpha_i^2 = 2^{1/2}\pi/\Omega_i^2$, $\Omega_i = W_{inert}^2/W^2$;

$$W_{inert} = \left(\frac{128\sqrt{2}\pi}{3}\frac{\omega L_s^2\chi_\perp}{k_y^2 c_{is}^2}\right)^{1/4}, \quad (3.10)$$

and c_{is} is the speed of sound defined as $c_{is} = (T_0/M_i)^{1/2}$, with M_i being the mass of an ion.

Substituting expression (3.9) into expression (2.21) and integrating the resulting formula yields (see Appendix B for details)

$$k_{mw}^\alpha = k_{mw}^{inert} \equiv 1.87/\Omega_i^{1/2}, \quad (3.11)$$

which is qualitatively analogous to expressions (3.4) and (3.8) with the replacement $(W_{col}, W_{conv}) \longrightarrow W_{inert}$.

3.4. Rotational Model

In the rotational model (see Appendix A), in contrast to the models considered in Sections 3.1–3.3, we deal only with the rigorous solution for the function $y^\alpha(u)$.

According to [17, 18], the rigorous expression for this function follows from the equation

$$\frac{dy^\alpha}{du} = -\frac{2^{5/2}\tau(z)}{\pi\Omega_r}, \quad (3.12)$$

where $\Omega_r = W_{rot}^2/W^2$,

$$W_{rot} = \left(\frac{128\sqrt{2}}{3\pi}\frac{\chi_\perp}{\omega}\right)^{1/2}, \quad (3.13)$$

$$z = [2^{5/2}/(\pi\Omega_r)]^{1/2}u. \quad (3.14)$$

The general expression for the function $\tau(z)$, which is required for calculating the bootstrap drive (see [17] for details), can be found in [17, 18]. In the problem under discussion here, this expression reduces to

$$\tau(z) = -e^{-z}\sin z\ln z_0, \quad (3.15)$$

where $z_0 \simeq 1/\Omega_r$. Using formulas (2.21), (3.12), (3.14), and (3.15), we find (see Appendix B for details)

$$k_{mw}^\alpha = k_{mw}^{rot} \equiv 2^{5/4}\ln^2(W_{rot}/W)/(\pi\Omega_r)^{1/2}$$
$$= \frac{1.34}{\Omega_r^{1/2}}\ln^2\left(\frac{W_{rot}}{W}\right). \quad (3.16)$$

We see that, in contrast to expressions (3.4), (3.8), and (3.11), the parameter k_{mw}^{rot} contains a coefficient with the squared logarithm of the ratio W_{rot}/W. This coefficient arises from the logarithmic dependence of the right-hand side of Eq. (3.12) on the parameter z_0 (see expression (3.15)).

3.5. Model Expressions for k_{mw}^α

Along with rigorous expressions (3.4), (3.8), and (3.11) for the parameter k_{mw}, model expressions for this parameter can also be derived in the collisional, convective, and inertial models. Using formulas (2.21), (C.1), (C.4), and (C.7), we obtain

$$k_{mw}^\alpha = (k_{mw}^{col})^{model} = \pi/(2u_{col})$$
$$\equiv \pi/(2^{5/4}3^{1/4}\Omega_{col}^{1/2}) = 1.00/\Omega_{col}^{1/2}, \quad (3.17)$$

$$k_{mw}^\alpha = (k_{mw}^{conv})^{model} = \pi/(2u_{conv})$$
$$\equiv \pi/(2^{5/6}5^{1/6}\Omega_{conv}^{1/2}) = 1.35/\Omega_{conv}^{1/2}, \quad (3.18)$$

$$k_{mw}^\alpha = (k_{mw}^{inert})^{model} = 1.73/\Omega_i^{1/2}. \quad (3.19)$$

As is seen, formulas (3.17)–(3.19) are in qualitative agreement with formulas (3.4), (3.8), and (3.11), respectively.

3.6. Basic Expressions for $\Delta_{mw}^{\alpha j}$ in the Case of Strong Transverse Heat Transport

In accordance with the above plasmophysical models, we introduce the parameters $\Delta_{mw}^{\alpha j}$, where the superscript j means $j = (\text{col, conv})$ for $\alpha = e$ and $j = (\text{inert, rot})$ for $\alpha = i$. For strong transverse heat transport, these parameters have the form

$$\Delta_{mw}^{\alpha j} = -h^{\alpha j} U_{MI}^{\alpha}/W_j, \tag{3.20}$$

where

$$W_j = (W_{\text{col}}, W_{\text{conv}}, W_{\text{inert}}, W_{\text{rot}}), \tag{3.21}$$

$$h^{\alpha j} = (h^{\text{col}}, h^{\text{conv}}, h^{\text{inert}}, h^{\text{rot}}). \tag{3.22}$$

The quantities W_j are the characteristic island widths determined by the corresponding competing mechanisms and given by formulas (3.2), (3.7), (3.10), and (3.13), respectively. The quantities $h^{\alpha j}$ are related to $k_{mw}^{\alpha j}$ by the relationships

$$h^{\alpha j} = 2^{3/2} W_j k_{mw}^{\alpha j}/W, \tag{3.23}$$

where

$$k_{mw}^{\alpha j} = (k_{mw}^{\text{col}}, k_{mw}^{\text{conv}}, k_{mw}^{\text{inert}}, k_{mw}^{\text{rot}}). \tag{3.24}$$

Using formulas (3.4), (3.8), (3.11), and (3.16), we can write relationships (3.23) as

$$h^{\alpha j} = [3.93, 6.05, 5.28, 3.79\ln^2(W_{\text{rot}}/W)]. \tag{3.25}$$

Note that the first of relationships (3.25) can be represented in the form

$$h^{\alpha, \text{col}} = \pi^{3/2}/2^{1/2}. \tag{3.26}$$

Hence, the parameters $\Delta_{mw}^{\alpha j}$ are determined by formulas (3.20), (3.21), and (3.25).

According to the expressions for integrals (3.24), representations (3.25) for the quantities $h^{\alpha j}$ can be derived from the rigorous profiles of the temperature perturbation. In the collisional, convective, and inertial models, we have not only the rigorous expressions for integrals (3.24) but also model expressions (3.17)–(3.19), which were obtained for $k_{mw}^{\alpha j}$ from the model profiles of the temperature perturbation. For such profiles, we must use, instead of representations (3.25), the representations

$$h^{\alpha j} = (h^{\alpha j})^{\text{model}} = (2.83, 3.02, 4.89). \tag{3.27}$$

As is seen, the approximate expressions for the coefficients $(h^{\alpha j})^{\text{model}}$ calculated from the model temperature profiles agree qualitatively with the rigorous expressions.

On the whole, formulas (3.20) and (3.25)–(3.27) show that, for strong transverse heat transport, the parameters $\Delta_{mw}^{\alpha j}$ are independent of the magnetic island width W in the collisional, convective, and inertial models and depend on W logarithmically in the rotational model.

4. TWO-CHANNEL MODEL OF THE MAGNETIC WELL EFFECT

It is obvious that, within the above approximations, the role of the parameters $\Delta_{mw, A}$ in formula (1.5) is played by the parameters Δ_{mw}^{α} introduced by expressions (2.16). For weak transverse heat transport, these parameters can be deduced by using formulas (2.8) and (2.18). For arbitrarily intense transverse heat transport, we obtain

$$\Delta_{mw}^{\alpha} = -\frac{3.16 U_{MI}^{\alpha}}{W + W_{mw, \alpha}}. \tag{4.1}$$

Here,

$$\frac{1}{W_{mw, \alpha}} = \sum_j \frac{1}{W_{j, mw, \alpha}}, \tag{4.2}$$

where the summation is carried out over the competing mechanisms and the subscript means $j = (\text{col, conv})$ for $\alpha = e$ and $j = (\text{inert, rot})$ for $\alpha = i$. The quantities $W_{j, mw}$ (the subscript α is omitted for brevity) are given by the expressions

$$W_{j, mw} = (W_{\text{col}, mw}, W_{\text{conv}, mw}, W_{\text{inert}, mw}, W_{\text{rot}, mw}), \tag{4.3}$$

where, in accordance with formulas (3.20)–(3.26), we have

$$(W_{\text{col}, mw}, W_{\text{conv}, mw}, W_{\text{inert}, mw}, W_{\text{rot}, mw})$$
$$= \{0.80 W_{\text{col}}, 0.52 W_{\text{conv}}, 0.60 W_{\text{inert}}, \tag{4.4}$$
$$0.83 W_{\text{rot}}/[1 + \ln^2(W_{\text{rot}}/W)]\}.$$

Here, the quantities W_{mw} play the same role as $W_{d, GGJ}$ in relationship (1.1).

Together with expressions (2.16), formulas (4.1)–(4.4) determine the parameter Δ_{mw} in the two-channel model of the magnetic well effect.

5. EXPRESSIONS FOR Δ'_{eff}

5.1. General Expressions for Δ'_{eff}

Following [9, 16], we introduce, by analogy with relationship (1.2), the parameter Δ'_{eff}, which includes the conventional parameter Δ' and takes into account the magnetic well effect for strong transverse heat

transport. According to Eq. (2.1), the expression for Δ'_{eff} that generalizes relationship (1.2) has the form

$$\Delta'_{\text{eff}} = \Delta' + 4 \sum_{\alpha = e, i} \Delta^\alpha_{mw}. \tag{5.1}$$

In this case, formula (4.1) reads

$$\Delta^\alpha_{mw} = -\frac{3.16 U^\alpha_{MI}}{W_{mw, \alpha}}, \tag{5.2}$$

so expression (5.1) becomes

$$\Delta'_{\text{eff}} = \Delta' - 4 \times 3.16 \sum_{\alpha = e, i} \frac{U^\alpha_{MI}}{W_{mw, \alpha}}. \tag{5.3}$$

For $U^\alpha_{MI} > 0$, we have $\Delta'_{\text{eff}} < \Delta'$.

5.2. Expressions for Δ'_{eff} without Allowance for Geodesic Effects

Taking into account expressions (2.22) and (2.23) and ignoring geodesic effects, we reduce expression (5.3) to

$$\Delta'_{\text{eff}} = \Delta' - 4 \times 3.16 \sum_{\alpha = e, i} \frac{U^\alpha_0}{W_{mw, \alpha}}. \tag{5.4}$$

In the collisional model ($j = \text{col}$), we ignore the effects associated with the ions and take into account expression (2.25) to obtain, instead of expression (5.4), the expression

$$\Delta'_{\text{eff}} = (\Delta'_{\text{eff}})^{\text{col}} = \Delta' + 2^{3/2} \pi^{3/2} D_R / W_{\text{col}}. \tag{5.5}$$

A comparison between expressions (5.5) and (1.2) shows that the parameter $(\Delta'_{\text{eff}})^{\text{col}}$ predicted by our analysis is two times larger than that obtained in [9].

5.3. Estimate of Δ'_{eff} with Allowance for Geodesic Effects

Formulas (2.26) and (5.3) yield the estimate

$$(\Delta'_{\text{eff}})^j \simeq \Delta' + O(1/W_j), \tag{5.6}$$

where j stands for the dominant mechanism among the competing ones. Hence, estimate (5.6) shows that, by virtue of the relationship $\Delta' \simeq 1/r_s$, the renormalization of the parameter Δ' in the second stability region of the ideal ballooning modes is essential if, in order of magnitude, we have $W_j \lesssim r_s$.

6. INVESTIGATION OF THE COMPOUND SUPPRESSION EFFECT

For the transverse heat transport conditions under consideration, the generalized Rutherford equation has the form (cf. Eq. (2.1))

$$\frac{\tau_s}{r_s} \frac{dW}{dt} = r_s [\Delta' + 4(\Delta_{bs} + \Delta_{mw} + \Delta_p + \Delta_{ECCD})]. \tag{6.1}$$

Here, τ_s is the resistive time [2] and the rest of the notation has been introduced above. The parameter Δ_{mw} is given by formulas (2.16) and (4.1), and the parameter Δ_{bs} represents the contribution of the bootstrap current; according to [17], this contribution is described by the expression

$$\Delta_{bs} = 2.46 \times 2 c_{bs} \frac{W \varepsilon^{1/2} r_s}{s}$$
$$\times \left[\frac{0.40 \beta_{pe}}{L_{Te}(W^2 + W^2_{d, e})} - \frac{0.17 \beta_{pi}}{L_{Ti}(W^2 + W^2_{d, i})} \right]. \tag{6.2}$$

Here,

$$\frac{1}{W^2_{d, \alpha}} = \sum_j \frac{1}{W^2_{d, \alpha, j}}, \tag{6.3}$$

where the summation is carried out over $j = (\text{col}, \text{conv})$ for electrons ($\alpha = e$) and over $j = (\text{inert}, \text{rot})$ for ions ($\alpha = i$). According to [17], the quantities $W_{d, j}$ are equal to

$$(W_{d, \text{col}}, W_{d, \text{conv}}, W_{d, \text{inert}}, W_{d, \text{rot}})$$
$$= (1.80 W_{\text{col}}, 1.27 W_{\text{conv}}, 1.47 W_{\text{inert}}, 1.17 W_{\text{rot}}). \tag{6.4}$$

The general criterion for suppression of the NTMs by the compound effect has the form

$$(-\Delta_{mw}) > \Delta_{bs}. \tag{6.5}$$

Using formulas (2.16), (4.1), and (6.2), we convert criterion (6.5) into the form

$$\sum_{\alpha = e, i} \frac{U^\alpha_{MI}}{W + W_{mw, \alpha}}$$
$$> 1.23 \frac{W \varepsilon^{1/2} r_s}{s} \left[\frac{0.40 \beta_{pe}}{L_{Te}(W^2 + W^2_{d, e})} - \frac{0.17 \beta_{pi}}{L_{Ti}(W^2 + W^2_{d, i})} \right], \tag{6.6}$$

where the components U^α_{MI} are given by relationship (2.24) or by the generalized versions of this relationship that follow from formula (2.18).

6.1. The Case of Strong Electron and Ion Heat Transport

In the case of strong heat transport by both of the plasma particle species, $(W_{d, \alpha}, W_{mw, \alpha}) \gg W$, criterion (6.6)

implies that NTMs are suppressed by the compound effect when

$$W < W^{\text{comp}}, \qquad (6.7)$$

where

$$W^{\text{comp}} \qquad (6.8)$$

$$= \frac{s}{1.23\varepsilon^{1/2}r_s} \frac{\sum\limits_{\alpha = e, i} U_{MI}^{\alpha}/W_{mw,\,\alpha}}{0.40\beta_{pe}/(L_{Te}W_{d,\,e}^2) - 0.17\beta_{pi}/(L_{Ti}W_{d,\,i}^2)}.$$

In order to illustrate expression (6.8), we consider the case $T_{0e} = T_{0i}$ and assume that the electron and ion temperature perturbation profiles are established via the competing collisional mechanism. We also assume that the magnetic well is described by formula (2.27). In this case, expression (6.8) becomes

$$W^{\text{comp}} = \frac{2 \times (1.8)^2 f(r_s)}{1.23 \times 0.23 \times 0.80} W_{\text{col}} = 28.63\,f(r_s)W_{\text{col}}. \ (6.9)$$

The qualitative dependence of the form $W^{\text{comp}} \sim f(r_s)W_{\text{col}}$ could be predicted in advance. It is somewhat surprising, however, that, in front of the function $f(r_s)$ in expression (6.9), there is so large a numerical coefficient (about 30). The reasons for this are as follows: First, relationship (2.31) implies that, when only the electron and ion temperature gradient channels are taken into account and when the ions are not colder than the electrons, the bootstrap drive even at weak heat transport is characterized by a small coefficient approximately equal to 1/4 (see the right-hand side of inequality (2.34)), which produces a coefficient of about 4 on the right-hand side of expression (6.9). The small coefficient 1/4, in turn, stems from the smallness of the electron partial contribution (the coefficient 0.40 in relationship (2.31)) and from the fact that the ion temperature gradient makes a stabilizing contribution to the parameter Δ_{bs}. In other words, the ions give rise not to the bootstrap drive but to the bootstrap suppression of the NTMs, thereby weakening the total effect of the bootstrap current. Second, the ratio W_d^2/W_{mw} turns out to be larger than W_{col} by a factor of about $(1.8)^2/0.80 \approx 4$. Finally, the contribution of the ion temperature gradient to the magnetic well effect, as well as the contribution of the electron temperature gradient, is stabilizing, which leads to an additional coefficient of about 2 on the right-hand side of expression (6.9).

From expression (2.28) it follows that, under the conditions prevailing in a circular tokamak and for $s \simeq 1$, the function $f(r_s)$ is on the order of $\varepsilon^{3/2}$. Consequently, if there were no large coefficient under discussion in expression (6.9), criterion (6.7) would imply that the compound effect can lead only to the suppression of small magnetic islands, $W \lesssim \varepsilon^{3/2}W_{\text{col}}$. On the other

hand, even when the values of ε are very small (but are such that $\varepsilon > (30)^{-2/3} \simeq 0.10$), the presence of the large coefficient in expression (6.9) ensures the suppression of all the islands whose width satisfies the conditions adopted in deriving this expression, i.e., the islands with the widths

$$W \lesssim (W_d, W_{mw}). \qquad (6.10)$$

This indicates that the condition for the heat transport to be strong is qualitatively equivalent to the condition for the suppression of the bootstrap drive of NTMs by the compound effect.

6.2. The Case of Strong Electron Heat Transport and Weak Ion Heat Transport

Under the assumption that the electron heat transport is strong, $(W_{d,\,e}, W_{mw,\,e}) \gg W$, and the ion heat transport is weak, $(W_{d,\,i}, W_{mw,\,i}) \ll W$, criterion (6.6) reduces to

$$U_{MI}^i + \frac{1.23 \times 0.17\varepsilon^{1/2}r_s\beta_{pi}}{sL_{Ti}}$$

$$> \frac{1.23 \times 0.40\varepsilon^{1/2}r_s\beta_{pe}}{sL_{Te}}\left(\frac{W}{W_{d,\,e}}\right)^2. \qquad (6.11)$$

This inequality describes the competition between the stabilizing effects of the ion magnetic well and the bootstrap suppression by the ions, on the one hand, and the bootstrap drive by the electrons, weakened by a factor of $(W/W_{d,\,e})^2$, on the other hand. We can see that the result of this competition is more favorable than was presumed in Section 6.1.

7. CONCLUSIONS

Based on the two-fluid MHD equations, we have developed an approach to calculating the contribution of the magnetic well to the generalized Rutherford equation for the evolution of the magnetic island width Δ_{mw} in the problem of suppressing NTMs under strong transverse heat transport conditions. We have expressed this contribution in terms of the electron and ion partial components Δ_{mw}^{α}, $(\alpha = e, i)$. We have shown that the parameters Δ_{mw}^{α} depend on the radial profiles of the electron and ion temperature perturbations and, thereby, on the mechanisms by which these profiles are established. Using the results of previous investigations, we have considered four such mechanisms, namely, collisional, convective, inertial, and rotational. We have explained that the first of them is illustrative in character, the second is associated primarily with the electrons ($\alpha = e$), and the last two are governed by the ions ($\alpha = i$). We have found that, by analogy with the collisional model, which was considered in [8, 9], the

parameters Δ_{mw}^{α} in the remaining three (convective, inertial, and rotational) models are independent of the width W of the magnetic island and are inversely proportional to its critical width, $\Delta_{mw}^{\alpha} \sim 1/W_c$. In the rotational model, the parameter Δ_{mw}^{i} also depends weakly on a logarithmic factor of the form $[\ln(W_c/W)]^2$, see representations (3.25).

Using the expressions derived in our study for the partial components Δ_{mw}^{α} ($\alpha = e, i$) in the limiting case of strong transverse heat transport and also the known expressions in the opposite limiting case of weak heat transport, we have constructed extrapolation formulas (4.1)–(4.4) for these parameters at arbitrarily intense transverse heat transport. With these extrapolation formulas and expressions (2.16), we have developed a two-channel model of the magnetic well effect—one that accounts for the competition between the above four mechanisms whereby the temperature profiles are established.

In order to obtain physical results using the two-channel model, the magnetic well effect should be compared to the other effects that are incorporated in the generalized Rutherford equation for the island width evolution (see Eqs. (2.1) and (6.1), which are two versions of the generalized Rutherford equation, written for the theoretical and practical purposes, respectively). We think that the most important information has been gained from a comparison of the parameter Δ_{mw} to the parameter Δ_{bs}, which characterizes the bootstrap drive of NTMs. This comparison has been facilitated by the use of the two-channel model that was developed in [17] for the bootstrap drive at arbitrarily intense heat transport. The latter model is based on the same competing mechanisms that were taken into account in constructing the model for Δ_{mw} and is characterized by formulas (6.2)–(6.4). Such a comparison allowed us to derive general criterion (6.6) for suppression of the NTMs by the compound effect at an arbitrary level of the transverse heat transport and two particular criteria: in the case of strong electron and ion heat transport (see relationships (6.7) and (6.8)) and in the case in which the electron heat transport is strong and the ion heat transport is weak (see inequality (6.11)).

The compound effect under investigation turns out to be enhanced because the ion temperature gradient channel of the bootstrap current gives rise not to the bootstrap drive of the NTMs but to their bootstrap suppression and also because of the smallness of the electron partial component of the parameter Δ_{bs} and the smallness of the ratio between the critical island widths, which characterize the influence of strong heat transport on the magnetic well effect and on the bootstrap drive (see illustrative formula (6.9) and its subsequent discussion). Our calculations yielded criterion (6.10), which shows that the range of widths of the

islands stabilized by the compound effect is substantially wider than one might expect. From expressions (6.9), (2.28), and (2.29), it is clear that the compound effect can be enhanced by the plasma cross sectional shaping (i.e., by the combined influence of the triangularity and ellipticity of the magnetic surfaces) and also by accessing the second stability region of the ideal ballooning modes. When only the electron heat transport is strong, the compound effect is characterized by criterion (6.11), which means physically that the ion magnetic well effect and the bootstrap suppression by the ions predominate over the bootstrap drive by the electrons weakened by the electron heat transport.

It should also be kept in mind that, even when criterion (6.7) for stabilization of the NTMs by the compound effect is not satisfied, the bootstrap drive mechanism for producing moderately wide magnetic islands operates far less effectively. As a result, the conditions under which NTMs are suppressed by the electron cyclotron current drive become less restrictive (see the term with Δ_{ECCD} in Eq. (2.1) or (6.1)). On the other hand, it is known that sufficiently large islands can be suppressed by the effect described by the negative values of the parameter Δ' in Eqs. (2.1) and (6.1). Thereby, NTMs can be suppressed for magnetic islands of whatever width.

In the present paper, we have considered only one type of anomalous transverse transport, namely, transverse heat transport. In accordance with [6], however, it is obvious that the influence of anomalous diffusion on the compound effect also should to be studied. Another type of anomalous transverse transport—anomalous transverse viscosity—was incorporated into the theory of magnetic islands in [26, 27]. The development of a theory of NTMs that would include both the compound effect and the effect of strong transverse viscosity can be the subject of future studies.

When considering the anomalous transverse heat transport, we assumed that it is caused by a sort of small-scale turbulent pulsations, without specifying their nature. Such turbulence can originate from microislands that were discussed in [28] and in the papers cited therein.

Along with the compound effect, the magnetic islands can be suppressed by the feedback effect (for details, see [29] and the literature contained therein).

The dynamics of sufficiently narrow magnetic islands is largely determined by the polarization current effect, which is incorporated in the general terms in generalized Rutherford equations (2.1) and (6.1). Along with the review paper [24] cited above, useful information about the role of the polarization current can also be gained from a recent paper [30].

APPENDIX A

SUMMARY OF THE BASIC PLASMOPHYSICAL MODELS

In order to calculate the magnetic well effect with the help of formulas (2.17)–(2.21), it is necessary to know the profile of the perturbed temperature of the corresponding particle species. We find the temperature profiles by using the reduced transport equations that were systematized in [17]. In that paper, the model sets of reduced transport equations were called collisional, convective, inertial, and rotational plasmophysical models, depending on the dominant transport processes that compete with the transverse heat transport. The essence of these models can be summarized as follows:

A.1. Collisional Model

In the collisional model [10], it is assumed that the temperature of the corresponding particle species satisfies the heat-conduction equation

$$\mathbf{\nabla} \cdot \mathbf{q} = 0, \tag{A.1}$$

where $\mathbf{q}$ is the heat flux defined by the relationship

$$\mathbf{q} = -n_0(\chi_\| \mathbf{b}\nabla_\| + \chi_\perp \mathbf{\nabla}_\perp)T, \tag{A.2}$$

$\mathbf{b}$ is a unit vector in the direction of the total magnetic field, and $\nabla_\|$ and $\mathbf{\nabla}_\perp$ are the longitudinal and transverse gradient operators with respect to this field.

A.2. Convective Model

In the convective model [20], the perturbed temperature is determined from the equations

$$\nabla_\| q_\| - \frac{3}{2}\chi_\perp \frac{\partial^2 p}{\partial x^2} = 0, \tag{A.3}$$

$$\frac{5}{M}\nabla_\|(pT) - \chi_\perp \frac{\partial^2 q_\|}{\partial x^2} = 0, \tag{A.4}$$

where $q_\|$ is the longitudinal heat flux, $p = nT$ and n are the pressure and density of the corresponding particle species, and M is the mass of a particle.

A.3. Inertial Model

In the inertial model [19], the heat conduction equation has the form

$$\rho_0 c_{is}^2 \nabla_\| V_\| = -\frac{2}{3}\mathbf{\nabla} \cdot \mathbf{q}_\perp, \tag{A.5}$$

where $\mathbf{q}_\perp$ is the transverse heat flux determined by relationship (A.2) with $\chi_\| = 0$, $V_\|$ is the longitudinal plasma velocity, $\rho_0 = M_i n_0$, and $c_{is} = (T_0/M_i)^{1/2}$ is the ion-sound speed. Equation (A.5) is supplemented with the equation of longitudinal plasma motion

$$\rho_0 d_0 V_\|/dt = -n_0 \nabla_\| T, \tag{A.6}$$

where

$$d_0/dt = \partial/\partial t + \mathbf{V}_E \cdot \mathbf{\nabla}, \tag{A.7}$$

$\mathbf{V}_E$ is the $\mathbf{E}_\perp \times \mathbf{B}_0$ drift velocity, and $\mathbf{E}_\perp$ is the transverse electric field of the perturbations.

A.4. Rotational Model

The rotational model [18] is based on the heat conduction equation

$$n_0 \frac{d_0 T}{dt} = -\frac{2}{3}\mathbf{\nabla} \cdot \mathbf{q}_\perp. \tag{A.8}$$

The notation in this equation has been introduced above.

APPENDIX B

CALCULATION OF THE PARAMETERS k_{mw}^α FOR RIGOROUS TEMPERATURE PROFILES

B.1. Collisional Model

Substituting relationships (3.1) and (3.3) into expression (2.21) and switching from the variable u to the variable t, we obtain

$$k_{mw}^\alpha = k_{mw}^{col} \equiv I_{col}/(2^{3/2}\Omega_{col}^{1/2}), \tag{B.1}$$

where

$$I_{col} = \int_0^\infty \frac{dt}{t^{3/2}}\left[I_{1/4}(t)\int_t^\infty z^{1/4} K_{1/4}(z)dz \right.$$
$$\left. + K_{1/4}(t)\int_0^t z^{1/4} I_{1/4}(z)dz \right]. \tag{B.2}$$

Changing the order of integration in the first term on the right-hand side of this expression, we convert it into the form

$$
I_{col} = \int_0^\infty K_{1/4}(t) \left[t^{-3/4} \int_0^t z^{1/4} I_{1/4}(z)dz \right.
$$
$$
\left. + t^{1/4} \int_0^t z^{-3/4} I_{1/4}(z)dz \right] dt.
$$
(B.3)

We introduce the function $I_{\mu\nu}(t)$ through the relationship

$$
I_{\mu\nu}(t) = \int_0^t z^\mu I_\nu(z)dz.
$$
(B.4)

We expand the function $I_\nu(z)$ in powers of z^2, insert the result into relationship (B.4), and integrate over z to find

$$
I_{\mu\nu}(t) = \frac{t^{\mu+\nu+1}}{2^{\nu+1}}
$$
$$
\times \sum_{k=0}^\infty \left(\frac{t^2}{4}\right)^k \frac{\Gamma[k+(\mu+\nu+1)/2]}{\Gamma[k+(\mu+\nu+3)/2]\Gamma(k+\nu+1)k!}.
$$
(B.5)

With allowance for relationship (B.5), expression (B.2) reduces to

$$
I_{col}
$$
$$
= 2^{-3/2} \sum_{k=0}^\infty \frac{K_{3/4+2k,\,1/4}}{k!\Gamma(k+5/4)2^{2k}} \left(\frac{1}{k+3/4} + \frac{1}{k+5/4}\right),
$$
(B.6)

where

$$
K_{\mu,\nu} \equiv \int_0^\infty t^\mu K_\nu(t)dt.
$$
(B.7)

According to [31], we have

$$
K_{\mu,\nu} = 2^{\mu-1}\Gamma\left(\frac{1+\mu+\nu}{2}\right)\Gamma\left(\frac{1+\mu-\nu}{2}\right).
$$
(B.8)

Expression (B.6) then reads

$$
I_{col}
$$
$$
= 2^{-3/2} \sum_{k=0}^\infty \frac{\Gamma(k+1)\Gamma(k+3/4)}{k!\Gamma(k+5/4)} \left(\frac{1}{k+3/4} + \frac{1}{k+1/4}\right).
$$
(B.9)

The summation over k on the right-hand side of this

equality is carried out with the help of the formula [32]

$$
\sum_{k=0}^\infty \frac{(a)_k(b)_k}{(1-b+a)_k k!} \left[\left(\frac{a}{2}+k-x\right)^{-1} + \left(\frac{a}{2}+k+x\right)^{-1} \right]
$$
$$
= \frac{\Gamma(a/2-x)\Gamma(a/2+x)}{\Gamma(1-b+a/2-x)\Gamma(1-b+a/2+x)}
$$
$$
\times \frac{\Gamma(1-b+a)\Gamma(1-b)}{\Gamma(a)},
$$
(B.10)

where

$$
(\alpha)_k \equiv \Gamma(\alpha+k)/\Gamma(\alpha).
$$
(B.11)

In the case at hand, we have

$$
a = 1, \quad b = 3/4, \quad x = 1/4.
$$
(B.12)

As a result, the expression becomes

$$
I_{col} = \pi^{3/2}/2^{1/2}.
$$
(B.13)

Substituting expression (B.13) into expression (B.1) yields expression (3.4).

B.2. Convective Model

By analogy with expression (B.1), we substitute relationships (3.5) and (3.6) into expression (2.21) to arrive at

$$
k_{mw}^\alpha = k_{mw}^{conv} \equiv 2^{4/3} I_{conv}/(3^{7/6}\Omega_{conv}^{1/2}),
$$
(B.14)

where

$$
I_{conv} = \int_0^\infty t^{-2/3}dt \left[I_{1/3}(t)\int_t^\infty K_{1/3}(x)dx \right.
$$
$$
\left. + K_{1/3}(t)\int_0^t I_{1/3}(x)dx \right].
$$
(B.15)

By analogy with expression (B.3), we have

$$
I_{conv}
$$
$$
= \int_0^\infty dt K_{1/3}(t)\left[t^{-2/3}\int_0^t I_{1/3}(x)dx + \int_0^t x^{-2/3}I_{1/3}(x)dx \right].
$$
(B.16)

Using relationships (B.4) and (B.5) with $(\mu, \nu) = (0, 1/3)$ and with $(\mu, \nu) = (-2/3, 1/3)$, we reduce expression (B.16) to

$$
I_{conv} = 2^{-5/3} \sum_{k=0}^\infty \frac{\Gamma(k+1)\Gamma(k+2/3)}{k!\Gamma(k+4/3)}
$$
$$
\times \left[\frac{\Gamma(k+2/3)}{\Gamma(k+5/3)} + \frac{\Gamma(1/3)}{\Gamma(k+4/3)} \right].
$$
(B.17)

In order to take the sum of the series in expression (B.17), we refer to the familiar series expansion of the general-

ized hypergeometric function $F(a, b, c; d, e; z)$ with $z = 1$:

$$F(a, b, c; d, e; 1) = \sum_{k=0}^{\infty} \frac{(a)_k(b)_k(c)_k}{(d)_k(e)_k}, \qquad \text{(B.18)}$$

where the quantities $(\alpha)_k$ are defined by formula (B.11). Expression (B.17) then reads

$$I_{\text{conv}} = \frac{3\Gamma(2/3)}{2^{5/3}\Gamma(4/3)}$$

$$\times \left[F\left(1, \frac{2}{3}, \frac{1}{3}; \frac{4}{3}, \frac{4}{3}; 1\right) + \frac{1}{2}F\left(1, \frac{2}{3}, \frac{2}{3}; \frac{5}{3}, \frac{4}{3}; 1\right) \right]. \qquad \text{(B.19)}$$

Using the equalities

$$F\left(1, \frac{2}{3}, \frac{2}{3}; \frac{5}{3}, \frac{4}{3}; 1\right) = 1.60, \qquad \text{(B.20)}$$

$$F\left(1, \frac{2}{3}, \frac{1}{3}; \frac{4}{3}, \frac{4}{3}; 1\right) = 1.34, \qquad \text{(B.21)}$$

we transform expression (B.19) to

$$I_{\text{conv}} = 3.06. \qquad \text{(B.22)}$$

Substituting expression (B.22) into expression (B.14) yields expression (3.8).

B.3. Inertial Model

Using relationships (3.5), (3.9), and (2.21), we obtain

$$k_{mw}^{\alpha} = \pi^{1/4}\cos(\pi/8)I_i/(2^{11/8}\Omega_i^{1/2}), \qquad \text{(B.23)}$$

where

$$I_i = I_{\text{col}}, \qquad \text{(B.24)}$$

with I_{col} being given by formula (B.2). According to Section B.1, calculating I_{col} yields expression (B.13). Using relationships (B.22), (B.23), and (B.13), we arrive at expression (3.11).

B.4. Rotational Model

Integrating by parts puts expression (2.21) into the form

$$k_{mw}^{\alpha} = -\int_0^{\infty} \frac{dy^{\alpha}}{du}\ln u\,du. \qquad \text{(B.25)}$$

Inserting Eq. (3.12) for dy^{α}/du into this expression and using formula (3.15), we obtain

$$k_{mw}^{\alpha} = k_{mw}^{\text{rot}}, \qquad \text{(B.26)}$$

where

$$k_{mw}^{\text{rot}} = \frac{2^{5/2}}{\pi\Omega_r}\int_0^{\infty} \tau(z)\ln u\,du. \qquad \text{(B.27)}$$

Passing over from the variable u to the variable z, we reduce expression (B.26) to expression (3.16).

APPENDIX C

CALCULATION OF THE PARAMETERS k_{mw}^{α} FOR MODEL TEMPERATURE PROFILES

C.1. Collisional Model

According to [18], the model expression for the function $y^{\alpha}(u)$ in the collisional model has the form

$$y^{\alpha}(u) = \frac{u}{u^2 + u_{\text{col}}^2}, \qquad \text{(C.1)}$$

where

$$u_{\text{col}} = 6^{1/4}\Omega_{\text{col}}^{1/2}. \qquad \text{(C.2)}$$

Substituting expression (C.1) into expression (2.21) yields expression (3.17).

C.2. Convective Model

By analogy with expression (C.1), the model expression obtained in [18] for the function $y^{\alpha}(u)$ has the form

$$y^{\alpha}(u) = \frac{u}{u^2 + u_{\text{conv}}^2}, \qquad \text{(C.3)}$$

where

$$u_{\text{conv}} = (5/2)^{1/6}\Omega_{\text{conv}}^{1/2}. \qquad \text{(C.4)}$$

By analogy with expression (3.17), expressions (2.21) and (C.3) lead to model expression (3.18) for k_{mw}^{α}.

C.3. Inertial Model

According to [19] (see also [17]), the model expression for the function $y^{\alpha}(u)$ in the inertial model has the form

$$y(u) = \frac{u}{u^2 + (1 + i)u_i^2}, \qquad \text{(C.5)}$$

where

$$u_i = 3^{1/4}/\alpha_i^{1/2}. \qquad \text{(C.6)}$$

Using expressions (2.21) and (C.5) (cf. expressions (3.17), (3.18)), we arrive at expression (3.19) for k_{mw}^{α}.

APPENDIX D

ANALYSIS OF THE INFLUENCE OF STRONG TRANSVERSE HEAT TRANSPORT ON THE MAGNETIC WELL IN [8]

The starting point for the analysis carried out in [8] was the following expression for the magnetic-well-related current:

$$\nabla_{\parallel} J_{mw} = -c \nabla p \cdot \left[\nabla \times \frac{\mathbf{B}}{\mathbf{B}^2} \right]. \tag{D.1}$$

The analysis included two steps. In the first step, the transverse transport was assumed to be sufficiently weak, and, in the second step, it was assumed to be sufficiently strong. These steps will be described in Sections D.1 and D.2.

D.1. Weak Transverse Transport Approximation

By switching to the magnetic-island variables (ψ, ξ) and ignoring the product of the derivative $(\partial \tilde{p} / \partial \theta)_{\xi}$, which describes poloidal plasma density oscillations, with the geodesic curvature, Eq. (D.1) in [8] was reduced to the equation

$$\frac{\partial J_{mw}}{\partial \xi} = \frac{\sqrt{2} c w' q R \sigma_x}{w s B_0^3} \frac{\sin \xi}{(\Omega + \cos \xi)^{1/2}} \frac{\partial p}{\partial \Omega}, \tag{D.2}$$

where $w' \equiv d \langle (B_0^2 + 8\pi p_0) \rangle_{\theta} / dr$ and $\langle \ldots \rangle_{\theta}$ denotes averaging over the equilibrium magnetic surface. In [8], the function w' was expressed in terms of the parameter U_0 (cf. expressions (4.3)).

D.2. Strong Transverse Transport Approximation

In [8], in considering the strong transverse transport, use was made of Eq. (2.7) rather than of formulas (2.8) and (2.9). With allowance for Eq. (2.10), Eq. (2.7) was converted into the form

$$\left(\frac{\partial J_{mw}}{\partial \xi} \right)_{\Omega} = \frac{\sigma_x c B_0 U_0}{2^{3/2} T_0' w L_s} \frac{T_c(x) \sin \xi}{(\Omega + \cos \xi)^{1/2}}. \tag{D.3}$$

This was done with the help of the relationship (cf. expression (2.17))

$$T_c(x) = -\sigma_x T_0' w^2 y(x)/4, \tag{D.4}$$

where (cf. expression (C.1))

$$y(x) = \frac{x}{x^2 + x_{col}^2}. \tag{D.5}$$

Here, the quantity x_{col} was introduced through the relationship $x_{col}^2 = k_{col} w_{col}^2 / 2$ with $k_{col} = (3/2)^{1/2}$ and $w_{col} =$

$W_{col}/2^{1/2}$, where W_{col} was given by formula (3.2). As a result, Eq. (D.3) was transformed to

$$\left(\frac{\partial J_{mw}}{\partial \xi} \right)_{\Omega} = -\frac{c B_0 U_0 w y(x)}{2^{7/2} \pi L_s} \frac{\sin \xi}{(\Omega + \cos \xi)^{1/2}}. \tag{D.6}$$

In this step of the analysis in [8], the variable x was expressed in terms of Ω and ξ with the help of relationships (2.4) and (2.5). Integrating over ξ then led to the expression

$$J_{mw} = \frac{c B_0 U_0}{4 \pi L_s} \left[\int^x y(x) dx - \langle \ldots \rangle \right], \tag{D.7}$$

where the symbol $\langle \ldots \rangle$ indicates averaging over the separatrix surface of the island.

Substitution of expression (D.7) into formula (2.2) yielded the relationship

$$\Delta_{mw} = -\frac{U_0}{w} c_F, \tag{D.8}$$

where

$$c_F = \frac{1}{2^{1/2} \pi} \sum_{\sigma_x} \int_{-1}^{\infty} d\Omega \oint \frac{\cos \xi}{(\Omega + \cos \xi)^{1/2}}$$
$$\times \left[\int^x y(x) dx - \langle \ldots \rangle \right], \tag{D.9}$$

and the subscript F stands for Fitzpatrick (the author of [10]).

By using formula (D.5), expression (D.9) was reduced to

$$c_F = \frac{1}{2^{3/2} \pi} \sum_{\sigma_x} \int_{-1}^{\infty} d\Omega \oint \frac{\cos \xi}{(\Omega + \cos \xi)^{1/2}}$$
$$\times \left[\ln \left(\frac{x^2}{x_{col}^2} + 1 \right) - \langle \ldots \rangle \right]. \tag{D.10}$$

The upper limit of integration over Ω was replaced with Ω_{eff} on the order of $\Omega_{eff} \simeq (x_{col}/w)^2$ and account was taken of the following approximate equality, which holds for $x \ll x_{col}$:

$$\ln \left(\frac{x^2}{x_{col}^2} + 1 \right) - \langle \ldots \rangle \sim (\cos \xi - \langle \cos \xi \rangle). \tag{D.11}$$

Under the above assumptions, expression (D.10) produced the estimate

$$c_F \simeq w/w_{col}, \tag{D.12}$$

with which relationship (D.8) yielded

$$\Delta_{mw} \simeq -U_0/W_{col}. \tag{D.13}$$

Approximate expression (D.13) is qualitatively equivalent to expression (2.20) with k_{mw}^{α} given by formula (3.4).

REFERENCES

1. ITER Physics Expert Group on Disruptions, Plasma Control, and MHD and ITER Physics Basis Editors, Nucl. Fusion **39**, 2251 (1999).

2. O. Sauter, R. J. LaHaye, Z. Chang, *et al.*, Phys. Plasmas **4**, 1654 (1997).

3. W. X. Qu and J. D. Callen, Report No. UWPR 85-5 (Univ. of Wisconsin, 1985).

4. R. Carrera, R. D. Hazeltine, and M. Kotschenreuther, Phys. Fluids **29**, 899 (1986).

5. M. Kotschenreuther, R. D. Hazeltine, and P. J. Morrison, Phys. Fluids **28**, 294 (1985).

6. A. B. Mikhaĭlovskiĭ, B. N. Kuvshinov, V. D. Pustovitov, and S. E. Sharapov, Fiz. Plazmy **26**, 403 (2000) [Plasma Phys. Rep. **26**, 375 (2000)].

7. A. B. Mikhaĭlovskiĭ, S. V. Konovalov, M. S. Shirokov, and V. S. Tsypin, Fiz. Plazmy **30**, 595 (2004) [Plasma Phys. Rep. **30**, 549 (2004)].

8. A. B. Mikhailovskii, private communication (2001).

9. H. Lutjens, J. F. Luciani, and X. Garbet, Phys. Plasmas **8**, 4267 (2001).

10. R. Fitzpatrick, Phys. Plasmas **2**, 825 (1995).

11. N. N. Gorelenkov, R. V. Budny, Z. Chang, *et al.*, Phys. Plasmas **3**, 3379 (1996).

12. A. H. Glasser, J. M. Greene, and J. L. Johnson, Phys. Fluids **18**, 875 (1975).

13. R. J. LaHaye and O. Sauter, Nucl. Fusion **38**, 987 (1998).

14. H. Reimerdes, T. Goodman, A. Pochelon, and O. Sauter, in *Proceedings of the 27th European Conference on Controlled Fusion and Plasma Physics, Budapest, 2000* (EPS, Geneva, 2001), Part 1, p. 25.

15. H. P. Furth, J. Killeen, and M. N. Rosenbluth, Phys. Fluids **6**, 459 (1963).

16. H. Lutjens and J. F. Luciani, Phys. Plasmas **9**, 4837 (2002).

17. A. B. Mikhailovskii, M. S. Shirokov, S. V. Konovalov, and V. S. Tsypin, Fiz. Plazmy **31**, 387 (2005) [Plasma Phys. Rep. **31**, 347 (2005)].

18. S. V. Konovalov, A. B. Mikhailovskii, M. S. Shirokov, and V. S. Tsypin, Plasma Phys. Controlled Fusion **44**, 579 (2002).

19. A. B. Mikhailovskii, M. S. Shirokov, V. S. Tsypin, *et al.*, Phys. Plasmas **10**, 3975 (2003).

20. A. B. Mikhailovskii, M. S. Shirokov, V. S. Tsypin, *et al.*, Phys. Plasmas **10**, 3790 (2003).

21. C. C. Hegna, Phys. Plasmas **6**, 3980 (1999).

22. A. B. Mikhailovskii, Nucl. Fusion **15**, 95 (1975).

23. A. H. Glasser, J. M. Greene, and J. L. Johnson, Phys. Fluids **19**, 567 (1976).

24. A. B. Mikhailovskii, Contrib. Plasma Phys. **43**, 275 (1998).

25. A. B. Mikhailovskii, *Instabilities in a Confined Plasma* (Inst. of Physics Publishing, Bristol, 1998).

26. S. V. Konovalov, A. B. Mikhailovskii, M. S. Shirokov, and V. S. Tsypin, Phys. Plasmas **9**, 4596 (2002).

27. S. V. Konovalov, A. B. Mikhailovskii, M. S. Shirokov, and V. S. Tsypin, Plasma Phys. Controlled Fusion **44**, L51 (2002).

28. A. B. Mikhailovskii, E. A. Kovalishen, M. S. Shirokov, *et al.*, Phys. Plasmas **11**, 666 (2004).

29. S. V. Konovalov, A. B. Mikhailovskii, E. A. Kovalishen, *et al.*, Dokl. Akad. Nauk **397**, 186 (2004) [Dokl. Phys. **49**, 405 (2004)].

30. S. V. Konovalov, A. B. Mikhailovskii, V. S. Tsypin, *et al.*, Phys. Lett. A **318**, 429 (2003).

31. I. S. Gradshteyn and I. M. Ryzhik, *Tables of Integrals, Series, and Products* (Nauka, Moscow, 1971; Academic, New York, 1980).

32. *Higher Transcendental Functions (Bateman Manuscript Project)*, Ed. by A. Erdelyi (McGraw-Hill, New York, 1953; Nauka, Moscow, 1965), Vol. 1.

Translated by I.A. Kalabalyk

<div align="center">

PLASMA OSCILLATIONS
AND WAVES

</div>

Anomalous Doppler Effect and Stimulated Cherenkov Effect in a Plasma Waveguide with a Thin-Walled Annular Electron Beam

M. V. Kuzelev and A. A. Rukhadze

Prokhorov Institute of General Physics, Russian Academy of Sciences, ul. Vavilova 38, Moscow, 119991 Russia
Received August 25, 2004

Abstract—A dispersion relation for the complex frequencies of the E modes excited by a thin-walled annular low-density beam in a cylindrical plasma waveguide is derived using the methods of perturbation theory. The cases of an annular and a uniform plasma filling are considered, and the corresponding wave growth rates are determined. A condition is obtained under which the primary mechanism for the excitation of the waveguide is the anomalous Doppler effect. The possibility is discussed of suppressing Cherenkov generation in a plasma resonator at the expense of the normal Doppler effect. © *2005 Pleiades Publishing, Inc.*

1. The single-particle and collective Cherenkov effects are thought to be the main mechanisms for stimulated emission of slowed electromagnetic waves by a straight electron beam in plasma-filled waveguide systems. This is confirmed by numerous theoretical and experimental investigations [1, 2]. In experiments, the beam can interact with the plasma via the Cherenkov mechanism only in the presence of a strong external longitudinal magnetic field. In [3, 5], it was shown that, when the magnetic field is strong enough, its strength does not have any significant influence on the Cherenkov emission mechanisms, as well as on the spectra of the plasma waves excited by the beam. This is why, in relevant theoretical studies, the external magnetic field was usually assumed to be infinitely strong. On the other hand, under actual experimental conditions in plasma relativistic microwave electronics [6], the Langmuir frequency of the plasma electrons is comparable to their gyrofrequency; moreover, when the electron beam is dense enough, the Langmuir frequency of the beam electrons may also become close to these two frequencies. As regards the Cherenkov emission mechanisms, this circumstance is not of great importance. However, the external magnetic field of finite strength gives rise to a new stimulated emission mechanism—the anomalous Doppler effect [7–9], which comes into play under the condition $\omega - k_z u = -\Omega_e/\gamma < 0$, where $\omega > 0$ is the frequency, $k_z > 0$ is the longitudinal wavenumber of the emitted wave, u is the beam velocity, Ω_e is the electron gyrofrequency, and $\gamma = (1 - u^2/c^2)^{-1/2}$ is the relativistic factor of the beam electrons. The question then naturally arises of the competition between the Cherenkov effect and the anomalous Doppler effect. Indeed, though these effects occur in different frequency ranges and different wavelength ranges, the anomalous Doppler effect gives rise to transverse oscillations of the beam electrons and thereby can influence the efficiency of Cherenkov emission. The problem of the excitation of transverse oscillations of the beam electrons under anomalous Doppler effect conditions is studied by means of nonlinear theory [10, 11], and we are going to address it separately in our further studies. Here, however, we are adopting the linear approximation, which serves merely to derive dispersion relations in order to calculate the wave growth rates and compare them to one another.

We consider a cylindrical waveguide of radius R that is filled with a plasma homogeneous in the z direction. The waveguide is placed in an external uniform longitudinal magnetic field and is penetrated by a thin-walled annular electron beam with a mean radius r_b and wall thickness $\Delta_b \ll r_b < R$. Our objective is to investigate how the beam excites a symmetric ($\partial/\partial\varphi = 0$) low-frequency plasma wave in such a waveguide. It is known that the external magnetic field has little effect on the spectrum and electromagnetic field of this wave [12]; the wave in fact has the same structure as the *E*-type ordinary waveguide mode with the electric field $\mathbf{E} = \{E_z, E_r, 0\}$, such that $E_\varphi = 0$. For instance, for a thin-walled annular plasma with the mean radius r_p and thickness $\Delta_p \ll r_p < R$, the dispersion relation for the wave in question (known in the literature as a cable plasma wave or an E_{01} wave) depends on the frequency Ω_e only when $k_z\Delta_p \gg 1$. Consequently, a thin-walled plasma can be described in the limit of an arbitrarily strong external magnetic field. Note that this approach applies only to the cable plasma wave, rather than to the entire plasma filling the waveguide. When the plasma is not thin-walled (e.g., is continuous over the waveguide cross section), the external magnetic field should be taken into account more accurately.

Of course, the electron beam perturbs the plasma wave. However, if the beam density is low (or if the

beam thickness Δ_b is small), the perturbation is not large. Therefore, in considering the electron beam as a small perturbation, we begin with the following wave equation for the polarization potential ψ of the E-type plasma wave [13]:

$$ik_z\left(\frac{1}{r}\frac{d}{dr}r\frac{d}{dr} - \chi_0^2\right)\psi = 4\pi\rho_p + 4\pi\rho_b, \quad (1)$$

where ρ_p is the plasma charge density perturbation and ρ_b is the beam charge density perturbation produced by the components E_z and E_r of the electric field. The field components are given by the formulas

$$E_z = -\chi_0^2\psi, \quad E_r = ik_z\frac{d\psi}{dr}, \quad \chi_0^2 = k_z^2 - \omega^2/c^2. \quad (2)$$

The beam charge density perturbation can be calculated from the continuity equation

$$\rho_b = -\frac{i}{\omega}\nabla \cdot \mathbf{j}_b,$$

$$\nabla \cdot \mathbf{j}_b = \frac{1}{r}\frac{d}{dr}rj_r + ik_zj_z, \quad (3)$$

$$j_r = \sigma_{rr}E_r + \sigma_{rz}E_z,$$

$$j_z = \sigma_{zr}E_r + \sigma_{zz}E_z,$$

where $\mathbf{j}_b = \{j_z, j_r, 0\}$ is the beam current density. In cylindrical coordinates, the components of the beam conductivity tensor are operators. Using the known formulas [14, 15], we write out the conductivity tensor components that will be utilized in further analysis:

$$\sigma_{rr} = \sigma_\perp P_b(r),$$

$$\sigma_{zz} = \sigma_\parallel\frac{1}{r}\frac{d}{dr}rP_b(r)\frac{d}{dr},$$

$$\sigma_{rz} = \tilde{\sigma}P_b(r)\frac{d}{dr}, \quad \sigma_{zr} = \tilde{\sigma}\frac{1}{r}\frac{d}{dr}rP_b(r). \quad (4)$$

Here, $P_b(r)$ is the radial electron beam density profile, which will be specified below. For a straight beam with zero radial electron velocities in an unperturbed state, the tensor components $\sigma_\perp$, $\sigma_\parallel$, and $\tilde{\sigma}$ are given by the formulas

$$\sigma_\perp = -\frac{\omega}{4\pi i}\frac{\omega_b^2\tilde{\omega}^2\gamma^{-1}}{\omega^2(\tilde{\omega}^2 - \Omega_e^2)},$$

$$\sigma_\parallel = \frac{\omega}{4\pi i}\frac{\omega_b^2u^2\gamma}{\omega^2(\tilde{\omega}^2 - \Omega_e^2)}, \quad (5)$$

$$\tilde{\sigma} = \frac{\omega}{4\pi i}\frac{i\omega_b^2u\tilde{\omega}}{\omega^2(\tilde{\omega}^2 - \Omega_e^2)},$$

where $\tilde{\omega} = (\omega - k_zu)\gamma$ and ω_b is the Langmuir frequency of the beam electrons. In writing formulas (5), we have taken into account only the terms that describe the

cyclotron resonances associated with the normal and anomalous Doppler effects. As for the Cherenkov resonance, it will be taken into account later, in essentially the same way as in [5, 15]. From continuity equation (3) with formulas (2), (4), and (5), we obtain

$$\rho_b = -\frac{i}{\omega}(ik_z\sigma_\perp - (2k_z^2 - \omega^2/c^2)\tilde{\sigma} - ik_z\chi_0^2\sigma_\parallel)$$

$$\times \frac{1}{r}\frac{d}{dr}rP_b(r)\frac{d\psi}{dr}. \quad (6)$$

Substituting Eq. (6) into Eq. (1) yields the following differential equation for the polarization potential ψ:

$$\frac{1}{r}\frac{d}{dr}r\frac{d\psi}{dr} - \chi_0^2\psi + i4\pi k_z^{-1}\rho_p$$

$$= A_{\mathrm{Dop}}(\omega, k_z)\frac{1}{r}\frac{d}{dr}rP_b(r)\frac{d\psi}{dr}, \quad (7)$$

where, for a straight beam, we have

$$A_{\mathrm{Dop}}(\omega, k_z) = Q\frac{\omega_b^2\gamma^{-1}}{(\omega - k_zu)^2 - (\Omega_e/\gamma)^2},$$

$$Q = 1 - \frac{u^2}{c^2}\frac{\omega}{k_zu}. \quad (8)$$

It can be shown that the plasma charge density perturbation at the low-frequency branch of the E waves, which is of interest to us here, is calculated from the formula

$$i4\pi k_z^{-1}\rho_p$$

$$= -\frac{\omega_p^2}{\omega^2 - \Omega_e^2}\frac{1}{r}\frac{d}{dr}rP_p(r)\frac{d\psi}{dr} + \frac{\omega_p^2}{\omega^2}\chi_0^2P_p(r)\psi, \quad (9)$$

where $P_p(r)$ is the radial plasma density profile and ω_p is the Langmuir frequency of the plasma electrons.

If we know the solution $\psi_p(r)$ to the eigenvalue problem

$$\hat{L}_r\psi \equiv \frac{1}{r}\frac{d}{dr}r\frac{d\psi}{dr} + \delta\varepsilon_{\perp p}\frac{1}{r}\frac{d}{dr}rP_p(r)\frac{d\psi}{dr}$$

$$\left.\begin{array}{c} -\chi_0^2\left(1 - \frac{\omega_p^2}{\omega^2}P_p(r)\right)\psi = 0, \\ \\ \psi(R) = 0 \end{array}\right\} \longrightarrow \psi_p(r), \quad (10)$$

where $\psi_p(r)$ is the eigenfunction of the plasma waves and $\delta\varepsilon_{\perp p} = -\omega_p^2(\omega_p^2 - \Omega_e^2)^{-1}$ is the contribution of the plasma to the transverse component of the dielectric

tensor, then the dispersion relation for the plasma waves can be represented as [11]

$$D_p(\omega, k_z) \equiv \int_0^R \psi_p(r)\hat{L}_r\psi_p(r)rdr$$

$$= -\int_0^R \left(\left|\frac{d\psi_p}{dr}\right|^2 (1 + \delta\varepsilon_{\perp p}P_p(r))\right) \tag{11}$$

$$+ \chi_0^2\left(1 - \frac{\omega_p^2}{\omega^2}P_p(r)\right)|\psi_p|^2\right)rdr = 0.$$

We solve differential equation (7) using perturbation theory [16], specifically, by applying the methods of perturbation theory to the beam in order to evaluate the right-hand side of this equation. We multiply Eq. (7) by ψ_p from the left and integrate over r from zero to R to arrive at the following dispersion relation in the first-order beam-related perturbation theory:

$$D_p(\omega, k_z) = -A_{\mathrm{Dop}}(\omega, k_z)\int_0^R rP_b(r)\left(\frac{d\psi_p}{dr}\right)^2 dr$$

$$- \chi_0^2 B_{\mathrm{Cher}}(\omega, k_z)\int_0^R rP_b(r)\psi_p^2 dr. \tag{12}$$

In dispersion relation (12), we have already taken into account the contribution of the Cherenkov resonance between the beam and the plasma wave excited by it:

$$B_{\mathrm{Cher}}(\omega, k_z) = \frac{\omega_b^2\gamma^{-3}}{(\omega - k_z u)^2}. \tag{13}$$

2. Here, we consider important particular cases of the filling of a waveguide with plasma. For a waveguide completely filled with a plasma, $P_p(r) = 1$, we have the following two relationships, the second of which is a consequence of dispersion relation (11):

$$\psi_p(r) = J_0(k_{\perp m}r), \quad k_{\perp m} = \frac{\mu_{0m}}{R}, \quad m = 1, 2, \ldots,$$

$$D_p(\omega, k_z) = -\left[k_{\perp m}^2\left(1 - \frac{\omega_p^2}{\omega^2 - \Omega_e^2}\right) + \chi_0^2\left(1 - \frac{\omega_p^2}{\omega^2}\right)\right]$$

$$\times \|J_0(k_{\perp m}r)\|^2, \tag{14}$$

$$\|J_0(k_{\perp m}r)\|^2 = \frac{R^2}{2}J_1^2(\mu_{0m}),$$

where μ_{0m} are the roots of the Bessel function, $J_0(x) = 0$. In this case, dispersion relation (12) reads

$$k_{\perp m}^2\left(1 - \frac{\omega_p^2}{\omega^2 - \Omega_e^2}\right) + \chi_0^2\left(1 - \frac{\omega_p^2}{\omega^2}\right) \tag{15}$$

$$= k_{\perp m}^2 A_{\mathrm{Dop}}(\omega, k_z)G_{\mathrm{Dop}} + \chi_0^2 B_{\mathrm{Cher}}(\omega, k_z)G_{\mathrm{Cher}},$$

and the geometric factors of the beam are given by the formulas

$$G_{\mathrm{Dop}} = \|J_0(k_{\perp m}r)\|^{-2}\int_0^R rP_b J_1^2(k_{\perp m}r)dr,$$

$$G_{\mathrm{Cher}} = \|J_0(k_{\perp m}r)\|^{-2}\int_0^R rP_b J_0^2(k_{\perp m}r)dr. \tag{16}$$

It is convenient to write dispersion relation (15) in a more elaborate form:

$$k_{\perp m}^2\left(1 - \frac{\omega_p^2}{\omega^2 - \Omega_e^2} - Q\frac{G_{\mathrm{Dop}}\omega_b^2\gamma^{-1}}{(\omega - k_z u)^2 - (\Omega_e/\gamma)^2}\right)$$

$$+ \chi_0^2\left(1 - \frac{\omega_p^2}{\omega^2} - \frac{G_{\mathrm{Cher}}\omega_b^2\gamma^{-3}}{(\omega - k_z u)^2}\right) = 0. \tag{17}$$

For a beam that is continuous over the waveguide cross section, we have $P_b \equiv 1$ and $G_{\mathrm{Dop}} = G_{\mathrm{Cher}} = 1$. For a thin-walled beam ($P_b = \Delta_b\delta(r - r_b)$), the geometric factors are given by the formulas [15]

$$G_{\mathrm{Dop}} = 2\frac{\Delta_b r_b}{R^2}\frac{J_1^2(k_{\perp m}r_b)}{J_1^2(k_{\perp m}R)},$$

$$G_{\mathrm{Cher}} = 2\frac{\Delta_b r_b}{R^2}\frac{J_0^2(k_{\perp m}r_b)}{J_1^2(k_{\perp m}R)}. \tag{18}$$

The case of most practical interest is the excitation of the $m = 1$ fundamental plasma mode.

Dispersion relation (17) yields the following instability growth rates:

$$\delta\omega = \begin{cases} \dfrac{-1 + i\sqrt{3}}{2}\omega_{\mathrm{Cher}}\left(\dfrac{1}{2}\dfrac{G_{\mathrm{Cher}}\omega_b^2\gamma^{-3}}{\omega_p^2 + \beta^2 k_{\perp m}^2 u^2\gamma^4}\right)^{\frac{1}{3}} \\ \quad \text{for the Cherenkov effect,} \\[4pt] \dfrac{1}{2}i\omega_{\mathrm{Dop}}\left(SG_{\mathrm{Dop}}\dfrac{k_{\perp m}^2}{k_{\mathrm{Dop}}^2}\dfrac{\omega_{\mathrm{Dop}}\omega_b^2}{\Omega_e\omega_p^2}\right)^{\frac{1}{2}} \\ \quad \text{for the anomalous Doppler effect.} \end{cases} \tag{19}$$

Here, ω_{Cher} is the Cherenkov resonance frequency and ω_{Dop} and k_{Dop} are the frequency and wavenumber of the resonance associated with the anomalous Doppler effect. Recall that the resonance frequencies and resonance wavenumbers are determined from the set of equations

$$\omega = \Omega_p(k_z), \quad \omega = k_z u - n\Omega_e/\gamma, \quad (20)$$

where $\Omega_p(k_z)$ is the dispersion function of the plasma wave. For $n = 0$, Eqs. (20) determine the Cherenkov resonance, and, for $n = 1$, they determine the anomalous Doppler resonance (in these equations, it is assumed that $\omega > 0$ and $k_z > 0$). In formulas (19), we have introduced the following notation:

$$S = \frac{1-\beta^2 x}{1-\beta^2 x^2}, \quad \beta^2 = \frac{u^2}{c^2}, \quad x = \frac{\omega_{\mathrm{Dop}}}{\omega_{\mathrm{Dop}} + \Omega_e/\gamma}. \quad (21)$$

Since $0 < x < 1$, we have $1/2 < S < 1$.

Comparing growth rates (19), we determine the condition under which the instability growth rate due to the anomalous Doppler effect is faster than the growth rate of the Cherenkov instability. For a plasma with a density close to the threshold for the onset of the Cherenkov effect ($\omega_p^2 \approx k_{\perp m}^2 u^2 \gamma^2$), the corresponding condition has the form

$$\left(\gamma^5 \frac{\Delta_b r_b}{R^2} \frac{\omega_p \omega_b^2}{\Omega_e^3}\right)^{\frac{1}{3}} > 1. \quad (22)$$

This condition can be satisfied at fairly strong external magnetic fields, especially with highly relativistic beams. Hence, it is quite possible that, in experiments, the anomalous Doppler effect predominates over the Cherenkov effect.

3. Let us now consider an important case of a thin-walled annular plasma with the density profile $P_p(r) = \Delta_p \delta(r - r_p)$, the beam again being assumed to be thin-walled and annular. In this case, the eigenfunction of the plasma waves is independent of the external magnetic field (just because the plasma is thin-walled) and is given by the formula [3, 4, 11]

$$\psi_p(r)$$

$$= \begin{cases} I_0(\chi_0 r), \quad 0 < r < r_p \\ I_0(\chi_0 r_p) \dfrac{I_0(\chi_0 r)K_0(\chi_0 R) - K_0(\chi_0 r)I_0(\chi_0 R)}{I_0(\chi_0 r_p)K_0(\chi_0 R) - K_0(\chi_0 r_p)I_0(\chi_0 R)} \\ \quad r_p < r < R. \end{cases} \quad (23)$$

When substituting formula (23) into dispersion relation (11), it is convenient to use the first form of the dispersion function $D_p(\omega, k_z)$, namely, that with the operator $\hat{L}_r$, because the only contribution to the integral

comes from the surface $r = r_p$ at which the radial derivative of function (23) is discontinuous,

$$\psi''(r) = [\psi''(r)] + (\psi'(r_p + 0) - \psi'(r_p - 0))\delta(r - r_p), \quad (24)$$

where the symbol $[f(x)]$ stands for the function in the region of its continuity. The corresponding manipulations (see [3, 4] for details) yield the dispersion relation

$$\omega^2 - \Omega_p^2 = Q\frac{G_{\mathrm{Dop}}\omega^2 \omega_b^2 \gamma^{-1}}{(\omega - k_z u)^2 - (\Omega_e/\gamma)^2} + \frac{G_{\mathrm{Cher}}\omega^2 \omega_b^2 \gamma^{-3}}{(\omega - k_z u)^2}. \quad (25)$$

Here, the quantities

$$\Omega_p^2 = \omega_p^2 \frac{\chi_0^2}{k_{\perp p}^2},$$

$$\frac{1}{k_{\perp p}^2} = r_p \Delta_p I_0^2(\chi_0 r_p)\left[\frac{K_0(\chi_0 r_p)}{I_0(\chi_0 r_p)} - \frac{K_0(\chi_0 R)}{I_0(\chi_0 R)}\right] \quad (26)$$

determine the frequency Ω_p and transverse wavenumber $k_{\perp p}$ of the cable wave of a thin-walled annular plasma. In the case of a thin-walled annular plasma, the geometric factors of a thin-walled annular beam for anomalous Doppler effect conditions, G_{Dop}, and for Cherenkov effect conditions, G_{Cher}, are described by the formulas

$$G_{\mathrm{Dop}} = r_b \Delta_b \chi_0^2 I_1^2(\chi_0 r_b)\left[\frac{K_0(\chi_0 r_p)}{I_0(\chi_0 r_p)} - \frac{K_0(\chi_0 R)}{I_0(\chi_0 R)}\right],$$

$$r_b < r_p;$$

$$G_{\mathrm{Dop}} = r_b \Delta_b \chi_0^2 \frac{I_0(\chi_0 r_p)}{I_0(\chi_0 R)} \quad (27a)$$

$$\times \frac{[I_1(\chi_0 r_b)K_0(\chi_0 R) + K_1(\chi_0 r_b)I_0(\chi_0 R)]^2}{K_0(\chi_0 r_p)I_0(\chi_0 R) - I_0(\chi_0 r_p)K_0(\chi_0 R)},$$

$$r_b > r_p;$$

$$G_{\mathrm{Cher}} = r_b \Delta_b \chi_0^2 I_0^2(\chi_0 r_b)\left[\frac{K_0(\chi_0 r_p)}{I_0(\chi_0 r_p)} - \frac{K_0(\chi_0 R)}{I_0(\chi_0 R)}\right],$$

$$r_b < r_p;$$

$$G_{\mathrm{Cher}} = r_b \Delta_b \chi_0^2 \frac{I_0(\chi_0 r_p)}{I_0(\chi_0 R)} \quad (27b)$$

$$\times \frac{[I_0(\chi_0 r_b)K_0(\chi_0 R) - K_0(\chi_0 r_b)I_0(\chi_0 R)]^2}{K_0(\chi_0 r_p)I_0(\chi_0 R) - I_0(\chi_0 r_p)K_0(\chi_0 R)},$$
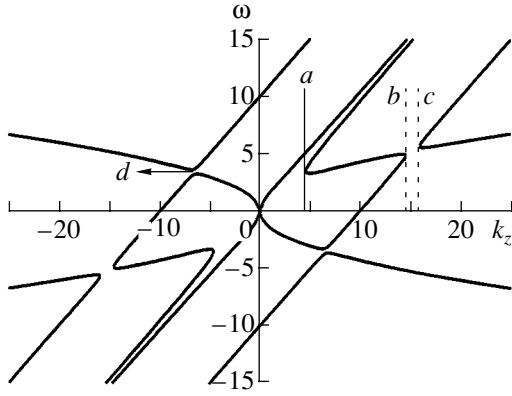
$$r_b > r_p.$$

Fig. 1. Dispersion curves of the waves in a waveguide with a beam and a plasma in a strong external magnetic field such that $\Omega_e = 10 \times 10^{10}$ rad/s and $\omega_p = 6 \times 10^{10}$ rad/s.

Dispersion relation (17), too, can be represented in the form similar to relation (25),

$$\omega^2 - \Omega_p^2 = Q \frac{k_{\perp m}^2}{k_{\perp m}^2 \varepsilon_{\perp p} + \chi_0^2} \frac{G_{\mathrm{Dop}} \omega^2 \omega_b^2 \gamma^{-1}}{(\omega - k_z u)^2 - (\Omega_e/\gamma)^2}$$
$$+ \frac{\chi_0^2}{k_{\perp m}^2 \varepsilon_{\perp p} + \chi_0^2} \frac{G_{\mathrm{Cher}} \omega^2 \omega_b^2 \gamma^{-3}}{(\omega - k_z u)^2}, \quad (28)$$

where $\varepsilon_{\perp p} = 1 + \delta\varepsilon_{\perp p}$,

$$\Omega_p^2 = \omega_p^2 \frac{\chi_0^2}{k_{\perp m}^2 \varepsilon_{\perp p} + \chi_0^2}, \quad (29)$$

and the geometric factors G_{Dop} and G_{Cher} are given by formulas (18). Consequently, in the case of a thin-walled annular plasma and a thin-walled annular beam, the instability growth rates have the same structure as those in formulas (19). Condition (22) also remain valid in this case. The resonance frequencies differ from the above frequencies, but we do not use explicit expressions for them here.

4. Let us further transform the already-derived dispersion relations in order to make them far simpler and far more convenient for obtaining estimates and performing particular calculations. In beam-related perturbation theory, in which the structure of oscillations in the system is assumed to be determined by the plasma, we must replace the frequency ω in the numerators on the right-hand side of dispersion relation (25) by the corresponding eigenfrequency Ω_p. This allows us to rewrite the dispersion relation in the form that includes

the geometric factors of the beam that were calculated by other methods [5], specifically,

$$\omega^2 - \Omega_p^2 = \chi_0^4 r_p \Delta_p r_b \Delta_b \tilde{G}_{\mathrm{Dop}} \frac{Q \omega_p^2 \omega_b^2 \gamma^{-1}}{(\omega - k_z u)^2 - (\Omega_e/\gamma)^2}$$
$$+ \chi_0^4 r_p \Delta_p r_b \Delta_b \tilde{G}_{\mathrm{Cher}} \frac{\omega_p^2 \omega_b^2 \gamma^{-3}}{(\omega - k_z u)^2}, \quad (30)$$

where

$$\tilde{G}_{\mathrm{Dop}} = I_1^2(\chi_0 r_b) I_0^2(\chi_0 r_p) \left(\frac{K_0(\chi_0 r_p)}{I_0(\chi_0 r_p)} - \frac{K_0(\chi_0 R)}{I_0(\chi_0 R)} \right)^2,$$
$$r_b \le r_p;$$
$$\tilde{G}_{\mathrm{Dop}} = I_1^2(\chi_0 r_b) I_0^2(\chi_0 r_p) \left(\frac{K_1(\chi_0 r_b)}{I_1(\chi_0 r_b)} + \frac{K_0(\chi_0 R)}{I_0(\chi_0 R)} \right)^2,$$
$$\quad (31a)$$
$$r_b \ge r_p;$$

$$\tilde{G}_{\mathrm{Cher}} = I_0^2(\chi_0 r_b) I_0^2(\chi_0 r_p) \left(\frac{K_0(\chi_0 r_p)}{I_0(\chi_0 r_p)} - \frac{K_0(\chi_0 R)}{I_0(\chi_0 R)} \right)^2,$$
$$r_b \le r_p;$$
$$\tilde{G}_{\mathrm{Cher}} = I_0^2(\chi_0 r_b) I_0^2(\chi_0 r_p) \left(\frac{K_0(\chi_0 r_b)}{I_0(\chi_0 r_b)} - \frac{K_0(\chi_0 R)}{I_0(\chi_0 R)} \right)^2,$$
$$\quad (31b)$$
$$r_b \ge r_p.$$

It is also convenient to write dispersion relation (28) in the same approximation:

$$\omega^2 - \Omega_p^2 = \frac{k_{\perp m}^2}{\chi_0^2} G_{\mathrm{Dop}} \frac{\Omega_p^2 \omega_b^2 \gamma^{-1} Q}{(\omega - k_z u)^2 - (\Omega_e/\gamma)^2}$$
$$+ G_{\mathrm{Cher}} \frac{\Omega_p^2 \omega_b^2 \gamma^{-3}}{(\omega - k_z u)^2}. \quad (32)$$

The geometric factors in dispersion relation (32) are again given by formulas (18). Dispersion relations (30) and (32) are identical in structure, reflecting the fact that the general physical properties of the beam–plasma interaction in a waveguide in an external magnetic field of finite strength are qualitatively independent of the geometric parameters of the system.

The dispersion curves plotted from dispersion relations (25) and (28) are especially informative. Let us consider the most characteristic curves obtained with the use of dispersion relation (25). As an example, we present the results that were calculated for the following geometric parameters of the waveguide: $R = 2$ cm, $r_b = 1$ cm, $r_p = 1.1$ cm, and $\Delta_b = \Delta_p = 0.1$ cm, the Langmuir frequency of the beam electrons and beam velocity being $\omega_b = 2 \times 10^{10}$ rad/s and $u = 2.6 \times 10^{10}$ cm/s ($\gamma = 2$), respectively. In calculations, we varied the cyclotron and plasma frequencies. In the figures to fol-
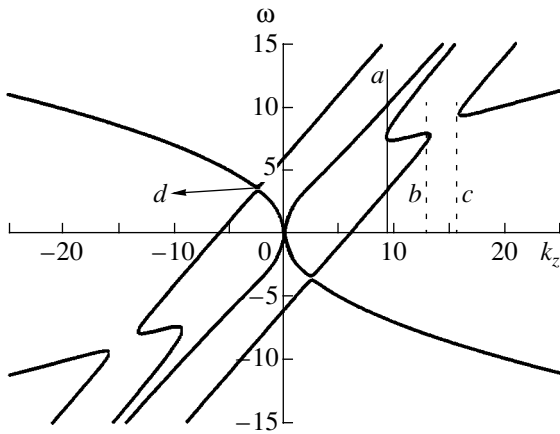
Fig. 2. Dispersion curves of the waves in a waveguide with a beam and a plasma in a weak external magnetic field such that $\Omega_e = 6 \times 10^{10}$ rad/s and $\omega_p = 10 \times 10^{10}$ rad/s.
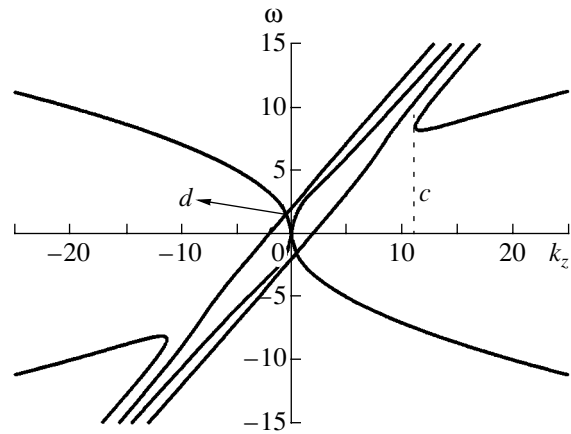

Fig. 3. Illustration of a change in the pattern of the dispersion curves from Fig. 2 for a weaker magnetic field such that $\Omega_e = 2 \times 10^{10}$ rad/s and $\omega_p = 10 \times 10^{10}$ rad/s.

low, we plot the dispersion curves $\omega = \omega(k_z)$ obtained by solving dispersion relation (25) numerically. The frequency is given in units of 10^{10} rad/s, and the wavenumber is in units of 1 cm^{-1}. Figure 1 illustrates the case of a strong external magnetic field such that $\Omega_e = 10 \times 10^{10}$ rad/s and $\omega_p = 6 \times 10^{10}$ rad/s. We can see that there are two instability regions: the one between the vertical axis $k_z = 0$ and vertical line a, and the other between vertical lines b and c (the pattern of the dispersion curves is antisymmetric about the origin of the coordinates). In the region between the vertical axis and vertical line a, the instability is due to the single-particle Cherenkov effect, and the instability in the region between vertical lines b and c is associated with the anomalous Doppler effect. Figure 2 illustrates the opposite case of a weak external magnetic field such that $\Omega_e = 6 \times 10^{10}$ rad/s and $\omega_p = 10 \times 10^{10}$ rad/s. We see the same two instability regions, which are now wider, however. In particular, the instability region associated with the anomalous Doppler effect becomes wider because the growth rate given by the second of formulas (19) increases as the frequency Ω_e decreases. In Fig. 1, as well as in Fig. 2, the instability regions associated with the Cherenkov effect and with the anomalous Doppler effect do not overlap: they are separated by the interval of wavelengths between vertical lines a and b. The situation changes when the external magnetic field is further decreased, i.e., when the Cherenkov effect loses its predominant role in favor of the anomalous Doppler effect, in accordance with condition (22). Figure 3 illustrates the case with $\Omega_e = 2 \times 10^{10}$ rad/s and $\omega_p = 10 \times 10^{10}$ rad/s. As may be seen, the two separate instability regions merge into one. The question of how this merging will change the dynamics of the Cherenkov instability can be answered only by recourse to the nonlinear model.

A waveguide with a thin-walled annular beam and plasma has an important property not possessed by a waveguide with a continuous plasma filling: it can operate with a spatially separated annular beam and plasma, thereby weakening the beam–plasma interaction regardless of which of the two effects dominates. Mathematically, this is expressed by the dependence of geometric factors (27) or (31) on r_b and r_p. Moreover, the higher the frequency, the stronger the dependence; this circumstance primarily concerns the efficiency of the anomalous Doppler effect. Figure 4 illustrates the same case as in Fig. 2, the only difference being that the plasma radius was increased by an amount as small as 1 mm ($r_p = 1.2$ cm). The pattern of the dispersion curves is seen to change substantially: the instability regions
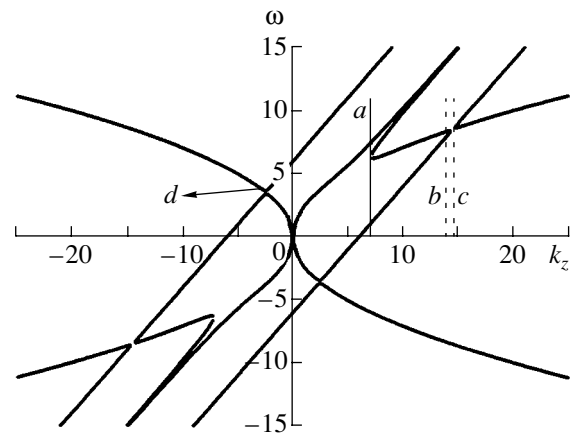

Fig. 4. Illustration of a change in the pattern of the dispersion curves from Fig. 2 for a plasma radius increased by 1 mm: $r_p = 1.2$ cm, $\Omega_e = 6 \times 10^{10}$ rad/s and $\omega_p = 10 \times 10^{10}$ rad/s.

both become narrower, but the instability region associated with the anomalous Doppler effect reduces to a greater extent because of the higher frequency of the emitted radiation. Hence, by increasing the spatial separation between the beam and the plasma, it is, in principle, possible to suppress Cherenkov emission under anomalous Doppler effect conditions.

In conclusion, we will touch on a problem that bears no direct relation to the subject of our paper; specifically, we will say a few words about the existence of a cutoff frequency band near the frequency of the resonant interaction between the beam and the backward plasma wave under normal Doppler effect conditions. In Figs. 1–4, this cutoff frequency band is indicated by arrow d. The authors of [17] proposed to use the normal Doppler effect for the suppression of feedback during the development of the beam instability in a resonator in order to terminate the generation when the latter is undesirable. The problem of preventing the self-excitation of the device is important, e.g., for the development of amplifiers. This problem was considered quite thoroughly in [17] in studying a dielectric-filled resonator penetrated by a straight electron beam in an external longitudinal magnetic field.

The cutoff frequency band for the feedback wave can exist under the following resonance conditions:

$$\omega_{\mathrm{Cher}} = k_{\mathrm{Cher}}u,$$
$$\omega_{\mathrm{Dop}} = k_{\mathrm{Dop}}u + \Omega_e/\gamma, \qquad (33)$$
$$\omega_{\mathrm{Dop}} = \omega_{\mathrm{Cher}}, \quad k_{\mathrm{Dop}} = -k_{\mathrm{Cher}}.$$

The first two of these conditions are the Cherenkov resonance condition and the normal Doppler resonance condition, and the last two are the conditions for the resonant waves to be the forward and the backward waves with respect to the beam. From conditions (33), we find the necessary condition for the external magnetic field:

$$\Omega_e = 2\gamma\omega_{\mathrm{Cher}}. \qquad (34)$$

The Cherenkov resonance frequency ω_{Cher} is determined from the equations $\omega = \Omega_p(k_z)$ and $\omega = k_z u$ (see the first of Eqs. (20)). In order to terminate the generation, it is sufficient that the feedback wave be cut off:

$$(\delta k_{\mathrm{Cher}} - \delta k_{\mathrm{Dop}})L < -\ln|\kappa|. \qquad (35)$$

Here, δk_{Cher} is the Cherenkov amplification coefficient for the forward wave, δk_{Dop} is the spatial damping coefficient for the backward wave, L is the resonator length, and κ is the reflection coefficient of the emitting end of the resonator for waves ($|\kappa| < 1$). The amplification and damping coefficients can easily be found from dispersion relation (25) or (28). For estimates, however, it is sufficient to use formulas (19) because we have $\delta k_{\mathrm{Cher}} \approx$

$|\delta\omega_{\mathrm{Cher}} V_g^{-1}|$ and $\delta k_{\mathrm{Dop}} \approx |\delta\omega_{\mathrm{Dop}} V_g^{-1}|$, where $V_g \approx u$ is the group velocity of the plasma wave excited by the beam.[1] As a result, even for a high-quality resonator ($|\kappa| \longrightarrow 1$), condition (35) reduces to inequality (22), which is easy to satisfy.

Hence, in plasma relativistic microwave electronics, the anomalous Doppler effect can in principle be successfully used for the suppression of feedback and for the termination of microwave generation. This conclusion, however, is largely theoretical. From Figs. 1–4, it can be seen that, under anomalous Doppler effect conditions, the cutoff frequency band for the feedback wave is fairly narrow. Consequently, condition (34) should be satisfied by a large margin, a difficult task when the pulsed magnetic field is strong.

REFERENCES

1. M. V. Kuzelev and O. T. Loza, Fiz. Plazmy **27**, 710 (2001) [Plasma Phys. Rep. **27**, 669 (2001)].

2. M. V. Kuzelev, A. A. Rukhadze, and P. S. Strelkov, *Plasma Relativistic Electronics* (Izd-vo MGTU im. N.É. Baumana, Moscow, 2002) [in Russian].

3. M. V. Kuzelev, Fiz. Plazmy **28**, 544 (2002) [Plasma Phys. Rep. **28**, 501 (2002)].

4. M. V. Kuzelev, R. V. Romanov, and A. A. Rukhadze, Prikl. Fiz., No. 3, 20 (2003).

5. I. N. Kartashov, M. V. Kuzelev, and A. A. Rukhadze, Fiz. Plazmy **30**, 60 (2004) [Plasma Phys. Rep. **30**, 56 (2004)].

6. A. V. Ponomarev and P. S. Strelkov, Fiz. Plazmy **30**, 66 (2004) [Plasma Phys. Rep. **30**, 62 (2004)].

7. V. L. Ginzburg, *Theoretical Physics and Astrophysics* (Nauka, Moscow, 1981) [in Russian].

8. M. V. Kuzelev and A. A. Rukhadze, Usp. Fiz. Nauk **152**, 285 (1987) [Sov. Phys. Usp. **30**, 507 (1987)].

9. M. V. Kuzelev and A. A. Rukhadze, in *Problems of Theoretical Physics and Astrophysics*, Ed. by L. V. Keldysh and V. Ya. Fainberg (Nauka, Moscow, 1989), p. 70 [in Russian].

---

[1] For the above-discussed anomalous Doppler effect in the interaction with the forward wave, we have $V_g \ll u < c$; consequently, the plasma wave excited by the beam under anomalous Doppler effect conditions is highly potential, which means that it is not emitted from the resonator. Such a wave can cause undesirable substantial changes in the electromagnetic properties of the plasma resonator.

10. M. V. Kuzelev, R. V. Romanov, and A. A. Rukhadze, Zh. Éksp. Teor. Fiz. **59**, 1625 (1989) [Sov. Phys. JETP **68**, 939 (1989)].

11. M. V. Kuzev and A. A. Rukhadze, *Electrodynamics of Dense Electron Beans in Plasma* (Nauka, Moscow, 1990) [in Russian].

12. M. V. Kuzelev, R. V. Romanov, and A. A. Rukhadze, Prikl. Fiz. **32** (3), 100 (2001).

13. M. Born and E. Wolf, *Principles of Optics* (Pergamon, Oxford, 1969; Nauka, Moscow, 1970).

14. A. F. Alexandrov, L. S. Bogdankevich, and A. A. Rukhadze, *Principles of Plasma Electrodynamics* (Vysshaya Shkola, Moscow, 1978; Springer-Verlag, Berlin, 1984).

15. N. S. Erokhin, M. V. Kuzelev, S. S. Moiseev, *et al.*, *Nonequilibrium and Nonresonance Processes in Plasma Radiophysics* (Nauka, Moscow, 1982) [in Russian].

16. L. D. Landau and E. M. Lifshitz, *Quantum Mechanics: Non-Relativistic Theory* (Nauka, Moscow, 1963; Pergamon, Oxford, 1977).

17. A. F. Aleksandrov, M. V. Kuzelev, and O. E. Pyrkina, Zh. Tekh. Fiz. **55**, 2399 (1985) [Sov. Phys. Tech. Phys. **30**, 1427 (1985)].

Translated by I.A. Kalabalyk

<center>

PLASMA OSCILLATIONS
AND WAVES

</center>

Generation of Low-Frequency Radiation by a Nonequilibrium Plasma of an RF Discharge in a Linear Mirror Magnetic Confinement System

V. V. Dobrokhotov*, N. M. Lyukshin*, G. A. Markov*, and Yu. V. Chugunov**

*Lobachevsky Nizhni Novgorod University, Nizhni Novgorod, 603950 Russia
**Institute of Applied Physics, Russian Academy of Sciences, ul. Ul'yanova 46, Nizhni Novgorod, 603600 Russia
Received September 16, 2004

Abstract—The generation of ion-cyclotron radiation in a plasma resonator formed by an RF discharge in a linear mirror magnetic confinement system is revealed and investigated. It is shown that the experimental setup makes it possible to study the composition of a multicomponent discharge plasma and to detect multiply charged ions. Collisional losses in such a resonator are estimated, and the pressure range within which the growth rate of the ion-cyclotron instability substantially exceeds the collisional damping rate is determined. © 2005 Pleiades Publishing, Inc.

1. INTRODUCTION

Plasma-wave RF discharge in a magnetic field (see [1–4]) is a steady-state plasma configuration stretched out along the magnetic field and localized in the transverse direction. The discharge exists in the form of a cylindrical plasma channel formed and maintained by plasma waves emitted by dipole (or quadrupole) RF sources. Such a discharge has been investigated under laboratory conditions and has also been produced in rocket experiments in the Earth's ionosphere in order to study its influence on sporadic phenomena occurring in geomagnetic flux tubes (see [5] and the literature cited therein). In recent years, a linear mirror magnetic system has been employed to examine plasma-wave RF discharges with the aim of modeling nonequilibrium magnetospheric processes that accompany the generation of electromagnetic waves (maser effect) in geomagnetic flux tubes. Conditions were determined under which such a discharge formed a plasma resonator for waves in the whistler and Alfvén frequency ranges. The distributions of the plasma density and magnetic field along the magnetic flux tube in the plasma resonator were similar to those in a natural magnetospheric resonator with a waveguide duct.[1] In this paper, we present the results from experimental studies of generation of ion-cyclotron waves in such a resonator. A simplified electrodynamic model of the resonator with allowance for collisional losses is proposed. Conditions are determined under which instabilities lead to the generation of ion cyclotron harmonics. It is shown that our experimental setup makes it possible to study the composi-

tion of a multicomponent discharge plasma and to detect multiply charged ions. The possibility of modeling magnetospheric maser effects in this device is also discussed.

2. EXPERIMENTAL CONDITIONS AND RESULTS

A schematic of the experimental setup is shown in Fig. 1. The magnetic field was produced by two solenoids (coils *1* and *2*) with independent power supplies. This allowed us to vary the longitudinal profile of the magnetic induction $B_z(z)$ from quasi-uniform to that corresponding to a magnetic-mirror configuration. The distance between the centers of the mirrors was 120 cm. A steady-state plasma column was produced by a plasma-wave RF discharge in the whistler frequency range ($\omega_{LH} < \omega < \omega_{Be}$, where ω_{LH} is the lower hybrid resonance frequency, ω_{Be} is the electron gyrofrequency, $\omega = 2\pi f$, and f is the radiation frequency). The discharge was excited in a 150-cm-long 6-cm-diameter glass tube (*3*) under conditions of the ionization self-ducting of waves excited in the above frequency range by a quadrupole antenna consisting of three copper rings placed around the tube in its central part, at a distance of 6 cm from one another. The RF voltage ($f_0 = 200$ MHz, $V_0 = 50$ V) was applied to the exciting rings from a GST-2 oscillator through a coaxial cable. The central conductor of the cable was connected to the central ring, whereas the outer conductor of the cable was connected to the side rings. The working gas was air at a pressure of $p \leq 10^{-3}$ torr. The input RF power W was about 10 W. The plasma density averaged over the transverse cross section of the discharge column, $N_e =$

---

[1] Note that, in the presence of a density duct localizing the excited wave fields, the threshold intensity of the charge particle flux required for the onset of electromagnetic instabilities is substantially reduced.
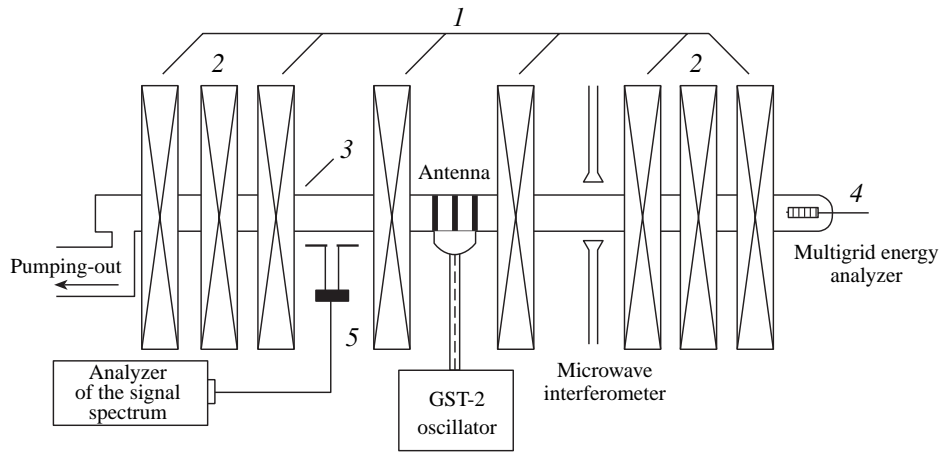
Fig. 1. Schematic of the experimental setup.

$\frac{1}{R_\perp}\int_0^a n_e(r)dr$ (where $R_\perp$ is the effective radius of the plasma column), was measured by a microwave interferometer operating at a frequency of 9.5 GHz and was also determined from the dispersion characteristics of surface waves guided by the plasma column [6]. The energy spectrum of the electrons escaping from the magnetic confinement system along the z axis was measured by a multigrid energy analyzer (*4*) located near the end of the magnetic confinement system. The spectra of low-frequency electromagnetic radiation emitted from the plasma were recorded with the help of a DSO Classic~6000 oscilloscope. We also analyzed Rogowski coil signals, which were proportional to the current to the body of the multigrid energy analyzer, and signals from a symmetric dipole antenna (*5*), which was aligned with the system axis and placed near the surface of the discharge tube, in the gap between the exciting antenna and the magnetic-mirror coil.

A distinctive feature of the ionization self-ducting of waves in the whistler frequency range in a nonuniform magnetic field is the narrowing of the plasma column and a substantial increase in the plasma density in the region where the field B_z is strong [4]. As the wave producing the plasma column propagates in the increasing field $B_z(z)$, it transforms from a strongly slowed-down quasi-potential (plasma) mode excited by a short RF source in a weak magnetic field ($B_z \leq 500$ G) into a weakly slowed-down whistler mode in the region of a strong field $B_z \geq 1500$ G [4]. Figure 2 shows the longitudinal profiles of the steady-state plasma density $N_e(z)$, the magnetic induction $B_z(z)$, and the radius $R_\perp(z)$ of the bright region of the plasma channel for a discharge excited at an air pressure of $p \approx 5 \times 10^{-5}$ torr and $W \approx 10$ W. If we describe the radial profile $n_e(r)$ by the power-law function $n_e(r, z) = N_0(z)/(1 + (r/d)^3)$ (which coincides with the measured density profile to within $\leq 10\%$), then $R_\perp$ is in fact the radius r at which the plasma density is one-half of its maximum value.

It should be noted that the profiles $B_z(z)$, $N_e(z)$, and $R_\perp(z)$ are similar to the longitudinal profiles of these quantities in a magnetospheric duct with an increased
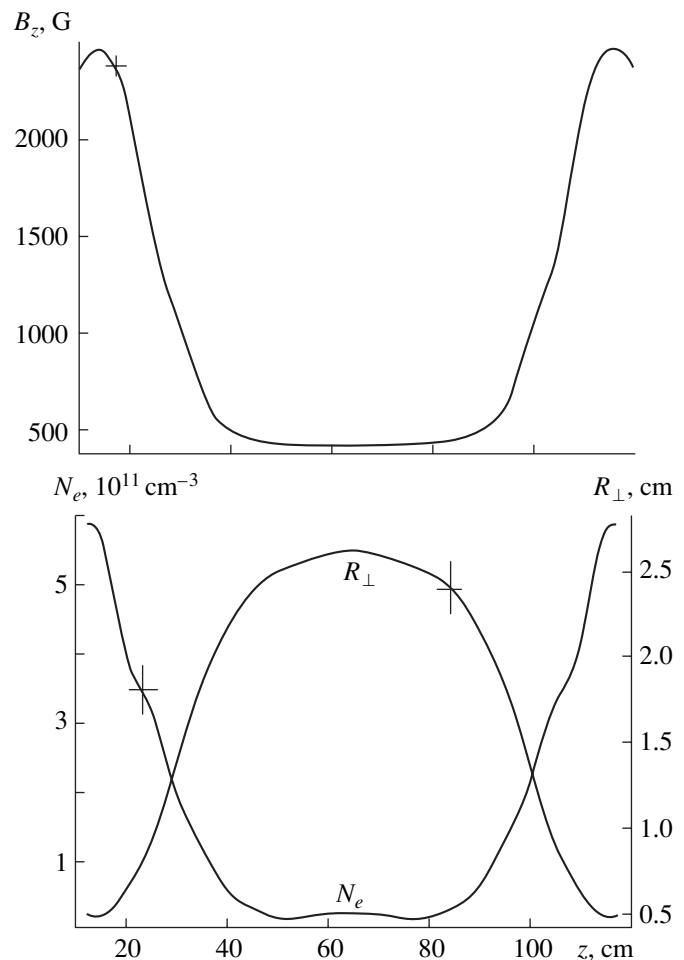

Fig. 2. Longitudinal profiles of the magnetic field B_z, the plasma density N_e, and the effective radius of the plasma column $R_\perp$ at $W = 10$ W and $p = 5 \times 10^{-5}$ torr.
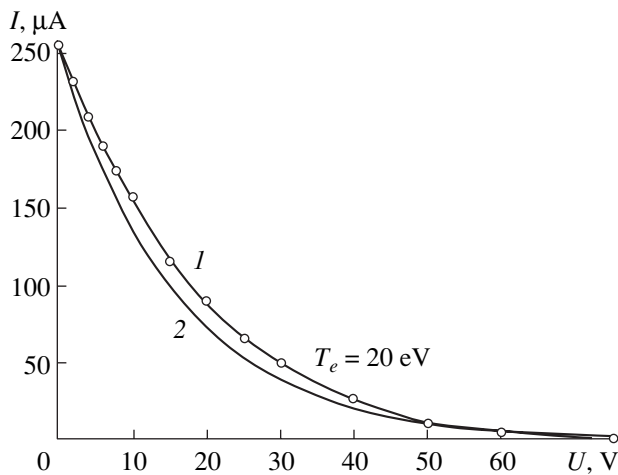
Fig. 3. (*1*) Measured and (*2*) calculated electron current to the collector of the multigrid energy analyzer vs. retarding potential for the same conditions as in Fig. 2.

plasma density and are typical of natural magnetospheric resonators in the whistler and Alfvén frequency ranges. This allows us to use our laboratory resonator to model resonant and nonstationary wave phenomena occurring in the Earth's magnetospheric resonators.

Figure 3 shows the electron current (curve *1*) to the collector of the multigrid energy analyzer versus the retarding field, $I(U)$, for the same conditions as in Fig. 2 and an analogous dependence (curve *2*) calculated for the electron flux from a plasma with an equilibrium (Maxwellian) electron energy distribution with a temperature of $T_e = 20$ eV.

The evident difference between curves *1* and *2* indicates that the discharge plasma in the magnetic confinement system is nonequilibrium. It is clear that the nonequilibrium electron and ion distributions can lead to an enhanced level of quasi-equilibrium and nonequilibrium noise emission from the plasma within a wide frequency range. It is also clear that the degree to which the plasma is far from equilibrium depends on the power deposited in the discharge and the magnetic field geometry.

In our experiments, we observed nonequilibrium spectra of low-frequency electromagnetic radiation in the ion-cyclotron frequency range characteristic of the gas mixture filling the discharge chamber. Experiments show that the spectrum of low-frequency radiation excited in the RF discharge plasma depends on the input RF power, the strength and configuration of the magnetic field, the ion composition of the plasma, and the pressure in the discharge tube. The most complicated spectra were observed at high input powers ($W >$ 10 W) in composite gas mixtures at pressures of $p <$ 10^{-4} torr.

Figure 4 presents an example of the spectrum of low-frequency radiation generated by a plasma-wave discharge excited in a mixture of air and vacuum oil vapor at a pressure of $p \sim 5 \times 10^{-5}$ torr and $W \sim 10$ W (the other experimental conditions being the same as in Figs. 2 and 3). The spectrum is averaged over a fairly large number of realizations arbitrarily chosen at different times. The spectrum contains three groups of fairly narrow lines, which can be attributed to the ion-cyclotron resonances of the main (singly, doubly, and triply charged) plasma ions. Moreover, one can see rather wide maxima associated with the generation of magnetoacoustic (MA) and ion-acoustic (IA) waves by the plasma wave exciting the discharge in the central region of the magnetic confinement system. Relatively low (at the noise level) resonant peaks in Fig. 4 correspond to the spectral lines of ions of the evaporated vacuum oil, silicon, and metals. Since the Q factor of the observed lines increases with frequency, the line of nitric oxide in the second and third groups of the ion cyclotron lines of air is clearly seen between the oxygen and nitrogen lines. As the pressure increases to $p > 10^{-4}$ torr, the ion-cyclotron lines disappear, but the lines associated with the generation of IA waves disappear only at $p > 6 \times 10^{-3}$ torr. After the magnetic field in the magnetic-mirror region is switched off, the ion-cyclotron lines cease to be generated.

3. DISCUSSION OF THE EXPERIMENTAL RESULTS

As was noted above, the intensities of the generated lines and their Q factors depend on the RF power deposited in the discharge, the magnetic field strength, the magnetic mirror ratio, and the pressure in the vacuum chamber. By varying these parameters, we could control the parameters of the generated lines. For example, we could tune to certain lines; as a result, these lines were distinguished among the other lines in their intensities and Q factors. For this purpose, the most convenient parameters were the magnetic field strength and the magnetic mirror ratio because they could easily be controlled over a relatively wide range. At high input RF powers ($W > 10$ W), the low-frequency spectra become strongly nonequilibrium. This manifests itself in a substantial increase in the noise level (the spectrum pedestal) and the appearance of many new lines in the spectrum. This indicates the presence of strong nonlinear wave–plasma interaction, including various "parasitic" processes, such as nonlinear detection and scattering.

It should also be noted that, at pressures of $p \sim$ 10^{-3} torr and a low magnetic field, the maximum value of Q ($\sim$40) is achieved for the IA line generated in a uniform magnetic field ($B \sim 200$ G) at a frequency of about 70 kHz. This indicates a rather efficient generation of IA waves via the decay of the plasma wave exciting the discharge.

It may be assumed that, in the frequency range under consideration, the excitation of oscillations in the
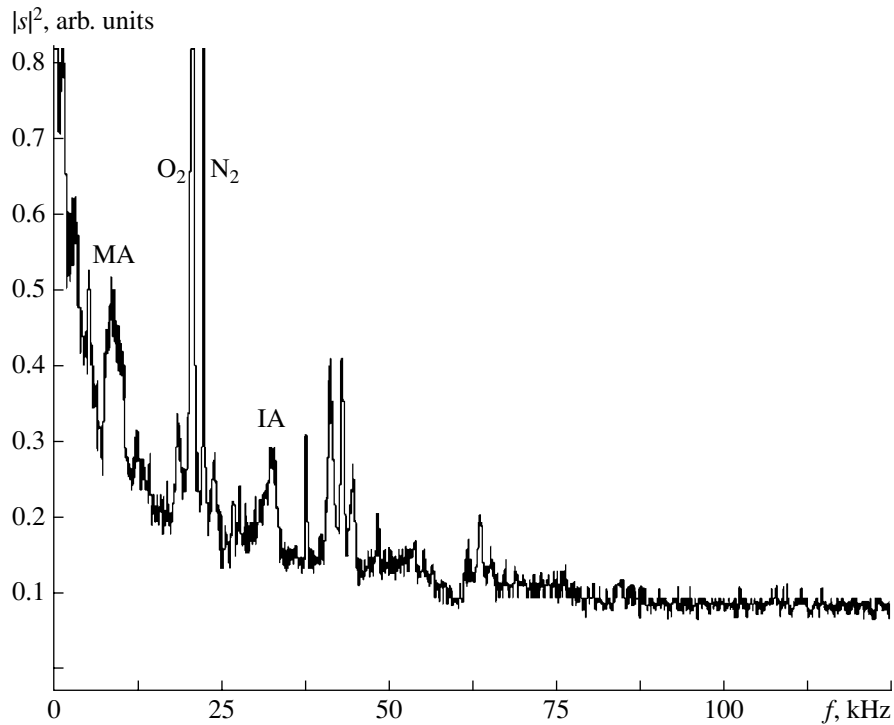
Fig. 4. Spectrum of the low-frequency radiation emitted from the discharge channel and recorded by dipole antenna *5* (see Fig. 1) at $W = 10$ W and $p = 5 \times 10^{-5}$ torr.

plasma resonator formed by a discharge column with a nonuniform longitudinal density profile is related to the onset of ion-cyclotron instability at frequencies of $\omega_\alpha = \omega_{B_i\alpha} + k v_{T_i}$ (where $\omega_{B_i\alpha} = 2\pi f_{B_i\alpha}$ is the gyrofrequency of the ions of species α, v_{T_i} is the ion thermal velocity, and $k = 2\pi/\lambda_\parallel$ is the wavenumber of the excited oscillations). In this case (as is confirmed by dipole antenna measurements), the most pronounced mode is an axisymmetric quasistatic mode. The electric field of this mode is localized within the plasma column and has a radial (E_r) and longitudinal (E_z) components. To provide the resonant excitation of oscillations and the efficient feedback, the following condition should be satisfied: $2n\lambda_\parallel = 2L_p$, where L_p is the resonator length and $n = 1, 2, 3, \ldots$ is an integer. This condition leads to the requirement that the waves be strongly sloweddown in the frequency range under consideration. An analysis of the dispersion of the waves guided by a plasma waveguide in a magnetic field shows that, under our experimental conditions, the slowing-down factor $p = \lambda_0/\lambda_\parallel$ (where λ_0 is the wavelength in free space) of electromagnetic waves in the frequency range $f \leq 1$ MHz can be sufficiently large only near ion-cyclotron resonances. Estimates show that, in this case, corrections related to the ion thermal motion can be ignored.

Figure 5 depicts dispersion curves for a magnetized plasma waveguide near the ion-cyclotron resonances for the main molecules of air: O_2, N_2, and NO. The curves were calculated for the following parameters: $B = 420$ G, $p \approx 3 \times 10^{-5}$ torr (the electron and ion collision frequencies are $v_e \sim 10^5$ s^{-1} and $v_i \sim 10^3$ s^{-1}, respectively), $R_\perp = 2.5$ cm, and $N_e = 2 \times 10^{10}$ cm^{-3}. The curves show the frequency dependences of the real (p') and imaginary (p'') parts of the normalized longitudinal wavenumber $p = h/k_0$, where $k_0 = \omega/c$ is the wavenumber in free space and $h = h' - ih''$ is the longitudinal wavenumber in the waveguide. The dispersion curves were calculated from the dispersion relation for axisymmetric electrostatic waves [7]:

$$i(\varepsilon_\perp \varepsilon_\parallel)^{1/2} J_1(k_\perp R_\perp) K_0(p k_0 R_\perp) \\ - J_0(k_\perp R_\perp) K_1(p k_0 R_\perp) = 0, \tag{1}$$

where $J_n(k_\perp r)$ is the nth-order Bessel function of the first kind; $K_n(p k_0 r)$ is the nth-order modified Bessel function of the second kind;

$$\varepsilon_\perp = 1 - \sum_\alpha \frac{\omega_{p\alpha}^2(\omega - iv_\alpha)}{\omega[(\omega - iv_\alpha)^2 - \omega_{B\alpha}^2]},$$

$$\varepsilon_\parallel = 1 - \sum_\alpha \frac{\omega_{p\alpha}^2}{\omega(\omega - iv_\alpha)}$$

are the elements of the permittivity tensor of a magnetized plasma; $\omega_{p\alpha}^2 = 4\pi e_\alpha^2 N_\alpha/m_\alpha$ and $\omega_{B\alpha} = e_\alpha B/c m_\alpha$ are the plasma frequency and the gyrofrequency of parti-
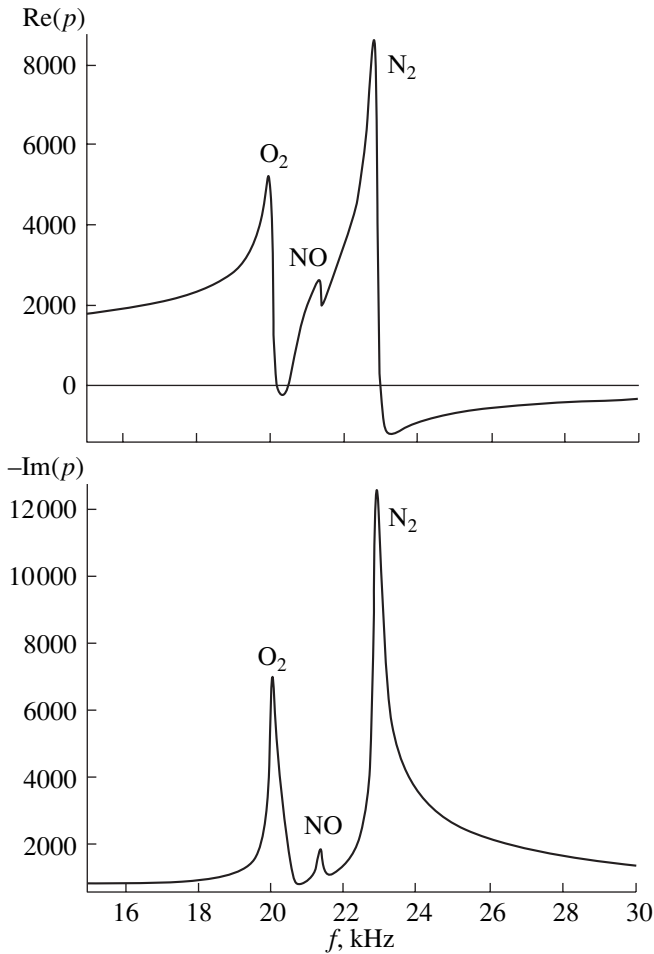
Fig. 5. Calculated frequency dependences of the real and imaginary parts of the normalized longitudinal wavenumber of axisymmetric electrostatic waves in a magnetized plasma waveguide near the ion-cyclotron frequencies of oxygen and nitrogen molecular ions for the parameters corresponding to the experimental conditions in the central region of the magnetic confinement system.

cles of species α, respectively; and ν_α is the collision frequency of particles of species α. The transverse wavenumber $k_\perp$ in a plasma waveguide is related to the longitudinal wavenumber h by the relation $k_\perp = i(\varepsilon_\parallel/\varepsilon_\perp)^{1/2}h$. The characteristic transverse decay length of the wave field near the discharge channel at $p \gg 1$ is equal to h^{-1}.

An important point is that, at frequencies close to (or somewhat below) the ion-cyclotron frequency, the wave damping can be small ($p'' \ll p'$). The numerical

Table

Molecular ion	Resonance frequency f_{res}, Hz	Damping rate γ, s^{-1}	Quality factor $Q = \omega_{res}/2\gamma$
Nitrogen N_2	22864	1074	67
Oxygen O_2	20023	1084	58

solution of a more exact dispersion relation allowing for the rotational component of the wave field [6, 7] for several values of the frequency f near and far from resonances shows that, under our experimental conditions, the difference between the exact and approximate solutions for p' and p'' does not exceed 10%.

The resonant properties of a nonuniform plasma resonator were analyzed within the approximation of a piecewise-uniform transmission line. The resonator region between the maxima of the magnetic field (see Fig. 2) was divided into 23 equal-length segments with constant B_z and N_e within each segment. The plasma density and the magnetic field within each segment were assumed constant and equal to their measured values at the center of the segment. The solution was sought in the form of a superposition of the fields of two counterpropagating waves satisfying dispersion relation (1) and the boundary conditions at the ends of the neighboring segments. The resonance frequencies f_{res} and the wave damping rates γ were calculated for the given reflection coefficients at the ends of the resonator ($\Gamma_{1,2} \sim 0.8$). The profiles of B_z and N_e corresponded to those shown in Fig. 2. The results of these calculations, together with the estimate for the Q factor of the resonator, are summarized in the table.

The theoretical analysis of the ion-cyclotron instability of a plasma with a nonequilibrium particle distribution over transverse velocities [8] shows that the instability growth rate γ is large ($\gamma \sim \omega_{Bi}$) when the ion plasma frequency ω_{pi} is high in comparison to the ion gyrofrequency ω_{Bi} and the ion gyroradius ρ_i is not small in comparison to the transverse scale of the field ($k_\perp\rho_i \gtrsim 2.4$). Under our experimental conditions, we have $\omega_{pi}/\omega_{Bi} \sim 10^2$ and $k_\perp\rho_i \sim 7$. Hence, we can conclude that the growth rate of ion-cyclotron instability substantially exceeds the collisional damping rate at air pressures of $p < 10^{-4}$ torr. In this pressure range, the resonance frequencies of hydrogen ions ($f_{O_2} = 20023$ Hz) and nitrogen ions ($f_{N_2} = 22864$ Hz) are close to their measured values and the oscillation damping rate $\gamma \sim 10^3$ s^{-1} is close to the ion collision frequency.

4. CONCLUSIONS

In our experiments, we have investigated various nonlinear effects accompanying the generation of low-frequency radiation near the gyrofrequencies of the ions of different species. Our experimental device allows us to study the composition of a multicomponent RF discharge plasma and to detect multiply charged ions; i.e., it can be used as a peculiar kind of mass-spectrometer of multiply charged ions. Our experiments have also shown that the plasma-wave discharge in a linear mirror magnetic system can be used to model nonequilibrium magnetospheric processes accompanying the generation of electromagnetic waves

in a geomagnetic flux tube containing a waveguide duct for these waves.

It should be noted that, in the Earth's magnetospheric resonator, charged particles drift across the magnetic field due to the finite curvature of the magnetic field lines. This drift causes the inflow of resonant ions from radiation belts and the outflow of used particles from the excited magnetic flux tube (the so-called "flow-through" effect [9]). Due to the large dimensions of the natural resonators and due to collisional and radiative losses, the ion-cyclotron lines in the Earth's magnetosphere are primarily generated at the higher order modes of the resonator. In our laboratory experiment, the ions were heated immediately in the discharge channel, so the resonance lines were primarily excited at the fundamental mode of the plasma resonator. This imposes certain restrictions on the modeling of the specific maser effects in relatively small laboratory devices. However, we believe that the fundamental problem of finding the physical mechanisms that govern the generation of low-frequency waves by a nonequilibrium plasma in mirror magnetic confinement systems, as well as the problem of controlling the excitation of these waves, can be resolved with the help of laboratory experiments similar to those described in this paper.

ACKNOWLEDGMENTS

REFERENCES

1. G. A. Markov, V. A. Mironov, and A. M. Sergeev, Pis'ma Zh. Éksp. Teor. Fiz. **29**, 672 (1979) [JETP Lett. **29**, 617 (1979)].
2. G. A. Markov, V. A. Mironov, A. M. Sergeev, and I. A. Sokolova, Zh. Éksp. Teor. Fiz. **80**, 2264 (1981) [Sov. Phys. JETP **53**, 1183 (1981)].
3. G. A. Markov, Zh. Éksp. Teor. Fiz. **113**, 1289 (1998) [JETP **86**, 703 (1998)].
4. V. V. Dobrokhotov and G. A. Markov, Izv. Vyssh. Uchebn. Zaved., Radiofiz. **46**, 392 (2003).
5. Yu. V. Chugunov and G. A. Markov, J. Atmos. Sol.-Terr. Phys. **63**, 1775 (2001).
6. S. B. Bodrov and G. A. Markov, Fiz. Plazmy **28**, 1077 (2002) [Plasma Phys. Rep. **28**, 992 (2002)].
7. A. N. Kondratenko, *Plasma Waveguides* (Atomizdat, Moscow, 1976).
8. A. B. Mikhailovskii, *Theory of Plasma Instabilities* (Atomizdat, Moscow, 1971; Consultants Bureau, New York, 1974), Vol. 1.
9. P. A. Bespalov and V. Yu. Trakhtengerts, in *Reviews of Plasma Physics*, Ed. by M. A. Leontovich (Atomizdat, Moscow, 1980; Consultants Bureau, New York, 1986), Vol. 10.

Translated by N.F. Larionova

Measurements of the Axial Magnetic Field during the Implosion of Wire Arrays in the Angara-5-1 Facility

G. G. Zukakishvili, K. N. Mitrofanov, E. V. Grabovskiĭ, and G. M. Oleĭnik

Troitsk Institute for Innovation and Fusion Research, Troitsk, Moscow oblast, 142190 Russia
Received September 15, 2004; in final form, March 24, 2005

Abstract—Results are presented from measurements of the axial magnetic field during the implosion of tungsten wire arrays in the Angara-5-1 facility at currents of 2.5–4.5 MA. The azimuthal structure of the plasma produced from the wires is examined using the effect of the compression of the axial magnetic flux by this plasma. It is shown that the plasma starts to penetrate into the axial region of the wire array at the very beginning of implosion. A mechanism other than the formation of a closed current-carrying shell is proposed for describing the transfer of the external axial magnetic field to the central region of the array. © *2005 Pleiades Publishing, Inc.*

1. INTRODUCTION

Our experiments on the compression of the axial magnetic flux were aimed on studying the azimuthal structure of the plasma produced during the implosion of wire arrays. In contrast to the flux compression scheme employed in [1–4], in which the initial axial magnetic field compressed by a liner was used to convert a considerable fraction of the liner kinetic energy into magnetic energy, the diagnostic axial magnetic field in our case does not perturb the plasma motion until the radius of the current-carrying shell decreases severalfold. It was assumed that, if a homogeneous thin plasma shell forms during the wire implosion, then, by virtue of the conservation of the initial magnetic flux $\Phi_{z0} = B_{z0}R_0^2$, the axial magnetic field should vary according to the law $B_z(t) = B_{z0}R_0^2/R(t)^2$. From the time dependence of the axial magnetic field, one can determine the law of motion of the inner boundary of the current-carrying shell, as well as the instant at which a plasma shell capable of compressing the magnetic flux forms.

It may be that no cylindrical plasma shell forms in the initial stage of implosion and the plasma produced from an individual wire moves toward the array axis without merging with the plasmas produced from the neighboring wires. (In what follows, the plasma flow from an individual wire will be referred to as a jet.) In this case, the axial magnetic field is expected to change only slightly during the implosion of the wire array.

Experiments show, however, that, in some cases, the actual behavior of the magnetic field is quite different. It was found that the axial magnetic flux can be compressed even in the absence of a continuous plasma shell. The results obtained can be explained more consistently if one assumes that, during the implosion, a considerable fraction of the initial magnetic flux is frozen in the plasma jets and is transferred with them. The remaining free magnetic flux either falls outside the plasma and is compressed only slightly or is captured and compressed in the initial stage of implosion due to the merging of individual jets and the formation of a closed conducting shell at the inner boundary of the imploding plasma.

2. COMPRESSION OF THE AXIAL MAGNETC FLUX BY THE PLASMA OF THE WIRE ARRAY

We used two methods for creating an axial magnetic flux inside a wire array:

(i) The screwing of the wire array [5, 6]. In this case, the axial magnetic field B_z is determined by the wire inclination angle α and the discharge current $B_z(t) \sim I_z(t)\sin\alpha(t)$.

(ii) The use of a multiturn solenoid placed in the liner section, as is shown in Fig. 1. The main discharge through the wire array was produced ≈2.2 ms after the axial magnetic field reached its maximum. Over this time, the magnetic field diffused into the electrodes to a depth of ≈2 cm. During the implosion of the wire array (≈0.1 μs), this fraction of the magnetic field remained frozen in the electrodes (see Fig. 1). The initial axial magnetic field at the location of the wire array was varied from 0 to 15 kG. The axial nonuniformity of the magnetic field, which was determined by the relative positions of the solenoid and the wire array and by the field skinning in the electrodes, did not exceed ≈30%.

In this series of experiments, we used wire arrays 20 mm in diameter. The azimuthal arrangement of the wires could be varied: the wires were uniformly distributed along the perimeter of the array or they were assembled in groups of several wires. The array linear mass was varied from 300 to 3685 μg/cm, and the num-
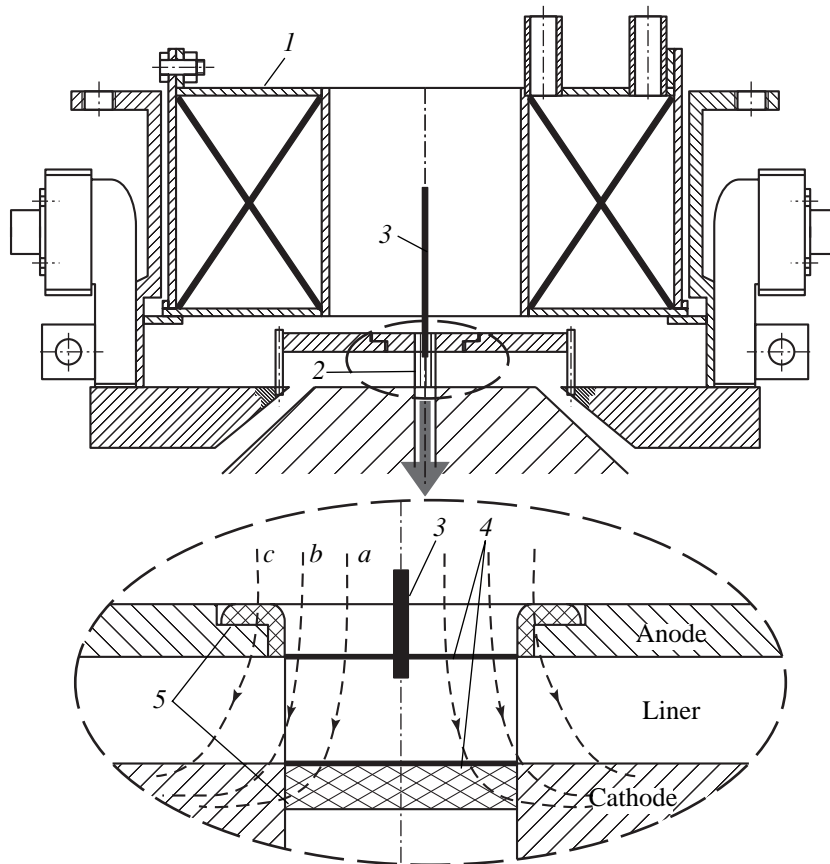
Fig. 1. Schematic of the experiment on the compression of an external axial magnetic flux: (*1*) solenoid for producing the axial magnetic field, (*2*) wire array, (*3*) B-dot probe, (*4*) foil, (*5*) array electrodes, (*a*, *b*) magnetic field lines that are not frozen in the electrodes, and (*c*) magnetic field lines frozen in the electrodes.

ber of wires was varied from 24 to 670. The spacing between individual wires or between groups of wires varied from ≈0.09 mm to ≈25 mm.

The time behavior of the axial magnetic field on the array axis was measured by a B-dot probe consisting of two small-size, oppositely wound coils, the bipolar signals from which (see Fig. 2a, curves *1*) were proportional to the time derivative of the axial magnetic field. The mutual symmetry of the signals indicated that they actually were of magnetic nature. The magnetic field was measured both inside the array at a distance of 2 mm from the anode and over the anode behind a NbTi foil 10 or 15 μm thick (the specific resistance of the foil was ≈60 μΩ cm). For a typical time of the array implosion, the foil thickness was much less than the skin depth [7]. The wire array electrodes (Fig. 1) were made of a dielectric coated with this foil in order to reduce the skin effect and, thus, to decrease the initial nonuniformity of the axial magnetic field at the array location.

For an axially symmetric current distribution in the wire array, the normal (with respect to the array axis) component of the magnetic field on the axis should be zero. In real experiments, the measured normal compo-

nent of the magnetic field may differ from zero because of an asymmetry of the current distribution and the imperfect positioning of the probe on the array axis.

In order to test the method, we performed measurements of the axial magnetic field by a B-dot probe positioned on the array axis in the presence and in the absence of an external axial magnetic field. The contribution from the azimuthal magnetic flux to the main signal was found to be as low as 0.8–2%.

In what follows, the experimental results are illustrated by the waveforms of the bipolar signals from the B-dot probe, the axial magnetic field, the total current through the wire array, and the soft X-ray (SXR) power, as well as by optical streak images of the discharge plasma.

3. CYLINDRICAL ARRAY WITH UNIFORMLY ARRANGED WIRES

In shot no. 3741, the load was an array with a height of 10 mm and linear mass of 330 μg/cm. Sixty tungsten wires 6 μm in diameter were arranged on the radius of 10 mm. The initial axial field at the probe location was
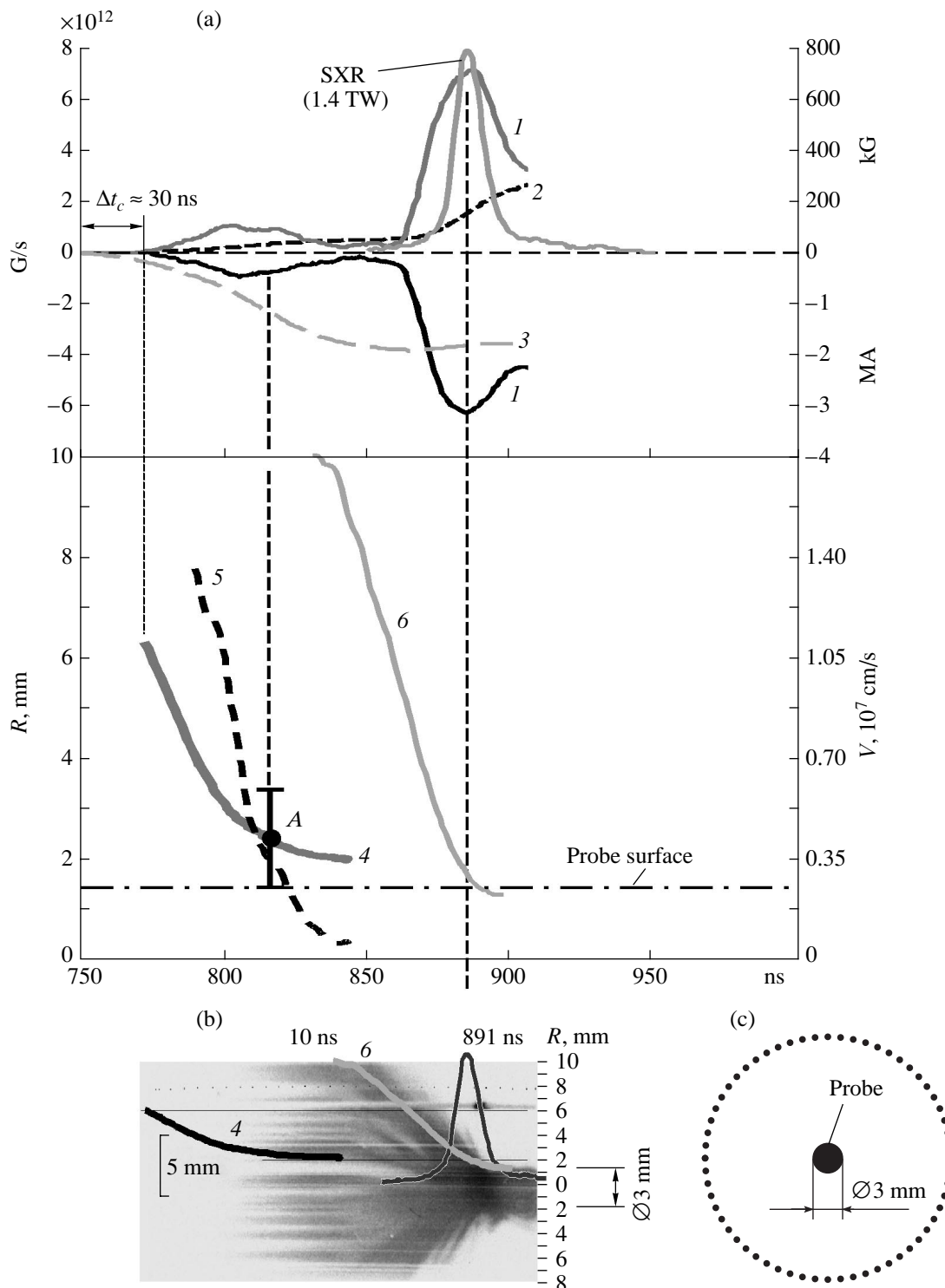
Fig. 2. Measurements of the axial magnetic field (shot no. 3741): (a) waveforms of (*1*) the bipolar signals from a B-dot probe located on the array axis (here and in the subsequent figures, these signals are recalculated to the time derivative of the axial magnetic field), (*2*) the axial magnetic field, (*3*) the total discharge current, (*4*) the calculated radius of the inner boundary of the azimuthal current I_φ, (*5*) the calculated velocity of the inner boundary of the azimuthal current I_φ, (*6*) the average radius of the current I_z calculated from the discharge inductance, and (SXR) the soft X-ray power; (b) an optical streak image (negative) synchronized in time with the waveforms shown in plot (a); and (c) the initial azimuthal structure of the wire array.

≈5.0 kG. The probe was positioned on the array axis and was inserted into the electrode gap to a depth of 2 mm (Fig. 1). Figure 2a shows the bipolar signals from the B-dot probe (curves *1*) (here and in the subsequent figures, these signals are recalculated to the time derivative of the axial magnetic field) and the waveforms of the axial magnetic field (curve *2*), the total discharge current (curve *3*), and the SXR power.

The probe signal appeared with a time delay of $\Delta t_c = 30$ ns after the beginning of the discharge, when the total current through the array reached ≈0.3 MA. This time is interpreted as the beginning of the compression of the free axial magnetic flux within a certain effective radius R_c. In this phase of the discharge, the plasma temperature is 20–30 eV [8]. We assume that the appearance of the probe signal corresponds to the formation of a current-carrying plasma shell closed in the azimuthal direction. The azimuthal current I_φ flowing through the shell leads to the compression of the magnetic flux. On this time scale, the shell thickness is larger than the skin depth ($\delta_s \approx 0.2$ cm). The radius R_c can be estimated as $R_c = R_0 - V_{pl}(t_{cap})\Delta t$, where R_0 is the initial radius of the array, $V_{pl}(t_{cap})$ is the velocity of the inner boundary of the current-carrying shell at the instant at which the axial magnetic flux is captured by it, and $\Delta t = 30$ ns is the time interval during which the plasma is accelerated before capturing the axial magnetic flux. The velocity $V_{pl}(t_{cap}) \approx (1-2) \times 10^7$ cm/s was determined in a separate experiment from the change in the azimuthal magnetic field during the implosion of a similar wire array. The radius R_c was found to be equal to ≈$0.6R_0 \pm 0.5\delta_s$. At the radius R_c, the plasma jets from individual wires merge to form a shell capable of compressing the magnetic flux within this radius. In the course of compression, the plasma density can be modulated in the azimuthal direction.

Assuming that the axial magnetic flux within the radius R_c is conserved ($\Phi = B_z\pi r^2 =$ const), we constructed the time dependences $r(t)$ and $v(t)$ (Fig. 2a; curves *4* and *5*, respectively), which illustrate the law of motion of the inner boundary of the azimuthal current I_φ. These dependences were constructed using the expressions

$$r = R_c\sqrt{\frac{B_{z0}}{B_z}},$$

$$|\mathbf{V}| = \frac{dr}{dt} = \frac{1}{2}R_c B_{z0}^{1/2} B_z^{-3/2}\frac{dB_z}{dt}.$$

For comparison, Figs. 2a and 2b also show the time evolution of the average radius of the axial current I_z (curves *6*). This radius was calculated from the measured variations in the load inductance, assuming that the system is axially symmetric. As was expected, the average radius of the axial current I_z is larger than the radius of the inner boundary of the azimuthal current I_φ.

Two stages can be distinguished in the time evolution of the axial magnetic field (Fig. 2a, curve *2*): the slow increase (plateau) over the first 100 ns and the rapid growth 25 ns before the maximum of the SXR signal. The axial magnetic field begins to rapidly grow when the plasma that carries most of the discharge current arrives at the array axis. The increase in the axial magnetic field is also observed over ≈50 ns after the instant of maximum plasma compression. In this case, the axial field reaches a value of ≈300 kG (Fig. 2a). Such a behavior of the axial magnetic field can be attributed to a fraction of this flux being frozen in the plasma in the course of plasma formation. After the instant of maximum compression, the frozen-in magnetic field diffuses from the plasma into the B-dot probe. After the plasma arrives at the probe surface, the probe measures the axial magnetic field frozen in the plasma. This time can be estimated by equating the radius of the inner boundary of the azimuthal current I_φ (to within the error in determining δ_s) to the radius of the probe shell (Fig. 2a, point *A*). For the given shot, this time is ≈60 ns.

Under our experimental conditions, the magnetic pressure wave propagates with the Alfvén velocity $V_A = B/(4\pi\rho)^{1/2}$, where $B = \sqrt{B_\varphi^2 + B_z^2}$. In the initial stage of implosion, the plasma mass within the radius R_c is small [9], so the Alfvén velocity is sufficiently high to satisfy the condition

$$V_A\Delta t \gg R_c,$$

where Δt is the characteristic time of the process. The magnetic pressure is uniform in this region, and the magnetic flux can be described as a free flux in vacuum.

In our experiments, four stages can be distinguished in the implosion of a wire array with an initial axial magnetic filed:

(i) The first stage lasts from the beginning of the discharge up to ≈30 ns. In this stage, the plasma that is generated by the wires and moves toward the array axis does not form a solid shell in the azimuthal direction.

(ii) The second stage lasts from 30 to ≈70 ns. At the beginning of this stage, an almost solid shell forms at the radius ≈$0.6R_c$, to which the plasma is displaced from the wires. This plasma compresses the free axial magnetic flux captured at the radius $0.6R_c$. In this case, the radius of the shell, which comprises only 1% of the total array mass, decreases from $0.6R_c$ to $0.2R_c$.

(iii) In the third stage, which lasts from ≈70 ns to the instant of maximum compression (which corresponds to the maximum of the SXR signal), the axial magnetic flux residing between $0.6R_c$ and R_0 is transferred to the axis by the bulk of the wire plasma.

(iv) In the fourth stage (after the instant of maximum compression), the axial magnetic field at the axis continues to increase. This may be related to two effects: the diffusion of the axial magnetic field from the plasma arriving at the axis into the probe and the

motion of the peripheral plasma with the frozen-in axial magnetic flux toward the axis.

Thus, there are two types of axial magnetic flux: the free flux outside the plasma and the flux frozen in the plasma.

To clarify the mechanism for the transfer of the axial flux in the second and third stages, we carried out experiments with wire arrays in which the wires were arranged in groups in the azimuthal direction.

4. CYLINDRICAL ARRAY COMPOSED OF WIRES ARRANGED IN SEVERAL GROUPS

The azimuthal structure of the plasma in the wire array was varied by dividing the wires into groups arranged along the perimeter of the array. The total number of wires, their diameter, and the array diameter remained the same, and only the number of groups was varied.

Figures 3–5 show the results of experiments with arrays consisting of 24 wires 10 μm in diameter that were arranged on the radius 10 mm and divided into groups. The interwire distance in each group was 0.26 mm, the linear mass of the wire array was 300 μg/cm, and the array height was 10 mm. The experiments were performed with different magnitudes of the initial axial magnetic field. The axial magnetic field was measured by a B-dot probe positioned at the array axis. The figures also show the waveforms of the discharge current and the SXR power.

In short no. 3739, the wires were divided into twelve groups (two wires in each group), as is shown in Fig. 3c. The initial axial field was ≈13.8 kG. The SXR power in this shot was 0.1 TW. The delay time between the beginning of the discharge and the appearance of the probe signal was $\Delta t_c \approx 30$ ns. In the optical streak image shown in Fig. 3b, one can see how the inner plasma boundary propagates toward the axis. For comparison, the figure also shows the $r(t)$ diagram calculated from the data on the compression of the free axial magnetic flux.

In shot no. 3744, the wires were divided into eight groups (three wires in each group), as is shown in Fig. 4c. The initial axial field was ≈3.4 kG. The SXR power in this shot was lower than 0.25 TW.

The signal behavior in this shot was similar to that observed with an array in which the wires were distributed uniformly. The axial magnetic field continued to increase after the maximum of the SXR signal. The delay time between the beginning of the discharge and the appearance of the probe signal was $\Delta t_c \approx 60$ ns. The radius R_c at which the free axial magnetic flux was captured was estimated to be ≈0.25 ± 0.1 cm; i.e., it was nearly equal to the probe radius (0.15 cm). In this case, the plasma was probably not closed in the azimuthal direction (the second stage was absent) and the probe measured only the axial magnetic field frozen in the plasma (the third stage).

In shot no. 3792, the wires were divided into two groups (twelve wires in each group), as is shown in Fig. 5d. The initial axial field was ≈13.5 kG. In contrast to the previous shots, the B-dot probe was positioned at mid-radius of the wire array, in front of one of the wire groups. With such an array, we did not expect the formation of a closed shell capable of compressing the free axial magnetic flux.

Eighty nanoseconds after the beginning of the discharge, we observed an SXR burst attributed to the compression of the plasmas produced from individual groups of wires. Within this time interval, no radial plasma motion was observed. This is clearly seen in the optical streak image (Fig. 5b). During about 35 ns after the SXR burst, the axial magnetic filed in the region that is not occupied by the plasma decreases gradually to almost zero: $1 - B_z^{\min}/B_{z0} \approx 0.8$ (Fig. 5a, curve *3*). When the plasma passes through the probe (see Fig. 5b), the axial magnetic field increases to ≈200 kG. This indicates that the axial magnetic flux frozen in the wire plasma is compressed and then is transferred by the two plasma jets toward the array axis.

Thus, in this shot, up to 80% of the initial magnetic flux turns out to be frozen in the wire array plasma in the course of plasma formation and the axial magnetic flux is compressed in the absence of a uniform current-carrying shell.

5. INFLUENCE OF THE INITIAL AXIAL MAGNETIC FIELD ON THE SXR YIELD

It can be seen from Figs. 6a and 6b that the SXR power is very sensitive to the magnitude of the initial axial magnetic field. As the initial axial magnetic field increases from 0 to 15 kG, the SXR power decreases from 2.5 TW to less than 0.1 TW. At the same time, the size of the region near the array axis from which intense X radiation is emitted somewhat increases (see Figs. 6c–6f) in discharges with a strong initial axial magnetic field ($B_{z0} > 6$ kG).

6. INFLUENCE OF THE INTERWIRE DISTANCE ON THE INSTANT AT WHICH THE PROBE SIGNAL APPEARS

By analyzing the results of experiments with arrays composed of uniformly distributed wires and with arrays in which the wires were divided into groups, we deduced the dependence of the time delay Δt_c between the beginning of the discharge current and the appearance of the probe signal on the interwire distance Δ (or the distance between groups of wires) at an array diameter of 20 mm (see Fig. 7). The value of Δt_c is also shown in Figs. 2–4. This time delay corresponds to the beginning of the second stage (for $\Delta < 5$ mm) or to the beginning of the third stage (for $\Delta > 5$ mm). From the time delay Δt_c of the second stage, we can determine
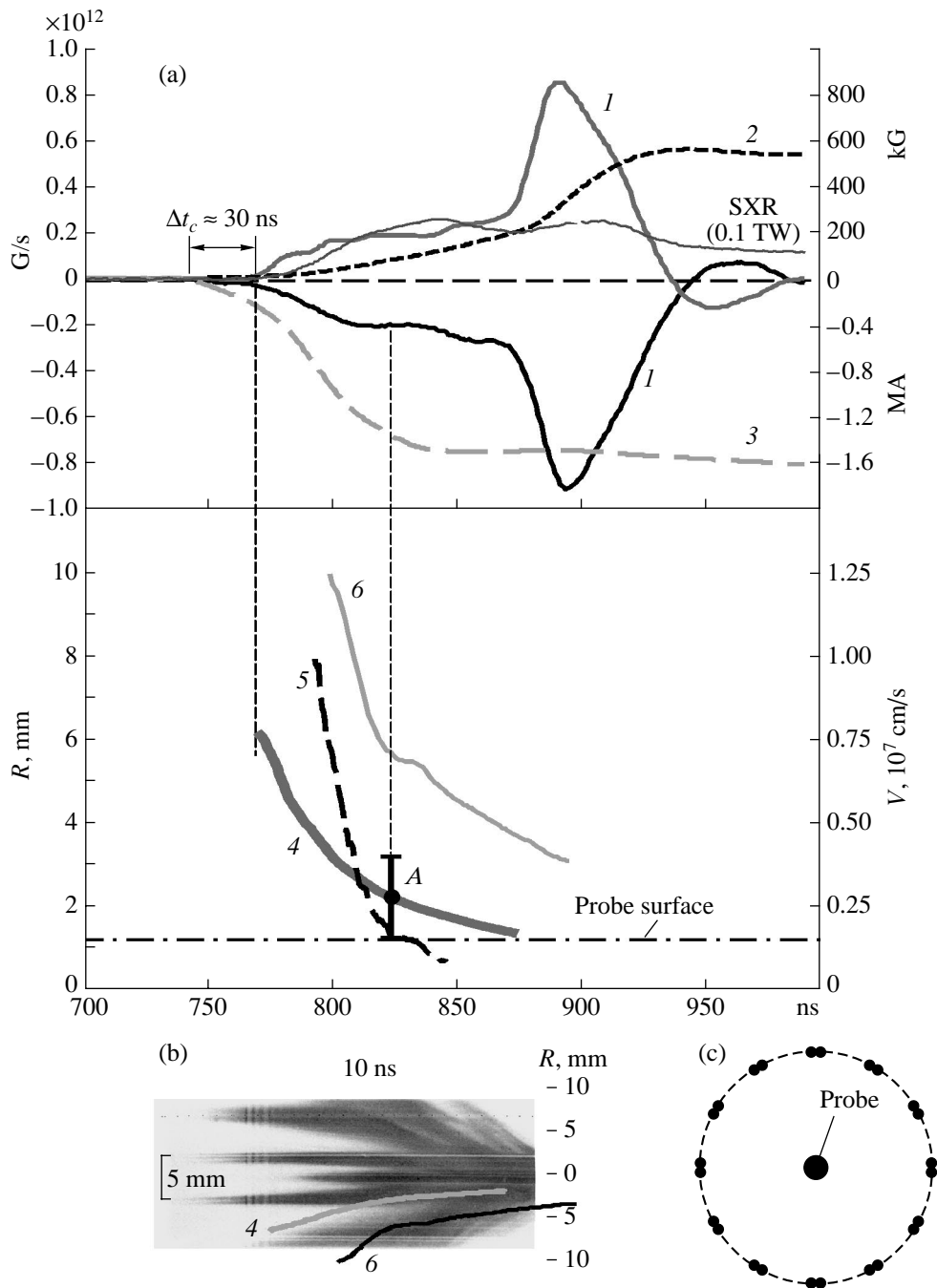
Fig. 3. Measurements of the axial magnetic field (shot no. 3739): (a) waveforms of (*1*) the bipolar signals from a B-dot probe located on the array axis, (*2*) the axial magnetic field, (*3*) the total discharge current, (*4*) the calculated radius of the inner boundary of the azimuthal current I_φ, (*5*) the calculated velocity of the inner boundary of the azimuthal current I_φ, (*6*) the average radius of the current I_z calculated from the discharge inductance, and (SXR) the soft X-ray power; (b) an optical streak image (negative) synchronized in time with the waveforms shown in plot (a); and (c) the initial azimuthal structure of the wire array.

the time t_{skin} required for the formation of a plasma shell that is closed in the azimuthal direction, whose thickness is larger than the skin length, and that is capable of compressing the free axial magnetic flux.

As was noted above, the appearance of the probe signal is determined by two processes:

(i) the compression of the free axial magnetic flux in the second stage and

(ii) the penetration of the axial magnetic field frozen in the plasma into the probe region in the third stage.

In some experiments (Fig. 7, $\Delta > 5$ mm), the probe signal was primarily determined by the second process,
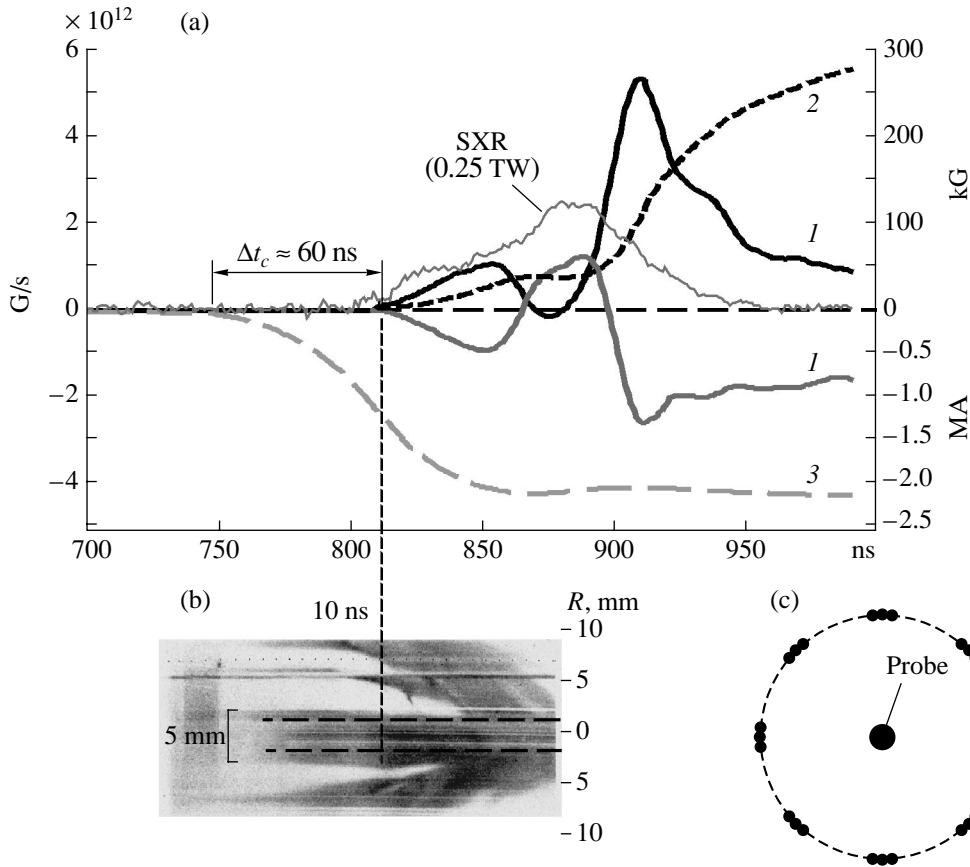
Fig. 4. Measurements of the axial magnetic field (shot no. 3744): (a) waveforms of (*1*) the bipolar signals from a B-dot probe located on the array axis, (*2*) the axial magnetic field, (*3*) the total discharge current, and (SXR) the soft X-ray power; (b) an optical streak image (negative) synchronized in time with the waveforms shown in plot (a); and (c) the initial azimuthal structure of the wire array.

whereas no contribution from the first process was detected. In this case, only the frozen-in axial magnetic field was detected on the array axis stating from 60 ns. This is why points measured at $\Delta > 5$ mm differ strongly in their positions from other points in Fig. 7. In wire arrays with interwire distances of $1 < \Delta < 5$ mm, the compression of the free axial magnetic flux in the axial region occurred 30 ns after the beginning of the discharge. When the distance between wires was decreased to less than 1 mm, the compression of the axial magnetic field occurred even sooner (at 20 ns).

7. SCREWED WIRE ARRAY

In shot no. 3632, we used a screwed wire array with a diameter of 20 mm, height of 10 mm, and linear mass of 200 µg/cm. The array consisted of 40 tungsten wires 6 µm in diameter. The wire inclination angle was $\alpha \approx 6°$. Figure 8 shows the results of measurements of the axial magnetic field. The maximum SXR power in this shot was ≈ 0.6 TW.

The average radius of the axial current I_z in Fig. 8 (as in Figs. 2 and 3) was estimated from the array inductance calculated using the results of electric measure-

ments of the current and voltage near the load under the assumption that the current is axially symmetric and the active voltage component is absent:

$$\bar{R}(t) = R_0 e^{\frac{\Delta L}{2h}}, \quad \Delta L = L(t) - L_0, \quad L(t) = \frac{\displaystyle\int_0^t U(\tau)d\tau}{I_z(t)},$$

where R_0 is the initial radius of the axial current I_z; ΔL is a change in the inductance over a time interval $\Delta t = t - t_0$ as compared to its initial value $L_0 = L(t_0)$; h is the wire length in cm; and $I_z(t)$ and $U(t)$ are the axial current and voltage measured at a radius of 55 mm, respectively. One can see that the average radius of the axial current I_z agrees well with the radius of the outer boundary of the wire plasma (Fig. 8b).

It can be seen from Fig. 8 that the time derivatives of the discharge current and the axial magnetic field are proportional to one another (Fig. 8a; curves *1*, *4*). The coincidence between the time derivatives of the magnetic field of the main current I_z and the magnetic field of the azimuthal current I_φ indicates that the current channels are inclined to the array axis at a fixed angle
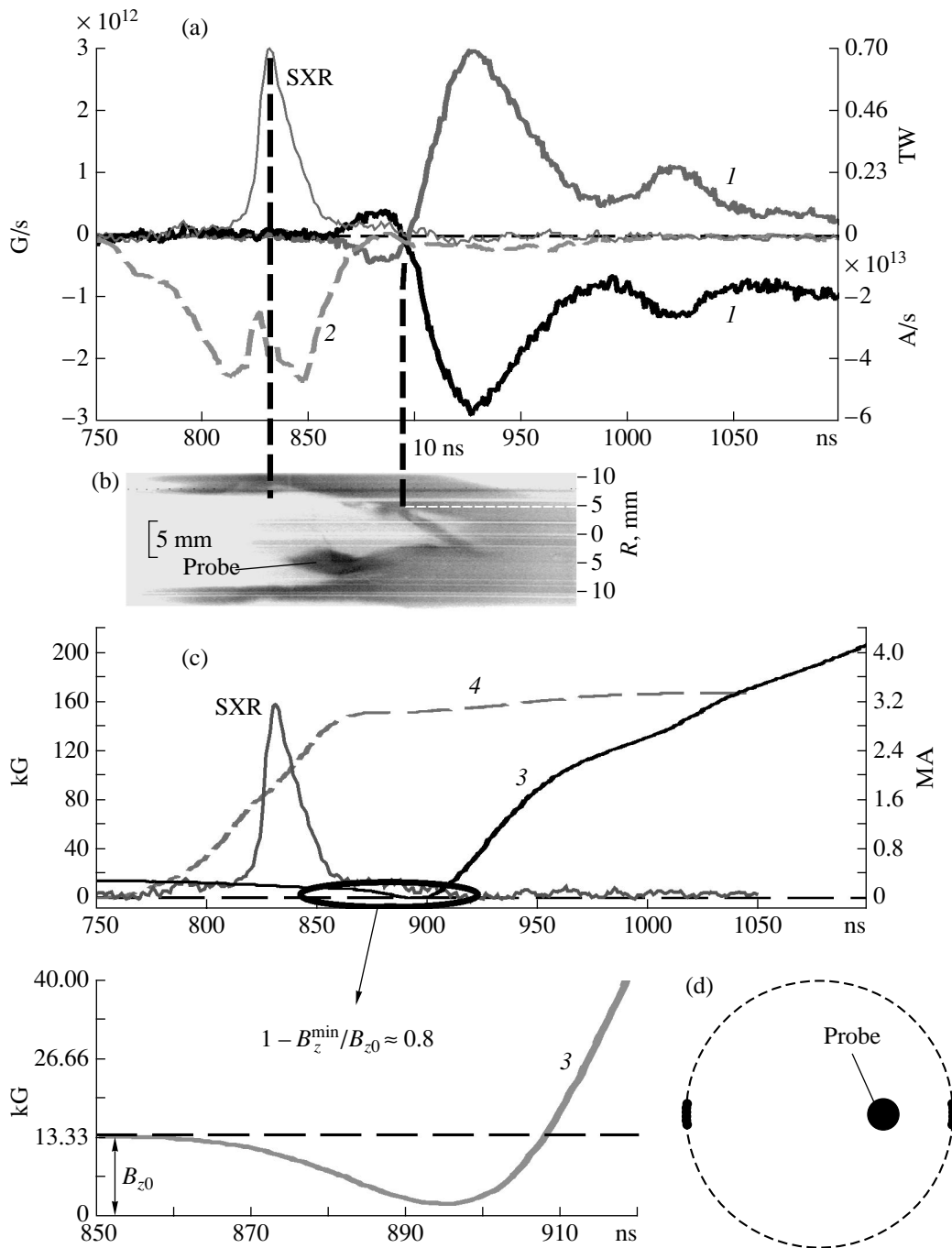
Fig. 5. Measurements of the axial magnetic field (shot no. 3792): (a) waveforms of (*1*) the bipolar signals from a B-dot probe located on mid-radius of the wire array, (*2*) the time derivative of the discharge current at a radius of 55 mm, and (SXR) the soft X-ray power; (b) an optical streak image (negative) synchronized in time with the waveforms shown in plot (a); (c) waveforms of (*3*) the axial magnetic field and (*4*) the total discharge current; and (d) the initial azimuthal structure of the wire array.

equal to the initial inclination angle of the wires. Such a coincidence is observed during the first 40 ns of the discharge (from 760 to 800 ns). This is additional evidence of the existence of the first stage of implosion. After 820 ns, the time derivative of the magnetic field of the main current deviates from that of the azimuthal current; this indicates the formation of a current-carrying plasma shell closed in the azimuthal direction.

In the time-resolved X-ray pinhole image of the wire array (Fig. 9) taken 57 ns after the beginning of the discharge, the shadows of the wire cores can be seen against the background of radiation from the forerunner
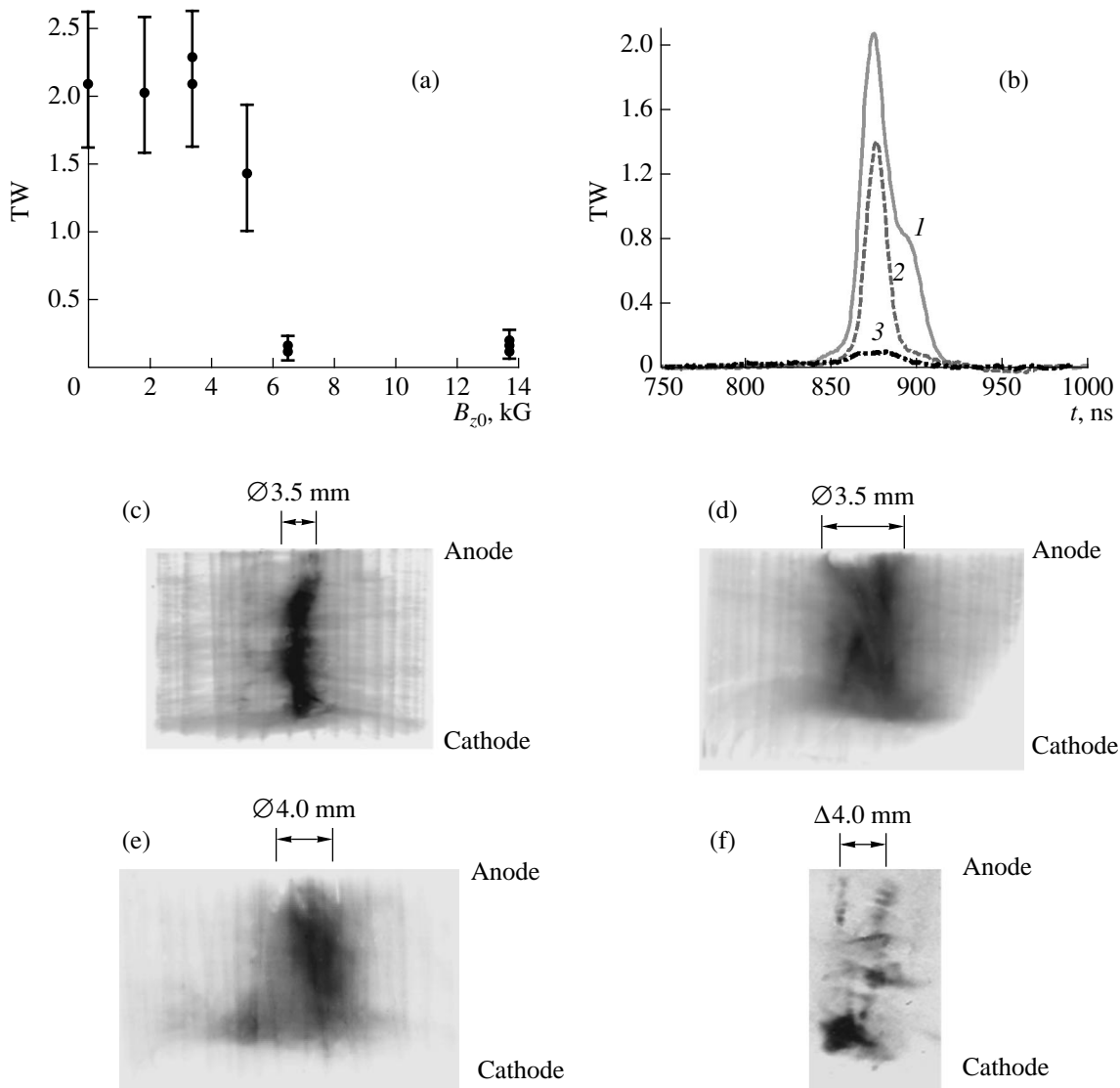
Fig. 6. Influence of the initial axial magnetic field on the emission characteristics of the wire-array plasma. The array consists of sixty 6-µm tungsten wires with a total linear mass of 330 µg/cm, the array radius is 10 mm, and the array height is 10 mm. (a) The SXR power as a function of the initial axial magnetic field B_{z0}; (b) the waveform of the SXR pulse for different values of the initial axial magnetic field: $B_{z0} = $ (*1*) 0, (*2*) ≈5, and (*3*) ≈13.5 kG (shot nos. 3730, 3741, and 3723, respectively); (c, d, e) integral X-ray ($E \geq 150$ eV) pinhole images (negatives) of the discharge at $B_{z0} = 0$, ≈6.5, and ≈13.5 kG, respectively; and (f) an integral X-ray ($E \geq 1$ keV) pinhole image (negative) of the discharge at $B_{z0} \approx 13.5$ kG.

plasma that has arrived at the array axis. One can see that the inclination angle of the plasma channels is equal to the initial inclination angle of the wires.

Curve *3* in Fig. 8a shows the axial magnetic field calculated at the location of the B-dot probe (7.5 mm over the cathode) under the assumption that the azimuthal current through the array is equal to $I_\varphi(t) = I_z(t)\sin\alpha$, where $I_z(t)$ is the total discharge current. One can see that curve *3* agrees well with the time behavior of the axial magnetic field measured by the probe (curve *2*). This indicates that the axial magnetic field is

generated by the discharge current flowing at the angle α through the wire plasma.

At later times (90 ns after the beginning of the discharge), when the current time derivative decreases, we observed a sharp increase in the time derivative of the axial magnetic field (Fig. 8a; curves *1*, *4*). This may be explained by the arrival of the bulk of the wire plasma with the frozen-in magnetic field at the probe. After the maximum of the SXR signal, which occurs near the instant of maximum plasma compression, the axial magnetic field does not drop, but rather continues to

increase (curve *2*). This may be attributed to the diffusion of the frozen-in axial magnetic field into the probe.

Thus, the compression of the axial magnetic flux by the plasma of a screwed wire array occurs in the same way as it occurs in arrays composed of vertical wires in the presence of an external axial magnetic field. The only difference is that the axial magnetic field is generated by the discharge current itself in the course of plasma formation.

8. MODEL OF THE COMPRESSION OF THE AXIAL MAGNETIC FLUX BY THE WIRE ARRAY PLASMA

Based on the results of our experiments, we propose the following model of the compression of the axial magnetic field B_z at the array axis.

In our experiments with a multiturn solenoid, a quasi-steady axial magnetic field is produced at the location of a wire array 2 ms before the beginning of the discharge. Over 2–5 ns after the beginning of the array implosion, a plasma corona that carries the bulk of the discharge current forms at the wire surfaces (Fig. 10). As a result, the array transforms into a heterogeneous core–corona system. One component is relatively cold wire cores whose density is close to the solid density. Another component is the corona plasma with a temperature of several tens of electronvolts. Under the action of the Ampère force, the plasma moves toward the array axis and entrains the frozen-in axial and azimuthal magnetic fields, whereas the wire cores remain undisplaced because their diameters are much smaller than the skin length (the core diameter is ≈ 20 μm [10], whereas the skin length for a plasma with $T_e \approx 10$ eV is ≈ 1 mm). The magnetic field (both axial and azimuthal) that was entrained toward the array axis by the plasma flow is replaced by the azimuthal magnetic field existing outside the wire array and by the axial magnetic field existing in the array volume that is not occupied by the plasma. As a result, the axial magnetic field near the wire cores decreases with time. A steady-state process is established: a fresh plasma is steadily produced and then moves together with the frozen-in magnetic field toward the array axis. This is a peculiar kind of "magnetic pump" that works while the plasma is being produced, i.e., until the wires become completely evaporated or the axial magnetic field becomes completely frozen in the plasma.

Plasma jets extended in the radial direction can partially displace the free axial magnetic flux from the region occupied by them. At a certain radius R_c, the plasma jets of individual wires merge to form a kind of shell with a thickness larger than the skin length. The shell compresses the free axial magnetic flux enveloped by it. In this case, the plasma density can be strongly modulated in the azimuthal direction. The efficiency of compression depends, in particular, on the number of plasma jets N_f (i.e., on the interwire distance at a fixed
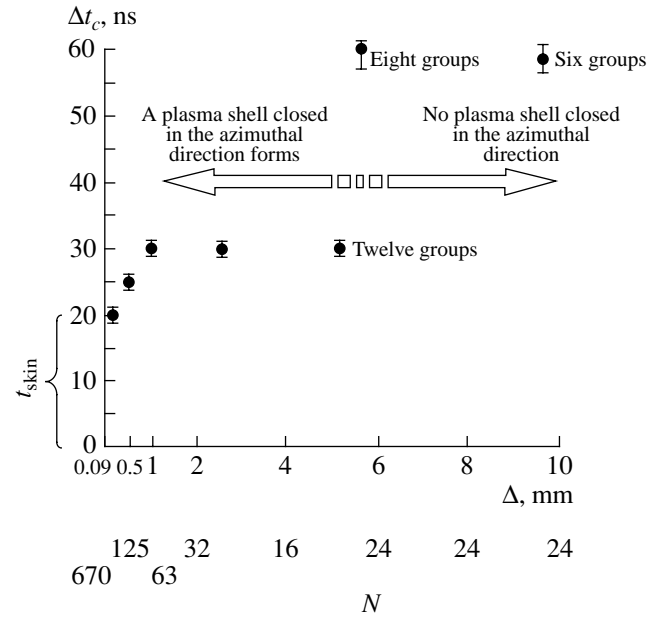
Fig. 7. Delay time Δt_c between the beginning of the discharge and the appearance of the probe signal as a function of the distance Δ between groups of wires. Here, N is the number of wires and t_{skin} is the time required for the formation of a plasma shell that is closed in the azimuthal direction, whose thickness is larger than the skin length, and that is capable of compressing the free axial magnetic flux.

array diameter) and on their azimuthal size Δl_f (Fig. 10). The greater the number of plasma jets at a fixed array radius, the sooner they merge (see Fig. 7).

The conditions for functioning of the "magnetic pump" (i.e., the process during which the axial magnetic flux is being frozen in the plasma and is then transferred together with the plasma toward the array axis) are as follows:

(i) the protracted plasma production,

(ii) the presence of spatial regions with an unmagnetized ($\omega_{ce}\tau_{ei} < 1$) and a magnetized ($\omega_{ce}\tau_{ei} > 1$) plasma, and

(iii) the radial plasma motion toward the array axis.

To find out whether the magnetic field can be frozen in the wire cores, corona, and plasma jets (see Fig. 10) in different stages of implosion, let us estimate the depth δ_{skin} (in m) to which the magnetic field can penetrate over the characteristic freezing time $t \approx (3–5) \times 10^{-9}$ s:

$$\delta_{skin} \approx 500 \sqrt{\frac{t}{\sigma_\perp}},$$

$$\sigma_\perp \approx 4.8 \times 10^3 T_e^{3/2}/z \ln \Lambda,$$

where $\sigma_\perp$ is the transverse Spitzer plasma conductivity (in Ω^{-1} m^{-1}), T_e is the plasma electron temperature
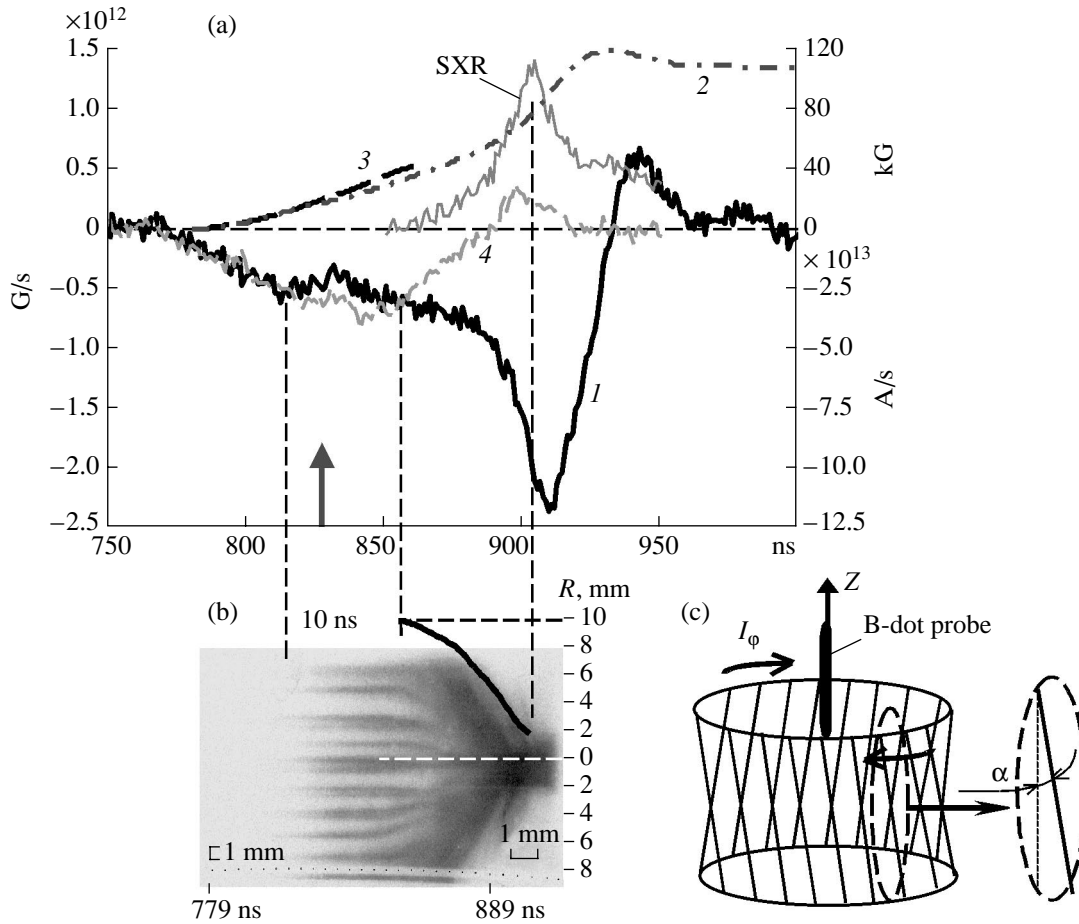
Fig. 8. Measurements of the axial magnetic field in a screwed wire array (shot no. 3632): (a) waveforms of (*1*) the signal from one of the two coils of a B-dot probe located on the array axis, (*2*) the measured axial magnetic field, (*3*) the axial magnetic field calculated under the assumption that the azimuthal current flowing through the array is equal to $I_\varphi = I_z \sin\alpha$, (*4*) the measured time derivative of the current at a radius of 55 mm, and (SXR) the soft X-ray power (0.6 TW at maximum); (b) an optical radial streak image (negative) of the discharge and the time behavior of the average current radius synchronized in time with the waveforms shown in plot (a), and (c) the initial azimuthal structure of the wire array. The arrow in plot (a) shows the instant corresponding to the X-ray image in Fig. 9.

(in eV), z is the ion charge number, and $\ln\Lambda$ is the Coulomb logarithm.

Let us also estimate the Hall parameter (the magnetization parameter) $\omega_{ce}\tau_{ei}$ for the same regions:

$$\omega_{ce}\tau_{ei} \approx 8.8 \times 10^{12} \frac{BT_e^{3/2}}{z n_e \ln\Lambda},$$

where ω_{ce} is the electron gyrofrequency, τ_{ei} is the electron–electron collision time in the plasma region of interest, and B is the magnetic field in this region (in G). The results of these estimates are listed in the table.

It can be seen that, over 3–5 ns, the magnetic field becomes frozen in the wire core plasma, which is unmagnetized ($\omega_{ce}\tau_{ei} \ll 1$). There exists a certain "transient" region between the corona plasma and the jet plasma into which the magnetic field can penetrate, be frozen-in, and be transferred by the plasma toward the array axis. In the final stage of implosion, a Z-pinch

forms on the array axis. The Z-pinch plasma is rather hot; according to spectral X-ray measurements, the electron temperature in this plasma is $T_e \approx 100$ eV. Such a high temperature is maintained over ~20–30 ns and then drops rapidly because of radiative cooling. The time during which the magnetic field diffuses from this plasma into the probe is ≈50–80 ns. This is why the probe signal is longer than the SXR pulse (see, e.g., Fig. 3).

Based on the above mechanism for compressing the axial magnetic flux ("magnetic pump"), we estimated the fraction of the initial axial magnetic field that is frozen in the plasma jets and is transferred toward the axial region.

The axial magnetic flux frozen in the plasma jets is approximately equal to
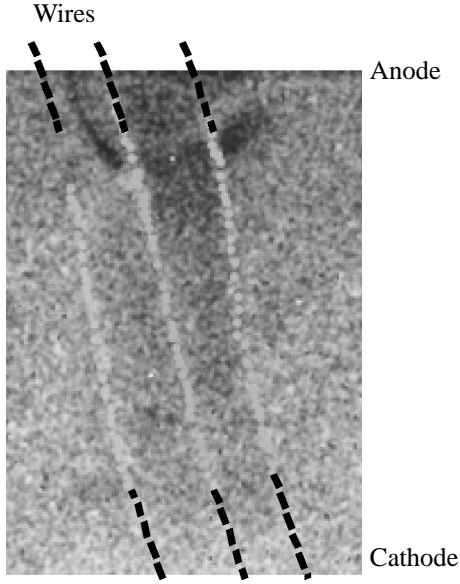
$$d\Phi_{z1}(t) = B_{z2}(t)N_f \Delta l_f V_a dt,$$

Fig. 9. Fragment of an X-ray ($E > 200$ eV) image (negative) of the wire array at 57 ns after the beginning of the discharge (22.5 kA/wire). The exposure time is ≈ 3 ns.

where $B_{z2}(t)$ is the axial magnetic field outside the plasma, V_a is the plasma velocity in the region near wires where the axial magnetic field becomes frozen in the plasma, N_f is the number of plasma jets (the number of wires), and Δl_f is the plasma jet width (Fig. 10). For the sake of simplicity, we assume that V_a, Δl_f, and N_f are space- and time-independent.

The area occupied by the plasma jets is defined as

$$S_1(t) = N_f \Delta l_f (R_0 - r(t)),$$

where R_0 is the initial radius of the array and $r(t)$ is the running radius to which the plasma jets penetrate into the array (this radius was calculated using the results of measurements of the velocity with which the current-carrying plasma penetrates into the array [13]). The area occupied by the free magnetic flux is defined as

$$S_2(t) = \pi R_0^2 - S_1(t).$$

We assume that the axial magnetic flux initially produced inside the array, $\Phi_{z0} = B_{z0} \pi R_0^2$, is conserved and is equal to the sum of the flux frozen in the plasma jets, $\Phi_{z1}(t) = B_{z1}(t) S_1(t)$, and the free magnetic flux $\Phi_{z2}(t) = B_{z2}(t) S_2(t)$.

From the above equations, we can find the ratio of the magnetic flux frozen in the plasma jets Φ_{z1} to the initial flux Φ_{z0}:

$$\frac{\Phi_{z1}(t)}{\Phi_{z0}} = 1 - \exp\left[-\int_0^t \frac{N_f \Delta l_f V_a}{(\pi R_0^2 - N_f \Delta l_f R_0) + N_f \Delta l_f r(t)} dt\right].$$

It is of interest to find the instant at which the plasma jets arrive at the axis ($r(t) = 0$). The above equation can be reduced to the simpler form

$$\Phi_{z1}(t)/\Phi_{z0} = 1 - e^{-t/\tau},$$

where $\tau = (\pi R_0^2 N_f \Delta l_f R_0)/N_f \Delta l_f V_a$.

For typical parameters of our experiments ($R_0 = 1$ cm, $N_f = 40$–60, $\Delta l_f \approx 0.03$ cm, and $V_a \approx 1 \times 10^7$ cm/s), we find that the ratio of the flux frozen in the plasma jets to Φ_{z0} is equal to
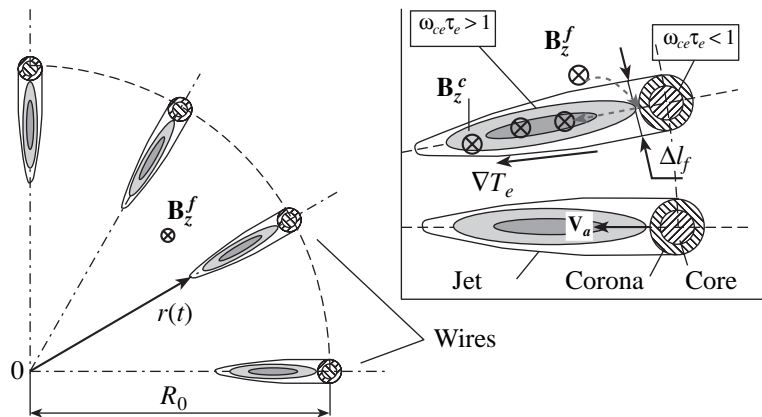
$$\Phi_{z1}(t)/\Phi_{z0} \approx 0.6\text{–}0.8.$$

Fig. 10. Model of the compression of the axial magnetic flux: B_z^f and B_z^c are the free and frozen-in axial magnetic fields, respectively; R_0 is the initial radius of the wire array; $r(t)$ is the radius of the front of a plasma jet penetrating into the array; ∇T_e is the electron temperature gradient; Δl_f is the azimuthal size of a plasma jet produced from an individual wire; and $\omega_{ce}\tau_e > 1$ and $\omega_{ce}\tau_e < 1$ are plasma regions in which the axial magnetic field is frozen and is not frozen in the plasma, respectively.

Typical plasma parameters in different stages of the wire array implosion

Region	n_e, cm^{-3}	n_i, cm^{-3}	z	T_e, eV	B, kG	$\omega_{ce}\tau_{ei}$	δ_{skin}
Wire core (at 75 ns) [11]	10^{21}	10^{21}	~1	0.2–0.5	$B_\varphi = 300$–1000 $B_z = 3$–10	$<10^{-4}$	≈2–3 mm
Plasma corona (at 75 ns) [8]	≈10^{19}	≈2×10^{18}	≈5	20–25	$B_\varphi = 300$–1000 $B_z = 3$–10	~0.5–2 ~10^{-3}–10^{-2}	≈300–350 μm
Plasma jet (at 40–80 ns) [8]	$(2-5) \times 10^{16}$	$(4$–$10) \times 10^{15}$	≈5	20–25	$B_\varphi = 120$ ($r = 0.5$ cm) $B_z = 10$–50	~10^2 ~2–50	≈350–400
3-mm-diameter Z-pinch (at 100 ns) [12]	$(8$–$20) \times 10^{19}$	$(8$–$10) \times 10^{18}$	10–20	≈100	$B_\varphi = 1000$–2000 $B_z = 300$–1000	–	–

This value agrees well with the above experimental results (see Fig. 5).

9. CONCLUSIONS

The results from measurements of the axial magnetic field can be summarized as follows:

(i) Both the axial and azimuthal magnetic fields are frozen in the plasma produced during the implosion of a wire array.

(ii) During the first 30–40 ns, the discharge current flows through individual plasma channels.

(iii) A kind of plasma shell closed in the azimuthal direction and capable of compressing the axial magnetic flux forms in arrays with a small interwire spacing.

(iv) The axial magnetic flux can be compressed even in the absence of a uniform current-carrying shell. In this case, the magnetic field becomes frozen in the plasma near the wires and is transferred and compressed in the plasma jets flowing toward the array axis (the so-called "magnetic pump").

(v) The SXR power decreases from 2.5 to <0.1 TW as the initial axial magnetic field increases from 0 to 15 kG.

(vi) The diameter of the central plasma region emitting in the SXR spectral range increases with increasing initial axial magnetic field.

ACKNOWLEDGMENTS

REFERENCES

1. Ya. P. Terletskiĭ, Zh. Éksp. Teor. Fiz. **32**, 387 (1957) [Sov. Phys. JETP **5**, 301 (1957)].

2. G. D. Bogomolov, A. L. Velikovich, and M. A. Liberman, Pis'ma Zh. Tekh. Fiz. **9**, 748 (1983) [Sov. Tech. Phys. Lett. **9**, 322 (1983)].

3. A. L. Velikovich, M. A. Liberman, R. B. Spielman, *et al.*, in *Proceedings of the 2nd International Conference on Dense Z-Pinches, Laguna Beach, CA, 1989*, p. 431.

4. A. B. Luchinskiĭ, N. A. Ratakhin, S. A. Sorokin, *et al.*, Pis'ma Zh. Tekh. Fiz. **15** (18), 83 (1989) [Sov. Tech. Phys. Lett. **15**, 739 (1989)].

5. S. V. Lebedev, R. Aliaga-Rossel, S. N. Bland, *et al.*, Phys. Plasmas **6**, 2016 (1999).

6. T. A. Golub, N. B. Volkov, R. B. Spielman, *et al.*, Appl. Phys. Lett. **74**, 3624 (1999).

7. E. V. Grabovskiĭ, G. G. Zukakishvili, K. N. Mitrofanov, *et al.*, Preprint No. 0091-A (Troitsk Inst. for Innovation and Fusion Research, Troitsk, 2002).

8. G. M. Oleĭnik, I. Yu. Porofeev, E. Bolkhovitinov, and A. A. Rupasov, *XXVII Zvenigorod Conference on Plasma Physics and Controlled Fusion, Zvenigorod, 2000*, Abstracts of Papers, p. 144.

9. G. S. Volkov, E. V. Grabovskiĭ, K. N. Mitrofanov, and G. M. Oleĭnik, Fiz. Plazmy **30**, 115 (2004) [Plasma Phys. Rep. **30**, 99 (2004)].

10. V. V. Alexandrov, E. V. Grabovsky, K. N. Mitrofanov, *et al.*, in *Proceedings of the European Conference on Advanced Diagnostics for Magnetic and Inertial Fusion, Varenna, 2001*, Ed. by P. E. Scott *et al.* (Kluwer, New York, 2001), p. 257.

11. V. V. Alexandrov, M. V. Fedulov, I. N. Frolov, *et al.*, in *Proceedings of the 5th International Conference on Dense Z-Pinches, Albuquerque, NM, 2002*, Ed. by J. Davis, C. Deeney, and N. R. Pereira; AIP Conf. Proc. **651**, 91 (2002).

12. I. K. Aĭvazov, M. B. Bekhtev, V. V. Bulan, *et al.*, Fiz. Plazmy **16**, 645 (1990) [Sov. J. Plasma Phys. **16**, 373 (1990)].

13. I. Frolov, E. Grabovsky, K. Mitrofanov, *et al.*, in *Proceedings of the European Conference on Advanced Diagnostics for Magnetic and Inertial Fusion, Varenna, 2001*, Ed. by P. E. Scott *et al.* (Kluwer, New York, 2001), p. 419.

Translated by N.F. Larionova

Modeling of the Tearing Instability in Unreduced Two-Fluid Magnetohydrodynamics

V. P. Zhukov

Institute of Computational Technologies, Siberian Division, Russian Academy of Sciences,
pr. Akademika Lavrent'eva 6, Novosibirsk, 630090 Russia
Received February 25, 2004

Abstract—The problem of the tearing instability is solved numerically in cylindrical geometry by using the unreduced two-fluid MHD model. It is shown that the duration of the nonlinear stage of the tearing instability in a hot plasma is rather sensitive to such factors as the initial radial density and temperature profiles, the initial ion-to-electron pressure ratio, and the longitudinal thermal conductivity. Depending on these factors, the two-fluid effects (primarily, the Hall effect) can either greatly hasten the magnetic reconnection process (in comparison to that in the one-fluid MHD model) or greatly slow it. An illustrative explanation of the results obtained is given. © 2005 Pleiades Publishing, Inc.

1. INTRODUCTION

Observations of solar flares and experimental data on sawtooth oscillations in tokamaks show that the magnetic reconnection time in a highly conducting (hot) plasma is several orders of magnitude less than that predicted by the one-fluid MHD model [1–4]. In order to explain this discrepancy, the models are invoked that are capable of describing the electron dynamics more adequately. That the electron dynamics should be taken into account follows from the picture of reconnection predicted by the one-fluid MHD model, according to which the reconnection process at a low plasma conductivity is accompanied by the onset of thin current sheets [5]. The one-fluid MHD model is inapplicable to current sheets whose thickness is smaller than the ion dispersion length $\delta_i = c/\omega_{pi}$ (where ω_{pi} is the ion plasma frequency). In this case, it is necessary to take into account two-fluid effects.

The mechanisms thought to be responsible for hastening the annihilation of magnetic fluxes are, e.g., the effects of electron viscosity [6] and electron inertia [7–9]. Both these effects hasten magnetic reconnection because, in a hot plasma, they disrupt the freezing-in of the magnetic field lines in the plasma to a larger extent than does the plasma resistivity. Note that, in this case, the electron inertia (in contrast to electron viscosity) is a nondissipative effect.

The reconnection process is also hastened by the Hall effect, which shows up as the freezing-in of magnetic field into the plasma electrons. The Hall effect is most pronounced in the electron MHD (EMHD) approximation, in which the ion are treated as immobile [10]. The EMHD model is applicable to the study of reconnection processes when the characteristic length of the system, L, does not exceed the ion dispersion length δ_i [11]. The most interesting result is that, in

the EMHD approximation, the reconnection time is independent of the transport coefficients and is equal in order of magnitude to [11, 12]

$$\omega_i^{-1} L^2/\delta_i^2, \qquad (1.1)$$

where ω_i is the ion gyrofrequency. It should be stressed that the Hall effect itself does not disrupt the freezing-in of the magnetic field.

Note that, when the electron viscosity and/or electron inertia is ignored, the solution to the reconnection problem even for a plasma with a finite conductivity is singular [12]: the current density approaches infinity in a finite time. It should be emphasized that, within this time, only an insignificant portion of the magnetic flux is subject to reconnection.

The above properties of the reconnection process in the EMHD theory stem from the types of nonlinearities in the EMHD equations [12].

The expression for the reconnection time in the EMHD model that was used in [11, 12], namely, expression (1.1), is not as illustrative as desired because it contains the ion-related parameters ω_i and δ_i. In the EMHD approximation, however, the ion motion is ignored; hence, on the whole, expression (1.1) carries no information about the ions (in particular, it does not contain the mass of an ion). This expression can be rewritten in the form

$$L/v_c \sim 4\pi e n L^2/(Hc), \qquad (1.2)$$

where e is the charge of an electron, n is the electron density, and $v_c = c|(\nabla \times \mathbf{H})|/(4\pi en) \sim cH/(4\pi enL)$ is the characteristic electron current velocity in the original magnetic configuration with a characteristic magnetic field strength H. Formula (1.2) implies that, in the EMHD model, the reconnection rate is determined by

the characteristic electron current velocity in the original magnetic configuration.

The reconnection mechanism in the EMHD theory can be elucidated as follows. On the one hand, the EMHD equations describe the transport of the magnetic field by the current associated with this field (the freezing-in of the magnetic field in the current field). On the other hand, the EMHD equations describe the rotation of the magnetic field perturbation vector (and, therefore, the current density perturbation vector) about the initial magnetic field, whose direction governs the direction of this rotation. Accordingly, on both sides of the surface separating regions of oppositely directed magnetic fields, the current density perturbation vector rotates in opposite directions. If the magnetic field perturbation gives rise to a current transporting the magnetic fluxes toward one another, then these magnetic fluxes will annihilate. Moreover, the magnetic field perturbation will then grow. It can be said that, in the EMHD model, the magnetic fluxes rotate about themselves and transport themselves toward one another.

The EMHD model is inapplicable to tokamak plasmas and solar flares because, in them, $L \gg \delta_i$. In this case, it is necessary to take into account the dynamics of both the ions and the electrons. For tearing instabilities in tokamaks, such investigations were carried out in [4, 14–17] on the basis of reduced (four-field [13]) two-fluid MHD models under the assumption that the initial plasma density distribution is uniform and the temperature does not vary in space and in time. In [4, 14–17], it was shown that two-fluid effects can substantially hasten the reconnection processes in the nonlinear stage of instability. In those papers, however, the case of spatially nonuniform initial distributions of the temperature and density was not considered at all. In our study, we show that, in a plasma with nonzero initial temperature and density gradients, the dynamics of the reconnection process is essentially different.

The reduced two-fluid MHD models have the same drawbacks as the one-fluid MHD models [18, 19]. One more drawback is that two-fluid MHD equations contain derivatives of higher order than those in one-fluid MHD equations. Since the gradients in reconnection problems are large, the terms with such higher-order derivatives are difficult to take into account accurately when reducing the general two-fluid MHD equations. In other words, the problem in fact involves a new parameter—the current sheet thickness.

In the present paper, the development of tearing instability is investigated numerically in a two-dimensional (helical) geometry corresponding to that of a straight cylinder with identified ends. For the above reasons, we investigate this problem in terms of an unreduced two-fluid MHD model. We consider two different relationships between the initial electron and ion temperatures: $T_e = 0$ and $T_e = T_i$. In studying the case $T_e = 0$, which is unlikely to be of interest for applications, we will merely try to determine the role of the

electron pressure gradients in the generalized Ohm's law. We also investigate how the initial gradients of the plasma temperature and density, the electron viscosity coefficients, and the longitudinal ion thermal conductivity affect the development of the tearing instability. We give a simple and illustrative explanation of the numerical results and discuss how well they correlate with the experimental data.

2. FORMULATION OF THE PROBLEM

We describe the plasma by two-fluid MHD equations, assuming that the generalized Ohm's law has the form

$$\mathbf{E} + \frac{1}{c}\mathbf{V} \times \mathbf{H}$$
$$= \frac{M}{e\rho c}\mathbf{j} \times \mathbf{H} - \frac{M}{e\rho}\nabla p_e + \sigma^{-1}\mathbf{j} - \nabla \times (\nu_e \nabla \times \mathbf{j}), \quad (2.1)$$

where M is the mass of an ion, ρ is the plasma density, σ is the plasma electrical conductivity, and ν_e is the electron viscosity. The generalized Ohm's law (2.1) is the equation of motion of a gas of inertialess electrons. It implies that the magnetic field is frozen not in the ion velocity field $\mathbf{V}$ but rather in the electron velocity field $\mathbf{V}_e = \mathbf{V} - M(e\rho)^{-1}\mathbf{j}$. The first term on the right-hand side of the generalized Ohm's law (2.1) describes the Hall effect, and the second term accounts for the effect of the electron pressure p_e.

For simplicity, the last term with the electron viscosity in Eq. (2.1) is taken in a model form. The exact expression for this term is rather complicated [20]. The only important point for our analysis is that, as the spatial scale of the magnetic field perturbation decreases, the electron viscosity leads to a stronger dissipation than does the plasma resistivity. As a result, we can eliminate the singularity that arises in the solution to the two-fluid MHD equations [12]. This singularity cannot be avoided by taking into account a low but finite plasma resistivity; it can be removed, however, by accounting for a low but nonzero electron viscosity [12].

Let us switch to dimensionless variables. As a length scale, we choose the characteristic transverse plasma dimension a (the tokamak minor radius), and, as the remaining normalizing factors, we adopt the characteristic toroidal magnetic field H_z, the density ρ_*, the Alfvén speed $V_A = H_z/\sqrt{4\pi\rho_*}$ in terms of the toroidal magnetic field, the time a/V_A, and the pressure $-H_z^2/4\pi$.

We consider a helically symmetric MHD flow. In this case, the scalars and the components of the vectors in cylindrical coordinates r, φ, and z (rather than the x and y Cartesian components) depend on the coordinates in such a way that

$$\partial/\partial z = -R^{-1}\partial/\partial\varphi \quad (2.2)$$

and all the functions depend on the combination $\varphi - z/R$ rather than on the coordinates φ and z separately. In what follows, by φ we will mean the quantity $\varphi - z/R$. In this way, it is convenient to work with the g and s vector components, which are related to the φ and z components by the formulas

$$f_s = f_\varphi - (r/R)f_z, \quad f_g = f_z + (r/R)f_\varphi. \quad (2.3)$$

It is also convenient to introduce the following vector components (referred to as Cartesian components for brevity), which are related to the r and φ components by the relationships

$$f_x = f_r \cos\varphi - f_\varphi \sin\varphi,$$
$$f_y = f_r \sin\varphi + f_\varphi \cos\varphi.$$

Strictly speaking, these are the actual Cartesian components of the vectors only in the limit $R \longrightarrow \infty$, since the role of the coordinate φ is played by the difference $\varphi - z/R$.

In view of the above, the two-fluid MHD equations take the form

$$\rho\left(\frac{\partial V_x}{\partial t} + (\mathbf{V} \cdot \nabla)V_x - \frac{V_z V_y}{R}\right)$$
$$= \nu\left(\Delta V_x - \left(V_x - 2\frac{\partial V_y}{\partial \varphi}\right)R^{-2}\right) + F_x, \quad (2.4)$$

$$\rho\left(\frac{\partial V_y}{\partial t} + (\mathbf{V} \cdot \nabla)V_y + \frac{V_z V_x}{R}\right)$$
$$= \nu\left(\Delta V_y - \left(V_y + 2\frac{\partial V_x}{\partial \varphi}\right)R^{-2}\right) + F_y, \quad (2.5)$$

$$\rho\left(\frac{\partial V_z}{\partial t} + (\mathbf{V} \cdot \nabla)V_z\right) = \nu\Delta V_z + F_z, \quad (2.6)$$

$$(F_r, F_s) = -\nabla\left(p - \frac{\nu}{3}\nabla \cdot \mathbf{V}\right)$$
$$+ G^{-1}(-\nabla(H_g^2/2) + j_g\nabla\psi), \quad (2.7)$$
$$F_g = (\mathbf{H} \cdot \nabla)H_g,$$

$$p = p_i + p_e,$$
$$j_g = -\Delta_g(\psi) + \frac{2H_g}{RG}, \quad (2.8)$$

$$\frac{\partial \psi}{\partial t} + \left(\mathbf{V} + \frac{\alpha}{\rho}(\mathbf{e} \times \nabla H_g)\right)\nabla\psi$$
$$= -\eta j_g + G\nabla \cdot (G^{-1}\nu_e\nabla j_g) + \frac{2\nu_e}{RG}\left(\Delta_g(H_g) - \frac{2j_g}{RG}\right), \quad (2.9)$$

$$\frac{\partial H_g}{\partial t} = G\nabla \cdot (G^{-1}\mathbf{S}) + \frac{2}{RG}\frac{\partial \psi}{\partial t},$$

$$\mathbf{S} = -\nabla H_g - \alpha\rho^{-1}H_g(\mathbf{e} \times \nabla H_g)$$
$$- (V_g - \alpha\rho^{-1}j_g)(\mathbf{e} \times \nabla\psi)$$
$$- G\alpha\rho^{-1}(\mathbf{e} \times \nabla p_e) + \eta\nabla H_g \quad (2.10)$$
$$- \nabla\left(\nu_e\left(\Delta_g H_g - \frac{2j_g}{RG}\right)\right),$$

$$\frac{\partial\rho}{\partial t} + \nabla \cdot (\mathbf{V}\rho) = 0, \quad (2.11)$$

$$\frac{1}{\gamma_i - 1}\left(\frac{\partial p_i}{\partial t} + \nabla \cdot (\mathbf{V}p_i)\right) = -p_i\nabla \cdot \mathbf{V}$$
$$+ \nabla \cdot (\chi_{\|i}\mathbf{h} \cdot (\mathbf{h} \cdot \nabla)T_i) + \nabla \cdot (\chi_i\nabla T_i) + Q_\nu, \quad (2.12)$$

$$\frac{1}{\gamma_e - 1}\left(\frac{\partial p_e}{\partial t} + \nabla \cdot (\mathbf{V}_e p_e)\right) = -p_e\nabla \cdot \mathbf{V}_e$$
$$+ \nabla \cdot (\chi_{\|e}\mathbf{h} \cdot (\mathbf{h} \cdot \nabla)T_e) + \nabla \cdot (\chi_e\nabla T_e) \quad (2.13)$$
$$+ \eta\mathbf{j}^2 + \nu_e(\nabla \times \mathbf{j})^2,$$

$$\mathbf{V}_e = \mathbf{V} + \frac{\alpha}{\rho}(\mathbf{e} \times \nabla H_g),$$
$$\mathbf{H} = (H_r, H_s) = -(\mathbf{e} \times \nabla\psi),$$
$$\mathbf{h} = \mathbf{H}/(H_r^2 + G^{-1}(H_s^2 + H_g^2))^{1/2}, \quad (2.14)$$
$$T_{i,e} = p_{i,e}/\rho, \quad G = 1 + r^2/R^2.$$

The explicit expressions for the differential operators in Eqs. (2.4)–(2.14) are presented in Appendix 1. The rest of the notation is as follows: ψ is the poloidal magnetic field flux (the g component of the vector potential), H_g is the g component of the magnetic field, ρ is the plasma density, $\mathbf{V}$ is the ion velocity, $\mathbf{V}_e$ is the electron velocity, ν and ν_e are the ion and electron dimensionless viscosity coefficients, η is the plasma conductivity, the term Q_ν describes plasma heating due to the work done by viscous forces, $p_{i,e}$ and $T_{i,e}$ are the ion and electron plasma temperatures and pressures, $\chi_{\|i,e}$ and $\chi_{i,e}$ are the longitudinal and isotropic dimensionless thermal conductivities (the subscripts i and e stand, respectively, for the ions and electrons), $\gamma_e = \gamma_i = \gamma = 5/3$ are the electron and ion adiabatic indices, and the coefficient $\alpha = \delta_i/a$ characterizes the role of the two-fluid effects (in particular, the Hall effect).

Equations (2.4)–(2.6) for the velocity are written in terms of the Cartesian components, in which they have a simple form. In addition, the use of the Cartesian velocity components is of primary importance for constructing a finite difference algorithm with which the problem under consideration was solved. A detailed description of this algorithm is given in [24].

The initial conditions are chosen to correspond to an equilibrium state of an axisymmetric configuration with a neutral surface and with a small magnetic flux
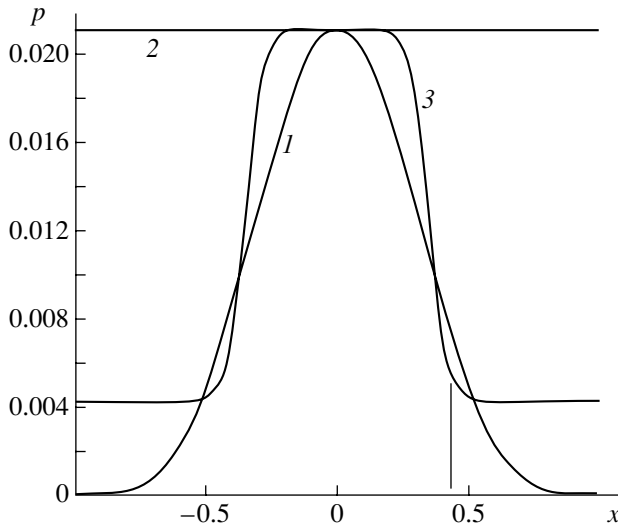
Fig. 1. Types of initial pressure profiles used in the calculations. Curves *1*, *2*, *3* correspond to profiles (i), (ii), and (iii) in Section 2, respectively. The vertical line shows the position of the neutral surface.

perturbation of amplitude ψ_p that breaks the equilibrium:

$$\mathbf{V} = 0, \quad \rho = 1, \quad \psi = \psi_0 + \psi_p r(1 - r^2)\cos\varphi,$$

$$\frac{\partial\psi_0}{\partial r} = -\left(\frac{1 - (1 - r^2)^{q+1}}{qr^2} - 1\right)\frac{r}{R}. \quad (2.15)$$

Hence, in the limit $\psi_p \longrightarrow 0$, we deal with a neutral sheet configuration. Near the coordinate axis, we have $H_s = -d\psi/dr > 0$, and, for large radii, we have $H_s < 0$. The position of the neutral surface, $H_s = 0$, depends on the quantity q. In what follows, we will discuss the results of numerically solving the problem in question that were obtained for $R = 4$ and $q = 3$, which corresponds to a neutral surface with the radius $r_n = 0.5$. The perturbation amplitude ψ_p was equal to 10^{-4}.

The distributions of the plasma pressure p and magnetic field component H_g were chosen so that, for $\psi_p = 0$, the total force acting on the plasma vanishes. We investigated the following three types of distributions of p, H_g, and ρ (see Fig. 1):

(i) A constant density $\rho = 1$ and a constant magnetic field component $H_z = 1$, which corresponds to $H_g = 1 + (1 - (1 - r^2)^{q+1})/(qR^2)$. The pressure p was determined from the equilibrium condition; in this case, $p(r = 1) = \beta$. For calculations, we chose the value $\beta = 10^{-4}$, for which the central plasma pressure was equal to $p_0 = 0.0212$.

(ii) A constant pressure $p = p_0$ and a constant density $\rho = 1$. The distribution of H_g was determined from the

equilibrium condition. It was assumed that $H_g(r = 1) = 1 + 1/(qR^2)$, which ensures the equality $j_g(r = 1) = 0$.

(iii) The distributions of p and ρ of the form

$$p = p_1 + \frac{p_0 - p_1}{2}\left(1 - \tanh\frac{r - r_0}{d}\right),$$

$$\rho = \rho_1 + \frac{1 - \rho_1}{2}\left(1 - \tanh\frac{r - r_0}{d}\right),$$

which are flat in the central regions and are sharply decreasing in the vicinity of the surface of radius r_0. At the origin of the coordinates, we have $p = p_0$ and $\rho = 1$, and, at the boundary $r = 1$, we have $p = p_1$ and $\rho = \rho_1$. For calculations, we used the values $p_1 = p_0/5$, $\rho_1 \in (0.2 : 0.5)$, $r_0 = 0.35 < r_n$, and $d = 0.07$. In versions (ii) and (iii) of the initial conditions, the p_0 value was equal to 0.0212. The distribution of H_g was determined in the same way as in version (i).

The initial distributions of p_e and p_i were chosen to be $p_e = p_i = p/2$ or $p_e = 0$ and $p_i = p$.

The problem was solved in the region ($0 \le r \le 1$, $0 \le \varphi \le 2\pi$). At the boundary $r = 1$, we set

$$\mathbf{V} = 0, \quad p_{e,i}/\rho = \text{const}, \quad (2.16)$$

the tangential components of the electric field being $E_z = E_b$ and $E_\varphi = 0$. Accordingly, we have

$$E_g = E_b, \quad E_s = -E_b/R. \quad (2.17)$$

For $\nu_e = 0$, boundary conditions (2.17) are sufficient to solve Eqs. (2.9) and (2.10). For $\nu_e \neq 0$, the order of the equations for the magnetic field is higher, so boundary conditions (2.17) for the electric field should be supplemented with the boundary conditions for the magnetic field. This is a separate physical problem. In the case at hand, however, the plasma is essentially unperturbed at $r = 1$. This is why we can impose a simple boundary condition, specifically, we require that the tangential currents at the boundary be equal to those following from Eqs. (2.9) and (2.10) with conditions (2.17) in the one-fluid MHD approximation ($\alpha = 0$) in which the electron viscosity is ignored ($\nu_e = 0$):

$$j_g = E_b/\eta, \quad \partial H_g/\partial r = E_b/(\eta R).$$

For our simulations, we set $E_b = 0$.

In order to describe the flow, it is convenient to introduce the parameter R_p as the ratio of the magnetic flux within the island (see Fig. 2) (i.e., the portion of the magnetic flux that has undergone reconnection) to the total magnetic flux within the neutral surface:

$$R_p = \frac{\psi_{\text{saddle}} - \psi_{\text{min}}}{\psi_{\text{max}} - \psi_{\text{min}}}.$$

Here, ψ_{max} is the value of the magnetic flux ψ at its greatest local maximum, ψ_{min} is the magnetic flux at its absolute minimum, and ψ_{saddle} is the value of ψ at the

saddle point with the maximum value of ψ. We are considering the greatest local maximum because, in the nonlinear stage of the processes, magnetic islands can generally form that are not associated with the initial perturbation. Accordingly, there may be more than one local maximum and more than one saddle point. At the initial time, when the island is small, the parameter R_p is close to zero; at the end of the reconnection process, it is close to unity, $R_p \longrightarrow 1$.

The duration t_n of the nonlinear stage of reconnection is defined as the time during which the parameter R_p increases from 1/2 to 1.

3. RESULTS OF NUMERICAL CALCULATIONS

We begin by noting that, in the parameter range under consideration, namely, $\eta < 10^{-8}$ and $\nu_e \sim 10^{-9}$, the plasma conductivity η has a minor effect on the flow in both cases $\alpha = 0$ and $\alpha \neq 0$. For this reason, the particular value of η will not be specified below. The values of the coefficients χ_i and χ_e that are important from a practical standpoint are also very small. The results presented were calculated for $\chi_i = \chi_e = 0$. Unless stated otherwise, the longitudinal electron thermal conductivity $\chi_{\|e}$ is equal to 100. Note also that, in the given numerical examples, the distributions of T and ρ correspond to distributions (ii) and (iii).

3.1. One-Fluid MHD Model ($\alpha = 0$)

For $\alpha = 0$, reconnection proceeds in the usual way (Fig. 3) to produce a characteristic pattern of magnetic field lines with an island (the region corresponding to the portion of the magnetic flux that has undergone reconnection) and with a current sheet stretched along the neutral surface. The distributions of p, ρ, and H_g are symmetric about the x axis. Note that the plasma density is elevated inside the island and is depressed inside the current sheet. This indicates that the plasma outflow from the current sheet is more intense than the plasma inflow into it.

For $\alpha = 0$, the duration t_n of the nonlinear stage of reconnection is determined by the value of the electron viscosity ν_e; more precisely, we have $t_n \sim \nu_e^{-\xi}$, where $\xi \approx 0.23$. The dependence of t_n on the type of the initial distributions of T and ρ is far weaker. Thus, for $\nu_e = 10^{-9}$, t_n varies between 130 and 150 Alfvén times, depending on the type of initial conditions. The dependence of t_n on the electron and ion thermal conductivities is insignificant.

Note that, at the very beginning of the reconnection process, the toroidal velocity component V_z is much lower than its poloidal component. However, as time elapses, the toroidal velocity component becomes on the order of the poloidal component. Consequently, the applicability of the reduced MHD (RMHD) model to a
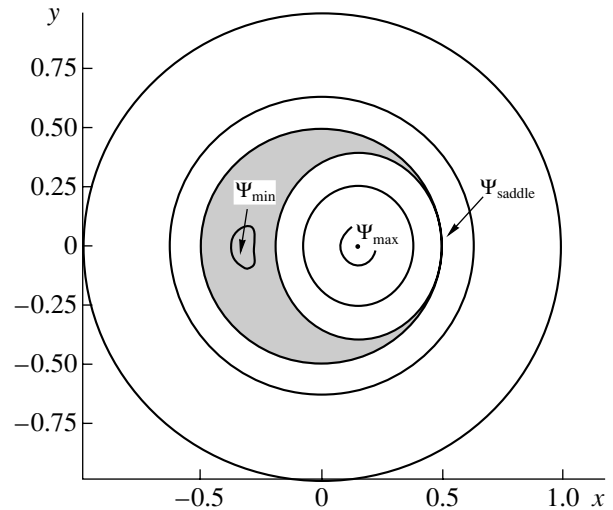

Fig. 2. A schematic pattern of the magnetic field lines illustrating the definition of the parameter R_p. The hatched region is a magnetic island.

description of tearing instability is, strictly speaking, limited, because this model implies that the toroidal component V_z of the velocity should be much lower than the poloidal component. The reasons for this are explained in [18, 19].

3.2. Two-Fluid MHD Model:
The Case $T(t = 0) = const$ and $\rho(t = 0) = 1$

Here, we consider the plasma flow pattern in the case with $\alpha \neq 0$ and with the initial distributions $T(t = 0) = const$ and $\rho(t = 0) = 1$.

For $\alpha \neq 0$, the flow pattern (Fig. 3) differs substantially from that in the case $\alpha = 0$. We can clearly observe the characteristic property of reconnection in the EMHD model: a tendency toward the formation of a current peak [12, 21] rather than a current sheet, as in the case $\alpha = 0$.

The contour lines of the quantities p, ρ, T, and H_g, as well as of the vorticity $\omega = (\nabla \times \mathbf{V})_g$, are very similar to one another. Hence, to a good approximation, it can be stated that these quantities depend only on one function. Note that, for $\alpha \neq 0$ and $\alpha = 0$, the distributions of ω are roughly the same, but such is not the case for the other quantities in question. In contrast to the symmetric distributions in the case $\alpha = 0$, the distributions of the deviations of the quantities p, ρ, T, and H_g from their equilibrium distributions are nearly antisymmetric about the x axis.

Let us consider how the duration of the reconnection process depends on the parameters of the problem.

Numerical calculations show that, for $\alpha \neq 0$, the time t_n is much shorter than that for $\alpha = 0$. Thus, for $\nu_e = 10^{-9}$, the duration t_n of the nonlinear reconnection stage is equal to 148 and 50 Alfvén times in the cases $\alpha = 0$
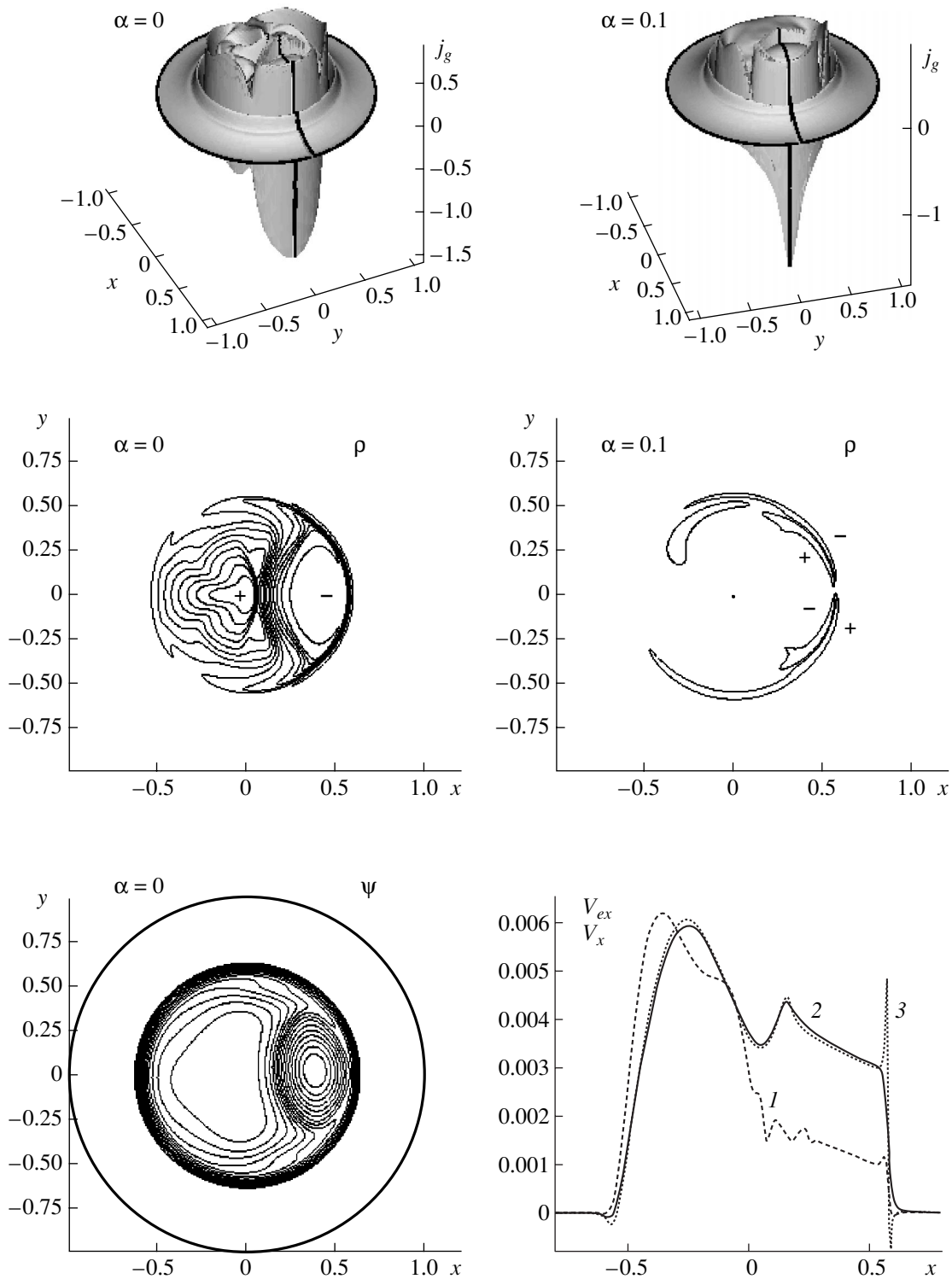
Fig. 3. Distributions of the current density j_g and plasma density ρ (the plus and minus signs indicate regions where $\rho > 1$ and $\rho < 1$, respectively), and patterns of the lines of the poloidal magnetic field (contour lines of the function ψ) for $\alpha = 0$ and $\alpha = 0.1$. The profiles of the velocities V_x and V_{ex} along the x axis (curve 1 is for V_x at $\alpha = 0$ and curves 2 and 3 are for V_x and V_{ex} at $\alpha = 0.1$) are also shown. The calculations were carried out for $p(t = 0) = \text{const}$, $\nu_e = 10^{-9}$, $\chi_{\|i} = 5$, and $p_e(t = 0) = 0$. The time corresponds to that at which $R_p = 1/2$ ($t = 632$ for $\alpha = 0$ and $t = 444$ for $\alpha = 0.1$). The pattern of the magnetic field lines for $\alpha = 0.1$ essentially coincides with that for $\alpha = 0$. The contour lines of p, T, H_g, and ω for $\alpha = 0.1$ are similar to the those of ρ.

and $\alpha = 0.1$, respectively. In the case $\alpha = 0.2$, the duration is shorter: it is equal to $t_n = 26$.

For $\alpha = 0$ and for a lower value of the electron viscosity, $\nu_e = 2.5 \times 10^{-10}$, the duration is longer, $t_n = 210$. For $\alpha = 0.1$, such a decrease in ν_e does not lead to an increase in t_n but rather reduces it to 38 Alfvén times. This dependence on the coefficient ν_e agrees with the results of [11, 12], in which it was shown that, in the EMHD approximation, the reconnection time is independent of the transport coefficients. Hence, for $\alpha \neq 0$, the duration t_n of the nonlinear reconnection stage is significantly shorter; moreover, as $\nu_e \longrightarrow 0$, the time t_n approaches a finite value.

An analysis of the dependence of t_n on the electron and ion thermal conductivities and on the ratio of the initial electron and ion pressures, $p_e(t = 0)$ and $p_i(t = 0)$, shows that t_n slightly increases with increasing thermal conductivities. The above values of t_n were calculated for the case of $\chi_{\|e} = \chi_{\|i} = 5$ at $p_e(t = 0) = p_i(t = 0)$ and for the case of $\chi_{\|i} = 5$ and an arbitrary $\chi_{\|e}$ value at $p_e(t = 0) = 0$. For longitudinal (relative to the magnetic field) thermal conductivities higher than 100, the time t_n increases to 60 Alfvén times.

The results presented above can be qualitatively explained in terms of the reduced model to be constructed below. Since this RMHD model, which differs fundamentally from that developed in [13], will serve merely to give a qualitative explanation of the results obtained in the two-fluid MHD approximation, it will be formulated in a fairly simple, unrigorous way, with particular reference to the results of numerically solving the two-fluid MHD equations. The main simplifications are as follows:

(i) In accordance with the conventional order of the quantities with respect to the parameter $R \gg 1$ in the RMHD model [13, 18, 19], we obtain from Eq. (2.10) the equation

$$\nabla \cdot \mathbf{V} = (\mathbf{H} \cdot \nabla)(V_g - \alpha j_g).$$

Calculations carried out in the two-fluid MHD approximation show that $V_g \ll \alpha j_g$. Consequently, we can write

$$\nabla \cdot \mathbf{V} = -\alpha(\mathbf{H} \cdot \nabla)j_g. \tag{3.1}$$

(ii) Calculations show that the inequalities

$$\nabla(p + H_g^2/2) \ll \nabla p \quad \text{and/or} \quad \nabla H_g^2/2 \tag{3.2}$$

are satisfied not only in the case $T(t = 0) = \text{const}$ and $\rho(t = 0) = 1$ but in all other cases as well. The conjunction "and/or" in inequalities (3.2) stands for situations in which, for example, the gradient of p at the very beginning of the reconnection process is equal to zero provided that $p(t = 0) = \text{const}$. At later stages of the process, we have $\nabla p \sim \nabla H_g^2/2$. Since the magnetic field

component H_g deviates only slightly from unity, inequalities (3.2) yield

$$\nabla H_g \approx -\nabla p. \tag{3.3}$$

Inequalities (3.2) do not result from an expansion in R but are obtained as follows:

By virtue of the equilibrium condition, the quantities ∇p and/or $\nabla H_g^2/2$ are on the order of $\nabla H_\varphi^2/2$. Moreover, the magnetic field configuration in a tokamak is such that, in the region where the plasma motion is most intense (i.e., within the surface $q = 1$), we have $H_s \ll H_\varphi$. At the plasma periphery, the field component H_s can be on the order of H_φ, but the plasma in the peripheral region is essentially unperturbed. The plasma motion is governed by changes in the field component H_s. In particular, the maximum plasma velocity is on the order of $H_s\rho^{-1/2} \sim H_s$. The relative order of different terms in Eqs. (2.4)–(2.7) is such that this condition can be satisfied only when $\nabla(p + H_g^2/2) \sim \nabla H_s^2/2 \ll \nabla H_\varphi^2/2 \sim \nabla p$ and/or $\nabla H_g^2/2$.

Substituting relationships (3.1) and (3.3) into Eqs. (2.11)–(2.13) and assuming that ρ and H_g are both close to unity, we obtain

$$\partial\rho/\partial t + (\mathbf{V} \cdot \nabla)\rho = \alpha(\mathbf{H} \cdot \nabla)j_g, \tag{3.4}$$

$$\partial p_{i,e}/\partial t + (\mathbf{V} \cdot \nabla)p_{i,e} = \alpha\gamma_{i,e}p_{i,e}(\mathbf{H} \cdot \nabla)j_g + (\gamma_{i,e} - 1)\nabla \cdot (\chi_{\|i,e}\mathbf{H} \cdot (\mathbf{H} \cdot \nabla)p_{i,e} + \chi_{i,e}\nabla p_{i,e}). \tag{3.5}$$

Note that the velocity $\mathbf{V}$ on the right-hand side of Eq. (3.5) (for both p_i and p_e) is the ion velocity.

Since the right-hand side of Eq. (3.1) is on the order of R^{-2}, and since $\mathbf{V} \sim R^{-1}$, we can assume that the plasma compressibility is low; in this case, in place of the equation for the velocity, we can use the equation for the vorticity $\omega = r^{-1}\partial(rV_s)/\partial r - r^{-1}\partial V_r/\partial\varphi$:

$$\partial\omega/\partial t + (\mathbf{V} \cdot \nabla)\omega = (\mathbf{H} \cdot \nabla)j_g + \nu\Delta\omega. \tag{3.6}$$

Together with the equation for ψ, which, with allowance for relationship (3.3), can be rewritten as

$$\frac{\partial\psi}{\partial t} + (\mathbf{V} - \alpha(\mathbf{e} \times \nabla p))\nabla\psi = -\eta j_g + \nabla \cdot (\nu_e\nabla j_g), \tag{3.7}$$

Eqs. (3.4)–(3.6) constitute a closed set of equations.

We can readily see that, with the initial conditions $T = \text{const}$ and $\rho = 1$, Eqs. (3.4)–(3.6) are similar in structure and the initial parameter values for them are nearly the same. Consequently, with some degree of accuracy, we can write the relationships $\rho \approx 1 + \alpha\omega$ and $p_{i,e} \approx p_{i,e}(t = 0)(1 + \tilde{\alpha}_{i,e}\omega)$, where $\tilde{\alpha}_{i,e} = \gamma_{i,e}\alpha$ for $\chi_{i,e} = \chi_{\|i,e} = 0$ and $\tilde{\alpha}_{i,e} = \alpha$ for $\chi_{i,e}, \chi_{\|i,e} \longrightarrow \infty$ (at a constant temperature). These relationships, along with relationship (3.3), explain why the contour lines of the quantities ρ, p, H_g, and ω for $\alpha \neq 0$ are essentially identical

(see Fig. 3). Note that the plasma density deviates only slightly from its initial distribution; moreover, in the RMHD approximation, this deviation is proportional to α. For $\alpha = 0$, the density in the RMHD approximation remains constant. That the contour lines of the density for $\alpha = 0$ (see Fig. 3) are symmetric stems from the use of the unreduced MHD model, which automatically incorporates higher order corrections in R^{-1} and thereby has a higher order of accuracy than the RMHD model.

With the above analysis in mind, we can rewrite Eq. (3.7) as

$$\frac{\partial \psi}{\partial t} + (\mathbf{V}_e \cdot \mathbf{\nabla})\psi = -\eta j_g + \mathbf{\nabla} \cdot (\nu_e \mathbf{\nabla} j_g), \qquad (3.8)$$

where

$$\mathbf{V}_e \approx \mathbf{V} - \alpha(\tilde{\alpha}_i p_i(t=0) + \tilde{\alpha}_e p_e(t=0))(\mathbf{e} \times \mathbf{\nabla}\omega).$$

Hence, with the initial conditions $p = $ const and $\rho = $ const, the magnetic field evolution can be described by only two equations, namely, Eqs. (3.6) and (3.8). A similar model was investigated in [4].

Equation (3.8) provides insight into the mechanism for hastening the reconnection process at $\alpha \neq 0$. The reconnection time depends on the velocity with which the oppositely directed magnetic fluxes are transported toward one another. For the configuration in question (see Fig. 3), this indicates that the reconnection time is determined by the derivative $\partial V_{ex}/\partial x$ at the reconnection point (the saddle point of the function ψ). For a plasma flow that runs into the current sheet in a direction perpendicular to it and runs out of the sheet in a direction parallel to it, the vorticity ω is distributed as shown in Fig. 3. It is obvious that, for $\alpha \neq 0$, and for such a distribution of ω, the value of $\partial V_{ex}/\partial x$ at the saddle point is larger than that of $\partial V_x/\partial x$ (Fig. 3). The higher the electron viscosity ν_e, the smaller the region of steep gradients of ω but the larger the value of ω and, consequently, the larger the value of $\partial V_{ex}/\partial x$. Accordingly, as ν_e decreases, the reconnection rate may not only be nondecreasing but may even increase.

Equations (3.8) and (3.5) give a clear insight into the dependence of the reconnection time on the electron and ion thermal conductivities and on the ratio of the initial electron and ion pressures, p_e and p_i. In particular, that the reconnection time t_n increases slightly with increasing thermal conductivities is attributed to a decrease in the quantities $\tilde{\alpha}_{i, e}$ in Eq. (3.8).

Note that the mechanism for hastening the reconnection process under investigation is associated with the Hall effect. The properties of the configuration in question are such that the terms associated with the Hall effect in the generalized Ohm's law can be expressed through the electron and ion pressure gradients. As for the term with ∇p_e in the generalized Ohm's law, it turns out to be unimportant in the RMHD approximation.

In addition, note that many of the terms that were discarded in deriving Eqs. (3.4)–(3.8) are small not only because of the condition $R \gg 1$ but also because of the specific features of the plasma flow in the case $T(t = 0) = $ const and $\rho(t = 0) = 1$. Thus, the fact that the functions ρ, p, and H_g, roughly speaking, depend only on ω implies that such terms as $\mathbf{\nabla} \cdot (\rho^{-1}(\mathbf{e} \times \mathbf{\nabla}p)$ are close to zero. For $T(t = 0) \neq $ const and/or $\rho(t = 0) \neq $ const, agreement between the reduced and unreduced MHD models is worse because Eqs. (3.4) and/or (3.5) in this case differ substantially from Eq. (3.6). In fact, calculations show (see below) that, for $T(t = 0) \neq $ const and $\alpha \neq 0$, the reconnection time depends strongly on the ratio of the initial electron and ion pressures, p_e and p_i, even when the electron and ion thermal conductivities are the same. As for the RMHD model, it does not include this dependence. The reason is that the retention of the electron pressure gradient ∇p_e in the generalized Ohm's law, as well as the retention of the ion velocity in Eq. (2.12) and of the electron velocity in Eq. (2.13), goes beyond the accuracy of this reduced model. Also, for $T(t = 0) \neq $ const, the plasma density can deviate from unity by almost 30%, whereas, for $p(t = 0) = $ const, this deviation does not exceed 10%. All this shows that it is expedient to solve the problem about the development of tearing instability in a tokamak by using unreduced MHD models.

3.3. Two-Fluid MHD Model: The Case $T(t = 0) \neq$ const and $\rho(t = 0) = 1$

For $\alpha = 0$, the poloidal magnetic field and poloidal plasma velocity in the case $T(t = 0) \neq $ const and $\rho(t = 0) = 1$ behave in essentially the same manner as in the case $T(t = 0) = $ const. But for $\alpha \neq 0$, the field, as well as the velocity, in these two cases exhibits qualitatively different behaviors.

For $\alpha \neq 0$ and for low values of $\chi_{\|i}$, the plasma motion in the nonlinear stage of reconnection is irregular: new magnetic islands are observed to appear and disappear (Fig. 4), several local maxima form in the current distribution within the current sheet, and the maximum current density varies nonmonotonically over time. The parameter $R_p(t)$, too, can exhibit a nonmonotonic behavior. In this case, however, the reconnection is complete; i.e., on sufficiently long time scales, we have $R_p = 1$.

The duration of the nonlinear reconnection stage in the case $T(t = 0) \neq $ const is far longer than that in the case $T(t = 0) = $ const. In certain situations (e.g., in the case of $p_e(t = 0) = 0$ and of low values of $\chi_{\|i}$ and ν_e), the reconnection time t_n for $\alpha \neq 0$ can substantially exceed t_n for $\alpha = 0$. This can be exemplified by reference to the numerical results.

We consider the case such that $p_e(t = 0) = 0$ and $\alpha = 0.1$. For $\nu_e = 10^{-9}$ and $\chi_{\|i} = 5$, the reconnection time is about $t_n \approx 209$. For one-quarter of this ν_e value, the t_n
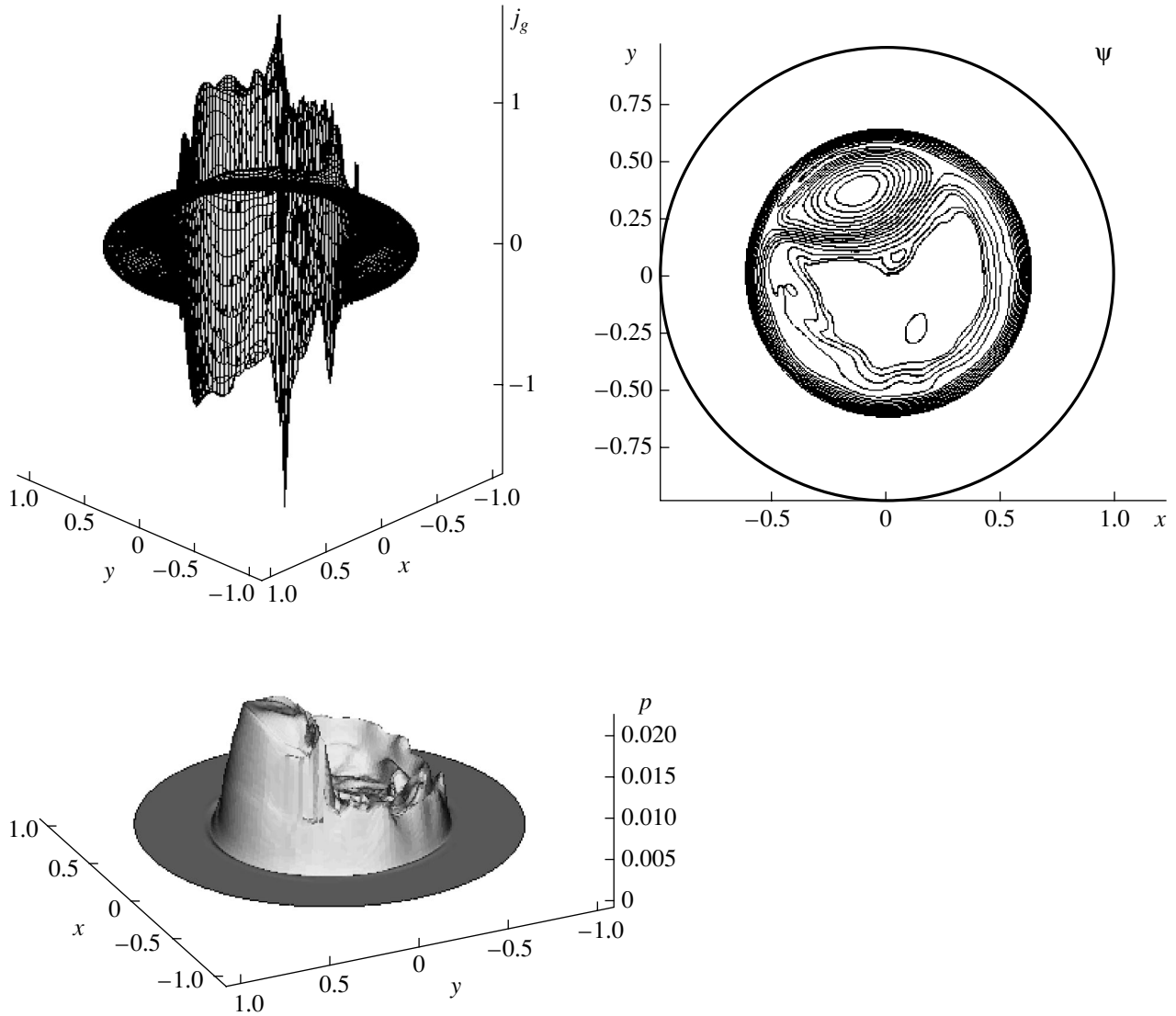
Fig. 4. Distributions of the current density j_g and total plasma pressure p and contour lines of ψ in the nonlinear stage of reconnection at $T(t=0) \neq$ const for $\alpha = 0.1$, $\nu_e = 2.5 \times 10^{-10}$, $\chi_{\|i} = 5$, and $p_e(t=0) = 0$.

value is essentially the same. Note that, for these two values of ν_e, and for $\alpha = 0$, the reconnection time t_n is equal to 140 and 193 Alfvén times. The duration of the nonlinear reconnection stage depends sensitively on the value of $\chi_{\|i}$. For instance, for $\nu_e = 10^{-9}$ and $\chi_{\|i} = 2$, we have $t_n \approx 278$, and, for $\chi_{\|i} = 100$, we have $t_n \approx 95$.

For a low $\chi_{\|i}$ value, the time t_n in the case $p_e(t=0) = p_i(t=0)$ is appreciably shorter than in the case $p_e(t=0) = 0$. Thus, for $\alpha = 0.1$, $\chi_{\|i} = 5$, and $p_e(t=0) = p_i(t=0)$, the reconnection time is $t_n = 100$. For $\chi_{\|i} = 100$, the reconnection time is nearly the same as in the case $p_e(t=0) = 0$. It should be stressed that, unlike in the case $p_e(t=0) = 0$, the reconnection process in the case $p_e(t=0) = p_i(t=0)$ is also hastened at a low value of the electron thermal conductivity, $\chi_{\|e} = 5$.

This dependence of the reconnection time t_n on the parameters of the problem can be partially explained by reference to RMHD equations (3.4)–(3.7). In the case $T(t=0) \neq$ const (in contrast to the case $T(t=0) =$ const), an essential role is played by a hot plasma core, which is transported toward the neutral surface during the evolution of the plasma flow. This gives rise to steep pressure gradients in the vicinity of the saddle point in a direction perpendicular to the current sheet. Accordingly, the electron velocity $\mathbf{V}_e$ acquires a large component,

$$\alpha\rho^{-1}(\mathbf{e} \times \boldsymbol{\nabla}H_g) \approx -\alpha(\mathbf{e} \times \boldsymbol{\nabla}p)$$
$$\equiv -\alpha\rho(\mathbf{e} \times \boldsymbol{\nabla}T) - \alpha T(\mathbf{e} \times \boldsymbol{\nabla}\rho), \tag{3.9}$$

along the lines of constant temperature. This component sets an island into rotation (Fig. 4). A more impor-

tant point is that such a velocity field breaks the structure of a plasma flow in which antiparallel magnetic fields are transported toward one another to meet at the saddle point. In some cases, the result is that, for $\alpha \neq 0$, the reconnection process proceeds at a far slower rate than it does for $\alpha = 0$. Roughly speaking, the azimuthal component of the electron velocity $\mathbf{V}_e$ acts to expel the magnetic field from the vicinity of the saddle point, thereby preventing it from reconnecting.

The rotation of an island and the slowing of reconnection are attributed to the temperature gradients. We emphasize that, in the nonlinear stage of development of the plasma flow, the values of these gradients are determined not so much by the initial temperature gradients in the vicinity of the neutral surface as by the difference between the temperatures at the plasma center and in the vicinity of the neutral surface at $t = 0$, i.e., by the value of the parameter p_1.

The effect of the longitudinal thermal conductivity is to equalize the temperature T along the magnetic field. Consequently, the higher the coefficient $\chi_{\parallel}$, the smaller the term $-\alpha\rho(\mathbf{e} \times \boldsymbol{\nabla}T)$ in relationship (3.9) and, accordingly, the less the extent to which the reconnection process is slowed. As a result, as ν_e decreases, the reconnection time t_n increases until it becomes long enough for the temperature T to be equalized along the magnetic field. As ν_e increases further, the duration t_n of the nonlinear reconnection stage changes only slightly.

There is as yet no simple explanation of why the reconnection time t_n for low $\chi_{\parallel i}$ values in the case $p_e(t = 0) = p_i(t = 0)$ is shorter than that in the case $p_e(t = 0) = 0$. It was pointed out earlier that, according to the RMHD model, these two cases should not differ fundamentally from one another. The difference may stem from the fact that the equation for the electron pressure contains $\mathbf{V}_e$ rather than $\mathbf{V}$. Therefore, the distributions of p will be different for different ratios between $p_e(t = 0)$ and $p_i(t = 0)$. Hence, according to approximate equation (3.7), which is well satisfied for all the parameter values used in our numerical calculations, the poloidal magnetic field flux ψ, too, will behave in different ways. The mechanism for hastening the reconnection process is again associated with the Hall effect and with the properties of the flow under consideration that follow from inequalities (3.2). The dependence of t_n on the ratio between $p_e(t = 0)$ and $p_i(t = 0)$ can also be attributed to the presence of the electron pressure gradient ∇p_e in the generalized Ohm's law with $p_e(t = 0) \neq 0$. It is impossible to distinguish between the Hall effect and the electron pressure gradient effect in the generalized Ohm's law.

3.4. Two-Fluid MHD Model: The Case $T(t = 0) \neq const$ and $\rho(t = 0) \neq const$

In the case $\rho(t = 0) \neq const$, the temperature T and density ρ behave in the same manner. A high-density plasma core is transported toward the neutral surface and acts to slow the reconnection process. The density of the plasma, however, does not depend on its thermal conductivity. This is why, as compared to the case $\alpha = 0$, the reconnection process can also be significantly slowed when the plasma heat conductivity along the magnetic field is high. Thus, for $\chi_{\parallel i} = 100$, $p_e(t = 0) = 0$, and $\rho_1 = 0.3$, we have $t_n(\alpha = 0.1)/t_n(\alpha = 0) = 265/131 > 1$, in contrast to the case $\rho(t = 0) = 1$.

For $\rho(t = 0) \neq const$, as well as for $\rho(t = 0) = 1$, the time t_n in the case $p_e(t = 0) = p_i(t = 0)$ is less than that in the case $p_e(t = 0) = 0$. However, in all calculation versions in which the spatial variation in the plasma density at the initial time is sufficiently large, the time t_n is characteristically longer than that in the case $\rho(t = 0) = 1$. Thus, for $\alpha = 0.1$, $\nu_e = 10^{-9}$, $\chi_{\parallel i} = 5$, and $p_e(t = 0) = p_i(t = 0)$, we have $t_n = 100$ in the case $\rho(t = 0) = 1$ and $t_n = 200$ in the case $\rho(t = 0) \neq const$ ($\rho_1 = 0.3$). Moreover, the lower the peripheral plasma density ρ_1, the longer the time t_n.

4. VALUES OF THE DIMENSIONLESS PARAMETERS

Here, we examine how well the above numerical results correlate with the experimental data. To do this, we consider parameter values typical of tokamaks: $H_z = 25$ kG, $T_e \approx T_i = 1$ keV, $n = 10^{14}$ cm^{-3}, $a = 50$ cm, and $R_0/a = 4$. In this case, the Alfvén speed is $V_A = 5.5 \times 10^8$ cm/s, the electron and ion thermal velocities are $V_{Te} = 1.3 \times 10^9$ cm/s and $V_{Ti} = 3.1 \times 10^7$ cm/s, the Alfvén time is $t_A = a/V_A = 8.4 \times 10^{-8}$ s, and the Hall parameter is $\alpha = 0.05$. The characteristic time of the tearing instability is $\sim 10^{-4}$ s, or ~ 1200 in dimensionless units. Let us estimate the dimensionless transport coefficients for these parameter values.

For a collision frequency equal to that of Coulomb collisions, the longitudinal (with respect to the magnetic field) thermal conductivities $\chi_{\parallel}$ and the longitudinal electron viscosity $\nu_{\parallel}$ are unrealistically high (the collisionless limit). In [22], these transport coefficients were estimated in investigating a microinstability of the drift type. In the case of interest to us, namely, for low collision frequencies and slow plasma flows, the estimates in dimensional form read $\nu_{\parallel j} \sim \chi_{\parallel j} \sim V_{Tj} l_{\parallel}$, where V_{Tj} is the thermal velocity of the particles of species j ($j = e$ for electrons and $j = i$ for ions), and $l_{\parallel}$ is the characteristic scale length of the perturbation along the magnetic field. These estimates correspond to the maximum possible values of the transport coefficients in question that were obtained from the following consideration: The values of $\nu_{\parallel j}$ and $\chi_{\parallel j}$ should not exceed a certain value D such that the time required for a perturbation described by the equation $\partial f/\partial t = D((\mathbf{H}/|\mathbf{H}|) \cdot \boldsymbol{\nabla})^2 f$ to propagate a distance $l_{\parallel}$ is shorter than the time required to pass this distance with the thermal velocity.

In dimensional form, we have $l_\parallel^{-1} \sim (H_s/H_z)r_n^{-1}$, where $r_n \approx a/2$ is the radius of the neutral surface. The dimensionless thermal conductivities can then be estimated by

$$\chi_{\parallel j} \sim 2(V_{Tj}/V_A)(l_\parallel/a) \sim 2(V_{Tj}/V_A)(H_z/H_s).$$

With allowance for the fact that, in the configuration under analysis, the maximum value of the ratio H_s/H_z in the region where the plasma motion is most intense is about 0.013, the dimensionless electron and ion thermal conductivities are approximately equal to $\chi_{\parallel e} \sim 90$ and $\chi_{\parallel i} \sim 2$. In the vicinity of the neutral surface, we have $H_s \longrightarrow 0$ and the thermal conductivities $\chi_{\parallel j}$ are higher.

Analogously, the dimensionless electron viscosity can be estimated by

$$\nu_e \sim (m_e/M)\delta_i^2 \nu_{\parallel e} t_A (H_s^2/H_z^2)/a^4$$
$$\sim (m_e/M)\alpha^2(H_s/H_z)(V_{Te}/V_A) \sim 4.2 \times 10^{-8},$$

where m_e is the mass of an electron. In this estimate, we took into account the fact that the coefficient $\nu_{\parallel e}$ corresponds to a viscous force that is proportional to the second derivative of **j** along the magnetic field, whereas in the present paper, a model expression for viscous terms is used in which transverse (with respect to the magnetic field) derivatives play a governing role. The ratio between the transverse and longitudinal gradients is proportional to H_s/H_z. In the vicinity of the neutral surface, we have $H_s \longrightarrow 0$ and the electron viscosity ν_e is lower.

It should be noticed that, when the instabilities, which always increase the effective collision frequency, are taken into account, the electron viscosity ν_e can only be lower. Note also that, in [22], the plasma conductivity was estimated to be two times that in the case of Coulomb collisions, $\eta \sim 10^{-8}$. Accounting for the anomalous collision frequency can only raise the plasma conductivity η.

5. CONCLUSIONS

An analysis of the results presented in Sections 3 and 4 shows that, with the electron viscosity taken into account, the fast rate of reconnection can be explained even in a one-fluid MHD model. The duration of the reconnection process was calculated to be about 140 Alfvén times, which is one order of magnitude shorter than that observed in experiments. We emphasize that the viscous terms are described here by isotropic model expressions. It cannot be excluded that the actual value of the electron viscosity differs substantially from the ν_e value used in our study. However, since the dependence of the reconnection time t_n on ν_e is weak ($t_n \sim \nu_e^{-1/4}$), these factors are unlikely to substantially alter the final results.

In the case $T(t=0) = $ const and $\rho(t=0) = 1$, the Hall effect greatly reduces the reconnection time. Moreover, this time is independent of transport coefficients.

In the case $T(t=0) \neq $ const and/or $\rho(t=0) \neq $ const, the Hall effect can substantially increase the reconnection time in comparison to that for $\alpha = 0$. The particular value of t_n depends on the ratio between the central and peripheral initial temperatures T, the ratio between the central and peripheral initial densities ρ, and on the thermal conductivity. It is notable that, whereas in the case $T(t=0) \neq $ const, the reconnection rate decreases substantially as $\chi_\parallel$ increases, in the case $\rho(t=0) \neq $ const, this rate is independent of the thermal conductivity. Note also that, in the case $T(t=0) \neq $ const and/or $\rho(t=0) \neq $ const, the reconnection process is nonuniform (nonmonotonic) in character: it proceeds through the generation of magnetic islands and the onset of several local maxima in the current density within the current sheet. In addition, the parameter R_p, which characterizes the portion of the magnetic flux that has undergone reconnection, behaves as a nonmonotonic function of time. It may well be that, when the dependence of ν_e and η on the plasma temperature is taken into account, such factors will terminate the reconnection process (i.e., the reconnection will be incomplete [1–3, 9]) because of the current collection effect [23].

APPENDIX

The scalar and vector products of the vectors with components (2.3) have the form

$$(\mathbf{a} \cdot \mathbf{b}) = a_r b_r + G^{-1}(a_s b_s + a_g b_g),$$

$$(\mathbf{a} \times \mathbf{b})_r = G^{-1}(a_s b_g - a_g b_s),$$

$$(\mathbf{a} \times \mathbf{b})_s = a_g b_r - a_r b_g,$$

$$(\mathbf{a} \times \mathbf{b})_g = a_r b_s - a_s b_r,$$

where $G = 1 + r^2/R^2$.

The expressions for the differential operators are

$$\nabla \cdot \mathbf{f} = \frac{1}{r}\frac{\partial(rf_r)}{\partial r} + \frac{1}{r}\frac{\partial f_s}{\partial \varphi},$$

$$(\nabla a)_r = \partial a/\partial r, \quad (\nabla a)_s = Gr^{-1}\partial a/\partial \varphi, \quad (\nabla a)_g = 0,$$

$$(\mathbf{f} \cdot \nabla)a = f_r\frac{\partial a}{\partial r} + f_s\frac{1}{r}\frac{\partial a}{\partial \varphi},$$

$$\Delta a = \nabla \cdot (\nabla a) \equiv \frac{1}{r}\frac{\partial}{\partial r}\left(r\frac{\partial a}{\partial r}\right) + G\frac{1}{r^2}\frac{\partial^2 a}{\partial \varphi^2}.$$

The components of the curl operator are given by the formulas

$$(\nabla \cdot \mathbf{f})_r = r^{-1}\partial f_g/\partial\varphi, \quad (\nabla \times \mathbf{f})_s = -\partial f_g/\partial r,$$

$$(\nabla \times \mathbf{f})_g = G\left(r^{-1}\frac{\partial(rG^{-1}f_s)}{\partial r} - r^{-1}\frac{\partial f_r}{\partial\varphi}\right) + \frac{2f_g}{RG}.$$

In terms of a unit vector $\mathbf{e}$ such that $e_r = e_s = 0$ and $e_g = 1$, the r and s components of the curl operator are written as

$$(\nabla \times \mathbf{f})_{r,s} = -(\mathbf{e} \times \nabla f_g),$$

$$(\nabla \times \mathbf{f})_g = -G\nabla \cdot (\mathbf{e} \times \mathbf{f}) + \frac{2f_g}{RG}.$$

Note also the relationship

$$\nabla \times (\nabla \times \mathbf{f})_g = -\Delta_g(f_g) + \frac{2(\nabla \times \mathbf{f})_g}{RG},$$

where

$$\Delta_g a = G\nabla \cdot (G^{-1}\nabla a)$$

$$\equiv G\left(\frac{1}{r}\frac{\partial}{\partial r}\left(\frac{r}{G}\frac{\partial a}{\partial r}\right) + \frac{1}{r^2}\frac{\partial^2 a}{\partial\varphi^2}\right).$$

REFERENCES

1. H. Soltwisch, W. Stodiek, J. Maniskamp, and J. Schluter, in *Proceedings of the 11th International Conference on Plasma Physics and Controlled Nuclear Fusion Research, Kyoto, 1986*, Vol. 6, p. 263.

2. H. Soltwisch, Rev. Sci. Instrum. **59**, 1599 (1988).

3. H. Soltwisch, Plasma Phys. Controlled Fusion **34**, 1669 (1992).

4. R. G. Kleva, J. F. Drake, and F. L. Waelbroeck, Phys. Plasmas **2**, 23 (1995).

5. B. B. Kadomtsev, Fiz. Plazmy **1**, 710 (1975) [Sov. J. Plasma Phys. **1**, 389 (1975)].

6. Y. Quingquan, Nucl. Fusion **35**, 1012 (1995).

7. M. Ottaviani and F. Porcelli, Phys. Rev. Lett. **71**, 3802 (1993).

8. F. Porcelli, D. Borgogno, F. Califani, *et al.*, Plasma Phys. Controlled Fusion **44**, B389 (2002).

9. D. Biskamp and J. F. Drake, Phys. Rev. Lett. **73**, 971 (1994).

10. A. S. Kingsep, K. V. Chukbar, and V. V. Yan'kov, *Reviews of Plasma Physics*, Ed. by B. B. Kadomtsev (Énergoizdat, Moscow, 1987; Consultants Bureau, New York, 1990), Vol. 16.

11. M. E. Mandt, R. E. Denton, and J. F. Drake, Geophys. Res. Lett. **21**, 73 (1994).

12. V. P. Zhukov, Fiz. Plazmy **28**, 451 (2002) [Plasma Phys. Rep. **28**, 411 (2002)].

13. R. D. Hazeltine, C. T. Hsu, and P. J. Morrison, Phys. Fluids **30**, 3204 (1987).

14. D. Biskamp, Phys. Rev. Lett. **46**, 1522 (1981).

15. A. Y. Ademir, Phys. Fluids **4**, 3469 (1992).

16. E. Lazzaro, M. Ferrero, L. Gianoli, and L. Valdettaro, Phys. Scr. **61**, 624 (2000).

17. Xiaogang Wang and A. Battacharjee, Phys. Rev. Lett. **70**, 1627 (1993).

18. V. P. Zhukov, Fiz. Plazmy **27**, 630 (2001) [Plasma Phys. Rep. **27**, 591 (2001)].

19. V. P. Pastukhov, Fiz. Plazmy **26**, 566 (2000) [Plasma Phys. Rep. **26**, 529 (2000)].

20. S. I. Braginskii, in *Reviews of Plasma Physics*, Ed. by M. A. Leontovich (Gosatomizdat, Moscow, 1963; Consultants Bureau, New York, 1965), Vol. 1.

21. G. Valori, *Fluid and Kinetic Aspects of Collisionless Magnetic Reconnection* (Ipskamp, Enschede, 2001).

22. Zuoyang Chang and J. D. Callen, Phys. Fluids **4**, 1182 (1992).

23. Yu. N. Dnestrovskii and D. P. Kostomarov, *Numerical Simulation of Plasmas* (Mir, Moscow, 1982; Springer-Verlag, New York, 1986).

24. V. P. Zhukov, Zh. Vychisl. Mat. Mat. Fiz. **45**, 156 (2005) [Comp. Math. Math. Phys. **45**, 149 (2005)].

Translated by O.E. Khadin

Current Scaling for the Radiative Characteristics
of a Micropinch Discharge

A. N. Dolgov

Moscow Engineering Physics Institute, Kashirskoe sh. 31, Moscow, 115409 Russia
Received July 11, 2003; in final form, November 24, 2004

Abstract—The absolute VUV and soft X-ray ($h\nu > 100$ eV) yield from a micropinch discharge is measured for a fixed current of 150 kA. The current scaling in the range of 30–250 kA is found for a number of the discharge parameters: the VUV and soft X-ray yield, the electron temperature, the effective temperature of suprathermal electrons, and the energy of bremsstrahlung emission from thermal electrons. The experimental data are in good agreement with the simulations performed by using the model of radiative collapse in fast Z-pinches in plasmas of high-Z elements. © 2005 Pleiades Publishing, Inc.

1. INTRODUCTION

Interest in fast Z-pinches in plasmas of high-Z elements is related to the formation in them of a dense ($n_e > 10^{19}$ cm^{-3}), hot ($T_e \sim 1$ keV), multiply ionized plasma acting as an efficient source of high-power VUV and soft X-ray (SXR) emission.

A micropinch discharge can be produced in compact devices that are relatively simple in design and fairly reliable in operation [1–3]; this makes such discharges very attractive for various applications. Micropinch SXR sources have been used in developing X-ray lithography for replicating VLSI chips [4] and contact X-ray microscopy of biological objects [5, 6]. The effect was discovered of polishing high-temperature superconducting films exposed to VUV radiation from micropinch plasma [7].

The development of a radiation source for a particular application necessitates optimization of the discharge parameters in accordance with the required performance data of the source: the source size, the radiation yield, the radiation spectrum, the possibility of controlling the source parameters, etc. This makes it necessary to study the source characteristics over a wide range of the discharge parameters and to develop a reliable, well-grounded numerical model for describing the processes occurring in a discharge.

At present, a host of experimental data on highly emissive plasmas of fast Z-pinches are most adequately described (at least for currents of <1 MA) by the so-called radiative collapse model. It was shown in [8] that, for a plasma focus in hydrogen or deuterium at currents above 1.6 MA (the Pease–Braginskii critical current), bremsstrahlung losses lead to a reduction in the constriction radius (in principle, down to zero). However, the absorption of radiation and the heating caused by anomalous resistance can impede radiative collapse. In [9], this concept was extended to the case of multiple ionization in the plasma of a low-induc-

tance vacuum spark. Here, the generation of recombination and line emission (in addition to bremsstrahlung emission) leads to a sharp decrease in the critical current. Thus, for discharges in iron vapor, both the measured and theoretically predicted critical currents are equal to 50 kA [10]. For currents above 50 kA, the discharge plasma column undergoes sausage instability. In the constrictions, ≤10-μm hot plasma spots arise that are highly emissive in the X-ray spectral range [11] (the so-called micropinches [12]).

The aim of this study was to compare the measured and calculated emissive characteristics of fast Z-pinches in plasmas of high-Z elements, as well as to determine how these characteristics depend on the discharge current, which is one of the most important discharge parameters. A comparison between the experimentally obtained current scaling and theoretical predictions allows one to better estimate the reliability of the theoretical model than does an analysis of experiments performed within a narrow range of parameters.

2. EXPERIMENTAL TECHNIQUE

The experiments were performed in a low-inductance vacuum spark (LIVS) facility powered from a high-voltage capacitor bank [13]. The current rise time was $T/4 \approx 2$ μs, and the maximum discharge current was varied from 30 to 250 kA. The discharge chamber was pumped down to a pressure of 10^{-4} torr. The working medium was the erosion products of the iron electrodes (conical anode and plane cathode). The main discharge was triggered by producing an auxiliary low-current discharge between the electrodes. The micropinches were observed at the time close to the maximum of the discharge current.

The discharge radiation energy in a wide spectral range was measured with a thermocouple calorimeter. The radiation was received by a 8-mm-diameter plate

made of a blackened lead foil, to the rear side of which the "hot" ends of a copper–constantan thermocouple were fastened with a heat-conducting glue. The "cold" ends were glued to a massive metal brick. An important advantage of this calorimeter was the linearity of its characteristic throughout the entire energy range under study. The calorimeter was calibrated using a pulsed laser and an IMO-2I standard radiation detector. The amplitude of the calorimeter signal was measured by a microvoltmeter.

The radiation detector was placed inside the discharge chamber. To reduce the noise level, a ferrite stabilizer was introduced in the supply circuit of the microvoltmeter and an LC filter was installed at its input. The cases of the calorimeter and the discharge chamber were galvanically decoupled, and the microvoltmeter case was grounded through a separate earth lead that was uncoupled from the main grounding mat of the facility. The noise level was determined by measuring the calorimeter signal in the course of a test discharge during which the radiation detector was screened. It was found that the noise level was no higher than 10–15% of the useful signal in the spectral range under study.

To study the radiation spectrum, we used a set of absorption and band-pass filters made of 2- to 20-μm metal (Al, Cu) foils, 0.25- to 1-μm Zapon films, and 1-mm-thick LiF plates. The filters were set in front of the radiation detector and were protected from being damaged by the discharge plasma with a fine-mesh grid (with a mesh size of 8 μm and transmission coefficient of 50%) placed near the discharge. The reflected radiation was suppressed using a blind system. The filter transmittances were calculated by the data from [14, 15].

The radiation spectra within different wavelength intervals were recovered by the method described in [16] (a version of the Tarasko iteration algorithm [17]). An advantage of this method is that filters made of different materials can be used.

The discharge was monitored using the following diagnostics: a vacuum and an air pinhole camera placed inside and outside the vacuum chamber, respectively, to measure the spatial structure of the emitting plasma in the photon energy ranges of $h\nu \geq 1$ keV and $h\nu \geq 3$ keV; a B-dot probe to monitor the time derivative of the discharge current; and a planar vacuum photodiode to monitor radiation in the photon energy range of $h\nu \geq 10$ eV.

The measurement data are represented as functions of the discharge current amplitude.

3. ABSOLUTE VUV AND SXR YIELD

Let us first estimate the expected emissive characteristics of the LIVS plasma and compare them to the experimental results. It is obvious that it makes no sense to construct current scalings if there is no satis-

factory agreement between theoretical and experimental data at least at one value of the discharge current. Note that the dependence of the VUV and SXR radiation yield on the discharge current changes substantially when the current exceeds its critical value equal to 50 kA, i.e., when the micropinch regime is achieved. The estimates will be made for a 150-kA discharge in Fe vapor, for which there are available literature data [18–20].

Three stages can be distinguished in the process of the discharge plasma pinching: the "large" pinch (LP) of the plasma column before the onset of sausage instability, a micropinch produced after the first compression (MP1), and a micropinch produced during the second compression (MP2) in the course of the further development of the constriction. The plasma parameters in these stages are as follows:

$$T_e \approx 20 \text{ eV}, n_e \approx 5 \times 10^{19} \text{ cm}^{-3}, Z \approx 3, r \approx 10^{-1} \text{ cm},$$

$$h \approx 5 \times 10^{-1} \text{ cm, and } \tau \approx 5 \times 10^{-7} \text{ s in the LP stage;}$$

$$T_e \approx 40 \text{ eV}, n_e \approx 10^{21} \text{ cm}^{-3}, Z \approx 6, r \approx 10^{-2} \text{ cm},$$

$$h \approx 10^{-1} \text{ cm, and } \tau \approx 4 \times 10^{-8} \text{ s in the MP1 stage;}$$

and $T_e \approx 10^3$ eV, $n_e \approx 10^{24}$ cm^{-3}, $Z \approx 20$, $r \approx 5 \times 10^{-4}$ cm, $h \approx 10^{-3}$ cm, and $\tau \approx 10^{-10}$ s in the MP2 stage.

Here, T_e is the electron temperature; n_e is the electron density; Z is the average ion charge number; r and h are the pinch radius and height, respectively; and τ is the lifetime of the pinch plasma.

We begin by estimating the VUV radiation yield in the photon energy range $10 < h\nu < 100$ eV. The mean free path of the line emission photons ($h\nu \approx (1$–$3)T_e$) emitted from the plasma collapsing with the speed of sound is on the order of [21]

$$l \approx 10^{14} Z T_e^{1.5}/n_e \text{ [cm]}$$

(here and below, the temperature is in eV and the density is in cm^{-3}).

The parameter values $l/r^{LP} \approx 10^{-1}$ and $l/r^{MP1} \approx 10^{-2}$ indicate that the VUV line emission is trapped. The integral line emission power per unit length can be estimated by the formula accounting for the self-absorption of radiation [21]:

$$Q_l = 2 \times 10^2 T_e^{1.5} Z^{6.75} r/I^{0.5},$$

where Q_l is in W/cm and I is in MA.

The estimated total line emission yield is $E_l^{LP} \approx 3$ J and $E_l^{MP1} \approx 1$ J, which is much lower than the measured VUV yield ($E_{\text{VUV}} = 22$–32 J).

To estimate the specific power of recombination emission, we use the approximate formula for the photorecombination rate [22] averaged over a Maxwellian

distribution (assuming that the relaxation time of the electron distribution is short enough):

$$\langle v\sigma_r \rangle \approx 10^{-14} \tilde{Q}_r |E_{\gamma_0}/Ry|^{1/2} G_r(\beta),$$

$$\beta = E_{\gamma_0}/T_e,$$

$$G_r(\beta) = A\beta^{3/2}/(\beta + \chi),$$

where $\langle v\sigma_r \rangle$ is in cm^3/s, A and χ are the parameters of the analytic approximation, E_{γ_0} is the energy of the ion in the ground state, $\tilde{Q}_r$ is a factor depending on the quantum numbers of the angular momenta of the γ_0 level (here, this factor is close to unity), and Ry is the Rydberg constant. The approximation parameters and the E_{γ_0} value necessary were taken from [23].

The specific power of recombination radiation was estimated by the formula [22]

$$W_r \approx n_e n_i \langle v\sigma_r \rangle (T_e + |E_{\gamma_0}|),$$

where n_i is the density of ions in the ground state. The bremsstrahlung power was estimated in the Kramers approximation [24]:

$$W_{br} \approx 1.5 \times 10^{-32} n_e n_i Z^2 T_e^{1/2} \text{ [W/cm}^3\text{]}.$$

The resulting estimates for the yields of recombination and bremsstrahlung emission in the VUV spectral range are $E_r^{LP} \approx 30$ J, $E_{br}^{LP} \approx 10$ J, $E_r^{MP1} \approx 10$ J, and $E_{br}^{MP1} \approx 1$ J.

The excess of the calculated VUV yield over the measured one can be only partially explained by the inaccuracy of the above estimates because of the too large discrepancy between the calculated radiation yield from the LP plasma and the experimentally observed two- to threefold increase in the radiation intensity after passing to the micropinch regime (Fig. 1). The overestimated VUV yield is apparently related to the overestimation of the LP plasma density as compared to its actual value [25].

Let us now estimate the SXR yield in the photon energy range $h\nu \geq 100$ eV. This radiation is mainly emitted from the micropinch plasma during the second compression, when the L shell of Fe ions begins to be ionized. The estimated integral yield of recombination and bremsstrahlung emission during the second compression is $E_{br}^{MP2} \approx E_r^{MP2} \approx 10^{-2}$ J. In this stage, the line emission is no longer trapped and the mean free path of the line emission photons is comparable to the micropinch size $l^{MP2} \approx 10^{-3}$ cm. The integral yield of line emission in an optically thin plasma can be estimated from the expression for the volume power of such radiation [21]:

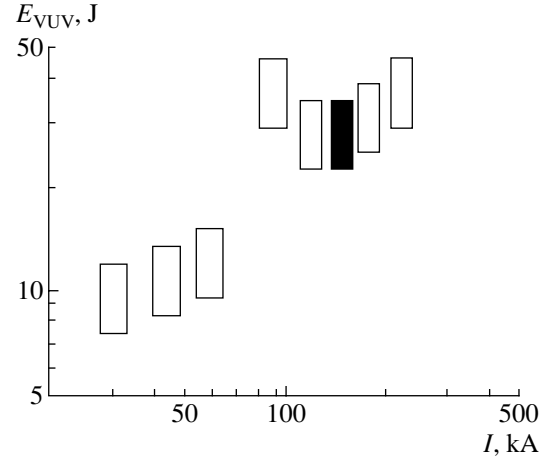$$W_l = 7 \times 10^{-25} Z n_e n_i / T_e \text{ [W/cm}^3\text{]}.$$

Fig. 1. VUV yield from the LIVS plasma vs. discharge current amplitude $I_{\max}$. The measurement result obtained for $I_{\max} = 150$ kA is shaded.

This estimate gives a line emission energy of $E_l^{MP2} \approx 10$ J, which is close to the measured SXR yield, $E_{SXR} = 12$–20 J. It should be noted that this estimate accounts not for the entire spectral range $h\nu \geq 100$ eV but only for the L-sell emission with $h\nu \geq 600$ eV. A certain contribution to the SXR line emission is made by the micropinch plasma heated after the first compression. The contribution from a single line can be estimated from the expression [26]

$$I_{\omega_0} \approx 4\pi B_P(\omega_0)(\Delta\omega_0)_{eq}$$

$$= 4\pi B_P \Gamma \{\pi\kappa_0 r[1 - \exp(-\hbar\omega_0/T_e)]\}^{1/2},$$

where B_P is the intensity of Planckian radiation into unit solid angle, $(\Delta\omega_0)_{eq}$ is the equivalent width of a Lorentzian line, $\Gamma \approx 10^{-2}\omega_0$ is the impact broadening of the line (here, the Doppler broadening is $\sim 10^{-4}\omega_0$), $\kappa_0 \approx \lambda n_i \gamma / \Gamma$ is the absorption coefficient in the center of the resonance line, $\lambda_0 = 2\pi c/\omega_0$, c is the speed of light, r is the constriction radius, and γ is the intrinsic line width.

The spectral range $h\nu \approx 100$–600 eV embraces the resonance lines of ten iron ions (from FeVII to FeXVI) [27], whose total contribution to the SXR yield is on the order of 5 J.

Thus, we may conclude that the results obtained in the radiative collapse model [9, 18, 19] agree satisfactorily with the measured VUV and SXR yield from a micropinch discharge for the given value of the discharge current.

4. CURRENT SCALING

In [28], based on the concepts of [9], the problem of micropinch dynamics that allowed analytic solutions was formulated and the relations between the discharge current and the main plasma parameters were derived.
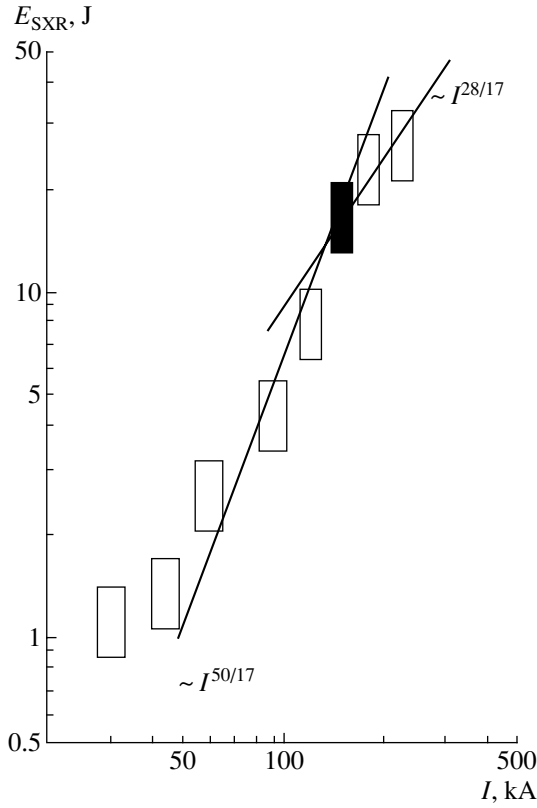
E_{SXR}, J

Fig. 2. SXR yield from the LIVS plasma vs. discharge current amplitude I_{max}. The measurement result obtained for $I_{max} = 150$ kA is shaded.

In what follows, we will use the following of these relations:

$$T_e \sim I^{12/17}, \quad n_i \sim I^2, \quad r \sim I^{-6/17}, \quad |\dot{r}| \sim I^{-16/17},$$

$$N_c \sim I^{22/17}, \quad r_c \sim I^{16/17}, \quad q \sim I^{46/17}, \quad \tau \sim I^{-12/17},$$

where r is the micropinch radius during the second compression, q is the maximum linear power of line emission during the second compression, N_c and r_c are the critical linear density $N = \pi r^2 n_i$ and the pinch radius at which the constriction region becomes transparent to the line emission, and τ is the micropinch lifetime in the second compression.

We will use the above relations to estimate the X-ray line emission yield during the second compression as a function of the discharge current. In our experiments, the parameters of the electrodes and the discharge circuit were chosen such that the micropinch formed at the instant of the maximum discharge current. For the X-ray line emission yield as a function of the discharge current, we have

$$E_{SXR} \approx qr\tau \sim I^{28/17}.$$

In [28], it was supposed that the plasma radiation time corresponds to the compression time determined by the Alfvén velocity

$$r/|\dot{r}| \sim I^{10/17}$$

rather than the micropinch lifetime τ. In this case, we obtain the following estimate:

$$E_{SXR} \approx qr\frac{r}{|\dot{r}|} \sim I^{50/17},$$

which is in better agreement with the measured dependence of the SXR yield on the discharge current (see Fig. 2). The measurement results indicate that the increase in the discharge current probably leads to a relative decrease in the contribution from the final stage of the second compression, when the plasma density is maximum.

Let us consider a simplified model of a quasi-equilibrium pinch under the following conditions [29]:

(i) The Bennet equilibrium condition is satisfied:

$$\frac{(Z+1)\rho kT}{m_a} = \frac{I^2}{2\pi c^2 r^2},$$

where m_a is the atomic mass of the plasma-forming element and ρ is the plasma mass density in the constriction region.

(ii) There is a balance between Joule heating and radiative losses:

$$\frac{I^2 l_R}{\pi^2 r^4 \sigma} = caT^4,$$

$$\sigma = \frac{1}{4\pi \times 0.08} \frac{(kT)^{3/2}}{m_e^{1/2} e^2 Z\Lambda},$$

where a is the Stefan–Boltzmann constant, σ is the classical plasma conductivity, $\Lambda \approx 20$ is the Coulomb logarithm, and l_R is the Rosseland mean free path.

(iii) The constriction radius is determined by the Rosseland mean free path in plasma:

$$r \approx l_R,$$

$$l_R \approx 0.5 \times 10^9 T_e^3/\rho^2 \text{ [cm]},$$

where T_e is in eV and ρ is in g/cm³.

To close the above set of equations, we supplement it with an expression relating the average ion charge number Z to the plasma electron temperature T_e. As a result, we obtain

$$r = \left(\frac{I}{0.7}\right)^{0.8} \frac{5.85 \times 10^{11}}{(Z+1)^{22/3} Z^{10/3}} \text{ [cm]},$$

$$T_e = \left(\frac{0.7}{I}\right)^4 \frac{(Z+1)^4 Z^2}{44.5} \text{ [eV]},$$

where I is in MA.

Substituting $Z \approx 6$ and $I = 0.15$ MA into these relationships yields $r \approx 100$ μm and $T_e \approx 50$ eV. This agrees well with both the results obtained in the radiative collapse model for the first compression and the experimental data from [11, 30]. For $Z \approx 20$, which corresponds to the second compression, we have $r \approx 10^{-4}$ μm and $T_e \approx 10^5$ eV. Such a small value of the constriction radius contradicts the MHD mechanism for pinching and disagrees with the predictions of the quasi-equilibrium pinch model.

In [31], relationships were derived that allow one to reliably estimate the Rosseland mean free path in a dense hot plasma with multicharged ions. The substitution of the measured parameters of the micropinch plasma during the second compression [32–34] into these relations shows that the Rosseland mean free path is several orders of magnitude larger than the measured micropinch size [11, 35].

Therefore, a decrease in the plasma transparency to its own emission during the second compression cannot suppress the sausage instability and the simplified model of a quasi-equilibrium pinch is capable of describing the process of micropinching only until the onset of anomalous plasma resistivity.

Let us now consider the simplified model of a quasi-equilibrium pinch with allowance for the measured dependence of the electron temperature on the discharge current (Fig. 3):

$$T_e \sim I^{3/4}.$$

We note that this dependence is close to that predicted in [28]. In this case, the average ion charge number is

$$Z \sim I^{19/24},$$

and, accordingly, the X-ray line emission yield from a micropinch is

$$E_{\mathrm{SXR}} \approx Z n_e n_i \frac{1}{T_e} \frac{r}{T_e^{1/2}} r^3 \sim I^{2.4},$$

which is close to the measured dependence. Apparently, the Z value changes insignificantly with current during the second compression. Ignoring variations in Z, we obtain the dependence

$$E_{\mathrm{SXR}} \sim I^{28/17},$$

which is in better agreement with the dependence observed at relatively high currents.

It was shown in [36] that, when the recorded micropinch X-ray emission with $h\nu > 1$ keV is integrated over a time interval much longer than the lifetime of the dense hot plasma in the second compression, the character of the absorption curve is mainly determined by bremsstrahlung emission. Moreover, the analysis of the absorption curve in the spectral ranges
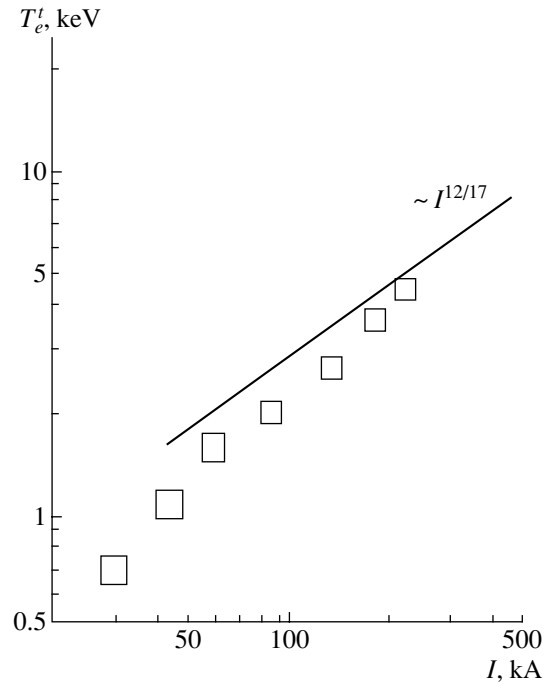
Fig. 3. Temperature of the thermal electron component determined from the X-ray bremsstrahlung continuum vs. discharge current amplitude.

of $1 < h\nu < 5$ keV and $5 < h\nu < 25$ keV gives different values of the effective plasma electron temperature. Therefore, it is necessary to use a two-temperature approximation in which the electron component is assumed to consist of the thermal and suprathermal components.

The experimental current scalings for the effective temperatures of the two electron components were obtained from the absorption curves in aluminum and copper (Figs. 3 and 4). We used two sets of absorption filters such that the cutoff energy of the first set lay in the photon energy range of 1–5 keV, whereas that of the second set lay in the photon energy range of 5–25 keV.

It is likely that the effective electron temperature measured from bremsstrahlung emission in the photon energy range of 1–5 keV corresponds to the plasma temperature in the second compression. This is confirmed by the results of high-resolution spectroscopic measurements of emission from multicharged ions [20, 32].

It is of interest to find out how the bremsstrahlung yield from the thermal electron component depends on the discharge current. This will allow better understanding of the nature of the emission source observed with the X-ray pinhole cameras. The bremsstrahlung yield was determined from the absorption curve at the point corresponding to the absorption filter of zero thickness (zero cutoff energy).

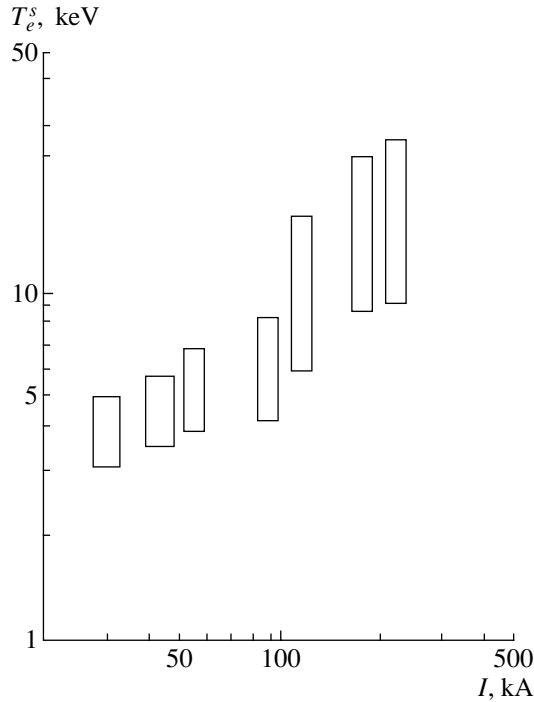Let us consider three possible mechanisms for the generation of bremsstrahlung emission:

Fig. 4. Effective temperature of the suprathermal electron component determined from the X-ray bremsstrahlung continuum vs. discharge current amplitude.
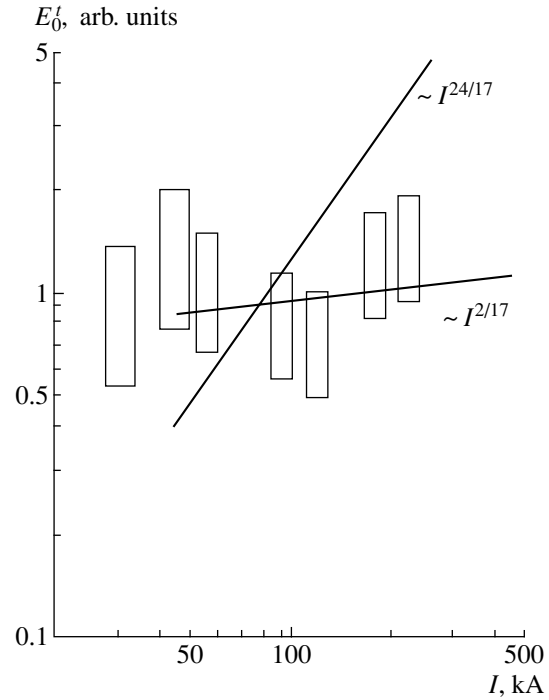

Fig. 5. X-ray bremsstrahlung yield from the thermal electron component vs. discharge current amplitude.

(i) Bremsstrahlung emission is generated in the micropinch plasma during the second compression; in this case, we have

$$E_{br} \approx W r^3 \frac{r}{|\dot{r}|}.$$

Since the degree of ionization during the second compression is close to its limiting value and dependent slightly on the current at currents higher than the critical one, the specific radiation power is

$$W \sim n_i^2 T_e^{1/2},$$

and the bremsstrahlung yield is

$$E_{br} \sim I^{56/17}.$$

(ii) Bremsstrahlung emission is associated with the hot electrons that are heated in the micropinch during the second compression and drift in the region where the plasma parameters correspond to those immediately preceding the second compression. In this case, we have

$$E_{br} \sim W\tau_{ee} \sim n_i r^3 T_e^{1/2}[T_e^{3/2}/(N_c r_c)] \sim I^{2/17}.$$

(iii) Bremsstrahlung emission is generated by the hot electrons that escape from the constriction region after the decay of the micropinch plasma to the cold peripheral plasma, whose parameters depend slightly on the current. In this case, we have

$$E_{br} \sim W\tau_{ee} \sim T_e^{1/2} T_e^{3/2} \sim I^{24/17}.$$

If we also consider the increase in the peripheral plasma density with increasing discharge current, the dependence of E_{br} on I will be even stronger.

A comparison to the measurement data (see Fig. 5) shows that the second model for the generation of bremsstrahlung emission best fits the experimental results. This model also accounts for the fact that the micropinch size determined from pinhole images obtained in the same spectral range is sometimes larger by one order of magnitude than that predicted by theory.

5. CONCLUSIONS

The measured absolute VUV and SXR yield from the micropinch plasma in an LIVS at a discharge current of 150 kA agrees well with the predictions of the radiative collapse model.

For the first time, the current scaling for the VUV and SXR yield from the micropinch plasma in an LVS is determined experimentally.

A comparison between the measured and theoretically predicted current scalings for the SXR yield shows that an increase in the discharge current leads to a decrease in the relative SXR yield in the final stage of the second compression, i.e., to a decrease in the plasma density and temperature.

The plasma electron component in the region of radiative collapse is in a strongly nonequilibrium state. It is shown for the first time that an increase in the discharge current leads to an increase in the ratio between

the temperature T_e^t of the thermal component and the effective temperature T_e^s of the suprathermal component. The measured current scaling for T_e^t is close to that predicted by the radiative collapse model.

It is confirmed experimentally that the energy transfer via hot electrons can affect the structure of X-ray sources in a micropinch [36, 37].

REFERENCES

1. Ch. K. Erbert, O. H. Herzog, A. Schulz, *et al.*, Plasma Sources Sci. Technol. **5**, 436 (1996).

2. K. Takasugi, H. Suzuki, K. Moriyamu, and T. Miyamoto, Jpn. J. Appl. Phys. **35**, 4051 (1996).

3. S. A. Pikuz, T. A. Shelkovenko, and D. B. Sinars, J. Quant. Spectrosc. Radiat. Transf. **71**, 581 (2001).

4. O. G. Semenov, A. E. Gurey, A. P. Kanavin, and A. A. Tikhomurov, J. Vac. Technol. B **19**, 1235 (2001).

5. V. A. Veretennikov, A. E. Gureĭ, K. T. Karaev, *et al.*, Preprint No. 10 (Lebedev Physical Inst., Russ. Acad. Sci., Moscow, 1994).

6. H. Maeda, K. Shimoda, and M. Sato, Res. Rep. NIFS-PROC Ser., No. 45, 58 (2000).

7. Yu. V. Afanas'ev, V. A. Veretennikov, D. G. Emel'yanov, *et al.*, Preprint No. 59 (Lebedev Physical Inst., USSR Acad. Sci., Moscow, 1991).

8. V. V. Vikhrev, Pis'ma Zh. Éksp. Teor. Fiz. **27**, 104 (1978) [JETP Lett. **27**, 95 (1978)].

9. V. V. Vikhrev, V. V. Ivanov, and K. N. Koshelev, Preprint No. 3359/6 (Kurchatov Inst. of Atomic Energy, Moscow, 1980).

10. M. A. Gulin, A. N. Dolgov, O. N. Nikolaev, and A. S. Savelov, Fiz. Plazmy **16**, 1015 (1990) [Sov. J. Plasma Phys. **16**, 590 (1990)].

11. V. A. Veretennikov, A. N. Dolgov, O. N. Krokhin, and O. G. Semenov, Fiz. Plazmy **11**, 1007 (1985) [Sov. J. Plasma Phys. **11**, 587 (1985)].

12. E. D. Korop, B. É. Meĭerovich, Yu. V. Sidel'nikov, and S. T. Sukhorukov, Usp. Fiz. Nauk **129**, 87 (1979) [Sov. Phys. Usp. **22**, 727 (1979)].

13. A. A. Gorbunov, M. A. Gulin, A. N. Dolgov, *et al.*, Pis'ma Zh. Éksp. Teor. Fiz. **50**, 320 (1989) [JETP Lett. **50**, 355 (1989)].

14. M. A. Blokhin and I. G. Shveĭtser, *Handbook of X-ray Spectra* (Nauka, Moscow, 1982) [in Russian].

15. J. A. R. Samson, *Techniques of Vacuum Ultraviolet Spectroscopy* (Wiley, London, 1964), p. 184.

16. S. A. Zverev, *Candidate's Dissertation in Mathematics and Physics* (Moscow Engineering Physics Institute, Moscow, 1981).

17. *Diagnostics of Dense Plasmas*, Ed. by N. G. Basov (Nauka, Moscow, 1989) [in Russian].

18. V. V. Vikhrev, V. V. Ivanov, and K. N. Koshelev, Fiz. Plazmy **8**, 1211 (1982) [Sov. J. Plasma Phys. **8**, 688 (1982)].

19. V. V. Vikhrev, V. V. Ivanov, K. N. Koshelev, and Yu. V. Sidel'nikov, Dokl. Akad. Nauk SSSR **282**, 1361 (1982) [Sov. Phys. Dokl. **27**, 153 (1982)].

20. K. N. Koshelev, Yu. V. Sidel'nikov, V. V. Vikhrev, and V. V. Ivanov, in *Spectroscopy of Multicharged Ions in Hot Plasmas* (Nauka, Moscow, 1991), p. 163 [in Russian].

21. K. N. Koshelev, Yu. V. Sidel'nikov, and V. V. Vikhrev, Preprint No. 1 (Inst. of Spectroscopy, USSR Acad. Sci., 1985).

22. I. I. Sobel'man, *Introduction to the Theory of Atomic Spectra* (Moscow, 1977) [in Russian].

23. B. N. Chichkov, *Candidate's Dissertation in Mathematics and Physics* (Lebedev Physical Institute, USSR Acad. Sci., Moscow, 1981).

24. V. I. Gervids, V. P. Zhdanov, V. I. Kogan, *et al.*, in *Reviews of Plasma Physics*, Ed. by B. B. Kadomtsev (Énergoatomizdat, Moscow, 1982; Consultants Bureau, New York, 1987), Vol. 12.

25. V. A. Veretennikov, A. E. Gureĭ, T. Pisarchik, *et al.*, Fiz. Plazmy **16**, 818 (1990) [Sov. J. Plasma Phys. **16**, 475 (1990)].

26. V. A. Abramov, V. I. Kogan, and V. S. Lisitsa, in *Reviews of Plasma Physics*, Ed. by B. B. Kadomtsev (Énergoatomizdat, Moscow, 1982; Consultants Bureau, New York, 1987), Vol. 12.

27. R. L. Kelly and L. J. Palumbo, *Emission Lines below 2000 Angstroms: Hydrogen through Krypton* (Naval Research Laboratory, Washington, DC, 1973).

28. S. M. Zakharov, G. V. Ivanenkov, A. A. Kolomenskiĭ, *et al.*, Fiz. Plazmy **9**, 469 (1983) [Sov. J. Plasma Phys. **9**, 271 (1983)].

29. V. S. Imshennik and N. A. Bobrova, *Dynamics of Collisional Plasmas* (Énergoatomizdat, Moscow, 1997) [in Russian].

30. A. N. Dolgov, Fiz. Plazmy **22**, 629 (1996) [Plasma Phys. Rep. **22**, 569 (1996)].

31. V. S. Imshennik, I. N. Mikhaĭlov, M. M. Basko, and S. V. Molodtsov, Zh. Éksp. Teor. Fiz. **90**, 1669 (1986) [Sov. Phys. JETP **63**, 980 (1986)].

32. É. Ya. Kononov, K. N. Koshelev, and Yu. V. Sidel'nikov, Fiz. Plazmy **11**, 927 (1985) [Sov. J. Plasma Phys. **11**, 538 (1985)].

33. É. Ya. Kononov, K. N. Koshelev, U. I. Safronova, *et al.*, Pis'ma Zh. Éksp. Teor. Fiz. **31**, 720 (1980) [JETP Lett. **31**, 679 (1980)].

34. J. F. Seely and T. N. Lee, Phys. Rev. A **29**, 411 (1984).

35. E. V. Aglitskiĭ, P. S. Antsiferov, and A. M. Panin, Fiz. Plazmy **11**, 275 (1985) [Sov. J. Plasma Phys. **11**, 159 (1985)].

36. V. V. Averkiev, A. N. Dolgov, V. K. Lyapidevskiĭ, *et al.*, Fiz. Plazmy **18**, 724 (1992) [Sov. J. Plasma Phys. **18**, 374 (1992)].

37. V. V. Averkiev, A. N. Dolgov, N. N. Kirichenko, *et al.*, Fiz. Plazmy **19**, 97 (1993) [Plasma Phys. Rep. **19**, 50 (1993)].

Translated by N.N. Ustinovskiĭ

<center>

PLASMA
RADIATION

</center>

Modeling of the Composition of Materials for Soft X-ray Sources Used in Research on Inertial Confinement Fusion

O. B. Denisov*, N. Yu. Orlov*, S. Yu. Gus'kov**, V. B. Rozanov**, N. V. Zmitrenko***, and A. P. Mikhaĭlov***

*Institute for High Energy Densities, Russian Academy of Sciences, Izhorskaya ul. 13/19, Moscow, 125412 Russia
**Lebedev Physical Institute, Russian Academy of Sciences, Leninskiĭ pr. 53, Moscow, 119991 Russia
***Institute for Mathematical Modeling, Russian Academy of Sciences, Miusskaya pl. 4a, Moscow, 125047 Russia
Received August 2, 2004

Abstract—A method for calculating and optimizing the composition of materials for soft X-ray sources used in research on inertial confinement fusion is described. For a target-converter, a material composition is determined with which the conversion of laser light into X radiation is highly efficient. A comparative analysis is carried out of the efficiencies of generation of soft X-ray emission in the plasmas of some composite materials of thin conductors (wires) used as loads in X- and Z-pinches. Numerical calculations of the optical plasma properties are reported whose results make it possible to judge the emissivity of plasmas of different materials. The results obtained are compared to the data from other studies. © 2005 Pleiades Publishing, Inc.

1. INTRODUCTION

Theoretical and experimental research on inertial confinement fusion (ICF) requires reliable knowledge about the optical and transport properties of matter under conditions of extremely high temperatures and densities, in particular, about such plasma parameters as thermal conductivities, light-absorption spectral coefficients, and the Planck- and Rosseland-averaged radiation mean free paths.

The determination of the optical plasma properties is one of the most important problem in such lines of ICF research in which soft X-ray (SXR) pulses are used as energy pulses acting upon an ignition capsule. Another important field of applications is the choice of materials for X-ray sources in order to develop methods for diagnosing dense plasmas.

From the standpoint of practical applications, the following two methods for generating high-power SXR pulses with parameters satisfying the ICF requirements are now considered to be the most advanced: One of the methods makes use of the conversion of laser radiation acting upon a heavy-element target into X radiation. The line of ICF research that is based on the conversion of laser light into X radiation is called indirect compression. An X-ray converter is a separate part of an indirect compression target—a hohlraum within which there is a spherical capsule containing a fusion material. Laser radiation is fed into the target through special holes in the hohlraum and is focused at the hohlraum's inner surface in order that the X radiation produced can ignite a fusion capsule positioned at the center of the hohlraum. The second method makes use of the generation of an SXR pulse during the electric explosion of a set of fine wires (a wire array).

Of course, one of the most important tasks in the X-ray-based lines of ICF is to choose materials for the pulsed X-ray source and for the fusion capsule so as to guarantee the required optical properties of the high-temperature plasma produced. These properties should ensure the maximum X-ray yield. The optical properties of the plasma produced from the fusion capsule should in turn ensure the absorption of the incident X radiation over its entire spectral range.

The optical properties of the plasma in different ranges of its parameters are calculated based on such theoretical plasma models as the Thomas–Fermi (TF) model [1], the Hartree–Fock–Slater (HFS) model [2, 3], the detail configuration accounting (DCA) method [4], and the ion model (IM) [5]. The applicability ranges of these models, as well as the accuracy of the results obtained, were analyzed by Orlov and Fortov [6].

In studying the optical properties of a high-temperature plasma, it was found that the emissive properties of plasmas can be substantially changed by adding certain amounts of impurities of different chemical elements to the main target material. More recently, it was realized that such additions can also be utilized to increase the functional efficiency of materials used in the X-ray-based lines of ICF. Thus, the radiation yield from hohlraums made of a mixture of gold and gadolinium is significantly higher than that from hohlraums with a purely gold wall [7].

At the present stage of research, one of the problems is to choose the composition of the material so as to provide its optimal functional efficiency in using it for one or another element of a fusion target. In order to solve this problem, a method was developed based on the IM of the plasma [5] and a highly productive com-

puter code was devised [8]. In [8], it was also proposed to use a number of composite materials whose absorption coefficients for radiation in different spectral ranges are high enough to satisfy the requirements for the absorbers of X radiation in fusion capsules of indirect compression targets. The method for choosing and calculating the composition of materials for radiative plasma targets that was proposed and approved in [8] is used in the present study to optimize the composition of materials for X-ray sources. We determine the material's composition for a target-converter of laser light into X radiation and show that the energy conversion efficiency of this material is higher than that of the composite material proposed by Orzechowski *et al.* [7]. We also carry out a comparative analysis of the energy conversion efficiencies of a number of composite materials of fine wires that are used as loads in X- and Z-pinches. The analysis is performed in the optically thick and optically thin plasma approximations, in which the emissive plasma properties are determined, respectively, by the Rosseland, l_R, and Planck, l_P, mean free paths. We also present the results of numerical calculations of the Rosseland and Planck mean free paths in the plasma of the materials under investigation.

2. THEORETICAL APPROACH

The main requirement for an X-ray source capable of ensuring the compression of ICF targets is that the radiation energy yield should be as high as possible. Consequently, the emitting plasma should be optically thick. However, in some cases (primarily, those associated with diagnostic applications), it is necessary to solve the problem of achieving the maximum yield of radiation from an optically thin plasma. This problem arises, e.g., in creating a point source for X-pinch-based X-ray radiography. In both cases, the spontaneous radiation yield increases as the Rosseland (in an optically thick plasma) or Planck (in an optically thin plasma) radiation mean free path decreases in comparison to the length of the emitting plasma.

Let us consider the main properties of the spontaneous radiation yield from optically thick and optically thin plasmas.

2.1. Optically Thick Plasma

It is well known that the global parameters of the plasma are related to its atomic composition. Let a plasma consist of atoms and ions of a chemical element with the nuclear charge Z and atomic weight $\tilde{A}$ and let its temperature and density be Θ and $\tilde{\rho}$ (in g/cm^3), respectively. We are to analyze the optical properties of a plasma whose length L is much greater than the Rosseland mean free path l_R, $L \gg l_R$, in the case in which the energy is transported by a radiatively driven heat-conduction wave against an immobile plasma back-

ground. For a semi-infinite plasma in one-dimensional geometry (when the x coordinate runs through values from zero to plus infinity), the time-independent heat-conduction equation has the form

$$\frac{d}{dx}\left(k\frac{d\Theta}{dx}\right) = 0. \tag{1}$$

The thermal conductivity is given by the formula $k = \frac{4}{3}acl_R\Theta^3$, where $a = \frac{1}{15}\frac{\pi^2 k_B^4}{\hbar^3 c^3}$, k_B and $\hbar$ are Boltzmann's and Planck's constants, and c is the speed of light. The Rosseland mean free path is described by the expression

$$l_R = \frac{15}{4\pi^4}\int_0^\infty l_u \frac{u^4\exp(-u)}{(1-\exp(-u))^2}du, \tag{2}$$

where $u = \hbar\omega/\Theta$, with $\hbar\omega$ being the energy of an X-ray photon. Hereafter, we use the atomic system of units in which Planck's constant and the charge and mass of an electron are equal to unity, $\hbar = 1$, $e = 1$, and $m = 1$; in this case, the units of length, time, and energy are equal, respectively, to $\hbar^2/(me^2)$, $\hbar^3/(me^4)$, and $me^4/\hbar^2$. The function l_u can be written in the form $l_u = 1/K(\omega)$, where

$$K(\omega) = \tilde{n}\sum_j W_j\sigma^j(\omega), \tag{3}$$

and $\tilde{n}$ is the number of atomic nuclei per cubic centimeter. We are describing the plasma in terms of the Gibbs statistics. As subsystems for this statistical approach, we can adopt spherical atomic cells of radius r_0, with a nucleus at the center. The subsystems, numbered by the index j, differ from each other by the sets of occupation numbers of the bound (discrete) electronic states, $\{N_\alpha^j\}$, where α is a double subscript in which the first index is the principal quantum number n and the second is the orbital quantum number l. Each subsystem also contains unbound (continuum) electrons. The states of subsystems are regarded as the states of plasma atoms and ions. In expression (3), the notation W_j is used for the density of the atoms and ions having the electron configuration $\{N_\alpha^j\}$. The value of W_j is determined by the Gibbs distribution. The total cross section for photon absorption, $\sigma^j(\omega)$, is determined by the formula

$$\sigma^j(\omega) = \sigma_{bb}^j(\omega) + \sigma_{bf}^j(\omega) + \sigma_{ff}^j(\omega) \tag{4}$$

as the sum of the cross sections for absorption in spectral lines ($\sigma_{bb}^j(\omega)$), for photoabsorption ($\sigma_{bf}^j(\omega)$), and for bremsstrahlung absorption ($\sigma_{ff}^j(\omega)$). The processes of scattering and stimulated emission also can be incorporated into formula (4). For a plasma containing atoms

and ions of different chemical elements, the expression for $K(\omega)$ is more complicated [9].

When the energy flux density j at $x = 0$ is prescribed, the first boundary condition can be written as

$$j = -k\frac{d\Theta}{dx} \quad (x = 0). \tag{5}$$

The second boundary condition can be written at the point x_0 where the function $\Theta(x)$ is essentially zero,

$$\Theta(x_0) = 0. \tag{6}$$

Assuming that the temperature dependence of the Rosseland mean free path l_R has the form $l_R(\Theta) = A\Theta^\alpha$, we obtain $k = C\Theta^{\alpha+3}$, with $C = \frac{4}{3}acA$, and arrive at the following solution to heat-conduction equation (1):

$$\Theta^{\alpha+4}(x) = \Theta_0^{\alpha+4} - J\frac{\alpha+4}{C}x, \tag{7}$$

where $\Theta_0 = \Theta(0)$ and $\Theta_0^{\alpha+4} = J\frac{\alpha+4}{C}x_0$.

It is obvious that the plasma emissivity $B(\Theta_0) = a\Theta_0^4$ increases with decreasing l_R:

$$B(\Theta)|_{x=0} \propto \frac{1}{l_R}. \tag{8}$$

This relationship is valid when the energy lost in hydrodynamic motion is insignificant, as is the case, e.g., with the interaction of a short (picosecond) laser pulse with solid matter of normal density or the interaction of a nanosecond laser pulse with matter of low density (tens and hundreds of times less than the normal density of metals [10]).

In order to determine the operation efficiency of an indirect ICF target-converter based on the interaction of nanosecond laser pulses with solid matter of normal density, Orzechowski *et al.* [7] carried out numerical hydrodynamic simulations of the emitting plasma of the hohlraum wall. Based on the results obtained, they derived an approximate expression, according to which the spontaneous radiation yield from a hohlraum increases in inverse proportion to the square root of the Rosseland opacity k_R, which is defined by the relationship $k_R = 1/(l_R\tilde{\rho})$. This result agrees qualitatively with solution (8) to the above model problem, although, in [7], the rate of increase in the spontaneous radiation yield with decreasing mean free path is somewhat slower because the energy loss due to plasma motion was taken into account. What is important, however, is that both these estimates imply that the role of the criterion of efficiency is played by the value of the ratio between the Rosseland mean free paths in the original material and in a candidate composite material that is anticipated to be more efficient.

2.2. Optically Thin Plasma

The emissivity of an optically thin plasma is described by introducing another type of the photon mean free path. Let a one-dimensional plane plasma slab have the thickness L, and let $0 \le x \le L$. In the absence of external sources, the energy flux j^+ coming out of the slab through its right boundary is given by the formula [11]

$$j^+ \propto \frac{L}{l_P}ca\Theta^4, \tag{9}$$

where the Planck mean free path l_P is introduced through the relationship

$$\frac{1}{l_P} = \frac{15}{\pi^4}\int_0^\infty \frac{1}{l_u}\frac{u^3\exp(-u)}{1 - \exp(-u)}du. \tag{10}$$

The range of applicability of this approximation is represented by the inequality $L < l_P$.

We thus see that the plasma emissivity increases with decreasing Rosseland and Planck mean free paths in the cases of an optically thick and an optically thick plasma, respectively. Consequently, the criterion for comparing the efficiencies of materials for sources in which the emitted radiation is the spontaneous radiation from an optically thick and an optically thin plasma can naturally be formulated in terms of the ratios of, respectively, the Rosseland mean free paths and the Planck mean free paths.

The Rosseland, l_R, and Planck, l_P, mean free paths depend on the quantum-mechanical parameters of the entire ensemble of plasma atoms and ions. In order to calculate l_R and l_P, it is necessary to know the wave functions and energy levels of all the atoms and ions, in particular, all their excited states. An analysis of the recent theoretical models for calculating these parameters was carried out in [6] based on the density functional theory, and a brief review of the models was given in [12].

3. CALCULATED RESULTS AND DISCUSSION

3.1. Laser Radiation Converters

The first series of results refers to the composition of materials of the hohlraum wall. We have already mentioned that, in order to increase the radiation yield, Orzechowski *et al.* [7] proposed to use hohlraums with walls made of a 50 : 50 gold–gadolinium mixture instead of those with purely gold walls. Table 1 presents the results of calculating the Rosseland mean free paths for different materials on the basis of the IM of the plasma [5] by the method described in [8]. The calculations were carried out for the density $\tilde{\rho} = 1$ g/cm^3 and for several different values of the temperature T. The results included in the table refer to Au and to the composition Au : W : Gd : Pr : Ba : Sb = 25.7 : 23.1 : 18.1 : 10.0 : 10.4 : 12.7, which was determined by using a

Table 1. Rosseland mean free paths (in cm) calculated for different material compositions at a density of $\tilde{\rho} = 1 \text{ g/cm}^3$

T, eV	Au	Composition 1	$l_R^{\text{Au}}/l_R^{\text{comp1}}$	Au55.61/Gd44.39	$l_R^{\text{Au}}/l_R^{\text{comp2}}$	Au50/Gd50	$l_R^{\text{Au}}/l_R^{\text{comp3}}$
150	3.21×10^{-4}	1.29×10^{-4}	2.49	2.46×10^{-4}	1.30	2.47×10^{-4}	1.29
200	4.57×10^{-4}	1.53×10^{-4}	2.98	3.29×10^{-4}	1.39	3.29×10^{-4}	1.39
250	5.01×10^{-4}	1.61×10^{-4}	3.11	2.88×10^{-4}	1.74	2.89×10^{-4}	1.73
300	5.75×10^{-4}	1.87×10^{-4}	3.07	3.76×10^{-4}	1.53	3.89×10^{-4}	1.48
350	6.35×10^{-4}	1.92×10^{-4}	3.31	4.25×10^{-4}	1.49	4.37×10^{-4}	1.45

more elaborate method than that in [8]. Mathematically, this method ensures that the relevant iteration scheme converges for essentially all physical conditions. In Table 1, this composite material is denoted as composition 1. The percentages in the expression for the composition indicate the mass densities of the chemical elements. Table 1 also presents the results for two compositions of Au and Gd. The reason is that the notation 50 : 50 can be used in different senses. When there are equal numbers of Au and Gd atoms in a unit volume, this notation refers to the composition Au : Gd = 55.61 : 44.39, which is denoted as composition 2. For equal mass densities of gold and gadolinium, the composition in question is Au : Gd = 50 : 50, which is denoted as composition 3. To avoid confusion, the results of calculations carried out for the last two compositions are also included in Table 1.

Note, first of all, that these numerical results agree well with those of [7]. For instance, the ratio $l_R^{\text{Au}}/l_R^{\text{AuGd}}$ obtained in [7] for a temperature of $T = 250$ eV is equal to 1.67. Our calculations gave the values $l_R^{\text{Au}}/l_R^{\text{comp2}} = 1.74$ and $l_R^{\text{Au}}/l_R^{\text{comp 3}} = 1.73$. Figures 1–3 show the spectral absorption coefficients $K(x)$ (in units of cm^2/g) calculated in the present paper as functions of $x = \hbar\omega/T$ for different material compositions and for a temperature of $T = 250$ eV and density of $\tilde{\rho} = 1$ g/cm^3. Figure 1 displays the spectral absorption coefficients calculated for Au and for composition 1. We can see that, within the energy range $x = 3.5$–8.5, the coefficient of spectral absorption in pure Au is low, whereas, for composition 1, this energy range is superimposed by the spectral lines of impurities. Figure 2 displays the spectral
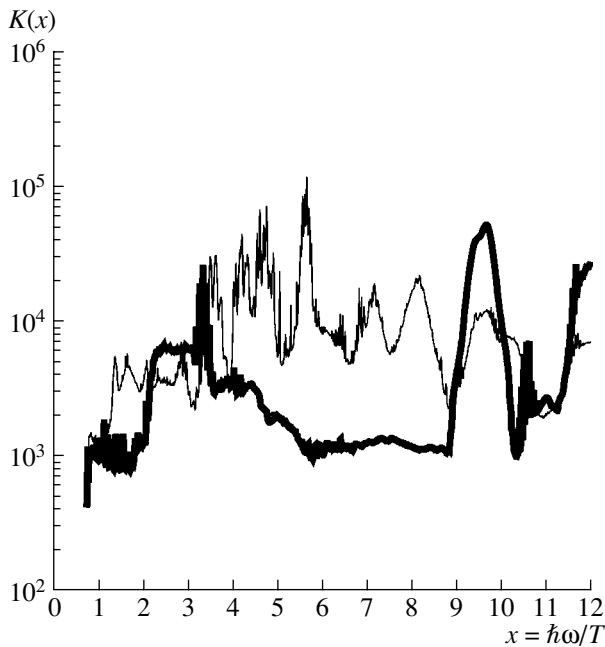

Fig. 1. Spectral absorption coefficients $K(x)$ (in cm^2/g) calculated for pure Au (heavy curve) and composition 1 (Au : W : Gd : Pr : Ba : Sb = 25.7 : 23.1 : 18.1 : 10.0 : 10.4 : 12.7) (light curve) at a density of $\tilde{\rho} = 1$ g/cm^3 and temperature of $T = 250$ eV.
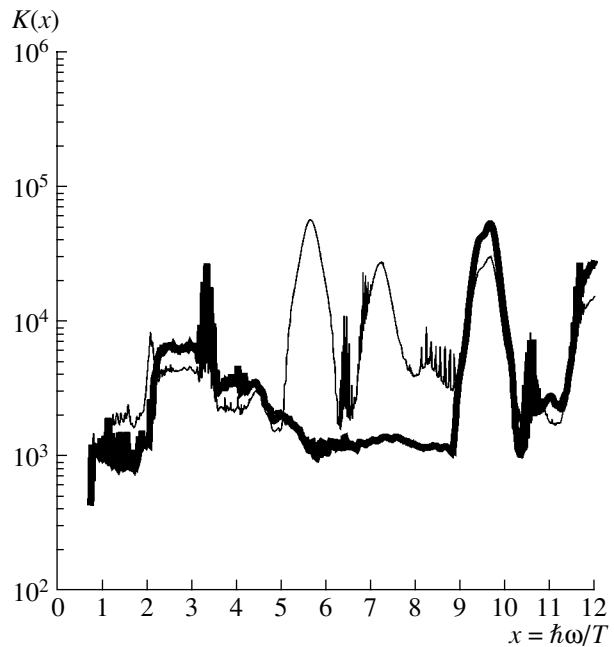

Fig. 2. Spectral absorption coefficients $K(x)$ (in cm^2/g) calculated for pure Au (heavy curve) and composition 2 (Au : Gd = 55.61 : 44.39) (light curve) at a density of $\tilde{\rho} = 1$ g/cm^3 and temperature of $T = 250$ eV.
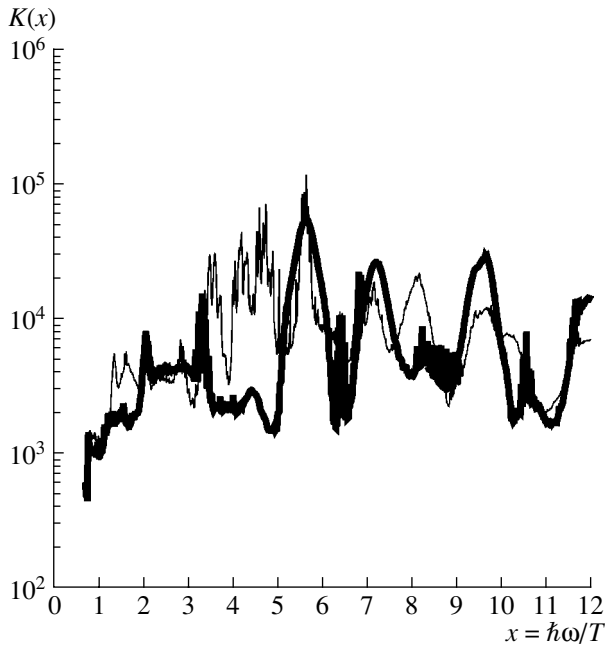
Fig. 3. Spectral absorption coefficients $K(x)$ (in cm^2/g) calculated for composition 2 (Au : Gd = 55.61 : 44.39) (heavy curve) and composition 1 (Au : W : Gd : Pr : Ba : Sb = 25.7 : 23.1 : 18.1 : 10.0 : 10.4 : 12.7) (light curve) at a density $\tilde{\rho}$ = 1 g/cm^3 and temperature of T = 250 eV.
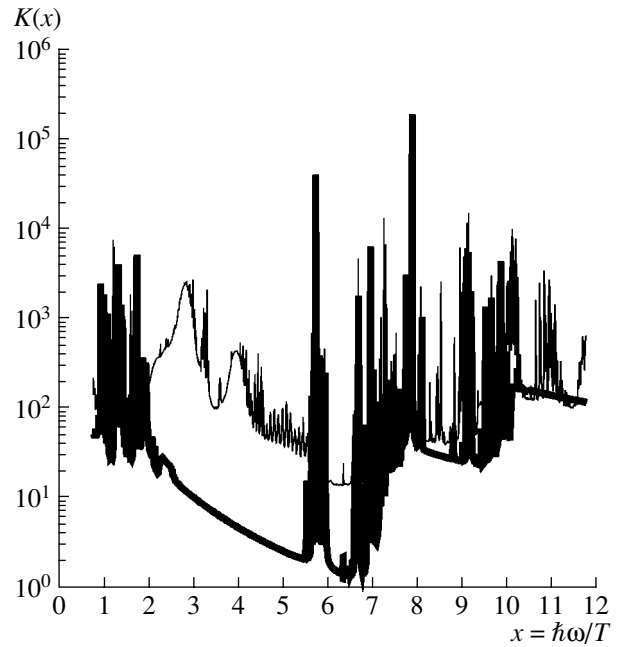
Fig. 4. Spectral absorption coefficients $K(x)$ (in cm^2/g) calculated for a NiCr composition (Ni : Cr = 80 : 20) (heavy curve) and for a composition known as Alloy 188 (Cr : Ni : Fe : Co : W = 21.72 : 22.92 : 2.24 : 39 : 13.93) (light curve) at a density of $\tilde{\rho}$ = 0.1 $\tilde{\rho}_{normal}$ and temperature of T = 1 keV.

absorption coefficients calculated for Au and for composition 2. This composition is also seen to ensure that the above energy range is superimposed by the impurity spectral lines, but to a markedly lesser extent than in the case of composition 1, as is illustrated by Fig. 3, which depicts the spectral absorption coefficients calculated for compositions 1 and 2. This circumstance explains why the ratio l_R^{Au}/l_R^{comp2} decreases at temperatures higher than and lower than T = 250 eV and why the ratio $l_R^{Au}/l_R^{comp\,1}$ also decreases in these two cases but to a much lesser extent. In our opinion, these effects can significantly influence the efficiency of the material. Since the temperature in the hohlraum changes in both time and space, the material should not only ensure the desired value of the ratio of the mean free paths but should also keep this value in the widest possible temperature range.

3.2. X- and Z-Pinch-Based Radiation Sources

Another group of results refers to the materials of the wires for X- and Z-pinches. Table 2 presents the Rosseland mean free paths calculated for a NiCr composition (Ni : Cr = 80 : 20) and a composition known as Alloy 188 (Cr : Ni : Fe : Co : W = 21.72 : 22.92 : 2.24 : 39 : 13.93), and Table 3 presents the Planck mean free paths calculated for the same compositions. The calculations were carried out for the temperature T = 1 keV and the normal density $\tilde{\rho} = \tilde{\rho}_{normal}$, as well as for the densities $\tilde{\rho}$ = 0.1 $\tilde{\rho}_{normal}$ and $\tilde{\rho}$ = 10 $\tilde{\rho}_{normal}$ at the same temperature. For NiCr, the normal density is equal to 8.49 g/cm^3, whereas for Alloy 188, it is equal to 9.05 g/cm^3.

Figure 4 shows the spectral absorption coefficients $K(x)$ (in units of cm^2/g) calculated in the present paper for the NiCr composition and for Alloy 188. The calcu-

Table 2. Rosseland mean free paths (in cm) calculated for NiCr and Alloy 188 at a temperature of 1 keV

Density	l_R^{NiCr}	$l_R^{Alloy\,188}$	$k = l_R^{NiCr}/l_R^{Alloy\,188}$
$0.1 \times \tilde{\rho}_{normal}$	2.54×10^{-1}	1.97×10^{-2}	12.89
$\tilde{\rho}_{normal}$	4.12×10^{-3}	1.37×10^{-3}	3.01
$10 \times \tilde{\rho}_{normal}$	1.11×10^{-4}	5.81×10^{-5}	1.91

Table 3. Planck mean free paths (in cm) calculated for NiCr and Alloy 188 at a temperature of 1 keV

Density	l_P^{NiCr}	$l_P^{\text{Alloy 188}}$	$k = l_P^{\text{NiCr}}/l_P^{\text{Alloy 188}}$
$0.1 \times \tilde{\rho}_{\text{normal}}$	1.16×10^{-2}	2.83×10^{-3}	4.06
$\tilde{\rho}_{\text{normal}}$	2.99×10^{-4}	2.16×10^{-4}	1.38
$10 \times \tilde{\rho}_{\text{normal}}$	3.29×10^{-5}	1.78×10^{-5}	1.84

lations were carried out for the temperature $T = 1$ keV and the density $\tilde{\rho} = 0.1\,\tilde{\rho}_{\text{normal}}$. In analogy with the previous case, the coefficient of spectral absorption in NiCr within the energy range $x = 2.0$–5.5 is relatively low. For Alloy 188, this energy range is covered by the spectral lines of impurities. Based on the results presented in Tables 2 and 3 and in Fig. 4, it can be concluded that the composition of Alloy 188 provides a higher efficiency for radiation yield than that of NiCr.

4. CONCLUSIONS

The results presented above demonstrate the possibility of modeling and optimizing the composition of materials for SXR sources in solving various problems in ICF research. Theoretical methods based on calculations of the optical properties of a plasma of complex ion composition can help to optimize the conditions of experimental investigations aimed at choosing materials for SXR sources and to make such experiments far less expensive.

ACKNOWLEDGMENTS

REFERENCES

1. R. Feynman, M. Metropolis, and E. Teller, Phys. Rev. **75**, 1561 (1949).

2. B. F. Rozsnyai, Phys. Rev. A **5**, 1137 (1972).

3. A. F. Nikiforov and V. B. Uvarov, Chislen. Metody Mekh. Splosh. Sredy **4**, 114 (1973).

4. D. Salzmann and A. Krumbein, Phys. Rev. A **32**, 3627 (1985).

5. N. Y. Orlov, Laser Part. Beams **15**, 627 (1997).

6. N. Yu. Orlov and V. E. Fortov, Fiz. Plazmy **27**, 45 (2001) [Plasma Phys. Rep. **27**, 44 (2001)].

7. T. J. Orzechowski, M. D. Rosen, H. N. Korblum, *et al.*, Phys. Rev. Lett. **77**, 3545 (1996).

8. N. Yu. Orlov, Fiz. Plazmy **25**, 700 (1999) [Plasma Phys. Rep. **25**, 642 (1999)].

9. T. R. Carson, D. F. Mayers, and D. W. N. Stibbs, Mon. Not. R. Astron. Soc. **140**, 483 (1968).

10. S. Yu. Gus'kov and Yu. A. Merkul'ev, Kvantovaya Élektron. **31**, 311 (2001).

11. Ya. B. Zel'dovich and Yu. P. Raizer, *Physics of Shock Waves and High-Temperature Hydrodynamic Phenomena* (Nauka, Moscow, 1966; Academic, New York, 1966, 1967), Vols. 1, 2.

12. N. Y. Orlov, Laser Part. Beams **20**, 547 (2002).

Translated by O.E. Khadin

**DUSTY
PLASMA**

Influence of the Trapped Ions on the Screening Effect and Frictional Force in a Dusty Plasma

S. A. Maĭorov

Prokhorov Institute of General Physics, Russian Academy of Sciences, ul. Vavilova 38, Moscow, 119991 Russia
Received May 20, 2004; in final form, September 11, 2004

Abstract—The problem of screening of the charge acquired by a dust grain in a two-temperature plasma is considered. The influence of the trapped ions on the screening effect and on the frictional force exerted on a dust grain by an ion flow is investigated. It is shown that the ions trapped by a grain radically reduce the frictional force in the ion flow because their distribution is determined by the temperature of the cold buffer gas. The mechanism for the onset of the reactive force that accelerates the grain in the direction opposite to that of the flow is explained. It is based on the momentum transfer from the flow of the ions that are additionally accelerated in the grain field to the atoms of the buffer gas. As a result, the momentum carried by the charge-exchange atoms out of the "ions + grain" system exceeds the momentum they have carried into the system; this gives rise to a reactive force directed opposite to the ion flow (the negative frictional force). The magnitude of the reactive force is estimated. © 2005 Pleiades Publishing, Inc.

1. INTRODUCTION

The problem of screening of the charge of a spherical body (a grain or a probe) in a nonmoving plasma has been studied for many years, beginning with the pioneering papers by Langmuir [1], who obtained results by using the Debye approximation for the distribution of plasma particles around an external charge. Further progress in solving this problem has been achieved with the use of the orbit motion limited (OML) approximation, which was first introduced by Bernshtein and Rabinovitz [2] for the case of monoenergetic ions and was then thoroughly investigated by Al'pert *et al.* [3] and Laframboise and Parker [4]. Recent progress in the experimental study of a dusty plasma (see, e.g., [5–7]) has necessitated a more detailed analysis of this problem, especially for the case of a moving plasma. It should be stressed that this analysis is aimed not at introducing slight refinements in the existing theory but rather at revealing the qualitative properties of the screening effect.

Under certain conditions, a negatively charged dust grain can trap a cloud of ions, which may have a substantial impact on the screening of the grain charge. In recent years, the question of the influence of the weak collisional relaxation of the ion component in a gas-discharge plasma on the screening of the grain charge has attracted much attention [8–10], although the possibility of the appearance of trapped ions was first pointed out by Bernshtein and Rabinovitz [2]. In this context, it is important to mention a book by Al'pert *et al.* [3], who investigated a wide scope of problems about the interaction of a plasma with macroparticles and, in particular, considered the problem of determining the density of the ions moving in finite orbits (using, as an example, the results of solving the problem of satellite motion in

a low-density plasma—a problem that was very important in the past).

Possible accumulation of trapped (finite-orbit) ions around a negatively charged grain was considered in many papers [4, 11–13]. Goree [12] was the first to recognize that the number of trapped ions (and, accordingly, their influence on the screening effect) is almost independent of the collision frequency. Consequently, even in an essentially collisionless plasma, very rare collisions can lead to the accumulation of a large number of trapped ions around a dust grain because the low rate of accumulation of trapped ions is compensated for by their long lifetime in finite orbits.

Based on the results of self-consistent particle-in-cell (PIC) simulations, Zobnin *et al.* [8] quantitatively investigated the influence of trapped ions on the magnitude of the grain charge. They found that, under conditions typical of most experiments on dusty plasmas, trapped ions play a significant role in grain charging; in this case, the OML approximation causes large errors. On the basis of correct calculations, they, however, came to the erroneous conclusion that the stronger the collisional relaxation, the weaker the screening effect.

In solving the equations of a self-consistent OML model, Lampe *et al.* [9] took into account trapped ions and obtained a linear integrodifferential equation for their balance. Their OML model, however, did not involve any parameter describing the intensity of collisional relaxation; in other words, they worked in the limit of infinitesimally weak relaxation. They numerically solved the OML equations by iteration in order to study the influence of trapped ions on the screening effect. They realized that even a weak relaxation leads to a qualitative change in the shape of the screened potential, so the OML approximation without allow-

ance for trapped ions fails to be valid. Their numerical simulations showed that the electron and ion distributions are close to those in the Debye approximation.

The influence of trapped ions on the screening effect in a self-consistent OML model was also studied by Bystrenko and Zagorodny [10], who revealed that, under conditions typical of dusty plasma experiments, trapped ions play an important role in the screening of the grain charge. They took trapped ions into account by introducing an explicit expression for their density into Poisson's equation and numerically solved the resulting set of equations by a shooting method. In the model used in that paper, the expression for the density of the trapped ions as a function of the electric potential contained a free parameter—the relative amount of these ions. As in [9], the authors of [10] noted that even a very weak collisional relaxation causes the grain screened potential to become close to the Debye potential.

In the present paper, which continues the studies reported in [14–17] (see also [18, 19]), results are presented from computer simulations that were carried out in order to study the screening of the electric charge of micron-size dust grains (macroparticles) in a dusty plasma. Under conditions typical of experiments with gas-discharge plasmas, the electron temperature is usually governed by the power supplied from an external source (microwave radiation, discharge current, photoionization, etc.), whereas the ions are in thermal equilibrium with the cold atoms of the buffer gas. This is why attention is focused on the case of two-temperature plasmas (including moving plasmas). Results are reported from numerical investigations of the screening of the dust grain charge with allowance for the charge fluctuations, the losses of charge carriers at the grain surface, and the stochastization of plasma ions due to their resonant charge exchange with the atoms of the buffer gas.

2. FORMULATION OF THE PROBLEM AND MAIN APPROXIMATIONS

Let us consider a plasma consisting of singly charged ions with a positive charge e and mass M and of electrons with charge $-e$ and mass m. Let there be an immobile point grain with a negative charge $-Z_{0e} < 0$ in the plasma. Note that the grains in a dusty plasma usually acquire a negative charge, but when the electron thermal emission is sufficiently intense, they can be charged positively. In its vicinity, a point charge $-Z_{0e}$ creates a spherically symmetric charged cloud of ions and electrons. The plasma density in the cloud depends only on the distance r from the point charge. Poisson's equation for the mean electric potential $\varphi(r)$ of an immobile point charge has the form

$$-\Delta\varphi = 4\pi e[n_i(r) - n_e(r) - Z_0\delta(r)]. \qquad (1)$$

In equilibrium, the density of the particles of species s around an immobile charge obeys a Boltzmann distribution,

$$n_s(r) = n_{s0}\exp(-z_s e\varphi/T_s), \qquad (2)$$

where n_{s0} is the volume-averaged density of the particles of species s; T_s is their temperature; and $z_s = -1$ and 1 for the electrons for the ions, respectively.

2.1. Debye Approximation

In the weak interaction approximation, $z_s e\varphi/T_s \ll 1$, we can expand the exponential function in distribution (2) in a series and, to within first-order corrections, obtain

$$n_i(r) = n_{i0}(1 - e\varphi/T_i) \equiv n_{i0}(1 - \psi),$$
$$\psi = e\varphi/T_i, \qquad (3a)$$

$$n_e(r) = n_{e0}(1 + e\varphi/T_e) \equiv n_{e0}(1 + \chi),$$
$$\chi = e\varphi/T_e. \qquad (3b)$$

In this case, the general solution to Poisson's equation (1) has the form

$$\varphi(r) = \frac{c_1}{r}\exp(-r/\lambda_D) + \frac{c_2}{r}\exp(r/\lambda_D). \qquad (4)$$

Assuming that the potential vanishes at infinity, we arrive at a solution in the form of the Yukawa potential:

$$\varphi(r) = -\frac{Z_0 e}{r}\exp(-r/\lambda_D), \qquad (5)$$

where the Debye radius $\lambda_D = (4\pi\sum_s z_s^2 e^2 N_{s0}/T_s)^{-1/2}$ defines the screening length for the Coulomb field of an immobile point charge.

When the charge $Q = -Z_a e$ is distributed uniformly over a sphere of radius a, the potential is given by the expressions

$$\varphi(r) = \varphi_{a\mathrm{Deb}} = -\frac{Z_a e}{a}\frac{1}{1 + a/\lambda_D} = \frac{\varphi_{a\mathrm{Coul}}}{1 + a/\lambda_D}, \qquad (6a)$$
$$\text{for} \quad r < a$$

$$\varphi(r) = \varphi_{\mathrm{Deb}} = -\frac{Z_a e}{r(1 + a/\lambda_D)}\exp\left(\frac{a - r}{\lambda_D}\right)$$
$$= \frac{a\varphi_a}{r}\exp\left(\frac{a - r}{\lambda_D}\right), \qquad (6b)$$
$$\text{for} \quad r > a.$$

For $r > a$, the potential of a uniformly charged sphere is equal to Debye potential (5) of a point charge $Z_0 = Z_a\dfrac{\exp(a/\lambda_D)}{1 + a/\lambda_D}$; for $r < a$, the potential is constant. Expression (6a) implies that the surface potential of a

small grain ($a \ll \lambda_D$) in the Debye model, $\varphi_{a\text{Deb}} \approx \varphi_{a\text{Coul}}(1 - a/\lambda_D)$, is lower in absolute value than the Coulomb potential $\varphi_{a\text{Coul}} = -Z_a e/a$.

In the problem about the charge distribution inside a sphere of radius R, with zero total charge, the boundary condition determining the values of the constants in solution (4) implies that the electric field at the sphere is zero. In this case, the solution to Eq. (1) differs from Debye potential (5). Far from the large sphere (of radius much greater than the Debye radius, $R \gg \lambda_D$), the potential is close to Debye potential (5), but it differs considerably from the latter near the sphere. This effect is especially pronounced in PIC simulations of a system of charges that is precisely neutral as a whole.

2.2. Orbit Motion Limited Approximation

The OML approximation is based on the following assumptions: (i) all processes are steady-state; (ii) there are no electron and ion collisions; (iii) all of the ions arrive from infinity, where their potential energy is zero and their total energy is positive; (iv) at an infinite distance from the grain, the electrons and ions obey Maxwellian velocity distributions; (v) the electrons and ions that strike the grain recombine at its surface; and (vi) the problem is spherically symmetric [1–4, 7, 10, 11]. Under these assumptions and under some additional assumptions about the rate at which the screened potential decreases with distance from an absorbing spherical grain, the electron and ion densities around the grain can be expressed as functions of the distance from it and of its potential. Specifically, the electron density is equal to [3, 9–11]

$$n_e(r)/n_{e0} = \exp\chi - \frac{1}{2}\exp\chi\, \text{erf}\sqrt{\Delta\chi}$$
$$+ \frac{1}{2}\sqrt{1-z^2}\,\text{erfc}\sqrt{\frac{\Delta\chi}{1-z^2}}\exp\frac{z^2\Delta\chi}{1-z^2}, \tag{7}$$

and the density of free ions is [3, 9–11]

$$n_{if}(r)/n_{i0} = \sqrt{-\psi/\pi}$$
$$+ \frac{1}{2}\exp(-\psi)\left\{\text{erfc}\sqrt{-\psi} + \sqrt{1-z^2}\exp\frac{\Delta\psi}{1-z^2}\right\}, \tag{8}$$

where $\Delta\chi = \chi(r) - \chi(a)$ and $z = a/r$. At large distances from the grain, the density of free ions and the potential are equal to

$$n_{if}(r)/n_{i0} = 1 - \psi(r) + \frac{z^2(2\psi(a)-1)}{4}, \tag{9}$$

$$\varphi(r) = -(2\varphi(a) - T_i/e)\frac{T_e}{T_e+T_i}\frac{a^2}{4r^2} \approx \frac{Z_a e a^2}{2r^2}. \tag{10}$$

At small distances, $r - a \ll \lambda_D$, the density of free ions behaves asymptotically [7, 14, 15] as

$$n_{if}(r)/n_{i0} \sim (-e\varphi/T_e)^{1/2}. \tag{11}$$

An expression for the density of trapped ions in the OML model in the limit of rare collisions was obtained by Bystrenko and Zagorodny [10]. In the model used here, however, the expression describing the dependence of this density on the grain potential contains the free parameter A, which has the meaning of the fraction of trapped ions:

$$n_{ib}(r)/n_{i0} = A\exp(-\psi)\sqrt{1-z^2}\exp\frac{-z^2\Delta\psi}{1-z^2}$$

$$\times \left[\text{erf}\sqrt{\frac{-\Delta_z\psi}{1-z^2}} - \frac{2}{\sqrt{\pi}}\sqrt{\frac{-\Delta_z\psi}{1-z^2}}\exp\frac{\Delta_z\psi}{1-z^2}\right]\theta(-\Delta_z\psi), \tag{12}$$

where $\Delta_z\psi(r) = \psi(r) - z^2\psi(a)$, and $z = a/r$.

In the OML model, the ion flux to a grain is given by the same expression as that derived in the simple Langmuir–Mott-Smith model,

$$J_i(a) = \pi a^2 n_{i0}\sqrt{\frac{8T_e}{\pi M}}(1 - e\varphi/T_i) \equiv J_{i0}[1 - \psi(a)], \tag{13}$$

and the electron flux to a grain is determined from the Boltzmann distribution,

$$J_e(a) = \pi a^2 n_{e0}\sqrt{\frac{8T_e}{\pi m}}\exp(e\varphi(a)/T_e)$$
$$\equiv J_{e0}\exp(\chi(a)). \tag{14}$$

In the present paper, the OML model was used to analyze the numerically calculated electron and ion distributions by substituting the calculated values of the grain potential into expressions (7), (8), and (10).

3. RESULTS FROM SIMULATIONS OF THE SCREENING EFFECT

The electron and ion densities, as well as the electric field distribution and potential, were determined by self-consistently solving the electron and ion dynamic equations together with Poisson's equation by the PIC method. The initial conditions corresponded to uniform particle distributions over the computation cell. The boundary conditions reflected the corresponding physical processes: the recombination of plasma particles at the grain surface and the thermostating conditions at the external boundary. The formulation of the problem was described in detail in [15–17], the only difference being the spherical shape of the computation cell in our simulations. This difference is responsible for the above-mentioned substantial discrepancy between the numerical results obtained for the region near the boundary of the computation cell and those calculated in the Debye model: in this region, the electric field

Table 1. Time-averaged parameters of grain charging, the surface potential $\varphi_{PIC}(a)$ normalized to the electron temperature, and the values of the surface potential in the Debye and Coulomb models for different ion mean free paths λ_{st}: $-Q/e$ is the grain charge in units of the electron charge; $J_{i,\,PIC}/J_{i0}$ is the numerically calculated ion flux onto the grain surface in units of the unperturbed ion flux $J_{i0} = \pi a^2 n_{i0}(8T_e/\pi M)^{1/2}$; and $J_{i,\,PIC}/J_{i,\,MS}$ is the ion flux in units of the flux $J_{i,\,MS} = J_{i0}[1 - \psi_{PIC}(a)]$, derived from the Mott-Smith model by using the numerically calculated surface potential $\varphi_{PIC}(a)$

Calculation version	1	2	3	4	5	6
λ_{st}, µm	∞	1000	500	200	100	50
$-Q/e$	4871	3393	2924	2337	1934	1766
J_i/J_{i0}	16.6	34.7	45.4	62.3	74.2	85.8
$J_i/J_{i,\,MS}$	0.118	0.372	0.553	0.955	1.379	1.741
$-\chi_{PIC}(a) = -e\varphi_{PIC}(a)/T_e$	3.413	2.324	1.997	1.593	1.319	1.211
$-\chi_{Deb}(a) = -e\varphi_{Deb}(a)/T_e$	3.331	2.320	1.999	1.597	1.322	1.206
$-\chi_{Coul}(a) = -e\varphi_{Coul}(a)/T_e$	3.508	2.444	2.106	1.683	1.392	1.271

should be exactly zero because of the precise electrical neutrality of the system. Zobnin *et al.* [8] carried out computer simulations for the problem stated in a similar manner, but they described the plasma electrons by a Boltzmann distribution in terms of an electron fluid model. It should be kept in mind, however, that this approach, which is in principle quite reasonable for a collisionless plasma, greatly underestimates the grain charge fluctuations.

Let us now discuss the results of simulations carried out for different plasma parameters and for grains of different radii. As an example, we consider the results from numerical calculations of the screening effect for a 2-µm-radius absorbing spherical grain in a nonmoving two-temperature plasma with $z = 1$, the ion temperature $T_i = 0.025$ eV, the electron temperature $T_e = 1$ eV, and the ion density $n_i = 10^9$ cm^{-3}. For these values of the plasma parameters, the total Debye radius is equal to

38 µm and there are 207 ions within the Debye sphere. In the simulation model, the number of ions was $N_i = 50000$ and the number of electrons was such that the total charge of the system, including the charge of the grains, was zero. The radius of the spherical computation cell depended on the number of particles and, for the simulations in question, was equal to 230 µm. The run time of the code corresponded to 34 µs in real time, or, equivalently, to about 35 Langmuir periods. The mean values of the parameters of the screening effect were calculated within a shorter run time: specifically, the initial stage during which the plasma relaxed from its original state to a steady state and which lasted about 20% of the total time was not simulated.

Table 1 presents the time-averaged parameters of the grain charging process calculated for different ion mean free paths λ_{st}. We can see that even rare collisions strongly affect the charging parameters. Figures 1–5
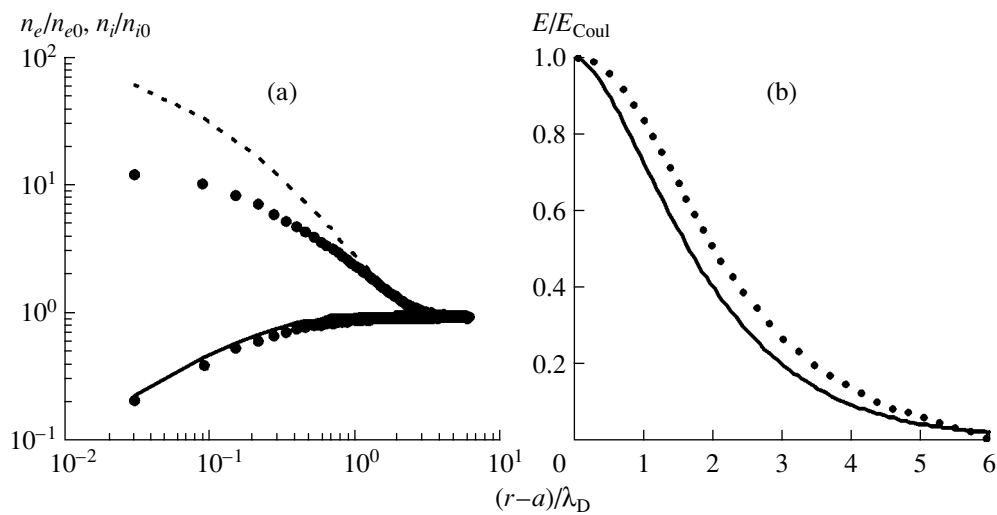

Fig. 1. (a) Ion and electron densities around an absorbing spherical grain: the solid and dashed curves are the radial profiles of the ion and electron densities in the Debye model, and the dots show the profiles obtained from computer simulations. (b) Radial profile of the field normalized to the Coulomb field of the grain charge: the dots show the profile obtained from computer simulations, and the solid curve is calculated from the Debye model.
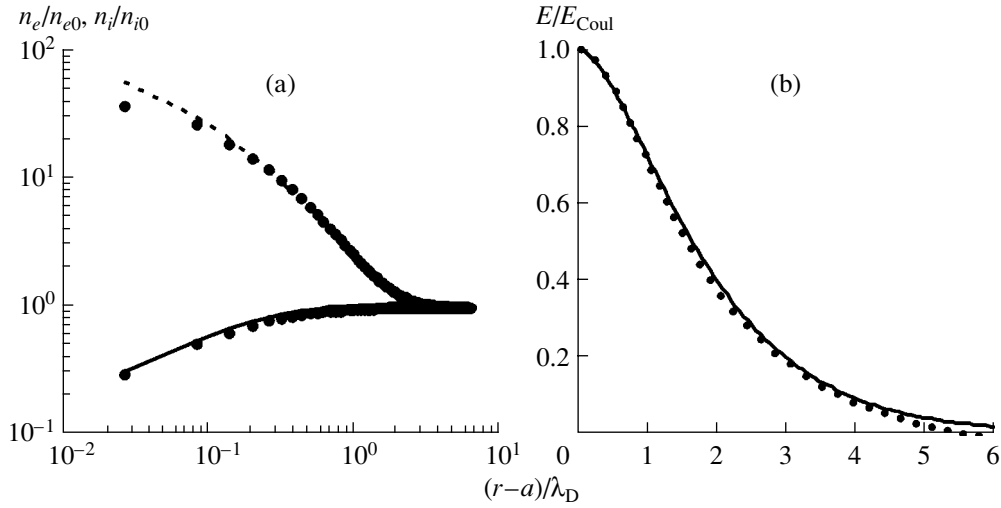
Fig. 2. Ion and electron densities and electric field strength around an absorbing spherical grain at $\lambda_{st} = 1000$ μm. The notation is the same as in Fig. 1.
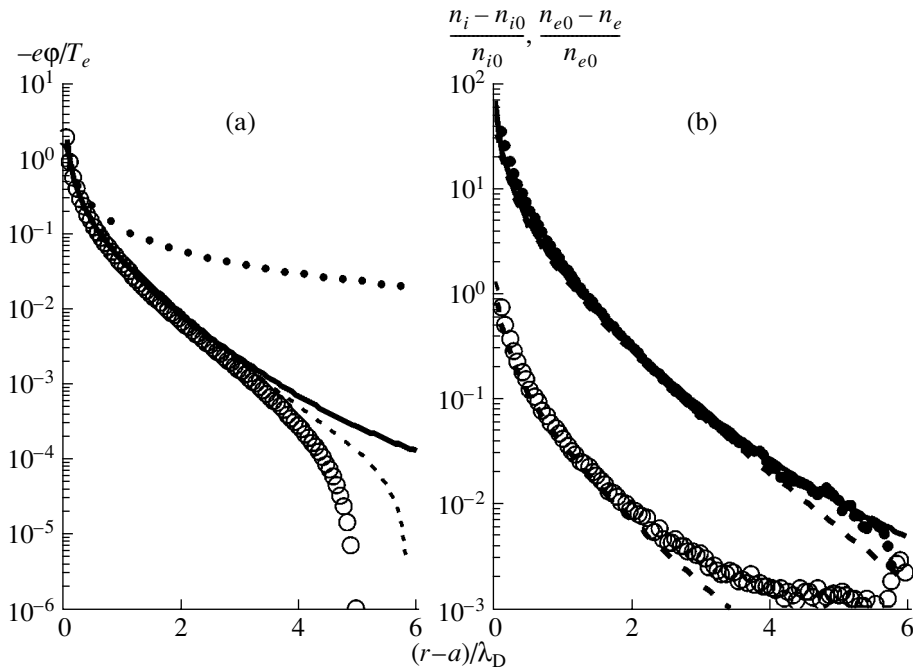

Fig. 3. (a) Radial profiles of the potential calculated for the ion mean free path $\lambda_{st} = 1000$ μm: the circles show the results of computer simulations, the dots show the Coulomb potential of a charged spherical grain, the solid curve is the potential profile calculated from formula (10) for large distances from the grain in the OML approximation, and the dashed curve is the Debye potential profile calculated from formula (4) with allowance for a perturbation from the plasma boundary. (b) Deviations of the ion and electron densities from their mean values around a spherical grain: the dots show the calculated deviations from the mean ion density, the circles show the calculated deviations (plotted with the opposite sign) from the mean electron density, the dashed curves are the deviations calculated from the Debye model, and the solid curve is the deviation calculated for large distances from the grain in the OML approximation.

show the ion and electron density distributions and potential distribution for calculation versions 1, 2, and 5 from Table 1.

The results presented in Table 1 and Figs. 1–5 indicate that collisional relaxation affects the screening parameters. The plasma evolves from a distribution cor-

responding to the collisionless OML model (calculation version 1) to a Debye distribution (in calculation versions 2–6). The last calculation version demonstrates a strong effect of collisions in the quasineutral plasma region. A detailed examination shows that, because of the weak collisional relaxation, the ion dis-
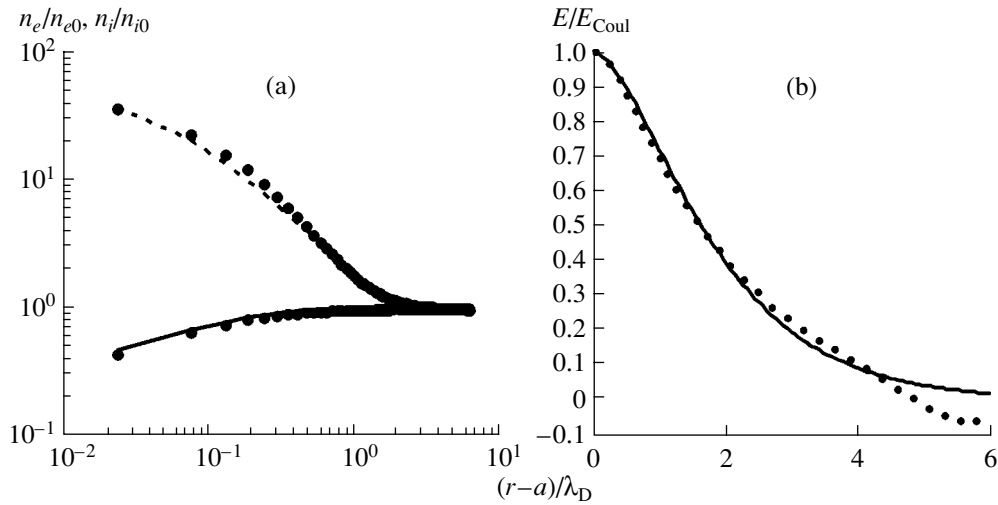
Fig. 4. Ion and electron densities and electric field strength around an absorbing spherical grain at $\lambda_{st} = 100\ \mu m$. The notation is the same as in Fig. 1.
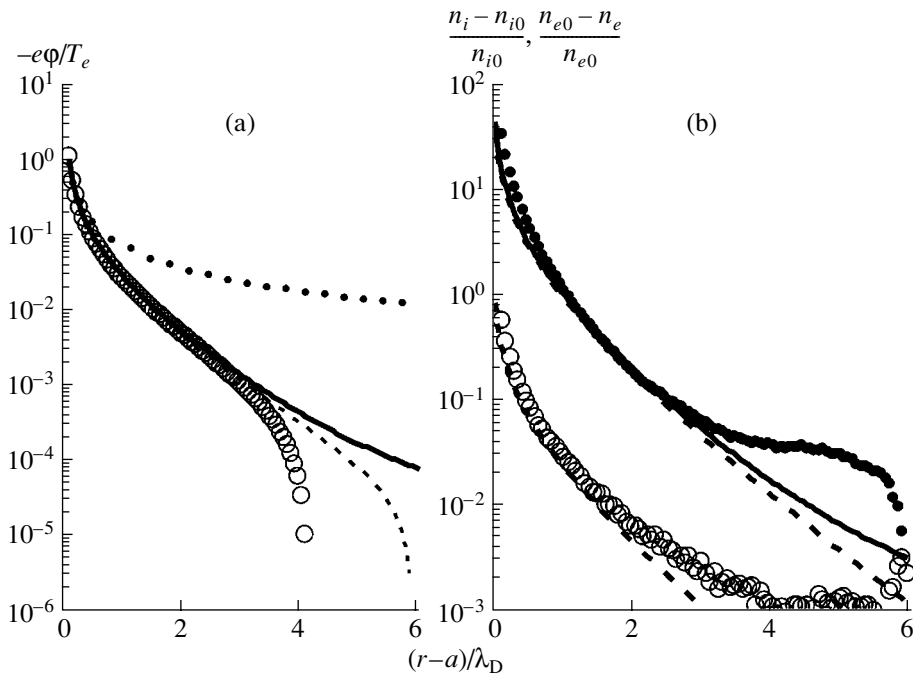

Fig. 5. (a) Radial profiles of the potential and (b) deviations of the ion and electron densities from their mean values around a spherical grain for $\lambda_{st} = 100\ \mu m$. The notation is the same as in Fig. 3.

tributions even near the grain surface essentially coincide with distribution (4) in the Debye approximation.

Based on the analysis of the numerical results, we can conclude that the collisional relaxation, as expected, enhances the screening effect rather than reduces it (as was mentioned in [8]). Due to a significant increase in the ion flux to the grain surface, the grain charge decreases in absolute value. As for the screening effect, it is enhanced even at small distances from the grain because of the appearance of a large

number of trapped ions. Even rare collisions cause the plasma to evolve from a distribution corresponding to the collisionless OML model to a Debye distribution.

4. FRICTIONAL FORCE

In the electrode sheath, the ions not only perform thermal motion but also are subject to directed motion with a velocity corresponding approximately to the electron thermal energy [20–22]. The structure of the

Table 2. Time-averaged parameters of grain charging at different ion temperatures for an ion mean free path of $L_{mfp} = 500$ μm: the grain charge, the ion flux onto the grain surface, and the grain potential

	$-Q/e$	J_i/J_{i0}	$-\chi_{PIC}(a)$	χ_{sDeb}
$T_i = 1$ eV	2805	48.8	1.902	1.996
$T_i = 0.025$ eV	2924	45.4	1.997	1.999

ion flow around dust grains having different shapes (a spherical and a needle-shaped grain) was considered in [23, 24] without allowance for the trapped ions. It would be of great interest to determine the ion drag force exerted on a grain by an ion flow. In the existing models, the frictional force is determined only on the basis of Coulomb interaction. Although there are several papers aimed at calculating the ion drag force [25–27], the final expression for it is still lacking, presumably because of the complexity of the problem of estimating the influence of ion focusing on the ion drag force. In such circumstances, different theoretical approaches can be verified by numerical simulations.

4.1. Influence of the Screening on the Frictional Force

Above, we have considered the influence of the trapped ions on the screening effect in a two-temperature plasma with a cold ion component. An analysis of this influence inevitably leads to the hypothesis that trapped ions also play an important role in a moving plasma. Although the kinetic energy of the ions in the flow is on the order of the electron temperature, the ions produced via resonant charge exchange are cold because they have the temperature of the buffer gas. Consequently, when trapped ions are present in large quantities, they can dominate the screening of the grain charges, thereby having an impact on the frictional force.

In order to verify this hypothesis, simulations were carried out for the same parameters as in calculation version 3 from Table 1, in particular, for the same ion and electron temperatures, $T_i = T_e = 1$ eV, but the gas temperature was set to be $T_a = 0.025$ eV and, accordingly, the temperature of the charge-exchange ions was set equal to the gas temperature. The results of these simulations are illustrated in Table 2, in which the second row replicates calculation version 3 from Table 1 for comparison. The data given in Table 2, along with the analysis of the ion and electron density distributions, show that, at short distances from the grain, the characteristic screening length is the ion Debye radius determined by the gas temperature.

The forces acting on a charged dust grain are mainly governed by the Coulomb interaction with the plasma particles. However, even rare resonant charge-exchange collisions of plasma ions with gas atoms can appreciably change the charge of the grain and strongly affect both its screening and the force with which the ion flow drags the grain. It is therefore of great interest to determine how trapped ions influence the frictional force exerted by the ion flow on the grain.

4.2. Molecular Dynamics Simulations

The influence of trapped ions on the screening of the grain charge in a moving plasma was simulated by the molecular dynamics (MD) method. The problem was treated in the same formulation and for the same parameter values as in [23]. The ion and electron densities and the distributions of the electric field and of its potential were calculated by solving the electron and ion dynamic equations together with Poisson's equation. The initial conditions corresponded to uniform particle distributions over the computation cell. The boundary conditions reflected the corresponding physical processes: the recombination of plasma particles at the grain surface and the thermostating conditions at the external boundary. A detailed formulation of the problem was given in [23], with the only difference being that the simulations were carried out with allowance for resonant charge-exchange collisions of ions with atoms and for the production of ions having the temperature of the cold gas.

A comparison of the results computed in [23] with those from analogous simulations carried out with allowance for ion–atom collisions showed that these collisions, as expected, produce a large number of trapped ions, so the calculated ion density distribution was qualitatively different in shape. In contrast to the distribution with a typical wake tail caused by ion focusing [23], the ion density distribution was found to be close to a spherically symmetric distribution.

The results of calculating the frictional force are even more impressive. It is found that, with the charge-exchange processes taken into account, the frictional force decreases by a factor of almost 100 and even changes its sign, i.e., becomes negative (the ion flow velocity is assumed to be positive). In the light of the results obtained in [25, 26], however, this change in the sign of the frictional force is in principle not surprising because, in those papers, the negative friction coefficient was predicted based on the analysis of kinetic models for a collisionless plasma. Since, in the simulations reported here, the frictional force was calculated statistically reliably, it is expedient to consider the charge exchange of the ions as a possible mechanism for the change in the sign of the frictional force.

4.3. Reactive Frictional Force

Let us consider the mechanism for the onset of a reactive force that accelerates a dust grain in the direction opposite to that of the ion flow (this corresponds to the negative frictional force). To do this, it is necessary to stress that the negative frictional force, acting to

increase the relative velocity of motion, should not be confused with the negative differential frictional force, which corresponds to a decrease in the absolute value of the frictional force with increasing velocity of motion but acts in the conventional direction of the friction force.

Under certain conditions, the specific dependence of the Coulomb frictional force can increase the mean energy of a dust grain in a potential well [28]. The possibility for the onset of a negative frictional force in the case of Coulomb collisions was discussed in [25, 26], and the ion drag force in the screened-potential region was considered in [27].

In the present paper, the force arising from charge-exchange collisions of the ions with atoms is analyzed for the first time. The mechanism for the onset of this force can be briefly described as follows. In collisions of the flow ions with the buffer gas atoms, the ions that have been additionally accelerated by the grain field transfer their momentum to the atoms in charge-exchange collisions. As a result, the momentum carried by the charge-exchange atoms out of the "ions + grain" system exceeds the momentum they have carried into the system, which gives rise to a reactive force directed opposite to the ion flow (the negative frictional force). Let us examine this situation in more detail in order to estimate the magnitude of the frictional force driven by resonant charge-exchange collisions of the ions with gas atoms.

4.4. Estimate of the Frictional Force Due to Charge Exchange of the Ions near a Grain

Let us consider a flow of ions with charge $e > 0$ and mass m that move with the velocity v_∞ from infinity along the x axis and are incident on an immobile, negatively charged, spherical dust grain with radius a and charge $Q = -eZ < 0$. We assume that the grain radius, the screening length, and the mean free path of an ion before it exchanges an electron with an atom satisfy the conditions

$$a \ll \lambda_{\mathrm{D}} \ll \lambda_{\mathrm{st}}, \tag{15}$$

and the electron, ion, and gas temperatures satisfy the conditions

$$T_e \gg T_i \approx T_a. \tag{16}$$

In experiments on the levitation of dust grains in the electrode sheath, the kinetic energy of the incident ions is equal in order of magnitude to the electron temperature; accordingly, we have $K_\infty = \frac{1}{2}mv_\infty^2 \gg T_a$. The ions produced from the gas atoms in charge-exchange collisions have a mean kinetic energy of $\frac{3}{2}T_a \ll K_\infty$ and obey a velocity distribution that is determined by the temperature of the atoms. Consequently, in each

charge-exchange collision, the total energy of the ion decreases on the average by an amount of $K_\infty - \frac{3}{2}T_a$, which is transferred to the atom.

The charge acquired by a dust grain is usually large enough to create a substantial Coulomb barrier for electrons. Under conditions (15) and (16), the grain surface potential is approximately equal to

$$e|\varphi(a)| \sim (2\text{–}4)T_e. \tag{17}$$

As a result, for $T_e \gg T_a$, an ion produced from an atom in a resonant charge-exchange collision within a certain region of volume V_0 around the grain turns out to be trapped in the grain's potential well. In this case, the most probable scenario of the ion evolution is that in which, after a series of subsequent collisions, the ion will reach the grain surface and will recombine on it.

The number of collisions that will occur in a small region of volume ΔV (around a point lying at a distance r from the grain center) within a time Δt is equal to $\Delta N_{\mathrm{st}}(r) = n_i v \Delta V \Delta t / \lambda_{\mathrm{st}}$, where n_i is the ion density, v is the ion velocity, and λ_{st} is the mean free path of an ion before a charge-exchange event. The mean momentum of the ions produced from the gas atoms in charge-exchange collisions is zero because the velocity distribution function of the atoms is isotropic (the velocity dependence of the charge-exchange cross section can be ignored since the atomic velocity is low). Consequently, the ions that have recombined on the surface of the grain will not change its momentum.

The momentum conservation law implies that the resulting change in the momentum of a grain is determined by the difference between the momentum of the ions at infinity and the momentum of the charge-exchange atoms: $\Delta p_x(r, \Delta V) = \Delta p_{1x}(r)\Delta N_{\mathrm{st}}$, where $\Delta p_{1x}(r) = m v_\infty - m v_x$ is the momentum transferred to the grain in one charge-exchange event. From the law of conservation of the total energy of an ion moving in the grain potential field, it follows that its kinetic energy is equal to $K(r) = K_\infty - e\varphi(r)$. In the approximation in which the ions move along straight trajectories in the field with the Coulomb potential $\varphi(r) = Q/r$, we obtain the following estimate for the mean momentum transferred to a grain in one collision event at any point in a region of volume V_0:

$$\Delta p_{1x} = m v_\infty - \sqrt{2mK(r)} \approx -\left|\frac{e\varphi(r)}{v_\infty}\right|. \tag{18}$$

The frictional force is defined as the change in the momentum in unit time; it is obtained by integrating over all collision events in a region of volume V_0:

$$F_x = \int_{V_0} \frac{n_i v}{\lambda_{\mathrm{st}}} \Delta p_{1x} dV. \tag{19}$$

We assume that the volume V_0 is that of a sphere of radius $r_0 \gg a$. We also assume that the potential within the sphere changes according to Coulomb's law $\varphi(r) = Q/r$ and the density and velocity variations are given by the formulas $n_i(r) \approx n_{i0}$ and $v(r) \approx v_\infty$. Under these assumptions, expression (19) becomes

$$F_x = \int_a^{r_0} \frac{n_{i0} v_\infty}{\lambda_{st}} \frac{eQ}{r v_\infty} 4\pi r^2 dr \approx -2\pi r_0^2 n_{i0} \frac{e^2 Z}{\lambda_{st}}. \qquad (20)$$

Setting the numerical coefficient in formula (17) equal to 3, we arrive at the estimate

$$F_x \approx -\pi r_0^2 n_{i0} T_e \frac{6a}{\lambda_{st}}. \qquad (21)$$

4.5. Properties of the Reactive Frictional Force

The main property of the reactive frictional force that follows from estimate (21) is its sign. The frictional force is directed opposite to the ion flow incident on a grain and acts to increase the grain velocity relative to the flow. Since this situation seems to be somewhat paradoxical, it is necessary to obtain a better insight into the onset of the negative frictional force.

Physically, the principles for the onset of such a force are equivalent to the principle of motion of a supersonic jetliner: the jet engine takes air from the incident airstream, heats the drawn-in air, accelerates it through a nozzle to a directed velocity higher than the stream speed, and then ejects it downstream. The fuel is needed only to heat the air, in contrast to a rocket, in which the fuel also plays the role of the working mass—an agent for momentum transfer. For a grain, the role of the energy source, or of the fuel, is played by the electrons that overcome the Coulomb barrier and charge the grain, thereby enabling it to collect and neutralize the slow charge-exchange ions at its surface.

Another interesting consequence of estimate (21) is that the frictional force is independent of the ion flow velocity. It should be kept in mind that there is still a weak dependence because the ion trajectories are bent near the grain, and more exact calculations are likely to yield a greater magnitude of the frictional force.

Estimate (21) also implies that the greatest contribution to the reactive force comes from the ions that fly at large distances from the grain—a situation analogous to that with the frictional force due to Coulomb collisions.

4.6. Comparison to Other Forces Acting on a Grain in a Dusty Plasma

In order to carry out a comparative analysis, it is necessary to determine the volume V_0. The simplest estimate can be derived in terms of the radial distance from the grain at which the potential energy of its field is on the order of the atom temperature. Setting $e|\varphi(a)| \sim 3T_e$, we obtain

$$r_0 = a \frac{e|\varphi(a)|}{T_a} \sim 3a \frac{T_e}{T_a}. \qquad (22)$$

It should be noted, however, that, when such factors as the screening effects, the non-Debye behavior of the potential of a grain at large distances from it, the presence of an external electric field, and ion focusing are taken into account, the problem of determining the volume V_0 becomes far more complicated. For instance, with allowance for a strong screening effect, we get $r_0 \sim \lambda_D$.

Substituting relationship (22) into estimate (21), we obtain

$$F_x \approx -\pi a^2 n_{i0} T_e \frac{60a}{\lambda_{st}} \left(\frac{T_e}{T_a}\right)^2 \propto a^3. \qquad (23)$$

For comparison, we also present the expression for the pressure force exerted on a grain by a flow of neutral particles (atoms) in inelastic interactions with it,

$$F_{flow} = 2\pi a^2 n K_\infty \propto a^2, \qquad (24)$$

and the expression for the single-direction gas-kinetic pressure force,

$$F_{GD} = \pi a^2 n T \propto a^2. \qquad (25)$$

For an absorbing spherical grain whose motion velocity v is much lower than the thermal velocity of the atoms and whose radius is smaller than their mean free path and for a Maxwellian velocity distribution of the atoms, the frictional force is equal to

$$F_{Maxw} = \frac{4\pi a^2 n v}{3} \sqrt{\frac{8T}{\pi m}} \propto a^2. \qquad (26)$$

The frictional force due to the scattering of an ion flow in the Coulomb potential $\varphi(r) = Q/r$ is given by the expression

$$F_{Coul} = n_{i0} \frac{2\pi e^4 Z^2}{K_\infty} \Lambda \sim 18\pi a^2 n_{i0} \frac{T_e^2}{K_\infty} \Lambda \propto a^2, \qquad (27)$$

and the gravitational force is

$$F_g = \frac{4\pi a^3}{3} \rho g \propto a^3. \qquad (28)$$

A comparison between formulas (23)–(28) shows that only two of the forces—reactive frictional force (23) and gravitational force (28)—are proportional to the grain volume, the remaining forces being proportional to the area of the grain surface. Consequently, in a gravitational field, the reactive force plays the role of a correction that changes the grain's weight. Under zero-gravity conditions, the reactive force may appear to be the strongest among the forces acting on a grain.

Near a vertical electrode, the reactive force can have a substantial impact on the dust.

5. CONCLUSIONS

The results of numerical simulations made it possible to check the existing theoretical models and to examine the kinetic processes that are responsible for the screening of a dust grain in a gas-discharge plasma in the case of rare collisions. Numerical and analytical analyses lead to the following conclusions:

(i) When even weak collisional relaxation is taken into account, the grain screened potential differs radically from that in the widely used OML model. The electric potential distributions calculated with allowance for resonant charge-exchange collisions are very close to those in the Debye model. The electron distribution is well described by the Boltzmann model with the Debye screening potential. The particle fluxes onto the grain surface depend strongly on the frequency of ion–atom collisions (i.e., on the gas pressure); accordingly, the grain charge cannot be correctly determined from the Mott-Smith model.

(ii) The distribution of the screening charge around a dust grain in an ion flow is largely governed by the temperature of the cold buffer gas. Consequently, under such conditions, the characteristic screening length scale is equal to the ion Debye radius determined by the gas temperature. The ions trapped by a grain in an ion flow radically reduce the frictional force in comparison to that predicted by the commonly accepted theory.

(iii) A dust grain in an ion flow is subject to a reactive force that is directed opposite to the flow and results from resonant charge exchange of the ions with buffer gas atoms near the grain. The reactive force has the meaning of the negative frictional force, which is directed opposite to the flow and tries to accelerate the grain. Estimates of the magnitude of this force show that it is proportional to the grain volume and to the rate of resonant charge exchange of the ions with buffer gas atoms, while being independent of the flow velocity.

ACKNOWLEDGMENTS

REFERENCES

1. H. Mott-Smith, Jr. and I. Langmuir, Phys. Rev. **28**, 27 (1926).
2. I. B. Bernshtein and I. N. Rabinovitz, Phys. Fluids **2**, 112 (1959).
3. Ya. L. Al'pert, A. V. Gurevich, and L. P. Pitaevsky, *Space Physics with Artificial Sattelites* (Nauka, Moscow, 1964; Consultants Bureau, New York, 1965).
4. J. G. Laframboise and L. W. Parker, Phys. Fluids **16**, 629 (1973).
5. H. Tomas and G. E. Morfill, Nature **379**, 806 (1996).
6. V. N. Tsytovich, Usp. Fiz. Nauk **167**, 57 (1997) [Phys. Usp. **40**, 53 (1997)].
7. M. Lampe, G. Jouce, G. Ganduli, and V. Gavrishchaka, Phys. Plasmas **7**, 3851 (2000).
8. A. V. Zobnin, A. P. Nefedov, V. A. Sinel'shchikov, and V. E. Fortov, Zh. Éksp. Teor. Fiz. **118**, 554 (2000) [JETP **91**, 483 (2000)].
9. M. Lampe, V. Gavrishchaka, G. Ganduli, and G. Jouce, Phys. Rev. Lett. **86**, 5278 (2001).
10. T. Bystrenko and A. Zagorodny, Phys. Lett. A **299**, 383 (2002).
11. J. E. Daugherty, R. K. Porteous, M. D. Kilgore, and D. B. Graves, J. Appl. Phys. **72**, 3934 (1992).
12. J. Goree, Phys. Rev. Lett. **69**, 277 (1992).
13. V. A. Shveĭgert, I. V. Shveĭgert, V. M. Bedanov, *et al.*, Zh. Éksp. Teor. Fiz. **115**, 877 (1999) [JETP **88**, 482 (1999)].
14. S. A. Maĭorov, Fiz. Plazmy **26**, 669 (2000) [Plasma Phys. Rep. **26**, 628 (2000)].
15. S. A. Maĭorov, Teplofiz. Vys. Temp. **39**, 858 (2001).
16. S. A. Maiorov, S. V. Vladimirov, and N. F. Kramer, Fiz. Plazmy **28**, 1025 (2002) [Plasma Phys. Rep. **28**, 946 (2002)].
17. S. V. Vladimirov and S. A. Maĭorov, Kratk. Soobshch. Fiz., No. 2, 30 (2002).
18. S. A. Maiorov and S. V. Vladimirov, in *Proceedings of the 29th EPS Conference on Plasma Physics and Controlled Fusion, Montreux, 2002*, p. 47.
19. S. A. Maĭorov, in *Proceedings of the 31st Zvenigorod Conference on Plasma Physics and Controlled Fusion, Zvenigorod, 2002*, p. 20.
20. A. M. Ignatov, Fiz. Plazmy **28**, 919 (2002) [Plasma Phys. Rep. **28**, 847 (2002)].
21. A. F. Pal', D. V. Sivokhin, A. N. Starostin, *et al.*, Fiz. Plazmy **28**, 32 (2002) [Plasma Phys. Rep. **28**, 847 (2002)].
22. A. Melzer, V. A. Schweigert, and A. Piel, Phys. Rev. Lett. **83**, 3194 (1999).
23. S. A. Maiorov, S. V. Vladimirov, and N. F. Cramer, Phys. Rev. E **63**, 017401 (2001).
24. S. A. Maĭorov, Fiz. Plazmy **23** 821 (2004) [Plasma Phys. Rep. **23**, 766 (2004)].
25. S. A. Trigger and A. G. Zagorodny, Contrib. Plasma Phys., Nos. 5–6, 381 (2003).
26. S. A. Trigger, Phys. Rev. E **67**, 046403 (2003).
27. S. A. Khrapak, A. V. Ivlev, G. E. Morfil, and S. K. Zhdanov, Phys. Rev. Lett. **90**, 225002 (2003).
28. S. A. Maĭorov, Kr. Soobshch. Fiz., No. 11, 3 (2002).
29. G. Ecker, *Theory of Fully Ionized Plasma* (McGraw-Hill, New York, 1972; Mir, Moscow, 1974).

Translated by O.E. Khadin

Calculation of the Shock Hugoniot of Deuterium at Pressures above 1 Mbar by the Path-Integral Monte Carlo Method

V. S. Filinov*, P. R. Levashov*, M. Bonitz**, and V. E. Fortov*

**Institute for High Energy Densities, Associated Institute for High Temperatures, Russian Academy of Sciences,
Izhorskaya ul. 13/19, Moscow, 125412 Russia*
**Institute of Theoretical Physics and Astrophysics, University of Kiel, Kiel, Germany
Received May 11, 2004; in final form, August 16, 2004

Abstract—The shock Hugoniot of deuterium at pressures above 1 Mbar is calculated by the path-integral Monte Carlo method without introducing additional physical assumptions and approximations. The results obtained are compared to calculations by other authors, various theoretical models, and experimental data. © 2005 Pleiades Publishing, Inc.

The problem of the shock compressibility of deuterium has been attracting much attention since the publication of the experimental data obtained in the NOVA laser facility [1, 2]. Studies in this field are of fundamental importance because they provide information about the behavior of materials at extremely high pressures. It is also of interest to find out whether liquid deuterium under shock compression exhibits the same properties as other diatomic liquids (e.g., N_2 and O_2) or its compressibility is determined by more complicated effects [3]. Knowledge of thermodynamic properties of hydrogen and deuterium is also needed to solve various problems of astrophysics and controlled nuclear fusion.

Our paper presents the results of calculating the shock Hugoniot of deuterium at pressures above 1 Mbar by the path-integral Monte Carlo method. In this method, the density matrix and, consequently, the thermodynamic quantities are represented in the form of path integrals. The low-temperature density matrix, for which there are no small physical parameters, is represented as a product of a great number n of high-temperature density matrices. This allows one to introduce intermediate coordinates, so integration over trajectories reduces to integration over these intermediate coordinates by the classical Monte Carlo method [4]. Using perturbation theory, it is possible to find explicit expressions for high-temperature factors with an error that is inversely proportional to, at least, the square of the number of the high-temperature factors. The total error of the product of the high-temperature density matrices ε is inversely proportional to the number of such matrices and, therefore, $\varepsilon \longrightarrow 0$ as $n \longrightarrow \infty$. The error of the method can be estimated by comparing the results obtained for different n. Thus, in contrast to other methods for modeling degenerate nonideal systems at nonzero temperature, this method does not employ any additional physical assumptions and approximations. Since, in this case, the calculation

accuracy is known in advance, various physical phenomena can be examined from "first principles." Below, we present a more detailed description of the calculation procedure used in our study.

The path-integral Monte Carlo method [4] is based on the Feynman formulation of the quantum statistical mechanics in the form of path integrals. All of the thermodynamic characteristics of a two-component plasma of volume V are defined by a statistical sum Z, which, in the case of N_e negatively charged particles (electrons) and N_i positively charged particles (protons), can be written in the form

$$Z(N_e, N_i, V, \beta) = Q(N_e, N_i, \beta)/N_e!N_i!,$$

$$Q(N_e, N_i, V, \beta) = \sum_\sigma \int_V dq\, dr\, \rho(q, r, \sigma; \beta). \tag{1}$$

Here, $\beta = 1/k_B T$, k_B is the Boltzmann constant, T is the plasma temperature, $q \equiv \{\mathbf{q}_1, \mathbf{q}_2, \ldots, \mathbf{q}_{N_i}\}$ are the proton coordinates, $r \equiv \{\mathbf{r}_1, \ldots, \mathbf{r}_{N_e}\}$ are the electron coordinates, and $\sigma = \{\sigma_1, \ldots, \sigma_{N_i}; \sigma_1, \ldots, \sigma_{N_e}\}$ are the proton and electron spins. The expression for the density matrix ρ in Eqs. (1) can be written in the form of a path integral

$$\int_V dR^{(0)} \sum_\sigma \rho(R^{(0)}, \sigma; \beta) = \sum_P \sum_\sigma (-1)^{\kappa_P}$$

$$\times \int_V dR^{(0)} \ldots dR^{(n)} \rho^{(1)} \rho^{(2)} \ldots \rho^{(n)} S(\sigma, \hat{P}\sigma') \hat{P} \rho^{(n+1)}, \tag{2}$$

where $\rho^{(i)} = \rho(R^{(i-1)}, R^{(i)}; \Delta\beta) \equiv \langle R^{(i-1)} | e^{-\Delta\beta \hat{H}} | R^{(i)} \rangle$ are the density matrices at a temperature of $(n + 1)T$ or at an inverse temperature of $\Delta\beta \equiv \beta/(n + 1)$; $\hat{P}$ is the per-

mutation operator; κ_P is the permutation parity; S is the spin matrix; $\hat{H}$ is the Hamiltonian of the system $\hat{H} = \hat{K} + \hat{U}_C$, $\hat{K}$ being the kinetic energy; and $\hat{U}_C$ is the potential energy, which is the sum of the Coulomb interaction energy of electrons (e), protons (p), and protons and electrons (ep): $\hat{U}_C = \hat{U}_C^p + \hat{U}_C^e + \hat{U}_C^{ep}$. The particle coordinates are designated as follows: $R^{(i)} = (q_i, r_i)$, $i = 1, \ldots, n + 1$, with $R^{(0)} \equiv (q, r)$, $R^{(n+1)} \equiv R^{(0)}$, and $\sigma' = \sigma$. Thus, all the particles are represented by closed loops, which can be designated symbolically as $[R] \equiv [R^{(0)}; R^{(1)}; \ldots; R^{(n)}; R^{(n+1)}]$. The exchange effects for the Fermi statistics are taken into account by the permutation operator $\hat{P}$, which acts on the spatial and spin coordinates of all of the particles. The transformation of expression (2) to a form in which the sum over all permutations is replaced with a determinant of the exchange matrix $\psi_{ab}^{n,1}$ allows us to avoid the so-called "sign problem" [5] and to improve the accuracy of calculations at high degeneration parameters.

For each factor $\rho^{(i)}$ ($i = 1, \ldots, n + 1$) in formula (2), we may use an explicit expression for the asymptote of the density matrix in the limit of high temperatures. Each of these N-particle high-temperature density matrices, in turn, may be represented as a product of two-particle density matrices. For a two-particle density matrix at high temperatures, there is the analytic solution to the Bloch equation in the first order of the perturbation theory [6]:

$$\rho_{a,b}(\mathbf{r}_a, \mathbf{r}_a', \mathbf{r}_b, \mathbf{r}_b', \beta)$$

$$= \frac{m_a m_b}{(2\pi\hbar\beta)^3} \exp\left[-\frac{m_a}{2\hbar^2\beta}(\mathbf{r}_a - \mathbf{r}_a')^2\right]$$

$$\times \exp\left[-\frac{m_b}{2\hbar^2\beta}(\mathbf{r}_b - \mathbf{r}_b')\right]\exp[-\beta\Phi^{ab}],$$

where $\Phi^{ab}(\mathbf{r}_a, \mathbf{r}_a', \mathbf{r}_b, \mathbf{r}_b', \beta)$ can be approximated by the half-sum of diagonal pseudopotentials,

$$\Phi^{ab}(|\mathbf{r}_{ab}|, \Delta\beta)$$

$$= \frac{e_a e_b}{\lambda_{ab} x_{ab}}\{1 - \exp(-x_{ab}^2) + \sqrt{\pi}x_{ab}[1 - \mathrm{erf}(x_{ab})]. \quad (3)$$

Here, $x_{ab} = |\mathbf{r}_{ab}|/\lambda_{ab}$, $\mathrm{erf}(x) = 2/\sqrt{\pi}\int_0^x \exp(-t^2)\,dt$ is the error function, $\lambda_{ab}^2 = \hbar^2\beta/2\mu_{ab}$, e_a and e_b are the particle charges, m_a and m_b are the particle masses, and $\mu_{ab} = (m_a^{-1} + m_b^{-1})^{-1}$ is the reduced mass. The resulting accuracy depends on the number of factors $n + 1$ in the integrand in formula (2), on the temperature T, and on the degeneration parameter $\chi = \max(n_e\lambda_e^3, n_i\lambda_i^3)$: $\varepsilon \sim$

$(\beta Ry)^2\chi/(n + 1)$, where $n_e = n_i$ are the electron and proton densities and $\lambda_{e,i}^3 = 2\pi\hbar^2\beta/m_{e,i}$. In [7], it was shown that pseudopotential (3) agrees well with the exact quantum potential at temperatures of $T > 2 \times 10^5$ K. This means, in particular, that at a temperature of 10^4 K, it is quite sufficient to take $n = 20$. In this case, the calculation error will be no more than 5%.

All the thermodynamic functions are expressed through derivatives of the statistical sum Z. In particular, for the total energy and pressure, we have

$$E = -\beta(\partial \ln Z/\partial\beta)_V,$$

$$\beta P = (\partial \ln Q/\partial V)_\beta.$$

Multiple integrals in these expressions are computed by a standard Metropolice method in a cubic cell with the use of periodic boundary conditions [4].

The thermodynamic properties of hydrogen and deuterium plasmas were calculated for temperatures equal to or higher than 10^4 K over a wide range of densities. Unlike the previous version of the method developed in [4], our model allows for the exchange effects both in the main Monte Carlo cell and in its nearest periodical images. Such a procedure is necessary when the thermal electron wavelength is larger than the Monte Carlo cell. As the thermal electron wavelength increases, the exchange interaction is taken into account for the nearest 3^3, 5^3, etc., Monte Carlo cells. To minimize the computation time, we used perturbation theory. The accuracy of calculating the exchange effects was tested by comparing with analytic dependences for the pressure and energy of an ideal degenerate plasma.

Since the path-integral Monte Carlo method is formulated for protons and electrons, the formation of bound states may be identified only if we introduce a criterion as to whether several chosen electrons and protons can be regarded, e.g., as an atom or a molecule. Within the formalism adopted in our problem, it is rather difficult to formulate a rigorous criterion of this kind. It is possible, however, to demonstrate the existence of bound states by analyzing the pair distribution functions, as was done in [8, 9]. In particular, it was found that, at temperatures below 1 Ry (13.6 eV), the probability density of the electron location was maximum at the electron-to-proton distance equal to the Bohr radius a_B. Moreover, within a certain interval of temperatures and densities, a maximum in the probability density of the proton location appeared at an interproton distance of $1.4a_B$ (the distance between the protons in a hydrogen molecule). In the latter case, a peak corresponding to a bound electron state in a molecule appeared in the electron–electron pair distribution function. When the simulation parameters were varied (e.g., the temperature was increased), the peaks in the distribution functions disappeared. The pair distribution functions were calculated by averaging over a great

Thermodynamic properties and the shock Hugoniot of deuterium

T, K	$r_{s1} = 1.7$		$r_{s2} = 1.86$		$r_{s3} = 2$		ρ_H, g/cm³	P_H, Mbar
	P_1, Mbar	E_1, eV	P_2, Mbar	E_2, eV	P_3, Mbar	E_3, eV		
15625	2.27	−19.00	1.01	−9.69	−	−	0.854	1.113
31250	1.86	−9.95	−	−	1.34	−6.02	0.837	1.605
62500	−	−	3.14	−1.23	2.61	−0.18	0.810	3.067
1.25×10^5	−	−	7.96	17.27	6.22	17.07	0.740	7.008
2.5×10^5	−	−	15.97	48.22	12.38	46.85	0.720	13.305
5×10^5	−	−	32.62	112.73	26.45	114.57	0.708	27.973
10^6	−	−	67.66	245.99	54.40	246.45	0.698	56.722

number of equilibrium configurations; this proves the stability of the bound states arising in calculations. The thermodynamic properties calculated by the path-integral Monte Carlo method were compared to the results of calculations performed using other methods in their applicability regions. Most of these methods are based on the chemical model of plasma, in which the influence of atoms, molecules, and ions on the plasma properties is described in the explicit form. Good agreement between radically different methods (see [10–12]) also

P, Mbar

10^1

◇   *1*
△   *2*
■   *3*
◆   *4*
----   *5*
-·-·   *6*
- - -   *7*
—✳—   *8*
—○—   *9*
—□—   *10*
——   *11*
——   *12*

10^0

10^{-1}

0.4   0.6   0.8   1.0 ρ, g/cm³

Shock Hugoniot of deuterium. Experimental data: (*1*) [1, 2], (*2*) [15], (*3*) [16], and (*4*) [21]; calculations: (*5*) [17], (*6*) [18], (*7*) [14], (*8*) [19], (*9*) [20], (*10*) [22], (*11*) [25], and (*12*) this study.

indicates that the bound states are correctly taken into account by the model formulated above.

In the present study, the shock Hugoniot of deuterium was determined by calculating its thermodynamic properties by the path-integral Monte Carlo method. The pressure (P), the specific volume (V), and the specific internal energy of matter (E) behind the front of a shock wave are related to the initial state (P_0, V_0, E_0) by the Hugoniot equation,

$$H(V) = E - E_0 + \frac{1}{2}(V - V_0)(P + P_0) = 0. \quad (4)$$

Following [14], the initial parameters were chosen to be equal to the parameters corresponding to liquid deuterium under the following conditions: $P_0 = 0$, $1/V_0 = \rho_0 = 0.171$ g/cm³, and $E_0 = -15.886$ eV per atom. We then calculated the pressure P_i and internal energy E_i at a given temperature T (from 10^4 to 10^6 K) and at three different values of the specific volume V_i corresponding to $r_{si} = 1.7$, 1.86, and 2 ($i = 1, 2, 3$), where $r_s = \langle r \rangle / a_B$, with $\langle r \rangle = (3/4\pi n_e)^{1/3}$. The results of calculations are listed in the table. Substituting P_i, E_i, and V_i into Eq. (4), we determine the range of the specific volumes in which the function $H(V)$ changes its sign. The value of the specific volume at the shock Hugoniot was then calculated by the linear interpolation at the point where the function $H(V)$ is equal to zero. In the table, the pressure and internal energy are shown only for the specific volumes such that the shock Hugoniot passes between them at a given temperature. The last two columns show the density ρ_H and pressure P_H of deuterium at the shock Hugoniot.

The figure summarizes the data from different experimental, theoretical, and numerical studies on the shock compressibility of deuterium. Measurements performed in the NOVA facility, where a shock wave was generated by a laser pulse [1, 2], show that the deuterium density behind the shock front can increase by a factor of more than 6. However, at high pressures, the maximum compression ratio ρ/ρ_0 for an ideal one-atom gas cannot exceed 4; at the same time, the dissociation of deuterium in the shock wave occurs at pressures of
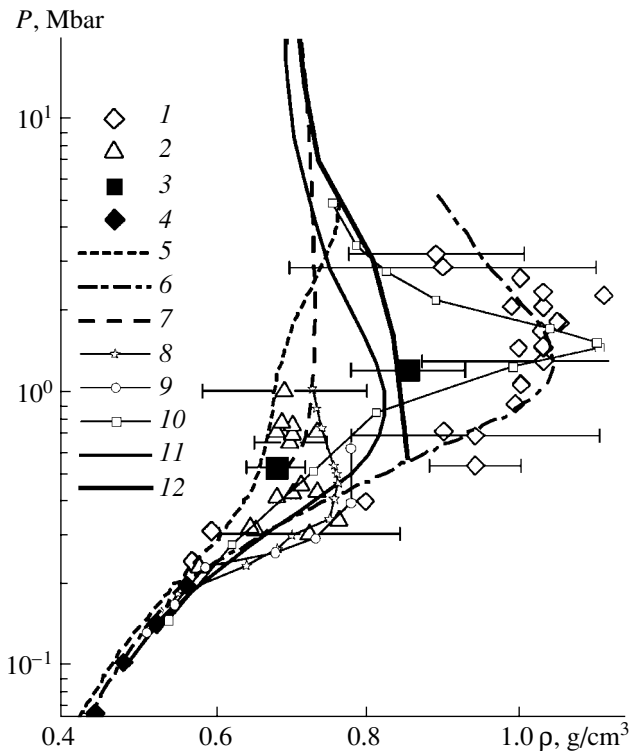
~0.5 Mbar [3]. For this reason, it was concluded in [3] that the data from [1, 2] cannot be considered reliable. Experiments with the acceleration of an aluminum foil by a magnetic field to velocities higher than 20 km/s [15] show a considerably lower compression ratio in comparison to [1, 2]. The results obtained in [1, 2] and [15] disagree within experimental errors. In contrast to [1, 2] and [15], where targets several hundred microns thick were used, in [16], the shock compressibility of solid deuterium was measured in a 4-mm-thick layer using a hemispherical explosive device. The experimental point obtained at a pressure of about 1 Mbar lies between the data from [1, 2] and [15].

Since 1997, many studies have been published in which attempts were made to calculate the shock Hugoniot of liquid deuterium by using different theoretical models. The well-known equation of state [17] ignores the effect of dissociation; therefore, the compression ratio behind a shock front turns out to be lower than that calculated by other methods. It is likely that the semi-empirical equation of state [18], in which the dissociation is taken into account by a simple linear-mixing model, overestimates the dissociation effect; for this reason, it agrees with the experimental data from [1, 2]. The use of the so-called *ab initio* methods does not clarify the situation, because almost all of these methods have their own drawbacks. In most of the papers devoted to calculating the shock Hugoniot of deuterium from the "first principles" (in particular, calculations by the restricted path-integral Monte Carlo method [14] and by the method of quantum molecular dynamics [19, 20]) agree with the experimental results of [15]. The shock Hugoniots of deuterium calculated in [19, 20] adequately describe measurements performed in a gas gun at relatively low pressures [21]. Calculations [22] performed by the method of molecular dynamics in which the electrons were regarded as antisymmetrized localized wave packets also agree with the data from [21], but, in contrast to [19, 20], show a considerably better agreement with the experiments [1, 2].

The shock Hugoniot of deuterium calculated in this work by the path-integral Monte Carlo method agrees well with that calculated in [14] at high pressures and arrives at a correct asymptote for the compression ratio in the limit of high pressures; however, at low pressures, it deviates from the curve obtained in [14] toward higher densities. The reason is that, in [14], a specific procedure for calculating the sum over all permutations in expression (2) was used. The authors of [14] took the sum over positive terms only and simultaneously reduced the integration region; thereby, the paths determined by the intermediate integration coordinates $R^{(i)}$, $i = 1, \ldots, n$ were forbidden from passing through the nodes of a certain specified density matrix. This procedure, which is not justified theoretically, introduces an additional repulsion into the system and evidently makes it less compressible. In [23], it was also shown that, using the approach proposed in [14] for calculating the density matrix, it is impossible to correctly derive analytical dependences for the pressure and energy of an ideal Fermi gas.

Thus, the shock Hugoniot calculated with allowance for bound states and degeneration effects is shifted toward higher densities in comparison to the curve calculated in [14], lies to the right of the data obtained in [15], and passes very close to the experimental point measured in [16]. At pressures below 1–2 Mbar, the effect of the phase transition revealed in [24] comes into play; therefore, a segment of the shock Hugoniot that lies below 1 Mbar is not quite reliable. It should be noted that the shock Hugoniot of hydrogen calculated in this study is closest to the curve calculated in [25] by the classical reaction ensemble Monte Carlo method. In this method, the effects of dissociation of deuterium molecules are taken into account most correctly; this allows one to achieve good agreement with the experimental data obtained at low temperatures and pressures [21], as well as with the experimental point obtained in [16], even if ionization is not taken into account.

To conclude, we note that the measurements of the shock compressibility of deuterium by three different methods [1, 2, 15, 16] predict different positions of the shock Hugoniot in the pressure–density diagram. Nevertheless, for all these cases, there are theoretical models that agree well with the corresponding experimental data. For this reason, the problem of the shock compressibility of deuterium requires more thorough investigation.

REFERENCES

1. L. B. Da Silva, P. Celliers, G. W. Collins, *et al.*, Phys. Rev. Lett. **78**, 483 (1997).

2. G. W. Collins, L. B. Da Silva, P. Celliers, *et al.*, Science **281**, 1178 (1998).

3. W. J. Nellis, Phys. Rev. Lett. **89**, 165 502 (2002).

4. V. M. Zamalin, G. E. Norman, and V. S. Filinov, *The Monte Carlo Method in Statistical Thermodynamics* (Nauka, Moscow, 1977) [in Russian].

5. *The Monte Carlo and Molecular Dynamics of Condensed Matter Systems*, Ed. by K. Binder and G. Ciccotti (SIF, Bologna, 1996).

6. W. Ebeling, H. J. Hoffmann, and G. Kelbg, Contrib. Plasma Phys. **7**, 233 (1967).

7. A. V. Filinov, M. Bonitz, and W. Ebeling, J. Phys. A **36**, 5957 (2003).

8. V. S. Filinov, M. Bonitz, and V. E. Fortov, Pis'ma Zh. Éksp. Teor. Fiz. **72**, 361 (2000) [JETP Lett. **72**, 245 (2000)].

9. V. S. Filinov, V. E. Fortov, M. Bonitz, and D. Kremp, Phys. Lett. A **274**, 228 (2000).

10. M. Bonitz, I. A. Mulenko, E. N. Oleĭnikova, *et al.*, Fiz. Plazmy **27**, 1085 (2001) [Plasma Phys. Rep. **27**, 1025 (2001)].

11. S. A. Trigger, W. Ebeling, V. S. Filinov, *et al.*, Zh. Éksp. Teor. Fiz. **123**, 527 (2003) [JETP **96**, 465 (2003)].

12. V. S. Filinov, M. Bonitz, P. R. Levashov, *et al.*, J. Phys. A **36**, 6069 (2003).

13. Ya. B. Zel'dovich and Yu. P. Raizer, *Physics of Shock Waves and High-Temperature Hydrodynamic Phenomena* (Academic, New York, 1966, 1967), Vols. 1, 2.

14. B. Militzer and D. M. Ceperley, Phys. Rev. Lett. **85**, 1890 (2000).

15. M. D. Knudson, D. L. Hanson, J. E. Bailey, *et al.*, Phys. Rev. Lett. **90**, 035 505 (2003).

16. S. I. Belov, G. V. Boriskov, and A. I. Bykov, in *Substances, Materials, and Constructions under Intense Dynamic Actions*, Ed. by A. L. Mikhaĭlova (VNIIÉF, Sarov, 2003), p. 100 [in Russian].

17. *SESAME: The Los Alamos National Laboratory Equation of State Database (LA-UR-92-3407)* (LANL, Los Alamos, 1992).

18. M. Ross, Phys. Rev. B **58**, 669 (1998).

19. M. P. Desjarlais, Phys. Rev. B **68**, 064 204 (2003).

20. S. A. Bonev, B. Militzer, and G. Galli, Phys. Rev. B **69**, 014 101 (2004).

21. W. J. Nellis, A. C. Mitchell, M. van Thiel, *et al.*, J. Chem. Phys. **79**, 1480 (1983).

22. M. Knaup, P. G. Reinhard, C. Toepferr, and G. Zwicknagel, J. Phys. A **36**, 6165 (2003).

23. V. S. Filinov, J. Phys. A **34**, 1665 (2001).

24. V. S. Filinov, V. E. Fortov, M. Bonitz, and R. R. Levashov, Pis'ma Zh. Éksp. Teor. Fiz. **74**, 422 (2001) [JETP Lett. **74**, 384 (2001)].

25. V. Bezkrovniy, M. Schlanges, D. Kremp, and W. D. Kraeft, Phys. Rev. E **69**, 061 204 (2004).

Translated by N.F. Larionova

Studies of the Optical Properties of a Nonequilibrium Plasma in the MKV-4 Facility

Yu. D. Bogunenko, A. V. Bessarab, G. A. Bondarenko, G. V. Dolgoleva, V. A. Zhmaïlo, A. G. Kravchenko, E. A. Novikova, A. V. Pinegin, V. A. Starodubtsev, and V. P. Statsenko

All-Russia Research Institute of Experimental Physics, Russian Federal Nuclear Center, Sarov, Nizhni Novgorod oblast, 607188 Russia

Received June 2, 2004; in final form, November 15, 2004

Abstract—Results are presented from experimental and theoretical studies of a glowing plasma object emerging behind a shock front that propagates through the background gas at a pressure of $p_0 = 6$ torr after laser irradiation of a hollow spherical target. The results of calculations are compared to the experimental results obtained in the MKV-4 device (a component of the Iskra-5 facility). © 2005 Pleiades Publishing, Inc.

1. INTRODUCTION

Experimental studies of the dynamics of shock waves (SWs) emerging in the atmosphere surrounding an evaporating laser target were described in [1, 2]. The main result of those studies was the determination of the r–t diagram of the SW front. Such experiments can, however, provide more extensive information. For example, in [3], the first experimental and simulation results were presented on the spatiotemporal characteristics of the plasma produced behind the shock front. Those results demonstrated the variety of intense kinetic and radiative transfer processes in this region. Moreover, it was shown that the character and scale of these processes can be controlled using different targets and varying the parameters of surrounding atmosphere.

In this study, which is a continuation of [3], we present experimental data on the glow and ionization behind an SW produced using a higher power laser pulse. The measurements were carried out with a more advanced technique than that used in [3]. We also performed simulations by the one-dimensional SND model [4], which incorporates gas-dynamics and radiative transfer processes.

2. EXPERIMENTAL SETUP AND RESULTS

The parameters of glowing plasma objects (GPOs) were studied experimentally in the MKV-4 device positioned in one of the channels of the Iskra-5 iodine laser facility [5]. MKV-4 is a 1.5-m-long 1-m-diameter cylindrical vacuum chamber with four windows for injecting laser beams (see Fig. 1). The device is equipped with a pumping-out and a gas-feed system and a number of optical diagnostics. GPOs were produced by irradiating a target from four sides. We used 4-mm-diameter hollow thin-walled spherical polyparaxylene $((C_8H_8)_n)$ targets with a mass of $\sim 10^{-4}$ g. Each target had four openings, through which laser radiation

was introduced. The targets were placed in air at a pressure of $p_0 \sim 6$ torr. The laser pulse energy and duration were $\sim 10^3$ J and ≈ 0.5 ns, respectively.

GPOs were studied by measuring the spectral and temporal characteristics of the GPO emission, as well as by taking their interferograms, streak camera images, and spectrograms.

(i) The spectral and temporal characteristics of the GPO emission were measured by a filtered detector. The detector was a system of coaxial photodetectors (*3*) operating in the spectral ranges of 0.4 (SDF7) and 0.7 μm (FÉK20). The system was precalibrated in order to perform absolute measurements of the GPO emission intensity.

(ii) The formation and development of a GPO were studied by the method of interference shadowgraphy. For backlighting, we used the second harmonics of an
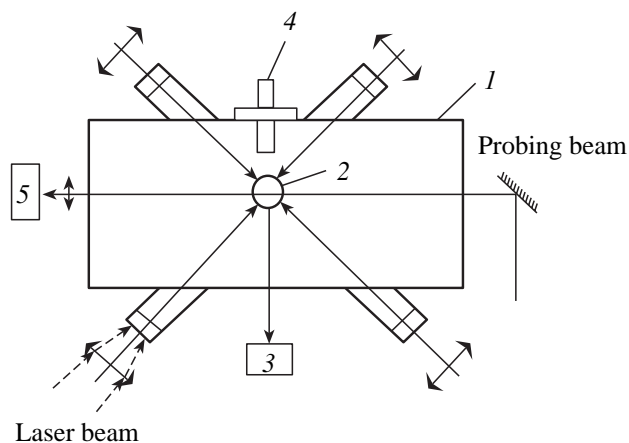

Fig. 1. Schematic of the experimental setup: (*1*) vacuum chamber, (*2*) target, (*3*) coaxial detectors of the GPO emission, (*4*) streak camera, and (*5*) interferometer.
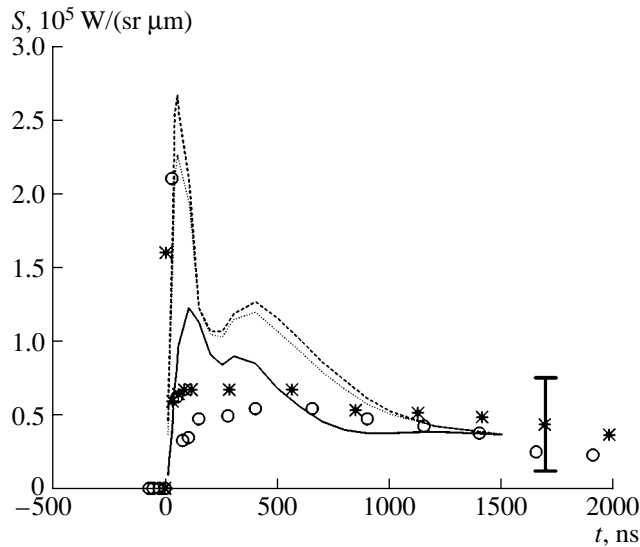
Fig. 2. Calculated time evolution of the emission intensity for the second ($E_v = 0.511$–1.41 eV; solid curve) and third ($E_v = 1.41$–2.71 eV; dashed curve) spectral groups. The dotted curve shows the linear interpolation between the second and third groups for $\lambda = 0.65$ μm. The symbols show the experimental data obtained with an FEK20 detector for $E = 520$ J (circles) and 735 J (asterisks).
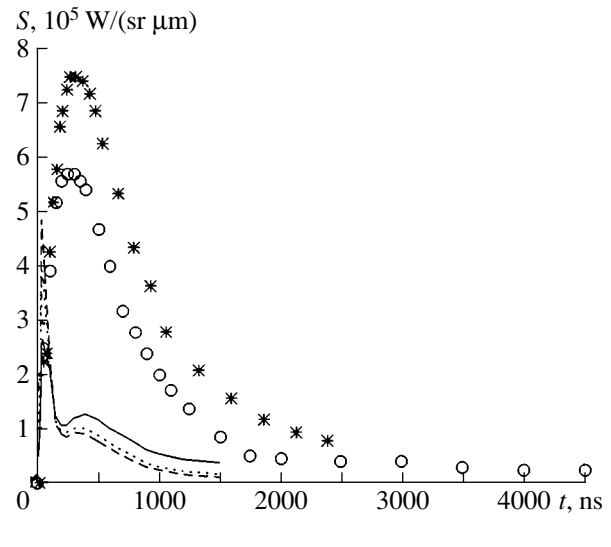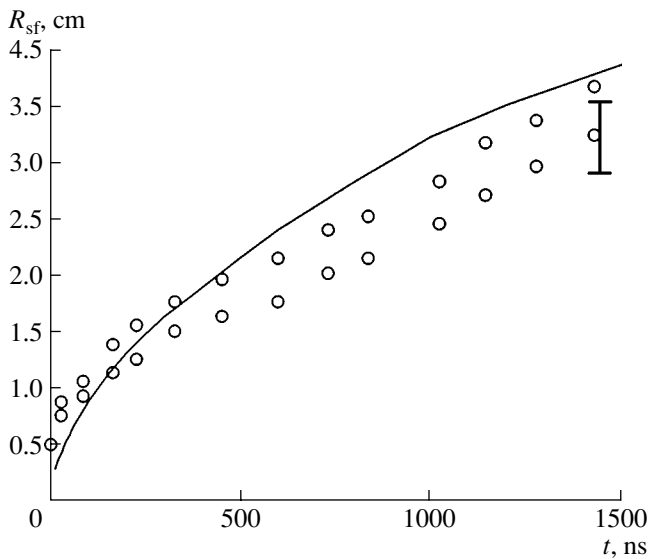

Fig. 3. Calculated time evolution of the emission intensity for the third second (solid curve) and fourth ($E_v = 2.71$–4.51 eV; dashed curve) spectral groups. The dotted curve shows the linear interpolation between the third and fourth groups for $\lambda = 0.4$ μm. The symbols show the experimental data obtained with an SDF7 detector for $E = 520$ J (circles) and 735 J (asterisks).

Fig. 4. Calculated (solid curve) and measured (circles) time evolution of the radius of the shock front in air at a pressure of 6 torr.
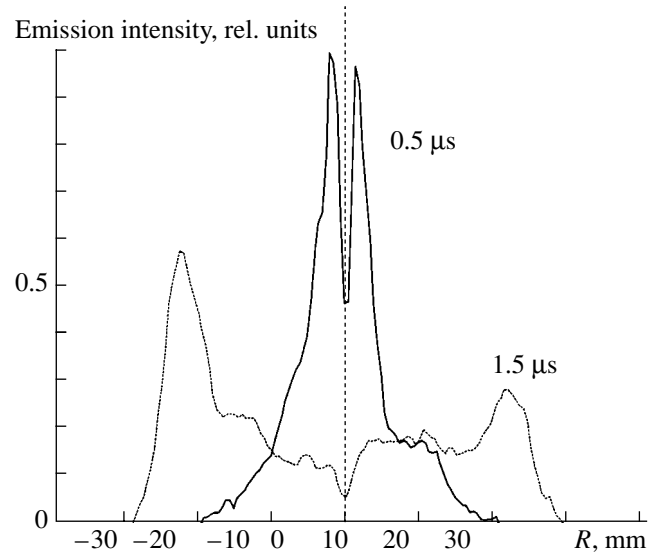
Fig. 5. Radial profiles of the GPO emission intensity at $t = 0.5$ and 1.5 μs.

iodine laser ($\lambda_{II} = 0.658$ μm). The phase shift of the probing radiation $\Delta N = \Delta \varphi / 2\pi$ was determined using interference patterns obtained with the help of a shearing and a Michelson interferometer. The measured phase shift was then compared to the calculated one.

(iii) The GPO dynamics was studied using a streak camera recording an *r–t* diagram of the GPO emission in the 0.7-μm spectral range.

(iv) The GPO emission spectrum in the 0.4- to 0.7-μm range was recorded using an ISP-28 spectrograph.

Typical time dependences of the GPO emission intensity at an air pressure of 6 torr are shown in Figs. 2 and 3. The maximum emission intensity is 8×10^5 W/(sr μm) in the 0.4-μm range and 2×10^5 W/(sr μm) in the 0.7-μm range.
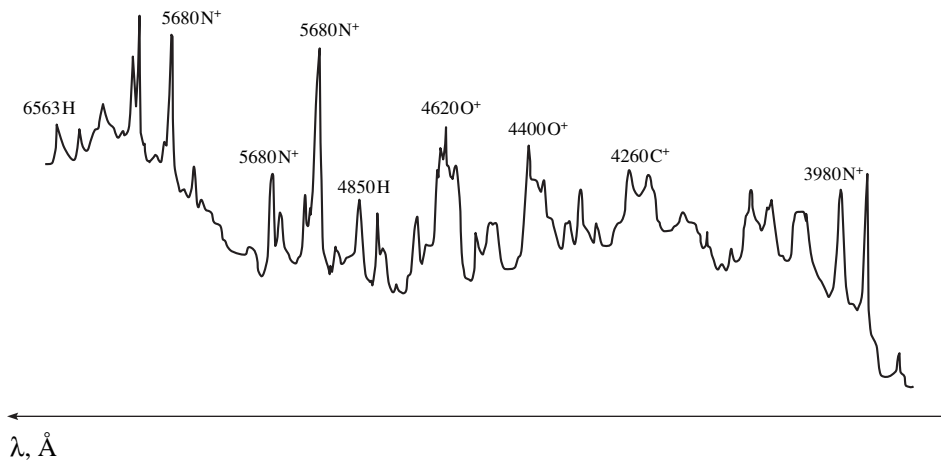
Fig. 6. GPO emission spectrum.

A streak image (an *r–t* diagram) of a GPO is shown in Fig. 4. The results obtained with a streak camera agree well with the results of interference shadowgraphy.

Figure 5 shows the radial profiles of the GPB emission intensity recorded with a streak camera at times of 0.5 and 1.5 μs.

Figure 6 shows the spectrum of the GPO emission. The spectrum is mainly composed of the spectral lines of the single-ionized components of the surrounding gas and target material.

An analysis of the interference pattern obtained at a time of 0.81 μs (Fig. 7) shows that the emerging optical inhomogeneity is almost spherically symmetric (with a diameter of 34 mm).The interference shift at a distance of 2 mm from the edge of the nonuniformity amounts

to three fringes, which corresponds to a change in the refractive index of $\Delta n > 10^{-4}$.

3. NUMERICAL SIMULATIONS AND THEIR COMPARISON WITH THE EXPERIMENT

The above experiments were simulated using the SND one-dimensional model [4], which incorporates gas-dynamics and radiative transfer equations (the latter were written in the multigroup quasi-diffusion approximation). The emission spectrum was divided into ten groups extending from the IR (the mean photon energy in the first group was $E_\nu = 0.25$ eV, and the width of the group was $\Delta E_\nu = 0.5$ eV) to the X-ray ($E_\nu = 624$ eV, $\Delta E_\nu = 752$ eV) spectral range. The absorption coefficients for each group were determined by averag-
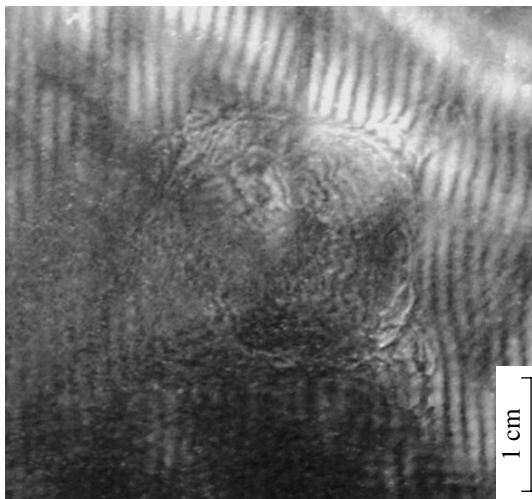

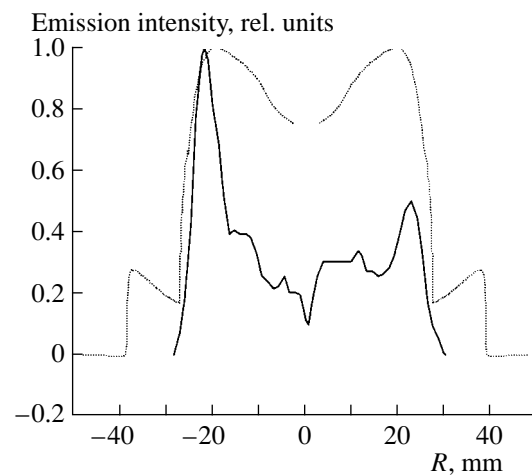
Fig. 7. GPO interference pattern at $t = 0.81$ μs.

Fig. 8. Measured (solid curve) and calculated (dotted curve) radial profiles of the GPO emission intensity at $t = 1.5$ μs.
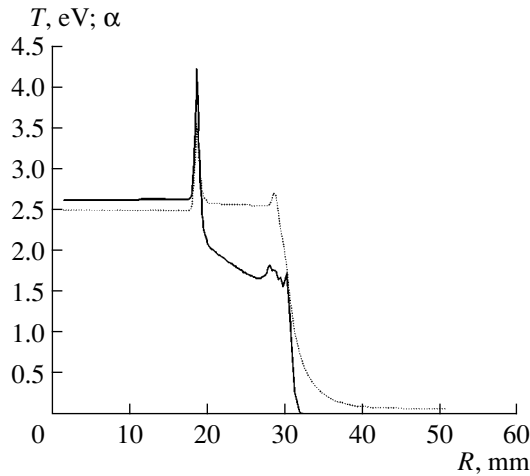
Fig. 9. Radial profiles of the temperature T (dotted curve) and α (solid curve) at $t = 1.5$ μs.

ing (over the Planckian distribution) the spectral coefficients obtained by K.L. Stepanov, G.S. Romanov, and L.K. Stanchits using the model [6].

A table equation of state for air [7] was used to describe the thermodynamic properties of hot air.

In simulations, the target radius was assumed to be $R_0 = 0.18$ cm and the shell thickness was set at $\Delta = 2.2$ μm. The initial specific density of the shell material was $\rho_0 = 1.1$ g/cm^3. An energy of $E = 735$ J was released in the inner region ($r_1 < r < r_2 = R_0 - \Delta$) with a initial density of $\rho_2 = 10^{-3}$ g/cm^3. This region modeled the evaporated shell substance. The value of r_1 was varied from 0.15 to 0.17 cm, which corresponded to the evaporated mass from 10^{-5} to 3.8×10^{-6} g. In order of magnitude, this corresponded to the estimates in [8]. At $r < r_1$ and $R_0 < r < R$, the initial density was set at $\rho_1 = 10^{-5}$ g/cm^3, which corresponded to a pressure of 6 torr at room temperature (0.025 eV). At the outer boundary ($r = R$), the free-emission condition was imposed.

The calculated GPO emission intensities in the 0.7- and 0.4-μm spectral ranges are shown in Figs. 2 and 3, respectively. For the "red" detector (0.65 μm), there is fair agreement with the experimental data, whereas for the "blue" detector (0.4 μm), the calculated emission intensity is much lower than the measured one. Since, according to our simulations, radiation in these spectral ranges is emitted from the region behind the shock front, this discrepancy may be related to the incorrect data on the ranges of photons with wavelengths of $\lambda \sim$ 0.4 μm in air.

The calculated size of the region covered by the shock wave is close to the GPO size measured by a streak camera (Fig. 8).

The calculated radial profiles of the emission intensity satisfactorily agree with the measured ones (see Fig. 7).

The calculated radial profiles of the temperature T and the degree of ionization α in a GPO are shown in Fig. 9. From these profiles one can estimate the change $\Delta n(r, t)$ in the refractive index of the GPO. For $t = 0.8$ μs and $r \approx 2$ cm, we have $\Delta n \approx 5 \times 10^{-5}$, which agrees with the experimental data.

REFERENCES

1. N. N. Zorev, G. V. Sklizkov, and A. S. Shikanov, Zh. Éksp. Teor. Fiz. **82**, 1104 (1982) [Sov. Phys. JETP **55**, 644 (1982)].
2. N. G. Basov, N. G. Mazur, N. G. Maksimchuk, *et al.*, Pis'ma Zh. Éksp. Teor. Fiz. **46**, 320 (1987) [JETP Lett. **46**, 402 (1987)].
3. G. A. Bondarenko, E. V. Gubkov, G. V. Dolgoleva, *et al.*, *II Zababakhin Scientific Talks, Snezhinsk, 1992*, Abstracts of Papers.
4. G. V. Dolgoleva, Metodiki Programmy Chisl. Resheniya Zadach Mat. Fiz., No. 2, 29 (1983).
5. V. I. Annenkov, V. A. Bagretsov, V. G. Bezuglov, *et al.*, Kvantovaya Élektron. **18**, 536 (1991).
6. K. L. Stepanov, G. S. Romanov, L. K. Stanchits, *et al.*, Dokl. Akad. Nauk BSSR **29**, 1094 (1985).
7. N. M. Kuznetsov, *Thermodynamical Functions and Shock Adiabats of Air* (Mashinostroenie, Moscow, 1965).
8. I. V. Nemchinov, Zh. Prikl. Mat. Mekh. **31**, 300 (1967).

Translated by N.N. Ustinovskiĭ